Quantifying Sediment Dynamics and Grain Size Characteristics in the Swiss Molasse and Quaternary Deposits

Inaugural dissertation
of the Faculty of Science,
University of Bern

presented by

Philippos Garefalakis
from Reutigen, Bern

Supervisors of the doctoral thesis:

Prof. Dr. Fritz Schlunegger
Institute of Geological Sciences

Dr. Alexander C. Whittaker
Imperial College London

License

Quantifying Sediment Dynamics and Grain Size Characteristics in the Swiss Molasse and Quaternary Deposits

Inaugural dissertation
of the Faculty of Science,
University of Bern

presented by

Philippos Garefalakis
from Reutigen, Bern

Supervisors of the doctoral thesis:

Prof. Dr. Fritz Schlunegger
Institute of Geological Sciences

Dr. Alexander C. Whittaker
Imperial College London

Accepted by the Faculty of Science

Bern, 8.12.2023

The Dean
Prof. Dr. Marco Herwegh

Für Karin,
Dimos & Eleni

Abstract

The Molasse basin recorded over the course of more than 30 Ma the evolution of the Central Alps, which underwent changes in tectonic processes and experienced shifts in the paleo climate. A common feature that records such changing conditions are variations in the sediment flux – the amount of supplied material – that was released from the catchment and stored in the foreland basin. Early attempts to estimate sediment fluxes date back to the 19th century, and subsequent approximations refined these estimates, leading to a more comprehensive understanding of sediment budgets throughout the Oligo- and Miocene times. However, these assessments were based on the entire basin's scale. This thesis shifts the focus to determine sediment fluxes at the scale of individual megafan systems that were recorded by numerous stratigraphic sections encountered in the Swiss Molasse Basin. It further delves into the topic to unravel the sedimentary dynamics of the paleorivers on these alluvial megafans and provides insights into the sedimentary dynamics and the broader tectono-geomorphological evolution of the Swiss Molasse Basin. A crucial part of this thesis bases on the application of models and quantitative approaches for simulating sediment fluxes. Amongst other parameters, the underlying concepts require information on grain sizes, which measurements build another important aspect of this thesis.

Accordingly, the first study in this thesis, *Chapter 2*, focuses on how grain sizes can be measured from stratigraphic deposits. For this, we measured grain sizes from outcrops in a Quaternary gravel pit near Bern, Switzerland, thereby following three different measuring approaches. To this end, we compared grain size data obtained from digital photos with data collected using callipers and mechanical sieving. The study highlights that the size of the longest visible axis, measured on digital photos, underestimates the full length of the grains' intermediate *b*-axis, measured by hand and calliper, by c. 17 %. We inferred that this underestimation arises from the occlusion of grains due to finer-grained matrix or particles.

The second research study, *Chapter 3*, explores the sediment transport dynamics of paleorivers on alluvial fans in the Swiss Molasse basin. It focuses on the intermittency of the dispersal systems as a proxy for the fan's activity, providing insights into the relative importance of tectonic and climatic controls. To this end, we calculated the intermittency factor for three paleo fan systems that were constructed during Oligo-Miocene times. These fans were recorded as stratigraphic sections where proximal-distal relationships are still preserved and are situated in the western, central, and eastern part of the Swiss Molasse basin. The results revealed variations in the sediment transport dynamics between the western, central, and eastern fans, shedding light on the Alpine's tectonic and climatic history. As such, the most active central fan and its paleorivers could accomplish its sediment transport work in c. 55 hours per year, whereas the paleorivers on the western and eastern fans were actively transporting sediment in c. 17 and 10 hours per year, respectively. While the construction of the central fan was most likely controlled by the legacy of the slab break-off of the oceanic European lithosphere at c. 32 – 30 Ma, the western fan was constructed when the related environmental adjustments reached a balance between

crustal uplift and surface erosion. For the eastern fan, the exhumation of the crystalline external massifs and associated tectonic unroofing in the core of the Alps possibly reduced the sediment supply to the Swiss Molasse Basin.

In the third research study, *Chapter 4*, we delved into the Swiss Molasse Basin's tectono-geomorphological evolution by analysing grain size data preserved in stratigraphic sections. The focus of this chapter lies on how the relative mobility, an indicator of the paleo streams' competence to transport the supplied material, evolved through space and time. We measured grain sizes along 15 stratigraphic sections that are situated in the Swiss Molasse Basin and which recorded the evolution of alluvial megafan sedimentation between c. 31 and 13 Ma. From the dataset of these systems, we determined the critical grain size of particles that were preferentially in transport, that is related to the concept of relative mobility. Our results revealed that the dispersal systems on these alluvial fans were capable to transport particles with grain sizes smaller than c. 12 mm. Throughout the investigated timespan, this critical grain size did not change significantly, despite the conditions that controlled the grain sizes in the paleostreams on the alluvial fans that underwent large changes, notably at the scale of the entire basin. We therefore suggested that the formation rate of accommodation space and the rate at which sediment was supplied to the fans, occurred in equilibrium.

In summary, this thesis provides insights into the challenges upon reading the stratigraphic record, on how to measure grain sizes from these and contributes to our understanding of the sedimentary processes and the dynamic evolution of the Swiss Molasse Basin.

Acknowledgements

My journey as a researcher began on Mt. Rigi in Central Switzerland, a place that not only captivated poets and authors like Johann Wolfgang von Goethe and Mark Twain, but also inspired me to discover the secrets of these steep 'Nagelfluh' walls. Academically, I made my first steps in these deposits during my bachelor's thesis, following in the footsteps of many other sedimentologists. Later, as part of my doctoral thesis, I went back to my research roots, because I was still captivated by the way that fluvial sediments build up into mighty mountains layer after layer. Beyond doubt, I have not travelled alone. Without the support of numerous individuals, the completion of the thesis you are currently holding in your hands, or rather viewing on your screen, would not have been possible. Hence, I would like to sincerely thank the following individuals and groups for their invaluable support and contributions throughout my research journey.

First and foremost, I am deeply indebted to my supervisor and mentor, Professor Dr. Fritz Schlunegger, for his unwavering guidance, profound knowledge, and constant encouragement. Fritz, I am truly grateful for granting me the opportunity to undertake this study, for providing me the freedom to explore my thoughts, and for your guidance that ensured I remained on track. Your friendly and supportive nature, coupled with your expertise, were very valuable during our discussions. I also wish to express my gratitude for your endless support in my academic growth over these years. Moreover, thank you for your patience, even when I occasionally stumbled in my expressions; it became somewhat of a recurring thing.

My sincere appreciation also extends to my co-supervisor, Dr. Alexander C. Whittaker, for his invaluable contributions, insightful guidance, and unwavering support throughout my doctoral studies. Alex, I would like to express my gratitude for your invaluable support during my stay in London. I greatly appreciate the focused discussions we had, and your counsel in deciphering the (at least to me) complex nature of the grain size fining model. My time at Imperial College was enriched by your welcoming presence, which made me feel an integral part of the research group.

I would also like to acknowledge my co-supervisor, Professor Dr. Jörg Hermann, for his valuable contributions and shared insights. Jörg, your experiences and, notably, your assistance in crafting the research proposal were very helpful and provided valuable guidance throughout this study.

I wish to express my appreciation to Professor Dr. Sébastien Castelltort for accepting the role of the external referee for this thesis.

Over these years, I learned to always anticipate the unexpected, a lesson that became evident as I found myself deeply dug in statistical topics and the grappling with numerous syntax errors. Without the technical and personal help of the people mentioned below, I would never have dared to delve into the convoluted world of programming.

I greatly appreciate the assistance provided by Ariel Henrique do Prado in my journey to master the Python programming language. Ariel, our scientific exchanges were not only motivating and greatly enriched my experience, but it was the countless discussions on movies, the Sandman, Star Wars, and even philosophical dialogues, such as profound conversations about infinity and time travel, that made the time fly by. I would also like to express my gratitude to Dr. David Mair for his unwavering positivity and support during various stages of this thesis. David, I highly appreciate your contributions to the research proposal's development and your valuable insights into various statistical subjects. Your guidance has been instrumental in my academic and personal progress.

My gratitude extends to many people who supported me in various aspects of this thesis. Dr. Dimitri Bandou is thanked for our very first attempt to remove pebbles from conglomerate beds while standing with me for two days in the rain. Dimitri, although we could not use the data, it greatly helped in shaping the subsequent experiments. Nils Güntert and Jonathan Pfander are acknowledged for their dedicated assistance in the field. Nils and Jone, your support in the field has been crucial in my research efforts, and you made the data collection process very efficient and enjoyable. Dr. Franziska Nyffenegger is thanked for her expert guidance in the process of sieving and the Berner Fachhochschule is thanked for providing access to the sieving facilities. Thank you, Franziska, to ensure the accuracy and precision of our laboratory work. Dr. Guilhem Amin Douillet is thanked for his thought-provoking and constructive discussions. I would also like to express my gratitude to Dr. Ferdinando Musso Piantelli and Sandro Truttmann for coffee-break conversations that not only offered a refreshing pause but also helped clarify my thoughts.

My friends are thanked for providing a welcome escape from the rigors of my doctoral studies, and my family is thanked for their unending support, although neither have full fully understood what I was doing with all these pebbles.

My deepest gratitude is reserved for Karin, who has been a steadfast presence throughout this journey and providing support from various angles while bringing joy into our lives; as well as to our two children, Dimos and Eleni, whose laughter have the remarkable ability to melt even the hardest rocks.

Contents

Chapter 3

Chapter 4

*"One's ideas must be as broad as Nature
if they are to interpret Nature."*

- Sir Arthur Conan Doyle [1]

[1] *A study in Scarlet, 1887*

1.

Introduction

1.1 Motivational overview

The Swiss Molasse Basin was, and still is, a playground for geologists. Undoubtedly, its appeal lies in the breathtaking landscapes, but even more in the processes that shaped this foreland basin. Since Bernhard Studer's (1825) first attempts to place its development into a larger geological context, it has become one of the best studied foreland basins from various perspectives. Not only because foreland basins generally serve as key to unravel the history of the adjacent hinterland, but also because particularly in Switzerland, large parts of the Swiss Molasse Basin are covered by cities and infrastructure, and thus serves as an important foundation ground. Moreover, rising interest in geothermal energy and CO_2 sequestration provided the basis to establish a 3D geological model of the Swiss Molasse Basin (GeoMol CH; Mock, 2017).

The Swiss Molasse Basin and its sedimentary fill recorded over the course of more than 30 million years valuable information of the evolution of the adjacent Alps and the foreland basin itself. The research of several decades has provided us with a profound knowledge on the distinct paleoenvironmental conditions (Keller, 1989; Platt and Keller, 1992; Schlunegger et al., 1997b; Kempf et al., 1999; Kuhlemann and Kempf, 2002; Strunck and Matter, 2002; Berger et al., 2005), the compositional and sedimentological properties of the deposits (Tanner, 1944; Büchi, 1958; Matter, 1964; Bürgisser, 1981; Eynatten, 2003) and the temporal relationships of the Molasse sediments (Engesser, 1990; Burbank et al., 1992; Schlunegger et al., 1996; Bolliger, 1998; Kempf and Matter, 1999; Kälin and Kempf, 2009), to name a few examples only. Amongst various landforms that dominated the Molasse basin throughout its evolution, alluvial megafans situated at the front of the rising Alps, particularly, improved our understanding of how the Molasse Basin and the adjacent hinterland are mechanically coupled (Beaumont, 1981; Allen et al., 1991; Sinclair and Allen, 1992; Schlunegger and Kissling, 2015; Kissling and Schlunegger, 2018). Therefore, numerous stratigraphic sections, that are considered as recorders of sedimentation on alluvial megafans, have been intensively explored according to their relationship to the formation of the Alps.

Consequently, shifts in the petrofacies of the sediments that build stratigraphic sections (Kempf et al., 1999; Schlunegger and Castelltort, 2016; Stutenbecker et al., 2019), the stacking pattern of the channel fills (Schlunegger et al., 1997b; Kempf and Matter, 1999) and the size of individual grains within the conglomerate beds (Kempf, 1998; Schlunegger, 1999; Schlunegger and Norton, 2013; Garefalakis and Schlunegger, 2018) were related to periods when major environmental adjustments took place in the Alps (Pfiffner, 2002). A common feature of many proxies that record changes in the environmental conditions is considered to be the amount of supplied material, or the sediment flux, that was released from the catchments and stored in the foreland basin (Hinderer, 2012). The advantage in determining the sediment flux of a specific system at various scales (e.g., of a single river or an entire fan) lies in the nature to use these estimates as a proxy for the denudation rates in the catchment, or for the underlying subsidence rates in the basin. Although determination of sediment fluxes or erosion rates are challenging, the very first attempts were already made in the 19th century (Studer, 1825; Kaufmann, 1860), yet on a qualitative basis. Subsequent approximations with a focus on estimating the amount of eroded material from the Alps, which was supplied to the Swiss Molasse Basin and other perialpine basins, were only attempted more recently (Schär, 1979; Hay et al., 1992; Schlunegger, 1999; Kuhlemann, 2000; Kuhlemann et al., 2001; Schlunegger et al., 2001). These authors approximated the volume or mass of sediments based on data collected in the Swiss Molasse Basin: They produced contour maps displaying thicknesses of deposited material, which in turn were drawn using information from restored cross-sections, stratigraphic sections and drill cores. Despite the various applied concepts, all these attempts of estimating sediment fluxes resulted in a similar trend of the sediment budget throughout Oligo- and Miocene times. Moreover, related outcomes have greatly improved our understanding on the evolution of the Alps and the Swiss Molasse basin.

However, the provided outcomes are based on the scale of the entire basin only. This opened the possibility to apply more recent concepts to determine sediment fluxes at the scale of individual megafan systems, and this idea frames the focus of this thesis, which is outlined in the next section.

1.2 Aims of the thesis

The rising interest in landscape evolution models provided us with a broad palette of quantitative approaches to simulate sediment fluxes using various approaches (Slaymaker, 2003; Bridge, 2009; Veldkamp et al., 2017). Amongst many, a concept that has particularly been applied to stratigraphic deposits, is the so-called grain size fining model, which has been developed in its current form by Fedele & Paola (2007). This model allows to predict grain sizes based on estimates of the volume of supplied sediments and upon using information of the underlying subsidence rates in the basin where stratigraphic architectures were built. Inversely, it allows to determine sediment fluxes from grain size measurements and estimates on the sediment accumulation rates only (Fedele and Paola, 2007; Duller et al., 2010; Whittaker et al., 2011). Both datasets can be extracted from stratigraphic deposits, particularly, from the numerous and thoroughly studied sections in the Swiss Molasse.

The application of the aforementioned model furthermore allows to investigate how regularly sediment transport occurred on an alluvial megafan. In this context, a proxy for expressing the activity on such fans is offered by the intermittency, which is a value that is defined as the ratio between the long-term sediment flux that arises from the Fedele & Paola (2007) model, and the short-term instantaneous sediment flux, calculated from equations that are based on concepts of bedload sediment transport (Meyer-Peter and Müller, 1948; Wong and Parker, 2006). In the latter context, the entrainment of clasts along a river bed bases on the inference that coarse-grained particles (> 2 mm) are transported if the drag force of the water flow exceeds a critical value, known as the critical shear stress (Shields, 1936). The related mechanisms have been elaborated through laboratory flume experiments and tested against field observations, and therefore build a robust first-order approximation to quantify and predict bedload fluxes (Ancey, 2020). Finally, the grain size fining model also allows to determine the critical grain size that is preferentially in transport. The related concepts have been referred to as relative mobility (Fedele and Paola, 2007). The technical details and explanations of the grain size fining model, the relative mobility and the bedload transport equations are given in the appendices of *Chapters 3* and *4*, as these would exceed by far the scope of an introduction.

Finally, to conduct the abovementioned models, one needs to establish a grain size dataset. In that context, of particular interest is the intermediate *b*-axis of a grain, as concepts and equations of sediment transport have been calibrated to this specific axis (Meyer-Peter and Müller, 1948). Therefore, the precise determination of this grain axis, (amongst the three axes of a grain that are oriented perpendicular to each other, i.e., *a*-, *b*- and *c*-axis) attained large interest in the grain size community over many decades (Zingg, 1935; Wolman, 1954; Wohl et al., 1996; Buscombe, 2008; Stähly et al., 2017). Nowadays, measurements of the sizes of coarse-grained clasts are commonly carried out on digital photographs, thereby using fully- or semi-automatic approaches (Bunte and Abt, 2001). Although related techniques to measure grain sizes from flat-lying deposits, such as in a riverbed, are rather straightforward, their direct application to stratigraphic deposits is ambiguous. This is mainly due to the nature of such sediments, because i) the identification of a specific grain axis is difficult, and ii) related sedimentary deposits often prevent the full exposure of the grain axes. The first objective is mainly because, when clasts are deposited in a river, they tend to be oriented with their *a*-/*b*-axes plane parallel to the riverbed, when viewed from above, and if the clasts are not imbricated. Consequently, the formation of the stratigraphic record, containing several layers of deposited material, disclose either the *a*-/*c*-axes or the *b*-/*c*-axes pairs, if the outcrops expose the sedimentary layering. Moreover, complex cutting-relationships of outcrop surfaces that are often oriented (sub-)vertical to the initial bedding of the sediments adds another obstacle upon identifying the grain sizes. The second objective is mainly related to the occlusion of grains, because the finer-grained matrix (e.g., small particles, sand) cover the coarser grains and thus occlude the full length of the grain axes, which is particularly the case for conglomerate beds. Conventionally, and for simplicity, the longest or largest visible axis (*LVA*) of particles in such deposits was measured as a proxy of the intermediate *b*-axis of a grain (Whittaker et al., 2010; Brooke et al., 2018; Garefalakis and Schlunegger, 2018). However, it remained to a certain degree unclear, to what extent the size of the *LVA* underestimates the size of the *b*-axis, particularly when measured from outcrops consisting sedimentary clasts. Therefore, the preparation of an answer to the question on how precisely grains can be measured from conglomerate beds builds an important aspect of this thesis. After this problem has been solved, the aforementioned models can be applied to tackle challenges on the relationships between grain size trends, sediment flux and the underlying controls thereof.

Therefore, in this thesis, I aim to answer the following research questions:

- *How precisely can grain sizes be measured from conglomerate beds?*
- *What were the magnitudes of sediment fluxes at the scale of individual megafans, and how frequently did these systems accomplish their transport work?*
- *What is the critical grain size that the paleorivers on these megafans could transport?*

Before we delve into the details, I provide a brief overview of the Swiss Molasse Basin's evolution, which serves as the study area, and then give an outline of the thesis' structure.

1.3 The evolution of the Swiss Molasse Basin

The North Alpine Foreland Basin (NAFB; Fig. 1.1) or Molasse Basin, located north to the European Alps, extends approximately 900 km from west to east through France, Switzerland, Germany and Austria. Its width can be as narrow as 10 km, particularly at its lateral ends, and reaches a maximum of 150 km in its centre (Pfiffner, 1986). The Swiss Molasse Basin (SMB; Fig 1.1) stretches from Geneva in the southwest to Lake Constance in the northeast and covers the area between the front of the Central Alps in the south, which has been referred to as the basal Alpine thrust in Alpine literature (e.g., Pfiffner, 1986), and the Jura Mountains in the north (Fig. 1.1). The Swiss Molasse Basin is further divided into the tilted, folded and thrusted Subalpine Molasse (SM; Fig. 1.1) at the proximal basin border, and the flat-lying and undeformed Plateau Molasse (PM; Fig. 1.1), situated at the more distal positions in relation to the Alps (Fig. 1.1).

The development of this peripheral foreland basin is mechanically coupled to the evolution of the Alps and started no later than in the Tertiary. The subduction of the European mantle lithosphere beneath the Adriatic plate induced a flexural bending of the European plate, thereby creating accommodation space (Beaumont, 1981; DeCelles and Giles, 1996; Pfiffner et al., 2002; Schlunegger and Kissling, 2022). This space was subsequently filled with the erosional products of the rising mountain range, resulting in a wedge-shaped basin in a cross-sectional view perpendicular to the strike of the Alps, with its thickest part (c. 5 km-thick) at the southern basin margin (Sommaruga et al., 2012). This basin-fill records two large-scale megacycles that were deposited between c. 35 and 10 – 5 Ma (Allen et al., 1991; Sinclair, 1997; Kuhlemann and Kempf, 2002). Each of these sedimentary cycles records the transition from a transgressive and thus marine to a regressive and terrestrial (freshwater) stage. The first transgressive-regressive cycle started with the North Helvetic Flysch unit (NHF; Pfiffner, 1986) and is associated to the Flysch stage of sedimentation that occurred from c. 35 Ma onwards (Sinclair, 1992). The following Molasse stages or Molasse type of sedimentation are characterised by four lithostratigraphic groups. Conventionally their German abbreviations are used (Matter et al., 1980), which are the UMM 'Untere Meeres Molasse' (Lower Marine Molasse), USM 'Untere Süsswasser Molasse' (Lower Freshwater Molasse), OMM 'Obere Meeres Molasse' (Upper Marine Molasse) and OSM 'Obere Süsswasser Molasse' (Upper Freshwater Molasse).

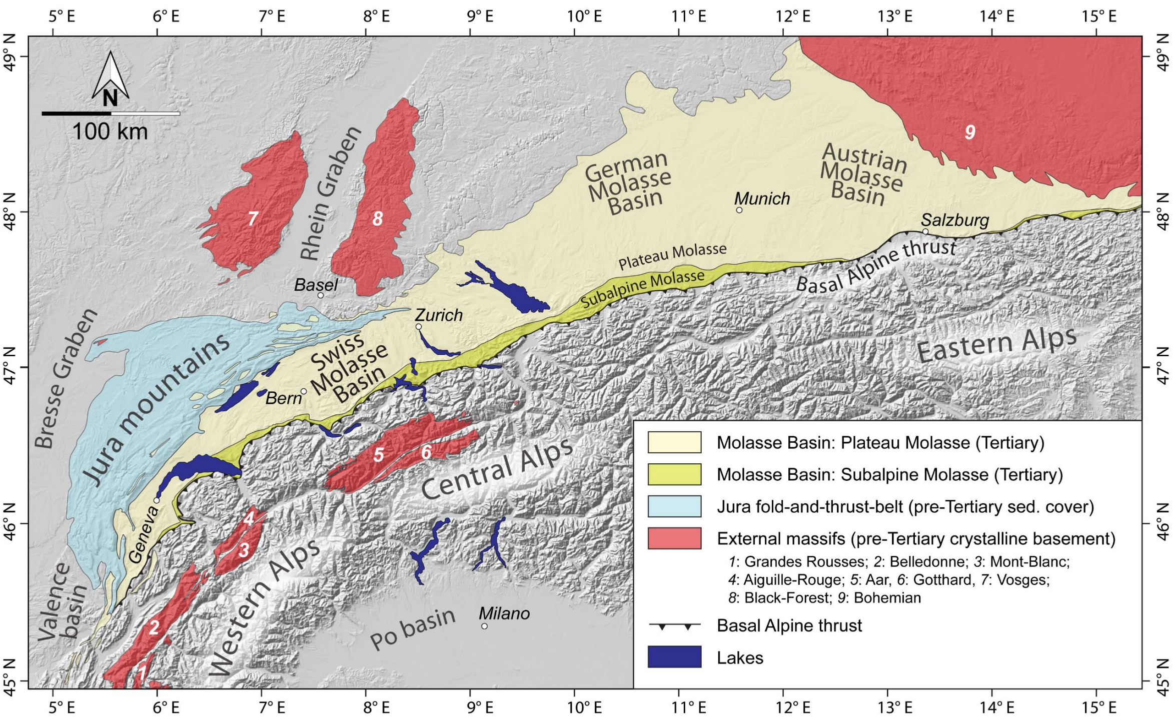

Figure 1.1: Simplified geological map of the Molasse Basin (North Alpine Foreland Basin) with the adjacent Alps, the Jura mountains and the external massifs. The study area of this thesis is situated in the Swiss Molasse Basin, north to the Central Alps. The geological units are modified after Schmid et al. (2004), and the underlying hillshade map is modified after Hengl et al. (2020).

The Flysch stage starting at c. 35 – 32 Ma (late Eocene to early Oligocene; Fig. 1.2a) was characterised by the sedimentation of sand- and mudstone sequences that were deposited on submarine fans in a deep marine trough (Allen et al., 1991). This period of the underfilled basin stage preceded the Molasse stages, which then recorded filled to overfilled basin conditions, but the Flysch type of sediments often build a seamless transition into the lowermost lithostratigraphic group of the Molasse, the UMM (Fig. 1.2; Pfiffner, 1986; Sinclair, 1997). The UMM deposits are characterised by sequences of deep marine marls and mudstones that transitioned into shallow-marine mud- and sandstones (Diem, 1986). As a consequence of the initial rise of the Alps and the retreat of the Alpine Tethys between c. 32 and 30 Ma (Allen et al., 1991; Handy et al., 2010; Schlunegger and Castelltort, 2016), these sediments gave way to the succeeding USM type of sediments. Sedimentation of the USM (middle to late Oligocene; Fig. 1.2) endured for c. 10 Myrs and was associated with large sediment fluxes that were recorded by several km-thick sedimentary sequences (Schlunegger et al., 2001). Related sediments are characterised by conglomerate, sandstone and mudstone beds of terrestrial origin (Stürm, 1973; Schlunegger et al., 1997c) which were deposited on alluvial megafans with a radial discharge pattern situated at the front of the Alps (Schlunegger et al., 1993; Kuhlemann and Kempf, 2002). Towards the north and thus at more distal positions in relation to the adjacent mountains, the alluvial megafans transitioned into meandering rivers that eventually merged with an axially oriented distributary system in the central part of the basin (Platt and Keller, 1992). The time around c. 21 – 20 Ma (Burdigalian; Fig. 1.2a) marks the end of the first transgressive-regressive megacycle when marine conditions were re-established in the Swiss Molasse Basin, marking the beginning of sedimentation of the OMM (Keller, 1989). A drop in the Alpine sediment fluxes (Kuhlemann et al., 2001), in combination with the marine transgression and the accelerated rise of the external massifs (Fig. 1.1; Boston et al., 2017; Herwegh et al., 2017) and enhanced subsidence of the foreland plate (Jost et al., 2016; Garefalakis and Schlunegger, 2019) enabled the establishment of underfilled basin conditions around these times. This caused the alluvial fans to back-step towards the Alps and sedimentation was dominated by sequences of shallow-marine sand- and mudstones formed under wave- and tidal-dominated conditions at both, proximal and distal positions in the Swiss Molasse Basin (Garefalakis and Schlunegger, 2019). The few remnants of the terrestrial depocenters at the southern basin margin, that interfingered with the Burdigalian seaway as fan deltas led to the construction of fanglomerates (Keller, 1989; Frieling et al., 2009). Thereafter, at c. 18 Ma, terrestrial sedimentation was re-established in the Molasse Basin, which initiated the stage of OSM sedimentation (late Burdigalian to late Serravallian; Fig. 1.2a). Related sediments consist of conglomerate, sandstone and mudstone beds that were deposited on alluvial megafans (Kempf and Matter, 1999). An increase in the supply rate of sediments from the Alps at that time supported the construction of the large depocenters that extended far into the basin, which laterally and distally partly interfingered with lacustrine and floodplain deposits (Kuhlemann and Kempf, 2002). OSM sedimentation continued up to 10 – 5 Ma (Fig. 1.2a), however, during the Pliocene an inversion of the Swiss Molasse Basin resulted in uplift and subsequent erosion of the Molasse deposits (Cederbom et al., 2004, 2011; Mazurek et al., 2006). Therefore, the youngest preserved OSM sediments date to c. 13 – 12 Ma, which are particularly preserved in the eastern basin only (Fig. 1.2b; Bolliger, 1998; Kälin and Kempf, 2009). This Pliocene phase of erosion (Baran et al., 2014) marked the end of the Molasse type of sedimentation.

During the Quaternary period, starting at 2.6 Ma, the Swiss Molasse Basin was dominated by recurring periods of glaciations and deglaciations (Preusser et al., 2011; Schlüchter et al., 2021). Phases of erosion, deposition and fluctuating ice extents led to the construction of several hundreds of meter-thick glacio-fluvial sequences of gravelly deposits covering the Molasse deposits (Claude et al., 2016). Commonly exposed in gravel quarries for industrial purposes, especially fluvially dominated deposits offer a high similarity to conglomerates. In contrast to these, the loosely packed gravels are astonishingly easy to excavate – advantageously to test various approaches of grain size measuring techniques.

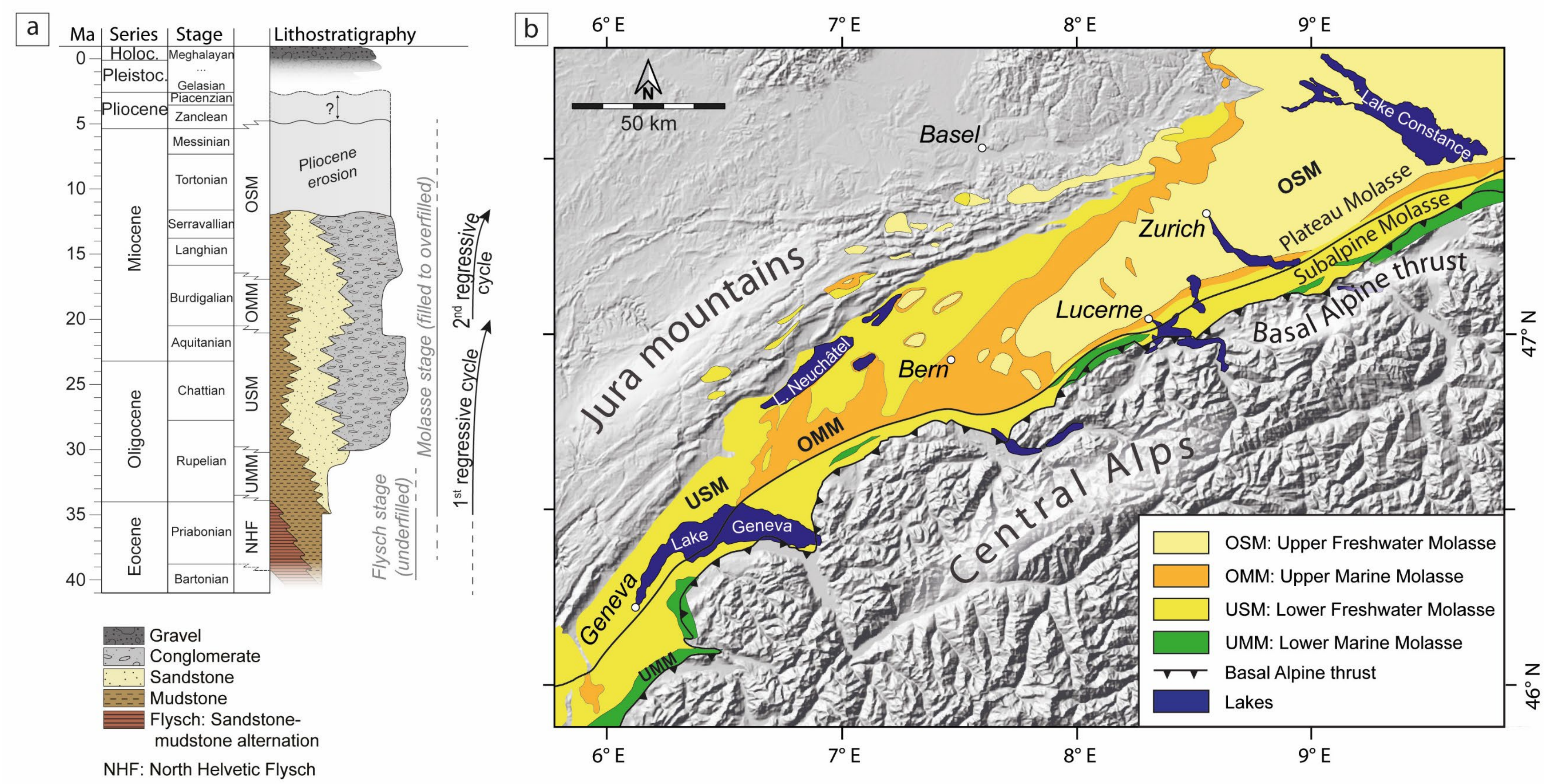

Figure 1.2: Stratigraphic architecture of the Molasse basin and preserved units in the basin. **a)** Generic lithostratigraphy of the Flysch and Molasse units, and the Quaternary Gravel deposits, and **b)** map showing the present-day preserved Molasse deposits in the Swiss Molasse Basin. a) and b) modified after Keller (2012) and b) modified after Schmid et al., (2004), and the underlying hillshade map is modified after Hengl et al. (2020).

1.4 Outline of the thesis

Chapter 2 provides a detailed description of how I measured the size of grains with the aim to answer the question whether the technique that I employed to measure the sizes of grains throughout all of my studies might be biased. To this extent, we carried out an experiment in a gravel pit (FIH in Fig. 1.3a) situated in the north-west of the Swiss Molasse Basin, where Quaternary deposits are exposed as steep headwalls. The advantage of these type of sediments is the loose packing of individual clasts, which can readily be excavated. Generally, I was interested in exploring how the various grain size measuring techniques yield different results. To this end, I particularly focused on measuring the size of grains i) upon sieving, ii) by hand with the help of callipers, and iii) on digital photographs, notably carried out on the same deposits. Upon statistically comparing the results with each other, grains measured through sieving and on photographs, albeit two different sampling techniques, yielded similar results for the intermediate *b*-axis. However, and which is the major outcome of *Chapter 2*, both approaches tend to underestimate the size of the fully-exposed *b*-axis by c. 17 %, when compared to the measurements by calliper. We suggest that this difference arises from the nature of the exposure where, the fine-grained matrix or other clasts might cover individual grains thereby preventing a full exposure of these.

Chapter 3 and *Chapter 4* can be considered as a composite study, because the core of both is offered by the grain size fining model developed in its present form by (Fedele and Paola, 2007). The scope of *Chapter 3*, however, lies on the determination of sediment fluxes at the scale of three alluvial megafans, whereas *Chapter 4* focuses on the concept of relative mobility, where I determine the critical grain size that is preferentially transported on the alluvial megafans in the Molasse Basin. The stratigraphic sections and related depositional systems that were analysed for the studies outlined in *Chapter 3* and *Chapter 4* are situated along the southern border of the Molasse basin, within the Plateau Molasse and the Subalpine Molasse (Fig. 1.3a). These several hundreds of m-thick stratigraphic sequences consist of alternations of conglomerate, sandstone and mudstone beds and are considered as the deposits on alluvial megafans. The individual sections have been analysed by previous authors regarding their petrofacies and sedimentologic properties, they have been placed in a chronological framework (Schlunegger et al., 1996, 1997a; Kempf et al., 1997; Kempf and Matter, 1999). Figure 1.3 provides an overview of the analysed stratigraphic sections, separated by their geographical location in the Swiss Molasse Basin (Fig. 1.3a), and the age ranges of the related deposits (Fig. 1.3b).

Figure 1.3 (next page): Study area and age range of the analysed sites. **a)** map with all sites that were analysed in this thesis, situated in the Swiss Molasse Basin. The geological units are based on GeoCover V2 (swisstopo, 2017) and the underlying digital elevation model is the LiDAR DEM Swiss ALTI3D (swisstopo, 2022). **b)** the age ranges of the stratigraphic sections, arranged against their geographical position in the SMB; Swiss Molasse Basin (see *Chapters 3* and *4* for the references that were used to obtain the chronological frameworks and more information on the construction of these).

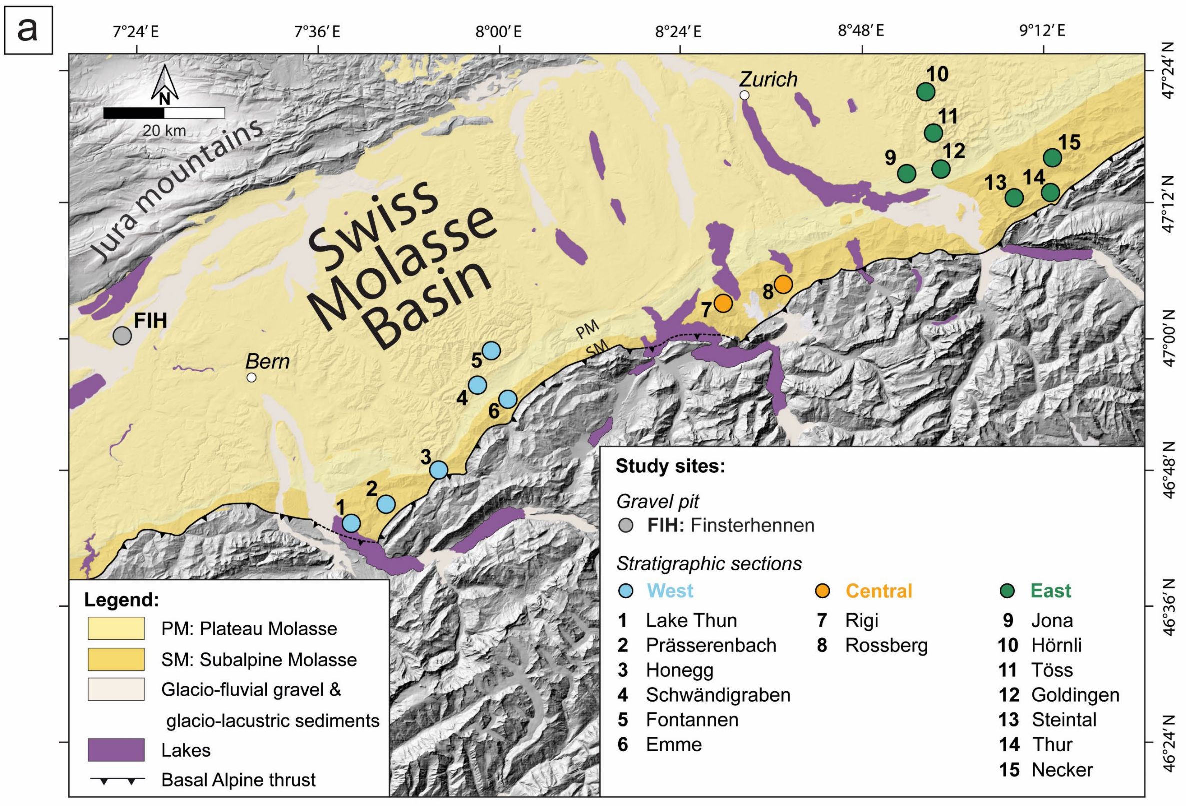
a
7°24′E
7°36′E
8°00′E
8°24′E
8°48′E
9°12′E
47°24′N
47°12′N
47°00′N
46°48′N
46°36′N
46°24′N
N
20 km
Jura mountains
Swiss Molasse Basin
Zurich
Bern
FIH
PM
SM
Legend:
PM: Plateau Molasse
SM: Subalpine Molasse
Glacio-fluvial gravel & glacio-lacustric sediments
Lakes
Basal Alpine thrust
Study sites:
Gravel pit
FIH: Finsterhennen
Stratigraphic sections
West
1 Lake Thun
2 Prässerenbach
3 Honegg
4 Schwändigraben
5 Fontannen
6 Emme
Central
7 Rigi
8 Rossberg
East
9 Jona
10 Hörnli
11 Töss
12 Goldingen
13 Steintal
14 Thur
15 Necker

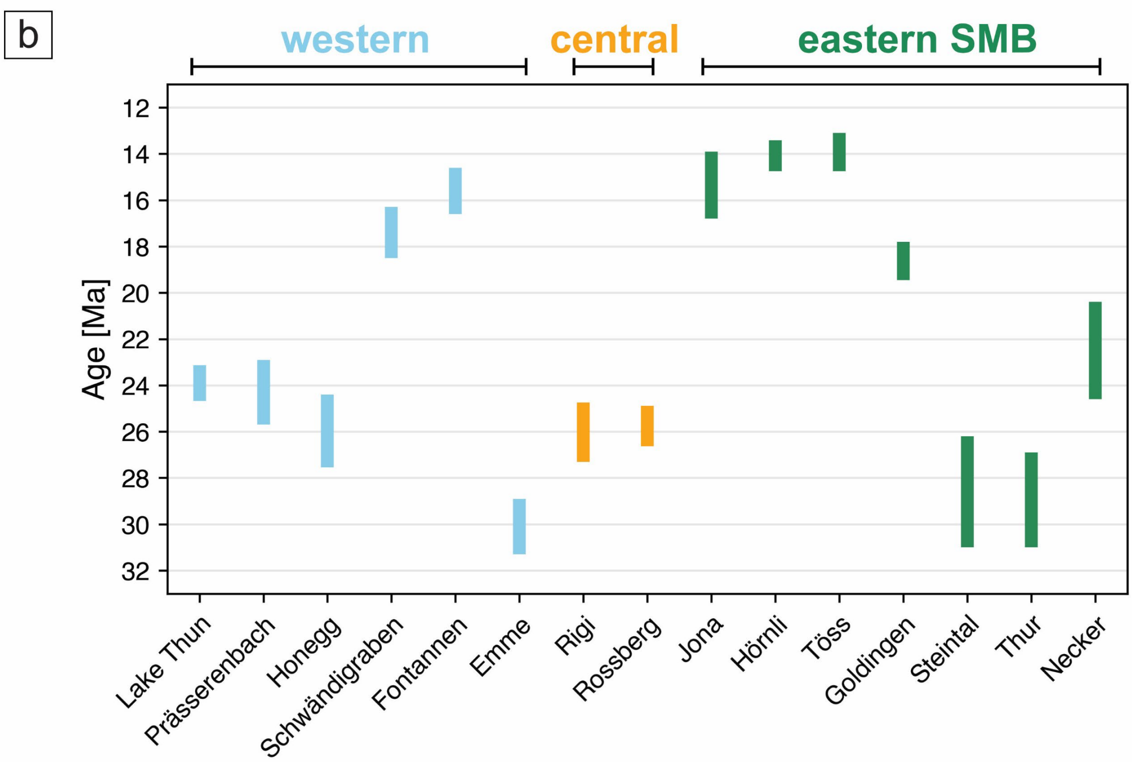
b
western
central
eastern SMB
Age [Ma]
12
14
16
18
20
22
24
26
28
30
32
Lake Thun
Prässerenbach
Honegg
Schwändigraben
Fontannen
Emme
Rigi
Rossberg
Jona
Hörnli
Töss
Goldingen
Steintal
Thur
Necker

The major scientific outcome of *Chapter 3* is that the streams constructing the analysed alluvial megafan deposits accomplished their transport work within a few hours to a few days per year. As will be shown, these outcomes are mostly explained by the different tectono-geomorphological conditions that were established particularly in the adjacent Alps at that time. *Chapter 4* highlights that the grain sizes of stratigraphic sections, when compared to each other at the scale of the entire basin, do not disclose significant differences. The application of the concept of the relative mobility, which offers a measure for estimating the size of particles that have the same probability of being in transport or deposited in the substrate, also disclosed no differences between the records of all analysed sections. We concluded that the lack of significant temporal trends in the granulometric data of the conglomerate beds points towards a long-term equilibrium between the rate at which sediment was supplied to the basin and the rate at which accommodation space was formed.

Finally, in *Chapter 5* I will provide a summary of the conclusions of the preceding chapters and give a brief reflexion on the outcomes of this thesis as well as an outlook.

1.5 Bibliography

Allen, P. A., Crampton, S. L., and Sinclair, H. D. (1991). The inception and early evolution of the north Alpine foreland basin, Switzerland. Basin Res. 3, pp. 143–163.
https://doi.org/10.1111/j.1365-2117.1991.tb00124.x

Ancey, C. (2020). Bedload transport: a walk between randomness and determinism. Part 1. The state of the art. J. Hydraul. Res. 58, pp. 1–17.
https://doi.org/10.1080/00221686.2019.1702594

Baran, R., Friedrich, A. M., and Schlunegger, F. (2014). The late Miocene to Holocene erosion pattern of the Alpine foreland basin reflects Eurasian slab unloading beneath the western Alps rather than global climate change. Lithosphere 6, pp. 124–131.
https://doi.org/10.1130/L307.1

Beaumont, C. (1981). Foreland Basins. pp. 291–329.
https://doi.org/10.1002/9781444303810

Berger, J.-P., Reichenbacher, B., Becker, D., Grimm, M., Grimm, K., Picot, L., et al. (2005). Paleogeography of the Upper Rhine Graben (URG) and the Swiss Molasse Basin (SMB) from Eocene to Pliocene. 94, pp. 697–710.
https://doi.org/10.1007/s00531-005-0475-2

Bolliger, T. (1998). Age and geographic distribution of the youngest Upper Freshwater Molasse (OSM) of eastern Switzerland. Eclogae Geol. Helv. 91, pp. 321–332.
https://doi.org/10.5169/seals-168426

Boston, K. R., Rubatto, D., Hermann, J., Engi, M., and Amelin, Y. (2017). Geochronology of accessory allanite and monazite in the Barrovian metamorphic sequence of the Central Alps, Switzerland. Lithos 286–287, pp. 502–518.
https://doi.org/10.1016/j.lithos.2017.06.025

Bridge, J. (2009). Numerical Modelling of Alluvial Deposits: Recent Developments.
https://doi.org/10.1002/9781444303131.ch4

Brooke, S. A. S., Whittaker, A. C., Armitage, J. J., D'Arcy, M., and Watkins, S. E. (2018). Quantifying Sediment Transport Dynamics on Alluvial Fans From Spatial and Temporal Changes in Grain Size, Death Valley, California. J. Geophys. Res. Earth Surf. 123, pp. 2039–2067.
https://doi.org/10.1029/2018JF004622

Büchi, U. P. (1958). Zur Geologie der Oberen Süsswassermolasse (OSM) zwischen Töss- und Glattal. Eclogae Geol. Helv. 51, pp. 73–105. (in German)
https://doi.org/10.5169/seals-162429

Bunte, K., and Abt, S. R. (2001). Sampling surface and subsurface particle-size distributions in wadable gravel-and cobble-bed streams for analyses in sediment transport, hydraulics, and streambed monitoring.
https://doi.org/10.2737/RMRS-GTR-74

Burbank, D. W., Engesser, B., Matter, A., and Weidmann, M. (1992). Magnetostratigraphic chronology, mammalian faunas, and stratigraphic evolution of the USM, Haute-Savoie, FR. Eclogae geol. Helv. 85, pp. 399–431.
https://doi.org/10.5169/seals-167013

Bürgisser, H. M. (1981). Fazies und Paläohydrogeologie der Oberen Süsswassermolasse im Hörnli-Fächer (Nordostschweiz). Eclogae Geol. Helv. 1, pp. 19–28. (in German)
https://doi.org/10.5169/seals-165087

Buscombe, D. (2008). Estimation of grain-size distributions and associated parameters from digital images of sediment. Sediment. Geol. 210, pp. 1–10.
https://doi.org/10.1016/j.sedgeo.2008.06.007

Cederbom, C. E., Sinclair, H. D., Schlunegger, F., and Rahn, M. K. (2004). Climate-induced rebound and exhumation of the European Alps. Geology 32, pp. 709–712.
https://doi.org/10.1130/G20491.1

Cederbom, C. E., van der Beek, P. A., Schlunegger, F., Sinclair, H. D., and Oncken, O. (2011). Rapid extensive erosion of the North Alpine foreland basin at 5-4Ma. Basin Res. 23, pp. 528–550.
https://doi.org/10.1111/j.1365-2117.2011.00501.x

Claude, A., Akçar, N., Ivy-Ochs, S. D., Schlunegger, F., Kubík, P. W., Dehnert, A., et al. (2016). Timing of early Quaternary gravel accumulation in the Swiss Alpine Foreland. Geomorphology, 276, pp. 71-85.
https://doi.org/10.1016/j.geomorph.2016.10.016

DeCelles, P. G., and Giles, K. A. (1996). Foreland basin systems. Basin Res. 8, pp. 105–123.
https://doi.org/10.1046/j.1365-2117.1996.01491.x

Diem, B. (1986). Die Untere Meeresmolasse zwischen der Saane (Westschweiz) und der Ammer (Oberbayern). Eclogae Geol. Helv. 79, pp. 493–559. (in German)
https://doi.org/10.5169/seals-165842

Duller, R. A., Whittaker, A. C., Fedele, J. J., Whitchurch, A. L., Springett, J., Smithells, R., et al. (2010). From grain size to tectonics. J. Geophys. Res. Earth Surf. 115, pp. 1–19.
https://doi.org/10.1029/2009JF001495

Engesser, B. (1990). Die Eomyidae (Rodentia, Mammalia) der Molasse der Schweiz und Savoyens. Systematik und Biostratigraphie. Schweizerische Paläontologische Abhandlungen 112, pp. 1–144. (in German)

Eynatten, H. v. (2003). Petrography and chemistry of sandstones from the Swiss Molasse Basin: An archive of the Oligocene to Miocene evolution of the Central Alps. Sedimentology 50, pp. 703–724.
https://doi.org/10.1046/j.1365-3091.2003.00571.x

Fedele, J. J., and Paola, C. (2007). Similarity solutions for fluvial sediment fining by selective deposition. J. Geophys. Res. Earth Surf. 112, pp. 1–13.
https://doi.org/10.1029/2005JF000409

Frieling, D., Ähnelt, M., Scholz, H., and Reichenbacher, B. (2009). Sequence stratigraphy of an alluvial fan-delta in the Upper Marine Molasse (Pfänder area, Late Burdigalian, Miocene). Zeitschrift der Deutschen Gesellschaft für Geowissenschaften 160, pp. 333–357.
https://doi.org/10.1127/1860-1804/2009/0160-0333

Garefalakis, P., and Schlunegger, F. (2018). Link between concentrations of sediment flux and deep crustal processes beneath the European Alps. Sci. Rep. 8, 183, pp. 11.
https://doi.org/10.1038/s41598-017-17182-8

Garefalakis, P., and Schlunegger, F. (2019). Tectonic processes, variations in sediment flux, and eustatic sea level recorded by the 20-Myr old Burdigalian transgression in the Swiss Molasse basin. Solid Earth 10, pp. 2045–2072.
https://doi.org/10.5194/se-10-2045-2019

Handy, M. R., M. Schmid, S., Bousquet, R., Kissling, E., and Bernoulli, D. (2010). Reconciling plate-tectonic reconstructions of Alpine Tethys with the geological-geophysical record of spreading and subduction in the Alps. Earth-Science Rev. 102, pp. 121–158.
https://doi.org/10.1016/j.earscirev.2010.06.002

Hay, W. W., Wold, C. N., and Herzog, J. M. (1992). "Preliminary Mass-Balance 3D Reconstructions of the Alps and the surrounding areas during the Miocene," in Computer Graphics in Geology. Lecture Notes in Earth Sciences, 41, eds. R. Pflug and J. W. Harbaugh (Springer, Berlin), pp. 99–110.
https://doi.org/10.1007/BFb0117790

Hengl, T., Leal Parente, L., Krizan, J., and Bonannella, C. (2020). Continental Europe Digital Terrain Model at 30 m resolution based on GEDI, ICESat-2, AW3D, GLO-30, EUDEM, MERIT DEM and background layers (v0.3) [Data set]. Zenodo.
https://doi.org/10.5281/zenodo.4724549

Herwegh, M., Berger, A., Baumberger, R., Wehrens, P., and Kissling, E. (2017). Large-Scale Crustal-Block-Extrusion During Late Alpine Collision. Sci. Rep. 7, 413.
https://doi.org/10.1038/s41598-017-00440-0

Hinderer, M. (2012). From gullies to mountain belts: A review of sediment budgets at various scales. Sediment. Geol. 280, pp. 21–59.
https://doi.org/10.1016/j.sedgeo.2012.03.009

Jost, J., Kempf, O., and Kälin, D. (2016). Stratigraphy and palaeoecology of the Upper Marine Molasse (OMM) of the central Swiss Plateau. Swiss J. Geosci. 109, pp. 149–169.
https://doi.org/10.1007/s00015-016-0223-6

Kälin, D., and Kempf, O. (2009). High-resolution stratigraphy from the continental record of the Middle Miocene Northern Alpine Foreland Basin of Switzerland. Neues Jahrbuch für Geol. und Paläontologie - Abhandlungen 254, pp. 177–235.
https://doi.org/10.1127/0077-7749/2009/0010

Kaufmann, J. F. (1860). Untersuchungen über die mittel- und ostschweizerische subalpine Molasse. Neue Denkschriften der Allg. Schweizerischen Gesellschaft für die Gesamten Naturwissenschaften 17. (in German)

Keller, B. (1989). Fazies und Stratigraphie der Oberen Meeresmolasse (unteres Miozän) zwischen Napf und Bodensee. Unpubl. PhD Thesis, University of Bern, Switzerland. pp. 401. (in German)

Keller, B. (2012). Facies of Molasse based on a section across the central part of the Swiss Plateau. Bull. für Angew. Geol. 17, pp. 3–19.
https://doi.org/10.5169/seals-349238

Kempf, O. (1998). Magnetostratigraphy and facies evolution of the Lower Freshwater Molasse (USM) of eastern Switzerland. Unpubl. PhD thesis, University of Bern, Switzerland. pp. 283.

Kempf, O., Bolliger, T., Kälin, D., Engesser, B., and Matter, A. (1997). “New Magnetostratigraphic Calibration of Early to Middle Miocene Mammal Biozones of the North Alpine Foreland Basin,” in Actes du Congrès BIochrom’97, eds. J. Aguilar, S. Legendre, J. Michaux, and B. Mammalienne, pp. 547–561.

Kempf, O., and Matter, A. (1999). Magnetostratigraphy and depositional history of the Upper Freshwater Molasse (OSM) of eastern Switzerland. Eclogae Geol. Helv. 92, pp. 97–103.
https://doi.org/10.5169/seals-168650

Kempf, O., Matter, A., Burbank, D. W., and Mange, M. (1999). Depositional and structural evolution of a foreland basin margin in a magnetostratigraphic framework: The eastern Swiss Molasse Basin. Int. J. Earth Sci. 88, pp. 253–275.
https://doi.org/10.1007/s005310050263

Kissling, E., and Schlunegger, F. (2018). Rollback Orogeny Model for the Evolution of the Swiss Alps. Tectonics 37, pp. 1097–1115.
https://doi.org/10.1002/2017TC004762

Kuhlemann, J. (2000). Post-Collisional Sediment Budget of Circum-Alpine Basins (Central Europe). Mem. Di Sci. Geol. Padova 52, pp. 1–93.

Kuhlemann, J., Frisch, W., Dunkl, I., and Székely, B. (2001). Quantifying tectonic versus erosive denudation by the sediment budget: the Miocene core complexes of the Alps. Tectonophysics 330, pp. 1–23.
https://doi.org/10.1016/S0040-1951(00)00209-2

Kuhlemann, J., and Kempf, O. (2002). Post-Eocene evolution of the North Alpine Foreland Basin and its response to Alpine tectonics. Sediment. Geol. 152, pp. 45–78.
https://doi.org/10.1016/S0037-0738(01)00285-8

Matter, A. (1964). Sedimentologische Untersuchungen im östlichen Napfgebiet (Entlebuch - Tal der Grossen Fontanne, Kt. Luzern). Eclogae Geol. Helv. 57, pp. 315–429. (in German)

Matter, A., Homewood, P., Caron, C., Rigassi, D., van Stuijvenberg, J., Weidmann, M., et al. (1980). “Flysch and Molasse of western and central Switzerland,” in Geology of Switzerland: A Guide Book. Part B Geological Excursions, eds. P. Homewood and R. Trümpy (Basel: Wepf & Co), pp. 261–293.

Mazurek, M., Hurford, A. J., and Leu, W. (2006). Unravelling the multi-stage burial history of the Swiss Molasse Basin: Integration of apatite fission track, vitrinite reflectance and biomarker isomerisation analysis. Basin Res. 18, pp. 27–50.
https://doi.org/10.1111/j.1365-2117.2006.00286.x

Meyer-Peter, E., and Müller, R. (1948). Formulas for Bed-Load Transport. Proc. 2nd Meet. Int. Assoc. Hydraul. Res., pp. 39–64. Available at: http://resolver.tudelft.nl/uuid:4fda9b61-be28-4703-ab06-43cdc2a21bd7

Mock, S. (2017). The Neogene tectonic and geodynamic evolution of the central Swiss Molasse Basin: An integrative 3-D modeling , tectonic and thermochronological study. Unpubl. PhD thesis, University of Bern, Switzerland. pp. 145.

Pfiffner, O. A. (1986). Evolution of the north Alpine foreland basin in the Central Alps (Switzerland). Spec. Publs int. Ass. Sediment. 8, pp. 219–228.
https://doi.org/10.1002/9781444303810.ch11

Pfiffner, O. A. (2002). The Swiss Alps and their peripheral foreland basin: Stratigraphic response to deep crustal processes. 21, 2, pp. 1-16.
https://doi.org/10.1029/2000TC900039

Pfiffner, O. A., Schlunegger, F., and Buiter, S. J. H. (2002). The Swiss Alps and their peripheral foreland basin: Stratigraphic response to deep crustal processes. Tectonics 21, pp. 1-16.
https://doi.org/10.1029/2000tc900039

Platt, N. H., and Keller, B. (1992). Distal alluvial deposits in a foreland basin setting-the Lower Freshwater Molasse (Lower Miocene), Switzerland: sedimentology, architecture and palaeosols. Sedimentology 39, pp. 545–565. https://doi.org/10.1111/j.1365-3091.1992.tb02136.x

Preusser, F., Graf, H. R., Keller, O., Krayss, E., and Schlüchter, C. (2011). Quaternary glaciation history of northern Switzerland. E G Quat. Sci. J. 60, pp. 282–305. https://doi.org/10.3285/eg.60.2-3.06

Schär, J.-P. (1979). Mouvements verticaux, érosion dans les Alpes, aujourd'hui et au cours du Miocène. Eclogae Geol. Helv. 1, pp. 263–270. (in French) https://doi.org/10.5169/seals-164836

Schlüchter, C., Akçar, N., and Ivy-Ochs, S. D. (2021). "The Quaternary Period in Switzerland," in Landscapes and Landforms of Switzerland. World Geomorphological Landscapes, ed. E. Reynard (Springer, Cham), pp. 47–69. https://doi.org/10.1007/978-3-030-43203-4_2

Schlunegger, F. (1999). Controls of surface erosion on the evolution of the Alps: Constraints from the stratigraphies of the adjacent foreland basins. Int. J. Earth Sci. 88, pp. 285–304. https://doi.org/10.1007/s005310050265

Schlunegger, F., Burbank, D. W., Matter, A., Engesser, B., and Mödden, C. (1996). Magnetostratigraphic calibration of the Oligocence to Middle Miocene (30-15 Ma) mammal biozones and depositional sequences of the Swiss Molasse Basin. Eclogae Geol. Helv. 89, pp. 753–788. https://doi.org/10.5169/seals-168650

Schlunegger, F., and Castelltort, S. (2016). Immediate and delayed signal of slab breakoff in Oligo / Miocene Molasse deposits from the European Alps. Nat. Sci. Rep. 6, pp. 1–11. https://doi.org/10.1038/srep31010

Schlunegger, F., Jordan, T. E., and Klaper, E. M. (1997a). Controls of erosional denudation in the orogen on foreland basin evolution: The Oligocene central Swiss Molasse Basin as an example. Tectonics 16, pp. 823–840. https://doi.org/10.1029/97TC01657

Schlunegger, F., and Kissling, E. (2015). Slab rollback orogeny in the Alps and evolution of the Swiss Molasse basin. Nat. Commun. 6, 8605. https://doi.org/10.1038/ncomms9605

Schlunegger, F., and Kissling, E. (2022). Slab Load Controls Beneath the Alps on the Source-to-Sink Sedimentary Pathways in the Molasse Basin. Geosci. 12. https://doi.org/10.3390/geosciences12060226

Schlunegger, F., Leu, W., and Matter, A. (1997b). Sedimentary sequences, seismic facies, subsidence analysis, and evolution of the Burdigalian Upper Marine Molasse Group, central Switzerland. AAPG Bull. 81, pp. 1185–1207. https://doi.org/10.1306/522B4A19-1727-11D7-8645000102C1865D

Schlunegger, F., Matter, A., Burbank, D. W., Leu, W., Mange, M., and Màtyàs, J. (1997c). Sedimentary sequences, seismofacies and evolution of depositional systems of the Oligo/Miocene Lower Freshwater Molasse Group, Switzerland. Basin Res. 9, pp. 1–26. https://doi.org/10.1046/j.1365-2117.1997.00029.x

Schlunegger, F., Matter, A., and Mange, M. A. (1993). Alluvial fan sedimentation and structure of the southern Molasse Basin margin, Lake Thun area, Switzerland. Eclogae Geol. Helv. 86, pp. 717–750. https://doi.org/10.5169/seals-167260

Schlunegger, F., Melzer, J., and Tucker, G. E. (2001). Climate, exposed source-rock lithologies, crustal uplift and surface erosion: A theoretical analysis calibrated with data from the Alps/North Alpine foreland basin system. Int. J. Earth Sci. 90, pp. 484–499. https://doi.org/10.1007/s005310100174

Schlunegger, F., and Norton, K. P. (2013). Headward retreat of streams in the Late Oligocene to Early Miocene Swiss Alps. Sedimentology 60, pp. 85–101. https://doi.org/10.1111/sed.12010

Schmid, S. M., Fügenschuh, B., Kissling, E., and Schuster, R. (2004). Tectonic map and overall architecture of the Alpine orogen. Eclogae Geol. Helv. 97, pp. 93–117. https://doi.org/10.1007/s00015-004-1113-x

Shields, A. (1936). Anwendung der Ähnlichkeitsmechanik und der Turbulenzforschung auf die Geschiebebewegung. Preuss. Versuchsanstalt für Wasserbau und Schiffbau 26. (in German)

Sinclair, H. D. (1992). Turbidite sedimentation during Alpine thrusting: the Taveyannaz sandstones of eastern Switzerland. Sedimentology 39, pp. 837–856. https://doi.org/10.1111/j.1365-3091.1992.tb02156.x

Sinclair, H. D. (1997). Flysch to molasse transition in peripheral foreland basins: The role of the passive margin versus slab breakoff. Geology 25, pp. 1123–1126. https://doi.org/10.1130/0091-7613(1997)025<1123:FTMTIP>2.3.CO;2

Sinclair, H. D., and Allen, P. A. (1992). Vertical vs. horizontal motions in the Alpine orogenic wedge: stratigraphic response in the foreland basin. Basin Research, 4, pp. 215-232.
https://doi.org/10.1111/j.1365-2117.1992.tb00046.x

Slaymaker, O. (2003). The sediment budget as conceptual framework and management tool. Interact. between Sediments Water, pp. 71–82.
https://doi.org/10.1007/978-94-017-3366-3_12

Sommaruga, A., Eichenberger, U., and Marillier, F. (2012). Seismic Atlas of the Molasse Basin. Ed. by Swiss Geophys. Com. - Matér. Géol. Suisse, Géophys. 44, 64 pp. Available at:
https://www.geologieportal.ch/en/themes/fundamentals-of-geology/geophysics/seismic-atlas.html

Stähly, S., Friedrich, H., and Detert, M. (2017). Size ratio of fluvial grains' intermediate axes assessed by image processing and square-hole sieving. J. Hydraul. Eng. 143, pp. 1–6.
https://doi.org/10.1061/(ASCE)HY.1943-7900.0001286

Strunck, P., and Matter, A. (2002). Depositional evolution of the western Swiss Molasse. Eclogae Geol. Helv. 95, pp. 197–222.
https://doi.org/10.5169/seals-168955

Studer, B. (1825). Beyträge zu einer Monographie der Molasse, oder geognostische Untersuchungen über die Steinarten und Petrefacten, die zwischen den Alpen und dem Jura gefunden warden. (in German)
Available at: http://dx.doi.org/10.3931/e-rara-10467

Stürm, B. (1973). Die Rigi Schüttung - Sedimentpetrographie, Sedimentologie, Palaeogeographie, Tektonik. Unpubl. PhD Thesis, University of Bern, Switzerland, pp. 96.

Stutenbecker, L., Tollan, P. M. E., Madella, A., and Lanari, P. (2019). Miocene basement exhumation in the Central Alps recorded by detrital garnet geochemistry in foreland basin deposits. Solid Earth, 1581–1595.
https://doi.org/10.5194/se-10-1581-2019

swisstopo (2017). Metadaten des Produkts GeoCover V2. Technical Report.
Available at: www.swisstopo.ch

swisstopo (2022). swissALTI-3D - Das hoch aufgelöste Terrainmodell der Schweiz.
Available at: www.swisstopo.ch

Tanner, H. J. (1944). Beitrag zur Geologie der Molasse zwischen Ricken und Hörnli. Mitteilungen der Thurgauischen Naturforschenden Gesellschaft 33, pp. 1–108. (in German)
https://doi.org/10.5169/seals-593971

Veldkamp, A., Baartman, J. E. M., Coulthard, T. J., Maddy, D., Schoorl, J. M., Storms, J. E. A., et al. (2017). Two decades of numerical modelling to understand long term fluvial archives: Advances and future perspectives. Quat. Sci. Rev. 166, pp. 177–187.
https://doi.org/10.1016/j.quascirev.2016.10.002

Whittaker, A. C., Attal, M., and Allen, P. A. (2010). Characterising the origin, nature and fate of sediment exported from catchments perturbed by active tectonics. Basin Res. 22, 809–828.
https://doi.org/10.1111/j.1365-2117.2009.00447.x

Whittaker, A. C., Duller, R. A., Springett, J., Smithells, R. A., Whitchurch, A. L., and Allen, P. A. (2011). Decoding downstream trends in stratigraphic grain size as a function of tectonic subsidence and sediment supply. pp. 1363–1382.
https://doi.org/10.1130/B30351.1

Wohl, E. E., Anthony, D. J., Madsen, S. W., and Thompson, D. M. (1996). A comparison of surface sampling methods for coarse fluvial sediments. Water Resour. Res. 32, pp. 3219–3226.
https://doi.org/10.1029/96WR01527

Wolman, M. G. (1954). A method of sampling coarse river-bed material. Am. Geophys. Union 35, pp. 951–956.
https://doi.org/10.1017/CBO9781107415324.004

Wong, M., and Parker, G. (2006). Reanalysis and Correction of Bed-Load Relation of Meyer-Peter and Müller Using Their Own Database. J. Hydraul. Eng. 132, pp. 1159–1168.
https://doi.org/10.1061/(asce)0733-9429(2006)132:11(1159)

Zingg, T. (1935). Beitrag zur Schotteranalyse. Schweiz. Miner. Petrogr. Mitt. 15, pp. 39–140. (in German)
https://doi.org/10.3929/ethz-a-000103455

2.

Comparison of three grain size measuring methods applied to coarse-grained gravel deposits

Philippos Garefalakis*, Ariel Henrique do Prado*, David Mair*, Guilhem Amin Douillet*, Franziska Nyffenegger** and Fritz Schlunegger*

* University of Bern, Institute of Geological Sciences, Baltzerstrasse 1+3, 3012 Bern, Switzerland

** Berner Fachhochschule (BFH), Institut Siedlungsentwicklung und Infrastruktur ISI, Kompetenzbereich Geotechnik und Naturereignisse, Pestalozzistrasse 20, 3400 Burgdorf, Switzerland

Published in Sedimentary Geology, 15 March 2023

DOI: https://doi.org/10.1016/j.sedgeo.2023.106340

Abstract

The size of grains in gravel and conglomerate deposits is most easily measured on photos taken from related outcrops. However, the occlusion of grains by the sedimentary matrix or other grains, and possible distortions of photos, could introduce a bias in such datasets. Here, we explore the uncertainties associated with datasets where the lengths of the grains were measured on photos. To this end, we analysed coarse-grained (>2 mm) fluvial material from a gravel pit (Bern, Switzerland). We compared grain size data collected from digital photos with the results where the same material was measured with a calliper and mechanically sieved. Our analyses reveal that the percentile values such as the D_{16}, D_{50} and D_{84} of datasets where the grains' longest visible axes were measured on digital photos best correlate to the corresponding percentile values of data collected through sieving. We also find that the longest visible axes of grains measured on digital photos are c. 17% smaller than the lengths of the intermediate *b*-axes of grains measured with a calliper. We therefore suggest to measure the longest visible axes on digital photos, and to correct the data by a corresponding factor such as +17% for the target grain size percentiles.

2.1 Introduction

Grain size distributions, percentiles values thereof and grain shapes are essential to quantify the dynamics and processes of sediment transport in rivers (e.g., Dade and Friend, 1998; Church, 2006; Petit et al., 2015). Grain size distributions additionally allow a classification of the sorting of a grain assemblage (e.g., Inman, 1952; Rice and Church, 2010; Schlunegger et al., 2020) and help to characterise the morphologies and bedforms of coarse-grained fluvial deposits (e.g., Lane, 1955; Brayshaw, 1984; Leopold, 1992; MacKenzie et al., 2018). Research in these fields has mainly focussed on material >2 mm, which is commonly referred to as the 'coarse-grained fraction' of the clastic material, and called gravel or conglomerate for unconsolidated or lithified material, respectively (Wentworth, 1922). Fluvial transport of such material starts if a grain-size dependent flow strength is exceeded, and the subsequent transport occurs as bedload through rolling and/or gliding along the riverbed (e.g., Dade and Friend, 1998; Recking, 2010). The transport of smaller grains (<2 mm, sand fraction and finer) either occurs as bedload or suspension load, depending on the strength and dynamics of the flow (e.g., Parker, 1990; Wong and Parker, 2006).

A single grain can be described as an ellipsoid, where its three axes, the largest-, the intermediate- and the smallest-axis (all oriented perpendicular to each other) are referred to the *a*-, *b*- and *c*-axis, respectively (Yuzyk and Winkler, 1991; Fig. 2.1a). The ratio of these individual grain axes allows for a quantitative characterisation of the grain shape (Zingg, 1935; Blott and Pye, 2007). From the three axes of a grain, the *a*-axis is generally oriented sub-perpendicular to the water flow direction whereas its orthogonal *b*-axis is aligned sub-parallel and the *c*-axis vertical to the discharge direction (Wadell, 1936; Brayshaw, 1984; Aberle and Nikora, 2006; Fig. 2.1a). Consequently, the *b*-axis is generally used for the calibration of hydraulic formulae elaborated from flume experiments and for the quantification of sediment fluxes (e.g., Meyer-Peter and Müller, 1948; Parker, 1990; Recking, 2013).

2.1.1 Challenges with measuring grains from outcrops and scope of the study

Most authors investigating the sizes and shapes of coarse-grained material have focused on modern systems where individual grains are lying flat on gravel bars and where the *a*-/*b*-axes plane can be viewed from above (Johansson, 1976; Brayshaw, 1984; Strom et al., 2010). However, the partial hiding of clasts due to imbrication or burial of individual grains poses major challenges when collecting grain size data from photos (e.g., Kellerhals and Bray, 1971; Adams, 1979; Graham et al., 2010). Furthermore, since photos display the grains as projections in 2D, they cannot resolve the full 3D-view of a single grain, which introduces an additional bias during the collection of such grain size datasets (e.g., Warrick et al., 2009; Stähly et al., 2017). This problem is amplified for photos taken from deposits of ancient fluvial systems like unconsolidated gravel or consolidated conglomerate beds, because larger grains might partially occlude neighbouring clasts, or the fine-grained matrix can hide parts of individual clasts. Such archives are commonly exposed through outcrops (Fig. 2.1), which cut (sub)-vertically through the bedding, thus exposing the thickness of a layer rather than the surface of a bed. Outcrops thus tend to display the *a*-and *c*- or the *b*- and *c*-axes (rather than the *a*- and *b*-axes when seen from above), which in turn depends on the paleoflow direction (Paola and Mohrig, 1996; Storz-Peretz and Laronne, 2013, Guerit et al., 2018). The entire length of a grain can thus only be seen if the material is completely excavated and measured with a calliper. Accordingly, the identification and measurement of specific grain axes (e.g., the *b*-axis), have remained a challenge.

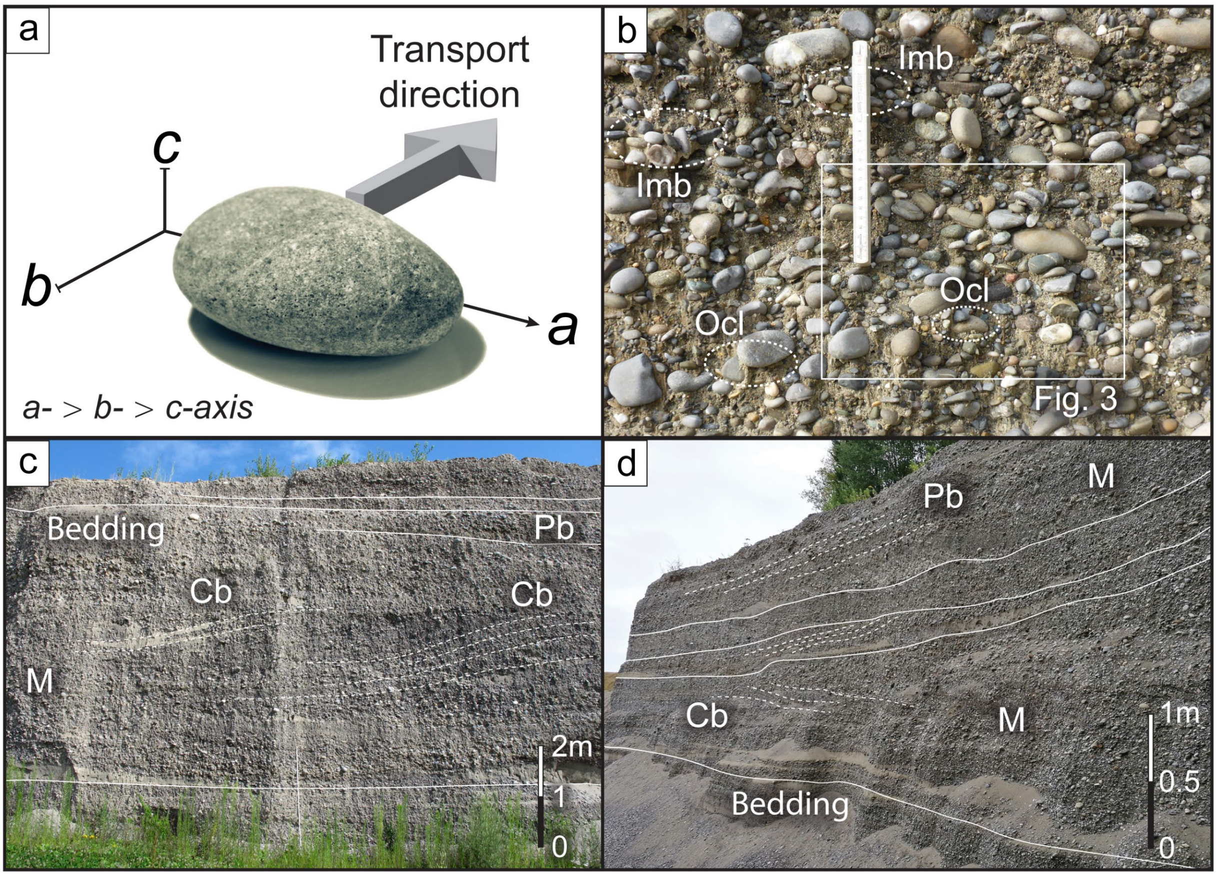

Cb: Cross-beds; *Pb:* Planar-beds; *M:* Massive-beds; *Imb*: Imbricated grains; *Ocl:* Occluded grains

Figure 2.1: Grain axes and coarse-grained gravelly outcrops. **a)** Grain axes in relation to each other and to the transport direction. **b)** Close-up image of gravel outcrop (location 3; Fig. 2.2a) where imbricated and occluded grains are visible. **c)** and **d)** Example of outcrops with bedding surfaces perpendicular to the wall exposure. Occasionally, cross-, parallel- and massive-bedded structures are visible. See also Fig. 2.2 for location of these outcrops. Photo c) © N. Akçar / J. Pfander, 2020.

Here, we address this problem and explore the uncertainties that can be associated upon collecting grain size datasets from outcrops of gravelly deposits. For this, we compare the percentile values of datasets where the grains were measured (i) by hand with a calliper, (ii) on digital photos and (iii) through sieving of the same material. Among the three methods, the presumably simplest, non-invasive, and least time-consuming one is the approach where the grains are measured on digital photos. We therefore put our major focus on the results of photo surveys and explore whether photo-specific factors (distorted or non-distorted, rectified photos), different approaches to select the grains on photos (either randomly or using a regular spaced grid), and the number of measurements introduce a bias upon collecting grain size datasets.

2.2 Previous studies

2.2.1 Measuring grains from gravelly riverbeds

Over the past decades, the quantification of coarse material in modern streams has undergone a significant development. Time-consuming in-situ class counting (e.g., Wolman, 1954) and sieving techniques (e.g., Batel, 1960) were partially substituted by manual collections of grain size datasets on photos (e.g., Ritter and Helley, 1969; Kellerhals and Bray, 1971; Adams, 1979) and approaches where clasts were semi-automatically measured (e.g., Butler et al, 2001; Buscombe, 2008; Graham et al., 2010; Purinton and Bookhagen, 2019). Grain measurements on photos (both manually or semi-automatic) are usually accomplished on a selection of grains only, using either grid-by-area (e.g., Ibbeken and Schleyer, 1986; Church et al., 1987) or grid-by-number concepts (i.e., class-based; e.g., Wolman, 1954; Kellerhals and Bray, 1971). Nowadays the flourishing use of uncrewed aerial vehicles (i.e., drones) allows simple and rapid surveys of large areas. This has proven an efficient method for the quantification of grain sizes (e.g., Carbonneau et al., 2018; Woodget et al., 2018; Marchetti et al., 2022). In the past years, applications of semi-automatic grain size measuring methods, where algorithms model ellipsoids around single grains, have gained an increasing popularity (Detert and Weitbrecht, 2012; Purinton and Bookhagen, 2019). Despite improvements in such techniques, measuring sizes of fluvial gravels in an accurate and reproducible way still bears challenges (e.g., Chardon et al., 2021; Purinton and Bookhagen, 2021; Mair et al., 2022).

2.2.2 Measuring grains from outcrops of sedimentary rocks

Sieving has been used to determine grain sizes from coarse-grained unconsolidated material (e.g., Claude et al., 2017; Preusser et al., 2021). It avoids selective picking of clasts, yet it delivers a single mesh-size value averaging a 3-parameter shape. Other attempts to measure grain sizes from such deposits were accomplished after the clasts were excavated from the outcrops. Individual grains were then measured manually with the help of callipers. However, this method is time consuming, yields a limited number of measurements, and bears the risk of shattering individual pebbles upon extraction, (Tanner, 1944; Haldemann, 1948; Nemec et al., 1980). Subsequently, the measurement of grains on photos has attracted interest because this has proven a simple, non-invasive, and least time-consuming method. This is especially the case when the deposits are lithified (such as conglomerate beds) and individual clasts cannot be readily extracted. Neumann-Mahlkau (1967) were among the first to conduct such surveys applied to outcrops. They particularly found that measuring the grains' longest visible axes on photos yield different results (differences of ±10–50%) than sieving the same material. Based on this work, the grains' longest visible axes have been preferably measured on photos taken from outcrops (e.g., Paola and Mohrig, 1996, Duller et al., 2010; Litty et al., 2016; Garefalakis & Schlunegger, 2018). Similarly, upon using material collected from a 1.2 m-deep trench in a gravel bed, Guerit et al. (2018) evidenced differences (±10–15%) between grain size data that was collected through sieving the material or through measuring the length of the *b*-axis by hand and calliper. In other contributions, Graham et al. (2005a, 2005b) introduced what they referred to as an automatic grain sizing (AGS) technique where the shape of individual grains (visible on photos) is automatically fitted through ellipsoids. These were then used to establish a grain size dataset. Such an approach yields area-by-number results, and the data needs to be converted following e.g., Kellerhals and Bray (1971). Storz-Peretz and Laronne (2013) built on this AGS method and found agreements ranging from ±3 to ±27% (values are method specific) between the results where grains were measured on photos, by hand and with a calliper after excavation of the material, and finally through sieving the material.

Storz-Peretz and Laronne (2013) showed that shaded photos taken from short distances provided better data than photos taken with either a flash or a strong exposure contrast. For volcaniclastic sediments, Smith and Maxwell (2021) applied photogrammetric techniques on photos taken with drones, on which they measured the longest and shortest visible axes of grains >2 cm with a workflow fully applicable to coarse-grained fluvial successions.

2.3 Study site and methods

2.3.1 Study site

The study was realised in the Finsterhennen gravel pit (approx. 47°00'55"N / 7°10'10"E; Bern, Switzerland) where unconsolidated coarse-grained fluvial material is exposed in large headwalls (Fig. 2.2). For these Quaternary deposits, measurements of cross-bed orientations and alignments of imbricated clasts revealed a paleoflow direction towards the N-NE (Fig. 2.2a; Pfander et al., 2022). We collected grain size data from eight locations that have four different orientations relative to the paleoflow direction (Fig. 2.2a). The grain size data from these locations were grouped as pairs (hereafter sites A – D), where sites A and C are oriented sub-perpendicular to the paleoflow, whereas sites B and D are aligned sub-parallel to the measured paleoflow direction (figs. 2.2a and b). All clasts were extracted from the same c. 7 m-thick stratigraphic layer (i.e., FIH-S – LFA 4 in Pfander et al., 2022). The analysed deposits comprise clast-supported coarse-grained gravels, which are mostly massive-bedded but show cross-beds and imbrications in places (figs. 2.1b, c and d). The grains consist of a large variety of lithologies, mostly derived from Alpine conglomerates, with a predominant occurrence of limestone constituents and a minor contribution of quartzites, granites and metamorphic pebbles (Pfander et al., 2022).

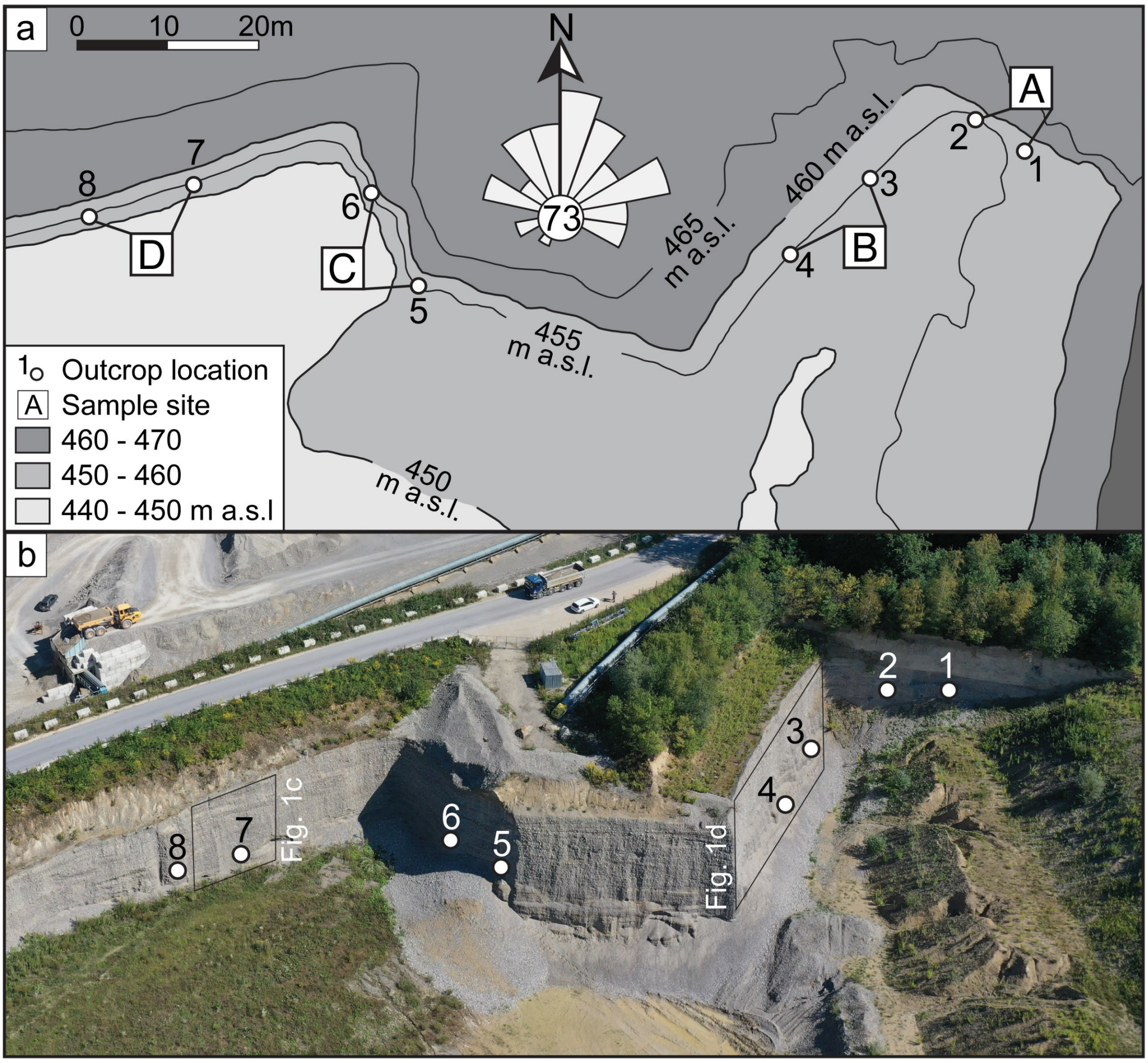

Figure 2.2: Study site. **a)** Contour map of the gravel pit near Finsterhennen (Bern, Switzerland) with locations 1-8 and sample sites A-D (© swisstopo). Discharge rose mod. After Pfander et al., 2022. **b)** Drone-photo showing the gravel pit with locations 1-8 and outcrops of Fig. 2.1. Photo b) © N. Akçar / J. Pfander, 2020.

2.3.2 Data collection

In the field, we first sprayed an outcrop surface spanning c. 0.5–1 m^2 using a biodegradable yellow paint for later identification of the grains. We then took digital photos with a hand-held camera (Panasonic Lumix FT5, digital single lens mirrorless camera, 16.6 megapixels, JPEG-photos of format 4:3). By taking photos at a distance of 1–1.5 m from the outcrops, enough (> 200) clasts are portrayed on one single photo, and the photo resolution is sufficient to allow identification of grains ≥2 mm (e.g., Storz-Peretz and Laronne, 2013). We took photos perpendicular to the outcrop to avoid perspective distortion effects. We then measured only grains situated approximately 10 cm away from the photo frame to reduce distortion introduced by the camera lens. Nevertheless, we measured grains on the original (distorted) and the ortho-corrected (undistorted) photos to explore whether this influences the resulting grain size datasets. The related orthorectification was accomplished using the method of Zhang (2000), which is implemented in *OpenCV* (Bradski, 2000). The resolution of the distorted and undistorted photos is quite similar and ranges between 0.14 and 0.29 mm/pixel. Next, the material was excavated with a shovel at a depth of approximately twice the size of the largest visible grain, and the material, which also includes the fines <2 mm and grains beyond the coloured surface, was collected in a tarpaulin to prevent any loss of coloured grains. We measured only the coloured grains (that are equally visible on the photos) by hand with a calliper, and we sieved the bulk-material (fines <2 mm included) in the laboratory. Hereafter, the results of the manual measurements with the help of a calliper are referred to as hand data, the datasets collected on photos as photo data and the datasets established through sieving as sieve data, respectively.

For each site A – D, individual samples from two neighbouring outcrop locations were merged so that the material composition of the sampled outcrop was better represented (Mosley and Tindale, 1985). We then measured 200 grains per sample site upon collecting the data by hand and calliper and on photos. This number is sufficient to calculate accurate percentile values for moderately- to well-sorted material (Daniels and McCusker, 2010; Galia et al., 2017; Eaton et al., 2019), as is the case in the Finsterhennen gravel pit (Pfander et al., 2022). Upon sieving, the minimum representative weight of the sample to be collected was estimated based on the length of the largest *b*-axis measured with a calliper. Ideally, as documented in the tables by various authors (e.g., Neumann-Mahlkau; 1967; Church et al., 1987; Bunte and Abt, 2001), the percentage of the largest grains should be 1% of the sampled bulk-material if the lengths of the *b*-axis lays between 32 and 128 mm. However, in case where this length is larger than 128 mm, the largest grains could constitute 5% to the sample mass (Church et al., 1987; Bunte and Abt, 2001; Attal et al., 2015). At each sample site (Fig. 2.2a) we excavated between 32 and 61 kg of bulk-sediment (Table 2.1) and yielded corresponding values between approximately 0.4 – 5.5%. Although these (e.g., site A; Table 2.1) are in cases slightly larger than suggested for an ideal survey (Church et al., 1987), they can be regarded as acceptable (Guerit et al., 2018; Watkins et al., 2020; Harvey et al., 2022). Note that grains <2 mm were then removed from the datasets for further analyses to ensure a consistent comparison between the different measuring methods, because grains <2 mm cannot be measured by hand with callipers and are barely detectable on photos taken with the setup (camera, distance) used in this study.

Sieve data	Bulk samples [kg]	Used samples [kg]	Fines <2 mm [kg]	Fines <2 mm [%]	Largest *b*-axis (hand data) [mm]	Approximate proportion of largest *b*-axis to bulk and used samples*
Site A	61.38	50.14	11.24	18.31	139.93	5.1% (bulk) / 5.5% (fines removed)
Site B	32.96	25.08	7.88	23.91	47.43	0.4% (bulk) / 0.6% (fines removed)
Site C	37.41	30.59	6.82	18.23	69.01	1.3% (bulk) / 1.6% (fines removed)
Site D	40.09	31.10	8.99	22.42	68.32	1.2% (bulk) / 1.6% (fines removed)

*after Church et al., 1987

Table 2.1: Sieve sample mass. Bulk-weight and truncated-weight (rounded to 2 decimals) of the sieve samples for each sample site.

2.3.3 Grain size measurement protocols

2.3.3.1 Measurements by hand and calliper

For the collection of the hand data (Table 2.2), the coloured grains were separated from the others, evenly poured on a tarpaulin, and we blindly picked grains for measuring the lengths of the *a*-, *b*- and *c*-axis with a digital calliper (resolution of 0.01 mm and precision of ±0.03 mm). Two grains larger >150 mm (*a*-axis) from site A were measured with a meter stick, yet at a lower precision (c. ±5 mm).

2.3.3.2 Measurements on digital photos

On each photo, we manually measured the longest visible axis (hereafter denoted as *LVA*) and the shortest visible axis (hereafter denoted as *SVA*), which are oriented perpendicular to each other. We followed two approaches upon selecting the grains to be measured (Table 2.2): A digital grid was added on each photograph as a first approach (grid-approach, *GA*; Fig. 2.3a); and randomly placed dots were generated on each photo as a second one (random-approach, *RA*; Fig. 2.3b). For the *GA* (e.g., Green, 2003; Warrick et al., 2009; Strom et al., 2010), we placed a regularly spaced grid of 4x4 cm calibrated to the meter stick on each photo (Fig. 2.3a). The grid size has been selected using the average grain size of c. 39 mm of the hand data (*a*-axis) of all 4 sample sites, which varies between 31.5 mm (site B) and 48.9 mm (site A). Following this method, we measured the *LVA* and *SVA* of each grain situated beneath an interception dot (Fig. 2.3a). The *RA* is a method where the *LVA* and *SVA* of coincidentally marked grains are measured (e.g., Wolman, 1954; Duller et al., 2010; Whittaker et al., 2011; Fig. 2.3b). Such a selection of grains is accomplished through superimposing randomly generated dots on the photos using a built-in ImageJ Macro (vs. 1.51f; Rasband, 1997-2018). In cases where the same grain was situated beneath multiple grid-intersection dots (*GA*) or several randomly placed dots (*RA*), this grain was measured only once. This approach is thought to reduce a potential bias caused by an overrepresentation of large grains (Diplas and Fripp, 1992; Bunte and Abt, 2001; Attal et al., 2015), but is different from other but similar grid-based measuring methods (e.g., Kellerhals and Bray, 1971). Additionally, both methods (*GA* and *RA*) were shown to yield consistent results, and they prevent a selective bias by the operator (e.g., Kellerhals and Bray, 1971; Adams, 1979; Ibbeken and Schleyer, 1986; Church et al., 1987; Strom et al., 2010). Following the aforementioned concepts, we manually measured a total of 100 grains per photo (i.e., 200 measurements per site) with the photo analysis software ImageJ. This resulted in four grain size datasets for each location, which are referred to as: *GAD* (grid-approach distorted photos), *GAU* (grid-approach undistorted photos), *RAD* (random-approach distorted photos) and *RAU* (random-approach undistorted photos), respectively (Table 2.2).

Method name	Measuring approach	Specific factor	Axes	Sample size	References (selection)
Hand	Measurement by calliper	Grains >150 mm by meter-stick	*a*-/*b*-/*c*-axis	200	Wolman, 1954 Green, 2003
Photo	*GAD*: measurement beneath grid-intersection	Distorted images	*LVA* / *SVA*	200	Kellerhals & Bray, 1971 Ibbeken & Schleyer, 1986 Paola & Mohrig, 1996 Bunte & Abt, 2001 Rice & Church, 2010
Photo	*GAU*: measurement beneath grid-intersection	Non-distorted images	*LVA* / *SVA*	200	
Photo	*RAD*: measurement when marked by random dot	Distorted images	*LVA* / *SVA*	200	
Photo	*RAU*: measurement when marked by random dot	Non-distorted images	*LVA* / *SVA*	200	
Sieving	dry-/wet-sieving	Weight-percentage; square-hole sieves	*Ds** (*b*-axis equiv.)	30-60 kg**	Church et al., 1987 Attal et al., 2015

**Ds*: sieve-axis; Square-hole sieves allow the *b*-axis of a grain to pass through (e.g., Church et al., 1987).
**Sampling weight depending on proportion of the largest *b*-axis from the hand data to the sampled mass (see also Table 2.1)

LVA: Longest; and ***SVA***: Shortest visible axis
GAD: Grid-approach, distorted images; ***GAU***: Grid-approach, undistorted images
RAD: Random-approach, distorted images; ***RAU***: Random-approach, undistorted images

Table 2.2: Grain size measuring approaches. Key properties of the methods used in this study.

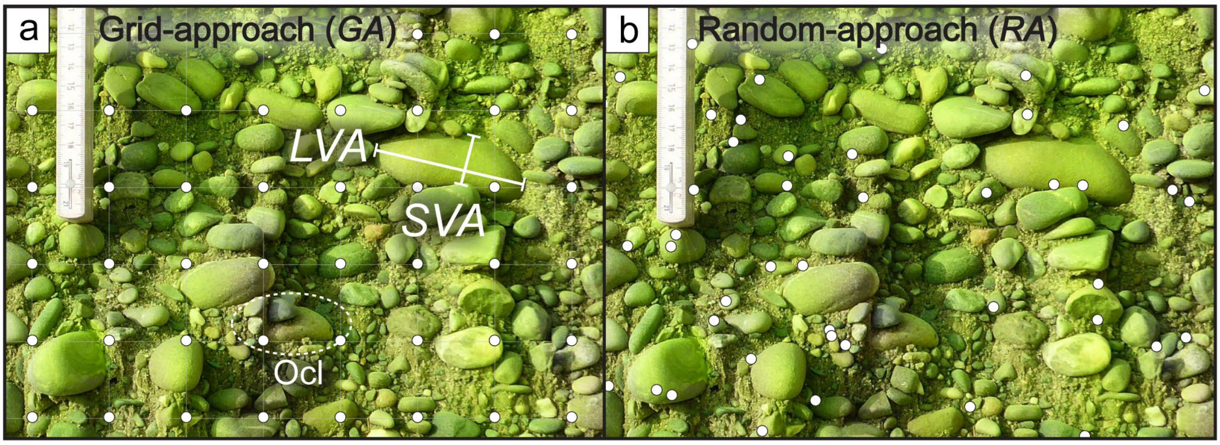

LVA: Longest visible axis *SVA:* Shortest visible axis *Ocl:* Occluded grains

Figure 2.3: Two approaches upon measuring grains on photos. **a)** Coloured outcrop (location 3; Fig. 2.2) with superimposed grid (Grid-approach, *GA*) or b) with randomly placed dots (Random-approach, *RA*) for grain size measurements on the photos. Please note that the dot size is enlarged for visualisation purposes.

2.3.3.3 Sieving of the material

The mechanical dry- (fraction >0.5 mm) and wet-sieving (fraction <0.5 mm) of the sediment was performed in a laboratory (Berner Fachhochschule, Switzerland) following SN EN-standards (SN EN 933-1/2012-03; Table 2.2). The dry-sieving was effectuated with a Haver EML 400 Digital Plus sieve shaker (Haver and Boecker OHG) with square-hole sieves (mesh sizes from 0.5 to 125 mm, with intervals of doubling each mesh size). Grains >125 mm were measured separately with a meter stick (*b*-axis), weighted, and assigned to the grain size class 125–250 mm. The wet-sieving was performed using a Retsch AS 200 sieve shaker (Retsch GmbH; sieve mesh sizes of 0.063 mm, 0.125 mm and 0.250 mm). This was accomplished on a homogenised sub-sample of 50 g that was previously separated from the <0.5 mm fraction. For the sieve data, the sieve mesh sizes (or sieve bin-openings) are thought to represent the length of the *b*-axis, because square-hole sieves allow in general individual grains with this specific axis to pass through (Church et al., 1987; Stähly et al., 2017). Therefore, the sizes of the percentile values are hereafter denoted as the sieve-axis.

2.3.4 Limitations and biases related to the three measuring methods

2.3.4.1 Measuring grains with a calliper

Measuring by hand and calliper involves the risk of a selective bias and under-sampling (e.g., Fripp and Diplas, 1993; Marcus et al., 1995; Wohl et al., 1996; Galia et al., 2017), and it may yield less precise results for large, small, or irregular-shaped grains (Fripp and Diplas, 1993; Marcus et al., 1995). Additionally, the shape of grains can lead to a misidentification of a specific axis, e.g., for rounded or spherical grains that might have similar long axes (Yuzyk and Winkler, 1991). Because we measured all three grain axes, we tested whether the resulting grain sizes, using the hand *b*-axes as a reference, depend on the grain shape. For this, we classified the hand data into four shape endmembers (Zingg, 1935; Blott and Pye, 2007) referred to as: flat if *b*-/*a*-axes ≥2/3 and *c*-/*b*-axes <2/3; spherical if *b*-/*a*-axes ≥2/3 and *c*-/*b*-axes ≥2/3; elongated if *b*-/*a*-axes <2/3 and *c*-/*b*-axes ≥2/3; and flat-elongated if *b*-/*a*-axes <2/3 and *c*-/*b*-axes <2/3.

2.3.4.2 Measuring grains on photos

On photos, we set the lower limit of a measurable grain to 2 mm, based on the pixel resolution of the photos. As outlined in the introduction, the projection of clasts onto the photo plane and the occlusion of clasts by the fine-grained matrix or other clasts (Fig. 2.1b) could either lead to an underestimation of the grain size and/or to a misidentification of a specific grain axis. We explore both biases by analysing the ratios between the lengths of the *LVA* and *SVA* measured on photos and the grain axes measured with a calliper. Additionally, we tested whether the exposed grain axes on the photos, reflecting the orientation of the grains after deposition, show a dependency on the paleoflow direction.

As mentioned above, images can be distorted, which could introduce a further bias upon data collection. We therefore tested whether the four different photo acquisition methods (*GAD, GAU, RAD, RAU;* see section 3.3.2) applied to the same outcrops yield identical results (Kolmogorov-Smirnov two-sample (KS2) test, Hodges, 1958). As null-hypothesis H_0 we considered that two grain size distributions are likely identical and drawn from similar populations. The H_0 is tested based on a significance level of alpha = 0.05 corresponding to the 95% confidence interval.

2.3.4.3 Sieving coarse-grained material

Sieving of the sampled material should significantly reduce or even eliminate a selective bias, as this approach includes the entire range of grain sizes (Leopold, 1970; Attal and Lavé, 2006), and sieving a sufficiently large sample mass can further reduce the errors associated to percentile values. Still, the results can depend on the grain shape particularly if square-hole sieves are used (Fernlund et al., 2007). This is because grains with small *c*-/*b*-axes ratios (flat or flat-elongated grains) are likely to pass to the smaller, lower sieve, whereas grains with large *c*-/*b*-axes ratios (spherical or elongated grains) are retained in the larger sieve (Church et al., 1987; Stähly et al., 2017). To account for this bias, Church et al., (1987) introduced a conversion factor, expressed as the ratio between the sieve mesh size D_s and the length of the *b*-axis of a grain:

$$D_s/b = \frac{1}{\sqrt{2}} * \sqrt{\left[1 + \left(\frac{c}{b}\right)^2\right]}\ [-] \qquad \text{Eq. (2.1).}$$

Here, *b* and *c* are the grain axes' lengths from the hand data, where the *c*/*b*-ratio denotes the flatness/roundness of a grain (Blott and Pye, 2007). We compared the sieve data (before and after correction) with the outcomes of the other two methods to investigate the effect of this shape correction.

2.3.5 Percentile and uncertainty calculations

The most used grain size percentiles for hydraulic calculations are the D_{16}, D_{50} or D_{84}. Here, D_i denotes the grain size where *i* percent of all grains are equal to or smaller than this specific length (e.g., Hoey and Ferguson, 1994; Ferguson and Paola, 1997; Green, 2003). The D_{50} is frequently employed for hydraulic calculations because the equivalent grain size is considered to characterize the material particularly during equal mobility conditions in a river (Parker, 1978; Wilcock and McArdel, 1993; Church, 2006). The D_{84} is considered as the frame building grain size of gravel bars (Hey, 1979; Leopold, 1992; MacKenzie and Eaton, 2017; MacKenzie et al., 2018), and the D_{16} acts as counterpart and characterizes the size of the fine-grained fraction (Kondolf and Li, 1992; Leopold, 1992; Bunte and Abt, 2001). For the hand and photo data, the D_{16}, D_{50} and D_{84} grain size percentiles were directly calculated from the grain size datasets. For the sieve data, we translated passed-weight percentages into grain size percentiles by linear interpolation between the sieve bins below and above the target percentiles.

For the calculations of the uncertainties on the hand and photo data, we conducted bootstrapping with replacement where the grain sizes are randomly sampled during 10^4 iterations (see e.g., Rice and Church, 1996 for description). We proceeded similarly to the approach of Mair et al., 2022, but did not consider the modelled measurement errors (see also Eaton et al., 2019, for alternative methods to estimate percentile uncertainties). We calculated the 95% confidence interval for each of the aforementioned percentiles. We used this confidence interval because not all the hand and photo datasets follow a normal Gaussian distribution. In contrast to the hand and photo data, the sieve data does not contain information on individual grain lengths. Therefore, for each percentile of interest we calculated a lower and upper confidence boundary following Watkins et al. (2020). For instance, error bars on the D_{50} values are expressed by the spread between the D_{45} (lower) and the D_{55} (upper boundary).

Additionally, we calculated how the number of measurements (sample size per site) influences the uncertainties of the percentile values extracted from the hand and photo data. For this, we determined the relative uncertainty on the percentile values (ε_i) following Eaton et al. (2019) where:

$$\varepsilon_i = 0.5 * \left(\frac{CI_{upper} - CI_{lower}}{D_i}\right) * 100\ [\%] \qquad \text{Eq. (2.2).}$$

Here, the confidence length ($CI_{upper} - CI_{lower}$) is dependent on the upper and lower confidence values from bootstrapping based on the 95% confidence interval. A normalisation by the related percentile values (D_i; e.g., the numerical value of the D_{50}) is required for comparing the uncertainties across the three percentiles of interest and various measuring approaches. A multiplication by 0.5 is applied to account for error margins (i.e., ± uncertainty). We additionally tested whether the uncertainties significantly decrease with a larger number of measurements. We did so by bootstrapping to 400 simulated measurements thereby doubling the sample size.

2.3.6 Comparison between different datasets

Two different measuring methods yield the same results, if the percentile values, once plotted against each other fit on the 1-1-line, also known as the line of equality, where x=y. This can be tested either visually or statistically. For a statistical test, we used a concordance correlation coefficient (*CCC*) following Lin (1989, 2000), which combines the degree to which all percentiles of a specific method adhere to their linear regression and the correlation between this best-fitting to the 1-1 line. Thus, it quantifies the similarity or discrepancy between the results of two different measurement methods for all percentiles. Here, the *CCC* is computed through:

$$CCC = \frac{2r\sigma_x\sigma_y}{\sigma_x{}^2 + \sigma_y{}^2 + (\mu_x - \mu_y)^2}\ [-] \qquad \text{Eq. (2.3).}$$

Here, r denotes the Pearson correlation coefficient of the linear regression, σ is the standard deviation, μ is the mean, and σ^2 the variance of the percentile values x and y derived from two different measuring approaches (e.g., photo and sieve), respectively. Because the *CCC* procedure can only be accomplished on data with ten or more data pairs (Lin, 1989, 2000), we used all percentiles values between the D_{16} and the D_{84} with a spacing of five, starting from the D_{20} and ending with the D_{80} (i.e., D_{16}, D_{20}, D_{25} … D_{80}, D_{84}). For the sake of clarity, the figures encompass the percentiles D_{16}, D_{50}, and D_{84} only. Lin's *CCC* can be considered to indicate a good correlation if the values are >0.80 (Altman; 1990). Thus, if the *CCC* values are close to 1.00, then all percentile values of the two methods are well correlated with respect to the line of equality and to each other (expressed by the Pearson r-value; full list in Fig. B.2.1, appendix B). We thus used the *CCC* values to identify those measuring methods that yield the highest similarity between the resulting percentile values.

2.4 Results

2.4.1 Data consistency

The grain size distributions of all hand datasets indicate that grain sizes <10 mm are scarce, especially for the a- and b-axes (Hand in Fig. 2.4). The grain size at site A is generally coarser than at sites B – D, especially for the D_{50} and D_{84} (Fig. 2.4). This concerns the hand, photo and especially the sieve data. The lengths of the *LVA* and *SVA,* which were measured on the photos of sites A, B and D, display very similar distributions (Fig. 2.4) that are independent on whether data collection was accomplished on distorted or undistorted photos, and whether grains were randomly selected (*RA*) on the photos or measured if located underneath a grid point (*GA*). This is supported by the results of the KS2 test where almost all comparisons failed to reject the H_0 at varying p-values (Fig. B.2.2, appendix B), meaning that the individual grain size distributions are comparable to each other. An exception is site C where some of the measurement approaches applied to photos yield in one case a different distribution for the *SVA* values (Fig. 2.4). In particular, at site C the lengths of the *SVA* appear to be different if the data was collected with either the *GAD* or the *RAU* approach (rejection of H_0 at a very low p-value of 0.003 upon comparing the two datasets; Fig. B.2.2, appendix B). Further details are shown in figures and tables A.2.1 – A.2.4 (both appendix A) for the curves of the grain size distributions and for the percentile values with confidence intervals and relative uncertainties, respectively.

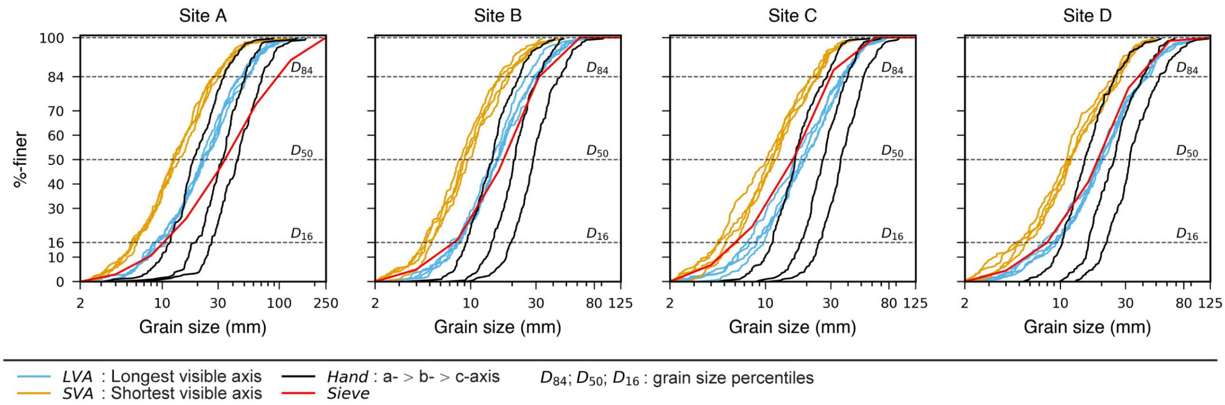

Figure 2.4: Grain size distributions. Data expressed as %-finer for all acquisition methods per sample sites A, B, C and D. Please note the logarithmic scale. The positions of the grain size percentile values (*D_{16}, D_{50}, D_{84}*) are marked by horizontal lines.

2.4.2 Comparison of percentile values

2.4.2.1 Photo versus sieve data

The closest similarity between the data can be found when comparing the *LVA* data collected on photos with the sieve data (*LVA* in Fig. 2.5a). This is particularly the case for datasets (and all related percentiles) collected with the *GAD, GAU, RAD* and *RAU* approaches at sites B – D, and this is also illustrated by the corresponding *CCC* (Eq. 2.3) values >0.9 (Fig. 2.5a). At site A, the *LVA* photo values deviate from such a correlation with the sieve data (average *CCC* value of 0.53; Fig. 2.5a), particularly for the D_{50} and D_{84}. In contrast, at all sites, the D_{50} and D_{84} values of the *SVA* (measured on photos) tend to be lower than the corresponding percentile values of the sieve data. The finer grained fraction (D_{16}) of both methods, photo measurements and sieving, yielded relatively consistent results (*SVA* in Fig. 2.5a). Yet the corresponding average *CCC* values are all below <0.70 and thus below the threshold of 0.80 (*SVA* in Fig. 2.5a). A complete table of all individual *CCC* values is shown in figure B.3 (appendix B).

2.4.2.2 Photo versus hand data

The lengths of the *LVAs* measured on photos are consistently shorter than those of the hand *a*-axes (*a*-axis in Fig. 2.5b). In contrast, measurements of the *LVA* yield D_{84} values that are comparable to the related percentile values of the hand *b*-axes. Regarding the D_{16} and D_{50}, however, the correlations between the related hand and photo values are only moderate (*b*-axis in Fig. 2.5b). Despite that, only site D has an average *CCC* value >0.87 if the comparison of the *LVA* with the hand *b*-axis and all percentile values are considered. A comparison of the *LVA* with the hand *c*-axes shows that the D_{84} percentile values of the photo data are larger than those of the hand data in most of the cases, whereas the D_{16} and D_{50} are in relatively good agreement (*c*-axis in Fig. 2.5b). Average *CCC* values for all percentiles are only above the threshold of 0.80 for site B, whereas they are below it for sites A, C and D in case of the hand *c*-axes (Fig. 2.5b). Measurements of the *SVA* on the photos yield percentile values that are generally smaller than those of the hand *a*-, *b*- and *c*-axes in almost all cases (Fig. 2.5c). In particular, only the D_{84} value of the hand *c*-axis is comparable to the corresponding percentile values of the *SVA* photo data, especially for site D (average *CCC* value of 0.81 for all percentiles; Fig. 2.5c).

2.4.2.3 Hand data versus sieve data

All percentile values of the hand *a*-axis data are clearly larger than those of the sieve datasets at sites B – D, yet site A shows an acceptable correlation between them (*CCC* = 0.80). Although the measurements of the hand *a*-axes of site A revealed larger D_{16} and smaller D_{84} values than sieving the same material, both methods return comparable D_{50} values (*a*-axis of site A, Fig. 2.5d). The hand *b*-axis data show good correlations to the sieve datasets only for the D_{84} (sites B and D), and moderate correlations for the D_{50} (sites A, B and D), respectively. In contrast, all D_{16} values of the hand *b*-axes are generally larger than the corresponding percentile values resulting from sieving (*b*-axis in Fig. 2.5d). Overall, sites B and D are best correlated if the lengths of the hand-*b*-axes and sieve-axes and all percentiles are considered (both *CCC* = 0.83 in average). The hand *c*-axes show a good correlation to the sieve data for the D_{16} (sites A, B and D), whereas site C shows a better correlation for the D_{50}. The data at site C has the highest average *CCC* = 0.89 for all percentiles (*c*-axis in Fig. 2.5d).

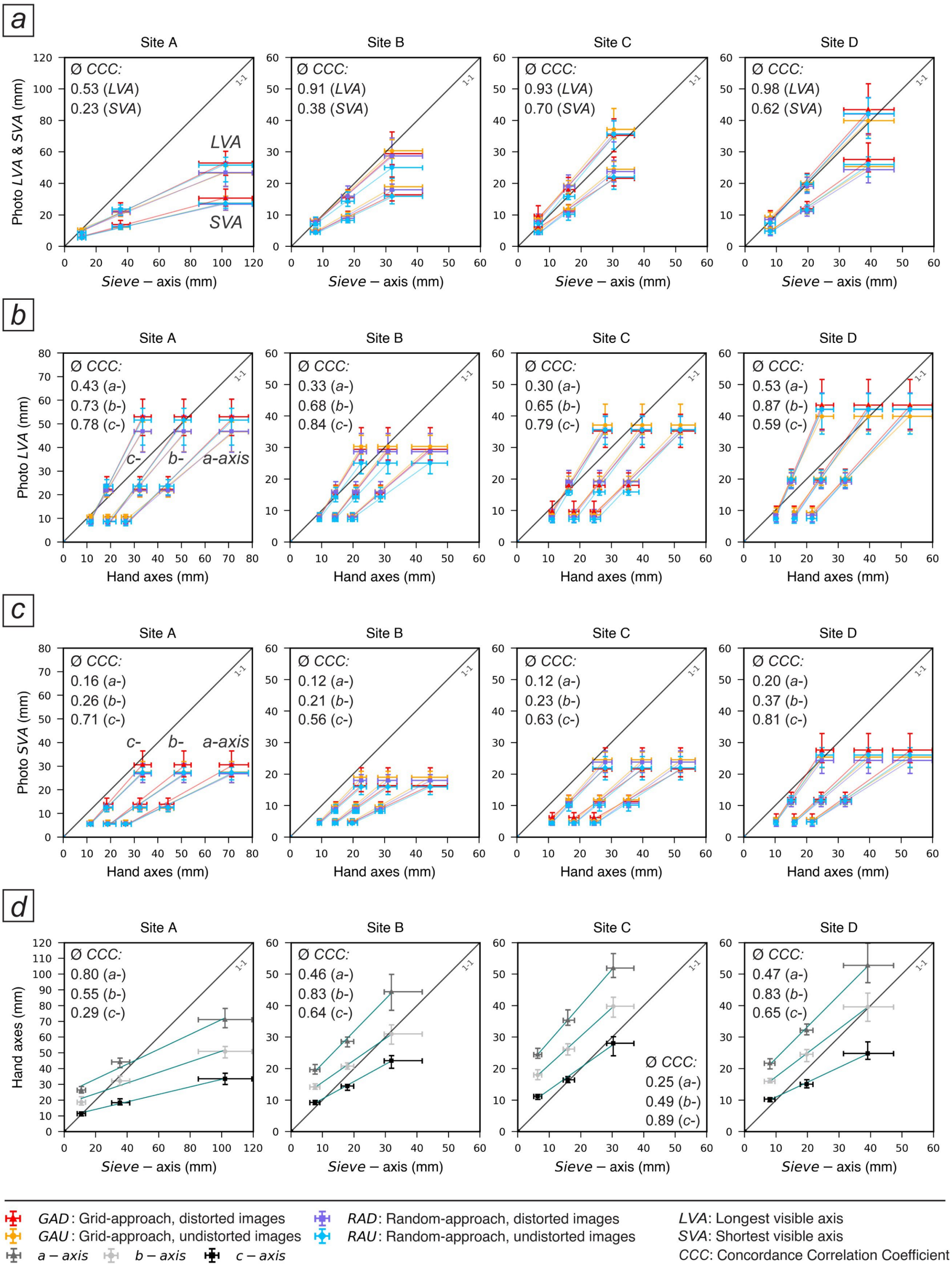

Figure 2.5: Comparison of percentile values from different measuring approaches. **a)** Comparison between the photo and the sieve data. **b)** Comparison of the hand data with the longest visible axis (LVA*)* and **c)** the shortest visible axis (*SVA*) on photos. **d)** Comparison between the hand and the sieve data. Percentile values in increasing order (i.e., $D_{16} < D_{50} < D_{84}$). Error bars represent the 95% confidence interval (hand and photo data). The sieve data uncertainties show a confidence range of ± 5 percentiles. Numbers represent average *CCC* values.

2.4.3 Uncertainty estimates

For all hand datasets and for 200 measurements, the relative uncertainties (ε_i; Eq. 2.2) are on average ±7.82% for the D_{16}, ±6.97% for the D_{50} and ±9.87% for the D_{84} (Table 2.3). For 400 measurements, the relative uncertainties for the hand data are reduced to ±5.71% for the D_{16}, ±4.83% for the D_{50}, and to ±6.60% for the D_{84} on average (Table 2.3). These relative uncertainties (95% confidence interval) concern all three grain axes measured by hand and calliper.

For the photo data (both *LVA* and *SVA*; see Table 2.3 for details) and for all photo acquisition methods, the average relative uncertainties are c. ±17.45% for the D_{16}, ±12.99% for the D_{50} and ±14.30% for the D_{84}. For 400 measurements, the average relative uncertainties for the photo data decrease to ±13.81% for the D_{16}, ±9.37% for the D_{50}, and to ±9.87% for the D_{84} (Table 2.3). These uncertainties (95% confidence interval) are independent of the grain axes (*LVA* and *SVA*). They concern all grain size percentiles (D_{16}, D_{50}, D_{84}), all sites A – D, and all approaches through which the photos were processed (distorted versus rectified photos) and the grains were selected on these photos (grains selected on a grid versus random selection of grains).

The average uncertainties of the sieve data (expressed by a lower and upper boundary of ±5 percentiles) are ±21.37% for the D_{16}, ±12.13% for the D_{50}, and ±17.55% for the D_{84} (Table 2.3). All individual uncertainty values are shown in tables A.2.1 – A.2.4 (appendix A). Figure B.2.7 (appendix B) shows the relative uncertainties of the hand and photo data plotted against increasing sample size.

Average relative uncertainty ε for all sites [± %]	ε_{16} (n = 200)*	ε_{16} (n = 400)*	ε_{50} (n = 200)*	ε_{50} (n = 400)*	ε_{84} (n = 200)*	ε_{84} (n = 400)*
Hand data (*a*-, *b*-, *c*-axes)	7.82	5.71	6.97	4.83	9.87	6.60
Photo data (*LVA*)	18.46	13.81	13.14	9.37	13.91	9.87
Photo data (*SVA*)	16.49	13.81	12.83	9.36	14.69	9.86
Sieve data (*Ds*)	21.37	-	12.13	-	17.55	-

Ds: Sieve-axis (Sieve-mesh size) ; ***LVA***: Longest; and ***SVA***: shortest visible axis (incl. all measuring approaches on photos)
* Sample size is valid for hand and photo data only. See table 2.1 for sieve sample mass.

Table 2.3: Uncertainties on the percentiles. Relative uncertainties are based on the 95% confidence interval (hand and photo data) or on a confidence range of ± 5 percentiles (sieve data).

2.4.4 Influence of grain shape and paleoflow direction

The ratios between the individual axes remain stable, over the entire range of grain lithologies and are independent of the grain size and the sample sites. On average, the *b*/*a*-axes ratio is c. 0.74, whereas the c/*b*-axes ratio is c. 0.67 (Table 2.4). Also, for all sites, the shape classification reveals that the majority of the grains are either flat (in average c. 38%) or spherical (c. 34%), whereas the rest corresponds to elongated (c. 17%) or flat-elongated grains (c. 11%; Table 2.5). Additionally, grain shapes are not correlated to the lengths of the hand *b*-axis nor to the *a*- and *c*-axis, in the sense that the shape classes spread over various grain sizes. Further details on the grain shape in relation to the *a*-, *b*- and *c*-axes of the hand data are shown in figures A.5a, b and c (appendix A), respectively.

The influence of the grains' shape on the sieving results is evaluated using Eq. 2.1. The average D_s/b-ratio of c. 0.85 (Table 2.4) for all four sites shows that the percentile values of the sieve data are c. 15% smaller than the corresponding values of the hand *b*-axes. Applying this factor to the sieve data thus yields in c. 15% larger percentile values compared to those before the correction (e.g., figs. 5a and d). The comparison of these corrected values (sieve data) with the results of the other grain size measuring methods shows that such corrections do not significantly improve the *CCC* values and thus the correlations (Fig. B.2.4, appendix B).

The comparisons of the grain size percentiles in relation to the exposure of the outcrop relative to the paleoflow (Fig. 2.2a) reveal that both, the *LVA* and *SVA* percentile values of site A, are generally larger than those of the perpendicularly oriented site B. This is particularly the case for the D_{50} and D_{84} values (Fig. 2.6). In contrast, the *LVA* and *SVA* of sites C and D (which are perpendicular to each other) disclose very similar percentile values, only the D_{84} values of site D are slightly larger than those of site C (Fig. 2.6).

Axes ratios [-]	Site A	Site B	Site C	Site D	Average
b/a	0.74	0.73	0.74	0.75	0.74
c/b	0.64	0.70	0.66	0.66	0.67
Ds/b	0.85	0.87	0.85	0.85	0.85
LVA/a	0.60	0.58	0.57	0.66	0.60
LVA/b	0.82	0.81	0.78	0.90	0.83
LVA/c	1.30	1.18	1.19	1.40	1.27
SVA/a	0.35	0.35	0.34	0.39	0.36
SVA/b	0.49	0.50	0.47	0.53	0.50
SVA/c	0.78	0.71	0.72	0.83	0.76

a, b, c: Grain axes (hand data); ***Ds:*** Sieve-axis (Sieve-mesh size);
LVA: Longest; and ***SVA***: shortest visible axis (incl. all measuring approaches on photos)
(Averages calculated from unrounded values per site)

Table 2.4: Grain axes' ratios. Based on the hand data (numbers rounded to 2 decimals).

Grain shape classes [%]	Site A	Site B	Site C	Site D	Average
Flat (*b/a* ≥ 2/3 & *c/b* < 2/3)	43.0	31.0	37.0	40.0	38.0
Spherical (*b/a* ≥ 2/3 & *c/b* ≥ 2/3)	29.0	39.0	34.0	33.0	34.0
Elongated (*b/a* < 2/3 & *c/b* ≥ 2/3)	16.0	21.0	16.0	16.0	17.0
Flat-elongated (*b/a* < 2/3 & *c/b* < 2/3)	13.0	9.0	12.0	10.0	11.0

a, b, c: Grain axes (hand data)

Table 2.5: Grain shapes. Classification after Zingg (1935) based on the grain axes ratios (hand data; rounded numbers, 1% rounding error).

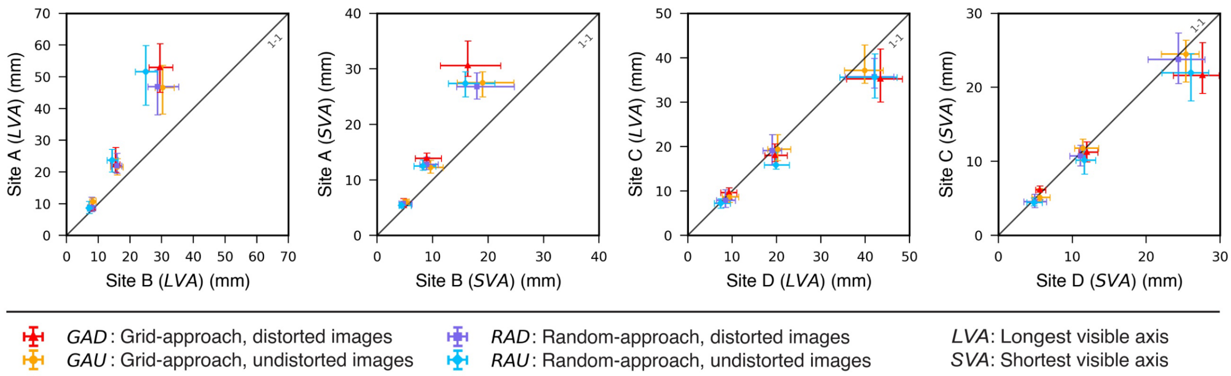

Figure 2.6: Photo data in relation to paleoflow direction. Comparison of percentile values (in increasing order, i.e., $D_{16} < D_{50} < D_{84}$) of sites with different orientations with respect to the paleoflow (Fig. 2.2a for orientation of sites).

2.4.5 Corrections of photo data to account for occlusion effects

Our results reveal that the lengths of the *LVAs* lay in general somewhere between those of the hand *b*- and *c*-axes (i.e., *a*-hand-measured > *b*-hand-measured ≥ *LVA* ≥ *c*-hand-measured; Fig. 2.5b), if considering the percentiles of interest. The lengths of the *SVA* measured on photos slightly underestimate, but generally correspond to those of the hand *c*-axis (Fig. 2.5c). By comparing the lengths of the *LVAs* (of all measuring approaches on images) to the hand *b*-axes, we found an average ratio of 0.83 for all sites (*LVA*/*b* in Table 2.4). In the same sense, the average ratio of the lengths of all *SVAs* and the lengths of the hand *c*-axes is 0.76 (*SVA*/*c* in Table 2.4). We corrected the *LVA* and *SVA* datasets by these factors and compared these new values with the hand *b*-axis datasets. Consequently, the values for data derived through both methods only slightly better aligned to each other for the D_{16}, whereas the same corrections resulted in a better correlation of the D_{50} (Fig. 2.7). Yet the alignment between the D_{84} values becomes worse but remains acceptable (Fig. 2.7). Besides, we found that for all percentiles the correlations between the photo and hand data highly improve (*CCC* values >0.80; Fig. 2.7 and Fig. B.2.5, appendix B). Corrections by other ratios (i.e., *LVA*/hand-*a*; *LVA*/hand-*c*; *SVA*/hand-*a;* and *SVA*/hand-*b*; Table 2.4) do not improve the correlations of the percentile values between the photo and hand data.

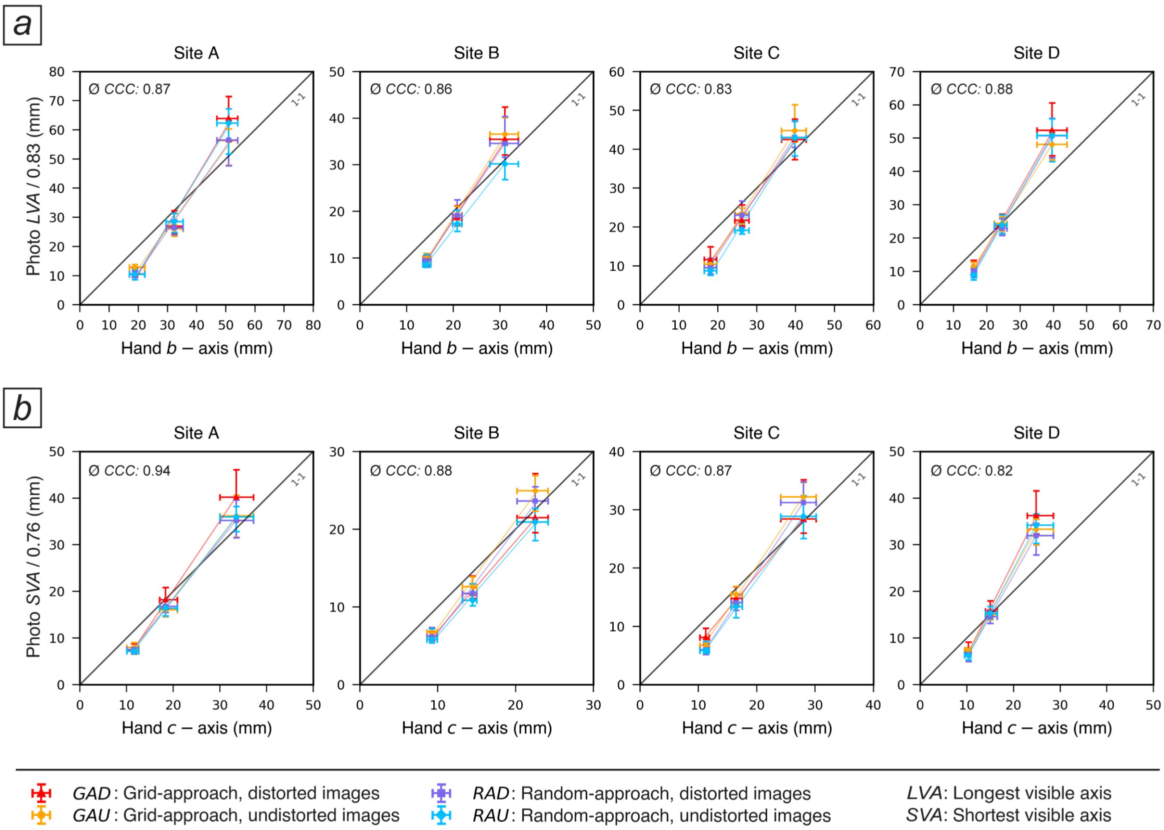

Figure 2.7: Comparison of percentile values of the corrected photo data. The photo data is now corrected by **a)** the average *LVA*/hand *b*-axes ratios of 0.83, and **b)** the average *SVA*/hand *c*-axes ratios of 0.76. Percentile values in increasing order (i.e., D_{16} < D_{50} < D_{84}). Error bars represent the 95% confidence interval. Numbers represent average *CCC* values.

2.5 Discussion

2.5.1 Biases related to data collection and measuring approaches

As shown by the results, the material at site A is coarser grained than at the other sites B – D and contains grains that are larger than 125 mm (largest sieve-mesh size; figs. 4 and 5). This allows us to explore, for site A, how the occurrence of such large grains adds a bias to the calculations of the percentile values. In particular, the hand data of site A comprises the lengths of 3 grains and the photo data of 1–2 grains (depending on the photo acquisition method) that were larger than the threshold of 125 mm. Removing these grains from the datasets do not significantly lower the percentile values of the D_{16}, D_{50} and D_{84} of both the hand and photo data. However, the sieve data of site A contains 4 grains >125 mm, which are 4.6 kg and contribute c. 9.3% to the sample mass after fines <2 mm were removed (or c. 7.6% to the bulk-mass). Upon removing these 4 grains from the sieve dataset, the D_{50} and especially the D_{84} are shifted towards smaller size values, and the corresponding *CCC* values for sample site A are consequently higher. This is illustrated for the comparison between the photo with the sieve data, where the average *CCC* values (site A in Fig. B.2.6, appendix B) for all percentiles shifted from

0.53 to now 0.97 (*LVA*) and from 0.23 to 0.64 (*SVA*). Although the sieve data were within acceptable uncertainty ranges concerning the sample weight, they are sensitive to a few large and heavy grains and thus sensitive to the particle shapes and the way of how clasts pass through the sieve openings (Church et al., 1987; Fernlund et al., 2007; Attal et al., 2015).

Data collection by hand is prone to under-sampling of grains <10 mm (Fig. 2.4). Furthermore, considering all percentile values, the lengths of the hand-axes reveal the least consistent correlation to those of resulting from the other measuring approaches, which is supported by large variations of the *CCC* values (figs. 5b and c). Even though the sampling was effectuated blindly, under-sampling of smaller grains is likely because larger grains tend to be unintentionally favoured upon picking (e.g., Marcus et al., 1995; Wohl et al., 1996; Daniels and McCusker, 2010). The under-sampling thus results in narrower underlying grain size distributions of the hand data, which likely yield in low uncertainties (Eaton et al., 2019; Table 2.3). The inconsistent correlations between the hand data and those collected with the other two methods might also reflect the lower precision upon measuring large, small, or irregular-shaped grains that are difficult to handle (Fripp and Diplas, 1993; Marcus et al., 1995). Yet our approach bears the advantage that the operator measured all available axes and had not to determine the length of a specific axis only (e.g., the *b*-axis), which sometimes has not been done in previous studies.

Grain size measurements on photos yield precise, consistent, and unbiased datasets, if performed by the mentioned sampling procedures. The result of the KS2 test shows that the various acquisition methods (*GA* and *RA*) and photo-specific factors (distorted and undistorted photos) yield comparable grain size datasets (Fig. B.2.2, appendix B). The average relative uncertainties (95% confidence interval and thus considering two standard deviations of the mean) on the grain size percentile values of the photo data (both *LVA* and *SVA*) range between ±12.83–18.46% for 200 grains (Table 2.3 and Fig. B.2.7, appendix B). Such values were considered as acceptable for coarse-grained material (e.g., Whittaker et al., 2011; Guerit et al., 2018; Eaton et al., 2019; Watkins et al., 2020).

2.5.2 Influence of particle shape, outcrop orientation and grain occlusion

The ratios between the individual hand axes (Table 2.4), and thus the general grain shape (Table 2.5), are identical at all sites, and they are in concordance with the outcomes of previous studies that present similar axes' ratios for coarse-grained fluvial deposits (e.g., Paola and Mohrig, 1996; Litty and Schlunegger, 2017). The grain shapes are furthermore independent of the lengths of the *b*-axes. Moreover, the axes' ratios of the coarse-grained material used in this study are similar to those reported for Alpine conglomerate beds (Tanner, 1944; Haldemann, 1948; Buergisser, 1980), most likely because parts of the material in the gravel pit was derived from these (Pfander et al., 2022).

We further investigated the influence of the grain flatness/roundness on the outcomes of sieving the material. By applying a correction of c. +15% to the percentile values of the sieve data (that is based on the average D_s/b-ratio of 0.85; Table 2.4), we particularly expected an improvement of the relationships between the sieve-axes and the hand *b*-axes' percentile values, which was generally not the case (Fig. B.2.4, appendix B). Yet, our calculated D_s/b-ratios reflect the outcome of other studies (Graham et al., 2010; Stähly et al., 2017), notably calculated for flat-lying grains only, showing that grain size lengths of the sieve data indeed underestimate the lengths of the hand *b*-axes. Note that this observation also considers possible biases upon measuring grains by hand and calliper. Nevertheless, we anticipate that the measuring approach with callipers provide the least biased datasets, and because it is the only method that provides information on all three grain axes, we use this data as benchmark for further discussion. Accordingly, we propose that the ratio between the lengths of the *LVA* and the hand *b*-axes can be used to correct for effects that result from the occlusion of grains and from distortions through projections on photos. Applying the *LVA*/hand-*b* and *SVA*/hand-*c* ratios (Table 2.4) to correct for these effects improves the comparison between the hand and photo percentile values for the D_{16} and especially for the D_{50} (Fig. 2.7). For the D_{84}, such a correction only slightly worsens the correlation between the hand and photo data, but the related uncertainties are acceptable (Fig. 2.7). Because *CCC* values consider all these percentiles, recalculations thereof revealed a highly better correlation between the hand data and the corrected photo datasets (Fig. B.2.5, appendix B). Therefore, we consider that these ratios, considering the entire grain size distribution, reflect the degree to which the lengths of the grain axes are underestimated on photos from outcrops, which is c. 17% (i.e., 0.83) for the *LVA* and c. 24% (i.e., 0.76) for the *SVA* (both Table 2.4). These values agree with similar outcomes from previous studies (Storz-Peretz and Laronne, 2013). Moreover, the average *LVA*/hand-*b* ratio of c. 0.83 is very consistent with the average D_s/b ratio of c. 0.85 (Table 2.4). This explains the significantly good correlations between grain size data collected through sieving and measurements on photos, because both methods yield lower *b*-axis values than measuring the material by hand and calliper. Similar effects have been observed for datasets collected on outcrops (Storz-Peretz and Laronne, 2013) and for flat-lying deposits (Adams, 1979; Stähly et al., 2017).

The dependency of the sample site orientations related to the paleoflow direction revealed no clear influence on the lengths of the exposed grain size axes measured on photos (*LVA* and *SVA;* Fig. 2.6). Particularly the outcrops of sites C and D, which are oriented perpendicular to each other, revealed similar *LVA* and *SVA* datasets. We therefore infer that the lengths of the exposed grain axes are independent on the outcrop orientation. We acknowledge that the data of site A depart from this picture, probably because the material is generally coarser grained than at the other sites.

2.6 Conclusions

Grain size measurements from outcrops with orientations (sub-)vertical to the initial bedding can be best achieved by photo-analysis. Our study reveals that the applied measuring approaches where grains are either randomly selected on a photo (random-approach; *RA*) or depicted if they occur on a grid intersection (grid-approach; *GA*) yield directly comparable and statistically similar grain size datasets. Our data additionally shows that photo-specific factors (distorted and undistorted photos) seem not to play a crucial role in short-distance surveys (c. 1–1.5 m from outcrops) with hand-held cameras. Also, the orientation of the outcrops relative to the paleoflow direction does not have a measurable impact on the grain size datasets. Uncertainties considering the 95% confidence interval of the percentile values for all datasets where 200 grains were measured on photos are on average ±16.45% for the D_{16}, ±12.80% for the D_{50} and ±14.00% for the D_{84}.

Measurements of the longest visible axis (*LVA*) on photos yield datasets that show a good correlation with grain size data established through sieving the same material. Both methods, however, underestimate the length of grains measured by hand with a calliper. If the lengths of these hand *b*-axes are taken as a reference, the sieving of the material underestimates these lengths by c. 15%, whereas measurements on photos (*LVA*) yield in an underestimation of c. 17%. The same is also the case where the lengths of the shortest visible axes (*SVA*) are measured on photos, which yields in an underestimation of the hand-measured *c*-axes by c. 24%. These underestimations are either based on the particles' shape expressed by the ratio between the size of the sieve mesh size (*Ds)* and the lengths of the hand-measured *b*-axes or explained by the occlusion of grains and their projection onto photos.

Finally, we find that the *LVA* measured on photos are comparable to the corresponding datasets where the *b*-axes were measured by hand with callipers, after some corrections are made. Such a correction is considering possible effects of grain occlusion and a foreshortened projection of grains onto the photo plane. Accordingly, we suggest correcting the underlying grain size distributions by c. +17%, yielding in significant good correlations between the hand and photo data for the D_{50} and the D_{16}. Interestingly, good agreements remained for the D_{84} of both datasets after such corrections (Fig. 2.7a). We close our work with the following recommendations for measuring grains >2 mm on outcrops of fluvial gravel and conglomerate:

1) Take photos at a distance of 1–1.5 m and as perpendicular as possible to the outcrop.
2) Ignore the outer c. 10 cm from the photo frame as they have the largest distortion. Photo corrections through photogrammetric methods are not necessary for such short distance surveys.
3) Either use a regularly spaced grid on the photos or randomly placed dots to mark the grains to be measured, and then measure the grains under multiple dots only once.
4) Measure the longest visible axis of at least 200 grains on one or more images from the same site.
5) Correct the underlying grain size distribution and thus the percentiles D_{16}, D_{50} and D_{84} by +17%.

2.7 Author contribution and Acknowledgments

The study has been created by PG with help by FS, AHP and DM. PG, AHP, DM collected the samples, PG analysed the data and interpreted the results with help by AHP, DM, GAD, FN and FS. PG wrote the text with help by FS, AHP, DM, GAD and FN. All authors contributed to the interpretation of the results and the discussion of the study.

2.8 Competing interests and funding sources

The authors declare that they have no conflict of interest. The authors declare the following financial interests/personal relationships which may be considered as potential competing interests: Philippos Garefalakis reports financial support was provided by the Swiss National Science Foundation (SNSF) [P1BEP2_200189].

2.9 Acknowledgments

We thank N. Akçar and J. Pfander for the photos (figs. 1c and 2b) of the gravel pit and thank J. Pfander for help to get access to the gravel pit and help with collection of the material. We thank the Berner Fachhochschule (BFH) for providing access to their laboratory sieving facilities.

The authors would like to thank Professor Brian Jones for handling our paper and thank the helpful reviews by Professor Carita Augustsson and Professor John S. Armstrong-Altrin, which helped to clarify and strengthen the arguments made in this paper.

2.10 Data availability

The raw data and the digital photos are available in the electronic appendix. All calculations were implemented in Python 3. The repository of the Python files is available on GitHub:
https://github.com/garefalakis/Gravel-Pit.git

2.11 Bibliography

Aberle, J., and Nikora, V., 2006. Statistical properties of armored gravel bed surfaces. Water Resources Research 42, pp. 1–11. https://doi.org/10.1029/2005WR004674

Adams, J., 1979. Gravel Size Analysis from Photographs. Journal of the Hydraulics Division 10, pp. 1247–1255. https://doi.org/10.1061/JYCEAJ.0005283

Altman, D.G., 1990. Practical Statistics for Medical Research. 1st edition. Chapman and Hall, New York, 624 p. https://doi.org/10.1201/9780429258589

Attal, M., and Lavé, J., 2006. Changes of bedload characteristics along the Marsyandi River (central Nepal): Implications for understanding hillslope sediment supply, sediment load evolution along fluvial networks, and denudation in active orogenic belts. Geological Society of America 398, pp. 143–171. https://doi.org/10.1130/2006.2398(09)

Attal, M., Mudd, S.M., Hurst, M.D., Weinman, B., Yoo, K., and Naylor, M., 2015. Impact of change in erosion rate and landscape steepness on hillslope and fluvial sediments grain size in the Feather River basin (Sierra Nevada, California): Earth Surface Dynamics 3, pp. 201–222. http://dx.doi.org/10.5194/esurf- 3-201-2015

Batel, W., 1960. Die Korngrössenanalyse. Einführung in die Korngrössenmesstechnik. Verfahrenstechnik in Einzeldarstellungen 8. Springer, Berlin, Heidelberg, 156 p. (in German) https://doi.org/10.1007/978-3-662-01501-8_4

Blott, S.J., and Pye, K., 2007. Particle shape: a review and new methods of characterization and classification. Sedimentology 55, pp. 31–63. https://doi.org/10.1111/j.1365-3091.2007.00892.x

Bradski, G., 2000, The OpenCV Library. Dr. Dobb's Journal of Software Tools, 120, pp. 122–125.

Brayshaw, A.C., 1984. Characteristics and Origin of Cluster Bedforms in Coarse-Grained Alluvial Channels. In: Koster, E.H. and Steel, R.J. (Eds.), Sedimentology of Gravels and Conglomerates, Canadian Society of Petroleum Geologists Memoir, pp. 77–85.

Bunte, K. and Abt, S.R., 2001. Sampling surface and subsurface particle-size distributions in wadable gravel-and cobble-bed streams for analyses in sediment transport, hydraulics, and streambed monitoring. General Technical Report RMRS-GTR-74. Fort Collins, CO, U.S. Department of Agriculture, Forest Service, Rocky Mountain Research Station. 428 p. https://doi.org/10.2737/RMRS-GTR-74

Bürgisser, Heinz, M., 1980. Zur Mittel-Miozänen Sedimentation im nordalpinen Molassebecken: Das “Appenzellergranit”-Leitniveau des Hörnli-Schuttfächers (OSM). Ph.D. Thesis, ETH Zurich, Switzerland, 196 p. (in German) https://doi.org/10.3929/ethz-a-000218245

Buscombe, D., 2008. Estimation of grain-size distributions and associated parameters from digital images of sediment, Sedimentary Geology 210, pp. 1–10. https://doi.org/10.1016/j.sedgeo.2008.06.007

Butler, J. B., Lane, S.N., and Chandler, J.H., 2001. Automated extraction of grain-size data from gravel surfaces using digital image processing. Journal of Hydraulic Research 39, pp. 519–529. https://doi.org/10.1080/00221686.2001.9628276

Carbonneau, P.E., Bizzi, S., and Marchetti, G., 2018. Robotic photosieving from low-cost multirotor sUAS : a proof-of-concept. Earth Surface Processes and Landforms 43, pp. 1160–1166. https://doi.org/10.1002/esp.4298

Chardon, V., Piasny, G., and Schmitt, L., 2021. Comparison of software accuracy to estimate the bed grain size distribution from digital images: A test performed along the Rhine River. River Research and Applications 38, pp. 358–367. https://doi.org/10.1002/rra.3910

Church, M.A., 2006. Bed Material Transport and the Morphology of Alluvial River Channels. Annual Review of Earth and Planetary Sciences 34, pp. 325–354. https://doi.org/10.1146/annurev.earth.33.092203.122721

Church, M.A., McLean, D.G., and Wolcott, J.F., 1987. River Bed Gravels: Sampling and Analysis. In: Thorne, C.R., Bathurst, J.C. and Hey, R.D. (Eds.), Sediment Transport in Gravel-Bed Rivers. John Wiley and Sons Ltd., Chichester, pp. 43–88.

Claude, A., Akçar, N., Ivy-Ochs, S., Schlunegger, F., Rentzel, P., Puempin, C., Tikhomirov, D., Kubik, P.W., Vockenhube, C., Dehnert, A., Rahn, M. and Schlüchter, C., 2017. Chronology of Quaternary terrace deposits at the locality Hohle Gasse (Pratteln, NW Switzerland). Swiss Journal of Geosciences 110, pp. 793–809. https://doi.org/10.1007/s00015-017-0278-z

Dade, W.B., and Friend, P.F., 1998. Grain-size, sediment-transport regime, and channel slope in alluvial rivers. Journal of Geology 106, pp. 661–675. https://doi.org/10.1086/516052

Daniels, M.D. and McCusker, M.H., 2010. Operator bias characterizing stream substrates using Wolman pebble counts with a standard measurement template. Geomorphology 115, pp. 194–198. https://doi.org/10.1016/j.geomorph.2009.09.038

Detert, M. and Weitbrecht, V., 2012. Automatic object detection to analyze the geometry of gravel grains – a free stand-alone tool. In: Muñoz, R.M. (Ed.), River Flow 2012: Proceedings of the International Conference on Fluvial Hydraulics. Taylor and Francis Group, London, pp. 595–600

Diplas, P., and Fripp, J. B., 1992. Properties of Various Sediment Sampling Procedures, Journal of Hydraulic Engineering-ASCE 118, pp. 955– 970. https://doi.org/10.1061/(ASCE)0733-9429(1992)118:7(955)

Duller, R.A., Whittaker, A.C., Fedele, J.J., Whitchurch, A.L., Springett, J., Smithells, R., Fordyce, S. and Allen, P.A., 2010. From grain size to tectonics. Journal of Geophysical Research: Earth Surface 115, pp. 1–19. https://doi.org/10.1029/2009JF001495

Eaton, B.C., Dan Moore, R., and Mackenzie, L.G., 2019. Percentile-based grain size distribution analysis tools (GSDtools)-Estimating confidence limits and hypothesis tests for comparing two samples. Earth Surface Dynamics 7, pp. 789–806. https://doi.org/10.5194/esurf-7-789-2019

Ferguson, R.I., and Paola, C., 1997. Bias and precision of percentiles of bulk grain size. Earth Surface Processes and Landforms 22, pp. 1061–1077. https://doi.org/10.1002/(SICI)1096-9837(199711)22:11%3C1061::AID-ESP809%3E3.0.CO;2-L

Fernlund, J.M.R., Zimmerman, R.W., and Kragic, D. 2007. Influence of volume/mass on grain-size curves and conversion of image-analysis size to sieve size. Engineering Geology 90, pp. 124–137. https://doi.org/10.1016/j.enggeo.2006.12.007

Fripp, J.B. and Diplas, P., 1993. Surface Sampling in Gravel Streams. Journal of Hydraulic Engineering 118, pp. 473–49. https://doi.org/10.1061/(ASCE)0733-9429(1993)119:4(473)

Galia, T., Škarpich, V., Gajdošová, K., and Krpec, P., 2017. Variability of Wolman pebble samples in gravel/cobble bed streams. Acta Scientiarum Polonorum, Formatio Circumiectus, 16, pp. 237–246. https://doi.org/10.15576/ASP.FC/2017.16.1.237

Garefalakis, P., and Schlunegger, F., 2018. Link between concentrations of sediment flux and deep crustal processes beneath the European Alps. Scientific Reports 8, pp. 1–11.
https://doi.org/10.1038/s41598-017-17182-8

Graham, D.J., Reid, I., and Rice, S.P., 2005a. Automated sizing of coarse-grained sediments: image-processing procedures. Mathematical Geology 37, pp. 1–28.
https://doi.org/10.1007/s11004-005-8745-x

Graham, D.J., Rice, S.P., and Reid, I., 2005b. A transferable method for the automated grain sizing of river gravels. Water Resources Research 41, W07020, pp. 1–12.
https://doi.org/10.1029/2004WR003868

Graham, D.J., Rollet, A. J., Piégay, H., and Rice, S.P., 2010. Maximizing the accuracy of image-based surface sediment sampling techniques. Water Resources Research 46, pp. 1–15.
https://doi.org/10.1029/2008WR006940

Green, J.C., 2003. The precision of sampling grain-size percentiles using the Wolman method. Earth Surface Processes and Landforms 28, pp. 979–991.
https://doi.org/10.1002/esp.513

Guerit, L., Barrier, L., Liu, Y., Narteau, C., Lajeunesse, E., Gayer, E., and Métivier, F., 2018. Uniform grain-size distribution in the active layer of a shallow, gravel-bedded, braided river (the Urumqi River, China) and implications for paleo-hydrology. Earth Surface Dynamics 6, pp. 1011–1021.
https://doi.org/10.5194/esurf-6-1011-2018

Haldemann, E.G., 1948. Geologie des Schallenberg-Honegg-Gebietes (Oberes Emmental). Unpubl. PhD Thesis, University of Bern, Switzerland, 124 p. (in German)

Harvey, E.L., Hales, T.C., Hobley, D.E. J., Liu, J., and Fan, X., 2022. Measuring the grain-size distributions of mass movement deposits. Earth Surface Processes and Landforms 47, pp. 1599–1614.
https://doi.org/10.1002/esp.5337

Hey, R.D., 1979. Flow resistance in gravel-bed rivers. Journal of the Hydraulics Division, American Society of Civil Engineers 105, pp. 365–379.
https://doi.org/10.1061/JYCEAJ.0005178

Hodges, J.L. Jr., 1958. The Significance Probability of the Smirnov Two-Sample Test. Arkiv för Matematik 3, pp. 469–486.
https://doi.org/10.1007/BF02589501

Hoey, T.B., and Ferguson, R., 1994. Numerical simulation of downstream fining by selective transport in gravel bed rivers: Model development and illustration: Water Resources Research 30, pp. 2251–2260,
https://doi.org/10.1029/94WR00556

Ibbeken, H., and Schleyer, R., 1986. Photo-Sieving: A Method for Grain-Size Analysis of Coarse-Grained, Unconsolidated Bedding Surfaces. Earth Surface Processes and Landforms 11, pp. 59–77.
https://doi.org/10.1002/esp.3290110108

Inman, D.L., 1952. Measures for describing the size distribution of sediments. Journal of Sed. Petrology 22, pp. 125–145.
https://doi.org/10.1306/D42694DB-2B26-11D7-8648000102C1865D

Johansson, C.E., 1976. Structural studies of frictional sediments. Geografiska Annaler: Series A, Physical Geography 58, pp. 201–301.
https://doi.org/10.1080/04353676.1976.11879939

Kellerhals, R., and Bray, D.I., 1971. Sampling Procedures for Coarse fluvial Sediments. Journal of the Hydraulics Division, 8, pp. 1165–1180.
https://doi.org/10.1061/JYCEAJ.0003044

Kondolf, G.M., and Li, S., 1992. The Pebble Count Technique for Quantifying Surface Bed Material Size in Instream Flow Studies. Rivers 3, pp. 80–87.

Lane, E.W., 1955. The importance of fluvial morphology in hydraulic engineering. Proceedings of the American Society of Civil Engineers, 81, pp. 1–17.

Leopold, L.B., 1970. An Improved Method for Size Distribution of Stream Bed Gravel. Water Resources Research 6, pp. 1357–1366.
https://doi.org/10.1029/WR006i005p01357

Leopold, L.B., 1992. Sediment Size That Determines Channel Morphology. Dynamics of Gravel-Bed Rivers, pp. 297–311.

Lin, L.I., 1989. A concordance correlation coefficient to evaluate reproducibility. Biometrics 45, pp. 255–268.
https://doi.org/10.2307/2532051

Lin, L. I., 2000. A Note on the Concordance Correlation Coefficient. Biometrics 56, pp. 324–325.
https://doi.org/10.1111/j.0006-341X.2000.00324.x

Litty, C., and Schlunegger, F., 2017. Controls on Pebbles' Size and Shape in Streams of the Swiss Alps. The Journal of Geology 125, pp. 101–112.
https://doi.org/10.1086/689183

Litty, C., Duller, R., and Schlunegger, F., 2016. Paleohydraulic reconstruction of a 40 ka-old terrace sequence implies that water discharge was larger than today. Earth Surface Processes and Landforms 41, pp. 884–898. https://doi.org/10.1002/esp.3872

MacKenzie, L. G., and Eaton, B. C., 2017. Large grains matter: contrasting bed stability and morphodynamics during two nearly identical experiments. Earth Surface Processes and Landforms 42, pp. 1287–1295. https://doi.org/10.1002/esp.4122

MacKenzie, L.G., Eaton, B.C., and Church, M., 2018. Breaking from the average: Why large grains matter in gravel-bed streams. Earth Surface Processes and Landforms 43, pp. 3190–3196. https://doi.org/10.1002/esp.4465

Mair, D., do Prado, A.H., Garefalakis, P., Lechmann, A., Whittaker, A., and Schlunegger, F. 2022. Grain size of fluvial gravel bars from close-range UAV imagery-uncertainty in segmentation-based data, Earth Surface Dynamics 10, pp. 953–973. https://doi.org/10.5194/esurf-2022-19

Marchetti, G., Comiti, F., Bizzi, S., Belletti, B., Lastoria, B., and Carbonneau, P.E., 2022. Mapping riverbed sediment size from Sentinel-2 satellite data. Earth Surface Processes and Landforms 47, pp. 2544–2559. https://doi.org/10.1002/esp.5394

Marcus, W.A., Ladd, S.C., Stoughton, J. A., and Stock, J.W., 1995. Pebble Counts and the Role of User-Dependent Bias in Documenting Sediment Size Distributions. Water Resources Research 31, pp. 2625–2631. https://doi.org/10.1029/95WR02171

Meyer-Peter, E., and Müller, R., 1948. Formulas for Bed-Load Transport. Proceedings of the 2nd Meeting of the International Association of Hydraulic Research, Delft, pp. 39–64. http://resolver.tudelft.nl/uuid:4fda9b61-be28-4703-ab06-43cdc2a21bd7

Mosley, M.P. and Tindale, D.S., 1985. Sediment variability and bed material sampling in gravel-bed rivers, Earth Surface Processes and Landforms 10, pp. 465–482. https://doi.org/10.1002/esp.3290100506

Nemec, W., Porebski, S.J., and Steel, R.J., 1980. Texture and structure of resedimented conglomerates: examples from Ksiaz Formation (Famenian–Tournaisian), southwestern Poland. Sedimentology 27, pp. 519–538. https://doi.org/10.1111/j.1365-3091.1980.tb01645.x

Neumann-Mahlkau, P., 1967. Korngrössenanalyse Grobklastischer Sedimente mit Hilfe von Aufschluss-Photographien. Sedimentology 9, pp. 245–261. (in German) https://doi.org/10.1111/j.1365-3091.1967.tb02040.x

Paola, C., and Mohrig, D.,1996. Palaeohydraulics revisited: Palaeoslope estimation in coarse-grained braided rivers. Basin Research 8, pp. 243–254. https://doi.org/10.1046/j.1365-2117.1996.00253.x

Parker, G., 1978. Self-formed straight rivers with equilibrium banks and mobile bed. Part 2. The gravel river. Journal of Fluid Mechanics 89, pp. 127–146. https://doi.org/10.1017/S0022112078002505

Parker, G., 1990. Surface-based bedload transport relation for gravel rivers. Journal of Hydraulic Research 28, pp. 417–436. https://doi.org/10.1080/00221689009499058

Petit, F., Houbrechts, G., Peeters, A., Hallot, E., Van Campenhout, J., and Denis, A.C., 2015. Dimensionless critical shear stress in gravel-bed rivers. Geomorphology 250, pp. 308–320. https://doi.org/10.1016/j.geomorph.2015.09.008

Pfander, J., Schlunegger, F., Serra, E., Gribenski, N., Garefalakis, P., and Akçar, N., 2022. Glaciofluvial sequences recording the Birrfeld Glaciation (MIS 5d–2) in the Bern area, Swiss Plateau. Swiss Journal of Geosciences 115, pp. 1–24. https://doi.org/10.1186/s00015-022-00414-z

Preusser, F., Büschelberger, M., Kemna, H.A., Miocic, J., Mueller, D. and May, J.H., 2021. Exploring possible links between Quaternary aggradation in the Upper Rhine Graben and the glaciation history of northern Switzerland. International Journal of Earth Sciences 110, pp. 1827–1846. https://doi.org/10.1007/s00531-021-02043-7

Purinton, B., and Bookhagen, B., 2019. Introducing PebbleCounts: A grain-sizing tool for photo surveys of dynamic gravel-bed rivers. Earth Surface Dynamics 7, pp. 859–877. https://doi.org/10.5194/esurf-7-859-2019

Purinton, B., and Bookhagen, B., 2021. Tracking Downstream Variability in Large Grain-Size Distributions in the South-Central Andes. Journal of Geophysical Research: Earth Surface 126, pp. 1–29. https://doi.org/10.1029/2021JF006260

Rasband, W.S., 1997-2018. ImageJ, U. S. National Institutes of Health, Bethesda, Maryland, USA, Available at: https://imagej.nih.gov/ij/

Recking, A., 2010. A comparison between flume and field bed load transport data and consequences for surface-based bed load transport prediction. Water Resources Research 46, pp. 1–16. https://doi.org/10.1029/2009WR008007

Recking, A., 2013. Simple method for calculating reach-averaged bed-load transport. Journal of Hydraulic Engineering 139, pp. 70–75.
https://doi.org/10.1061/(asce)hy.1943-7900.0000653
Rice, S., and Church, M., 1996. Sampling surficial fluvial gravels; the precision of size distribution percentile sediments. Journal of Sedimentary Research 66, pp. 654–665.
https://doi.org/110.2110/jsr.66.654
Rice, S.P., and Church, M., 2010. Grain-size sorting within river bars in relation to downstream fining along a wandering channel. Sedimentology 57, pp. 232–251.
https://doi.org/10.1111/j.1365-3091.2009.01108.x
Ritter, J.R. and Helley, E.J., 1969. Optical method for determining particle sizes of coarse sediment. Techniques of Water-Resources Investigations of the U.S. Geological Survey 5, pp. 33.
https://doi.org/10.3133/twri05C3
Schlunegger, F., Delunel, R., and Garefalakis, P., 2020. Short communication: Field data reveal that the transport probability of clasts in Peruvian and Swiss streams mainly depends on the sorting of the grains. Earth Surface Dynamics 8, pp. 717–728.
https://doi.org/10.5194/esurf-8-717-2020
Smith, Z.D., and Maxwell, D.J., 2021. Constructing vertical measurement logs using UAV-based photogrammetry: Applications for multiscale high-resolution analysis of coarse-grained volcaniclastic stratigraphy. Journal of Volcanology and Geothermal Research 409, 107122, pp. 1–20.
https://doi.org/10.1016/j.jvolgeores.2020.107122
Stähly, S., Friedrich, H., and Detert, M., 2017. Size ratio of fluvial grains' intermediate axes assessed by image processing and square-hole sieving. Journal of Hydraulic Engineering 143, pp. 1–6.
https://doi.org/10.1061/(ASCE)HY.1943-7900.0001286
Storz-Peretz, Y., and Laronne, J.B., 2013. Automatic grain sizing of vertical exposures of gravelly deposits. Sedimentary Geology 294, pp. 13–26.
https://doi.org/10.1016/j.sedgeo.2013.05.004
Strom, K.B., Kuhns, R.D., and Lucas, H.J., 2010. Comparison of automated image-based grain sizing to standard pebble-count methods. Journal of Hydraulic Engineering 136, pp. 461–473.
https://doi.org/10.1061/(ASCE)HY.1943-7900.0000198
Tanner, H., 1944. Beitrag zur Geologie der Molasse zwischen Ricken und Hörnli. Mitteilungen der Thurgauischen Naturforschenden Gesellschaft 33, pp. 1–108. (in German)
https://doi.org/10.5169/seals-593971
Wadell, H., 1936. Volume, Shape, and Shape Position of Rock Fragments in Openwork Gravel. Geografiska Ann. 18, pp. 74–92.
https://doi.org/10.1080/20014422.1936.11880607
Warrick, J.A., Rubin, D. M., Ruggiero, P., Harney, J.N., Draut, A.E., and Buscombe, D., 2009. Cobble cam: Grain-Size-measurements of sand to boulder from digital photographs and autocorrelation analyses. Earth Surface Processes and Landforms 34, pp. 155–161.
https://doi.org/10.1002/esp.1877
Watkins, S.E., Whittaker, A.C., Bell, R.E., Brooke, S.A.S., Ganti, V., Gawthorpe, R.L., Nixon, C.W., 2020. Straight from the source's mouth: Controls on field-constrained sediment export across the entire active Corinth Rift, central Greece. Basin Research 32, pp. 1600–1625.
https://doi.org/10.1111/bre.12444
Wentworth, C.K., 1922. A Scale of Grade and Class Terms for Clastic Sediments. The Journal of Geology 30, pp. 377–392.
https://doi.org/10.1086/622910
Whittaker, A.C., Duller, R.A., Springett, J., Smithells, R.A., Whitchurch, A.L., and Allen, P.A., 2011. Decoding downstream trends in stratigraphic grain size as a function of tectonic subsidence and sediment supply. Geological Society of America Bulletin 7, pp. 1363–1382.
https://doi.org/10.1130/B30351.1
Wilcock, P.R., McArdell, B.W., 1993. Surface-based fractional transport rates: Mobilization thresholds and partial transport of sand-gravel sediments. Water Resources Research 29, pp. 1297–1312.
https://doi.org/10.1029/92WR02748
Wohl, E.E., Anthony, D.J., Madsen, S.W., and Thompson, D.M., 1996. A comparison of surface sampling methods for coarse fluvial sediments. Water Resources Research 32, pp. 3219–3226.
https://doi.org/10.1029/96WR01527
Wolman, M.G., 1954. A method of sampling coarse river-bed material. EOS. Transactions of the American Geophysical Union 35, pp. 951–956.
https://doi.org/10.1029/TR035i006p00951
Wong, M., and Parker, G., 2006. Reanalysis and Correction of Bed-Load Relation of Meyer-Peter and Müller Using Their Own Database. Journal of Hydraulic Engineering 132, pp. 1159–1168.
https://doi.org/10.1061/(asce)0733-9429(2006)132:11(1159)

Woodget, A.S., Fyffe, C., and Carbonneau, P.E., 2018. From manned to unmanned aircraft: Adapting airborne particle size mapping methodologies to the characteristics of sUAS and SfM, Earth Surf. Proc. and Landforms 43, pp. 857–870. https://doi.org/10.1002/esp.4285

Yuzyk, T.R. and T. Winkler, 1991. Procedures for bed-material sampling. Lesson Package No. 28. Environment Canada, Water Resources Branch, Sediment Survey Section, Ottawa, Canada, pp. 100.

Zhang, Z., 2000. A Flexible New Technique for Camera Calibration. Technical Report MSR-TR-98-71. Microsoft Research, Microsoft Corporation. IEEE Transactions on Pattern Analysis and Machine Intelligence, 22, pp. 1330-1334, https://doi.org/10.1109/34.888718

Zingg, Th., 1935. Beitrag zur Schotteranalyse. Schweizerische mineralogische und petrographische Mitteilungen, 15, 39–140. Ph.D. Thesis, ETH Zurich, Switzerland, pp. 140. (in German) https://doi.org/10.3929/ethz-a-000103455

2.12 Appendix A

2.12.1 Figures

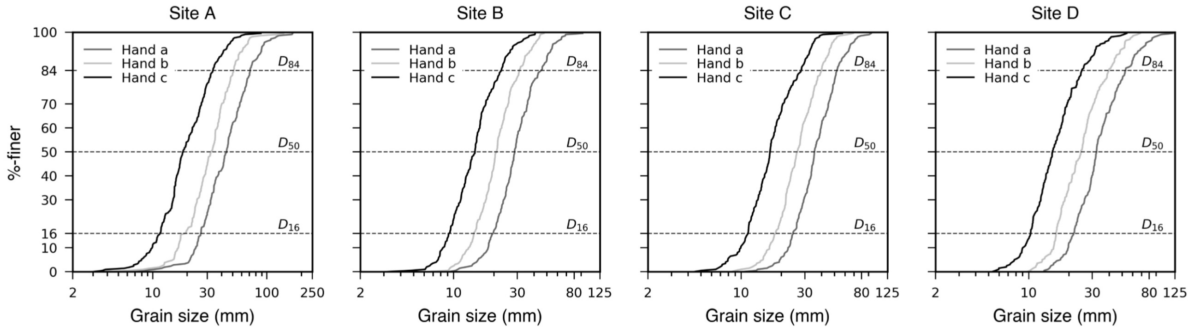

Figure A.2.1: Hand data. Grain size distribution for the *a*-, *b*- and *c*-axis from the hand data per sample site. The positions of the grain size percentile values (D_{16}, D_{50}, D_{84}) are marked by horizontal lines.

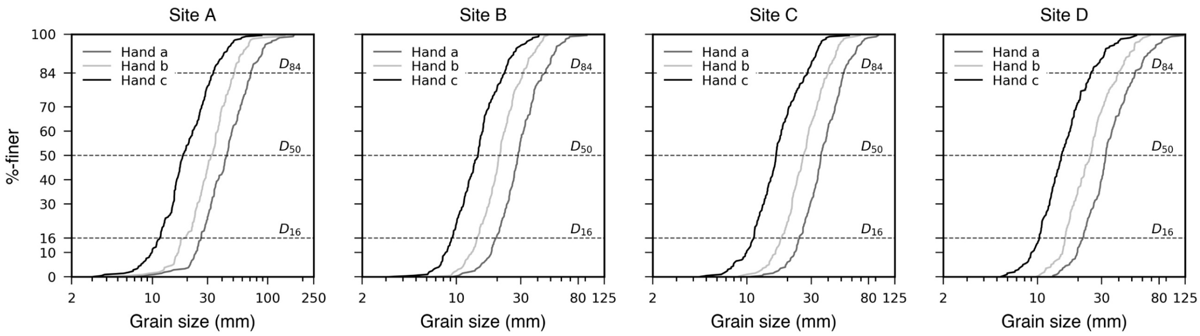

Figure A.2.2: Photo data (*LVA*). Lengths of the longest visible axis (*LVA*) of all sample sites from photo data. *GAD*: Grid-approach, distorted photos; *GAU*: Grid-approach, undistorted photos; *RAD*: Random-approach, distorted photos; *RAU*: Random-approach, undistorted photos. The positions of the grain size percentile values (D_{16}, D_{50}, D_{84}) are marked by horizontal lines.

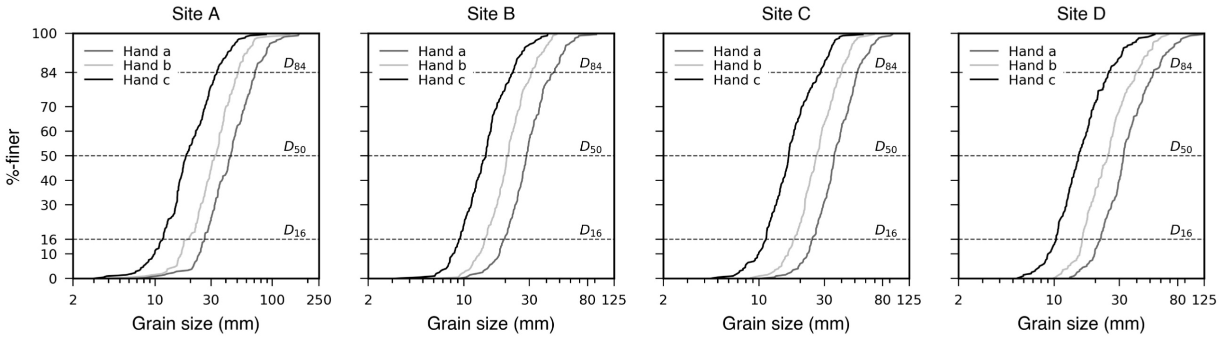

Figure A.2.3: Photo data (*SVA*). Lengths of the shortest visible axis (*SVA*) of all sample sites from photo data. *GAD*: Grid-approach, distorted photos; *GAU*: Grid-approach, undistorted photos; *RAD*: Random-approach, distorted photos; *RAU*: Random-approach, undistorted photos. The positions of the grain size percentile values (D_{16}, D_{50}, D_{84}) are marked by horizontal lines.

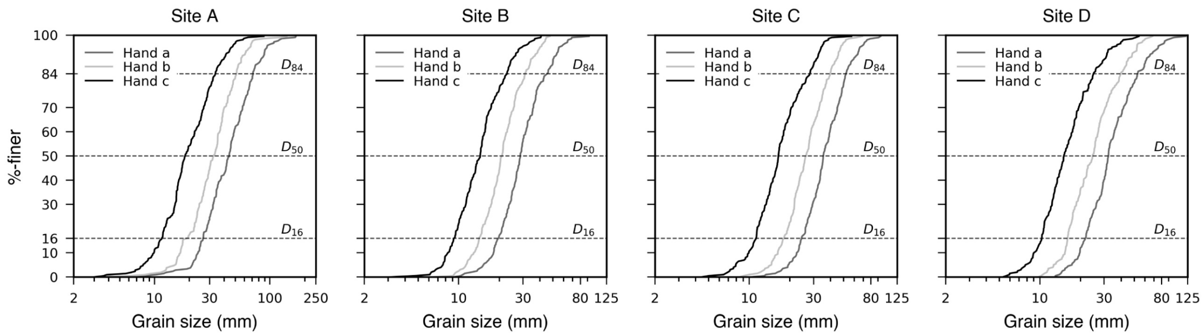

Figure A.2.4: Sieve data. Distribution of the sieve data of all sample sites. The positions of the grain size percentile values (D_{16}, D_{50}, D_{84}) are marked by horizontal lines.

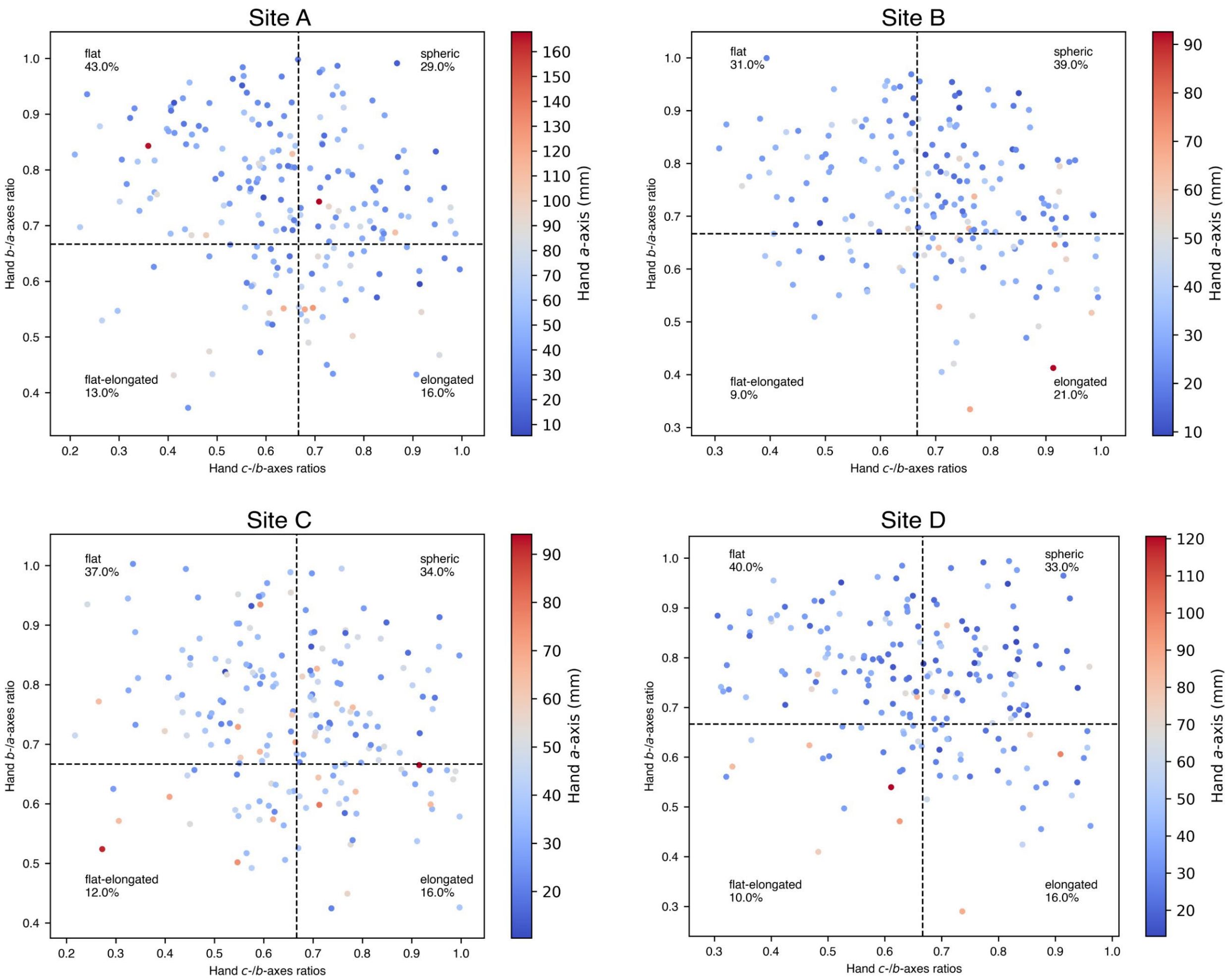

Figure A.2.5: Grain shape classification. Grain shapes expressed by the hand *b*-/*a*- and hand *c*-/*b*-axes ratios versus grain sizes of the **a)** hand *a*-axis; **b)** hand *b*-axis, and **c)** hand *c*-axis, respectively. Numbers of grain shape classes are rounded (1% rounding error).

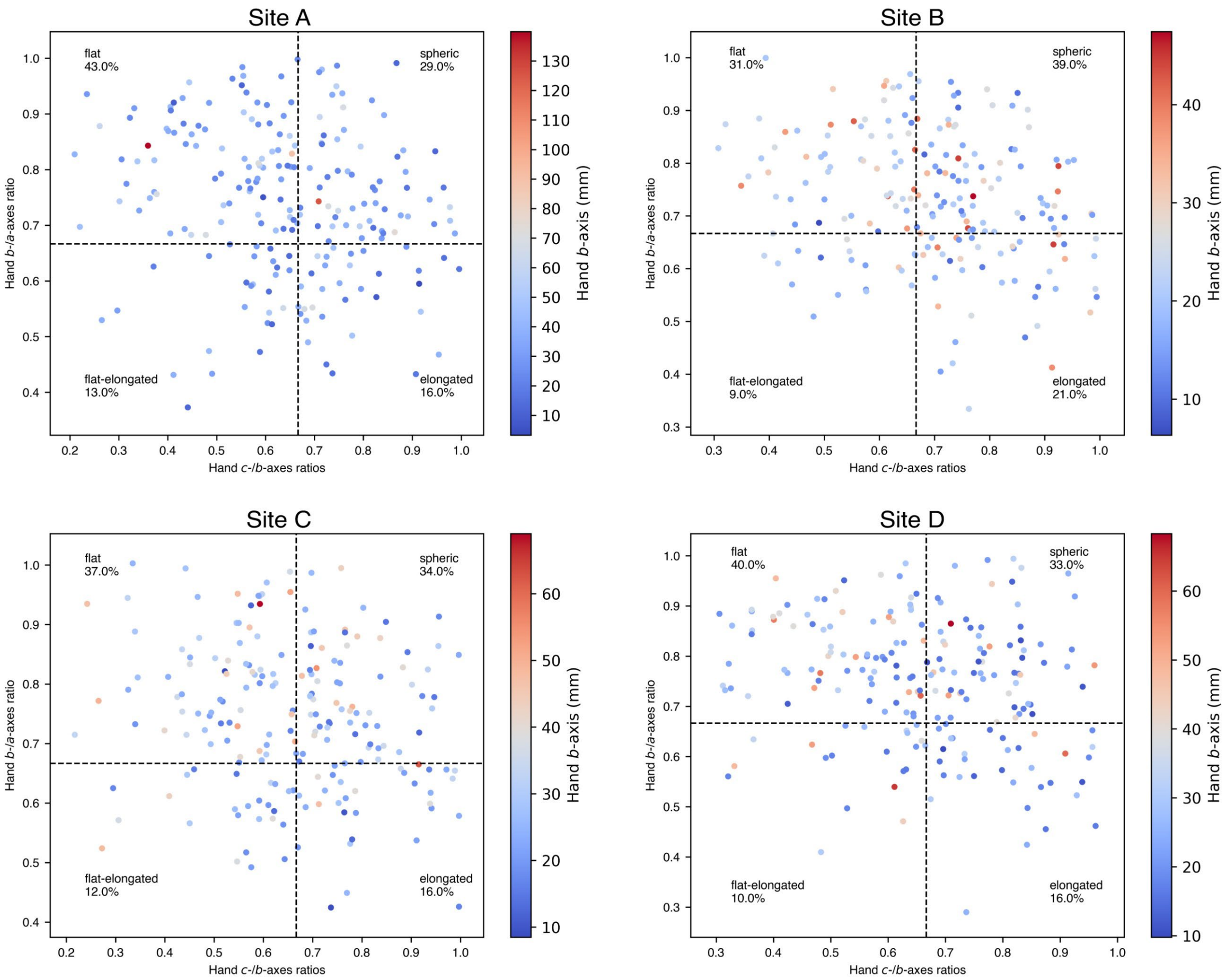

Figure A.2.5 (continued):b) hand *b*-axis. Numbers of grain shape classes are rounded (1% rounding error).

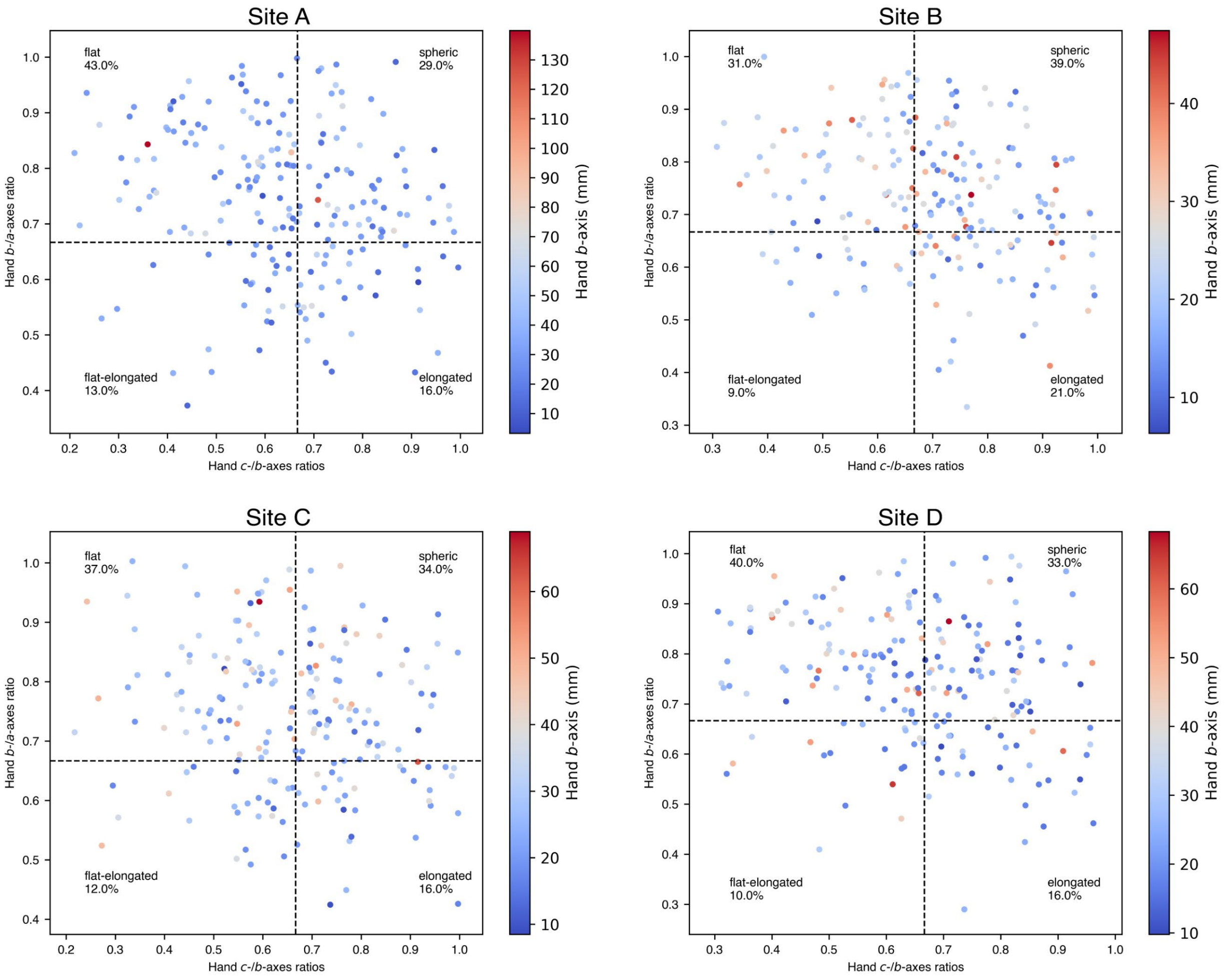

Figure A.2.5 (continued): c) hand *c*-axis. Numbers of grain shape classes are rounded (1% rounding error).

2.12.2 Tables

A.2.1a

Hand ***a*-axis**	D_{16} [mm]	95% CI [mm]	ε_{16} [± %]	D_{50} [mm]	95% CI [mm]	ε_{50} [± %]	D_{84} [mm]	95% CI [mm]	ε_{84} [± %]
Site A	26.37	[24.58 – 28.70]	7.81	44.28	[40.71 – 46.71]	6.78	71.16	[66.03 – 78.28]	8.61
Site B	19.69	[18.28 – 21.34]	7.77	28.67	[26.96 – 30.03]	5.35	44.41	[38.55 – 49.92]	12.80
Site C	24.47	[23.32 – 26.49]	6.48	35.40	[33.81 – 38.69]	6.89	51.92	[48.95 – 56.56]	7.33
Site D	21.75	[19.91 – 23.18]	7.51	32.19	[30.74 – 34.17]	5.33	52.79	[47.29 – 59.87]	11.91

A. 2.1b

Hand ***b*-axis**	D_{16} [mm]	95% CI [mm]	ε_{16} [± %]	D_{50} [mm]	95% CI [mm]	ε_{50} [± %]	D_{84} [mm]	95% CI [mm]	ε_{84} [± %]
Site A	18.82	[16.92 – 22.20]	14.03	32.28	[29.52 – 35.31]	8.97	50.98	[46.90 – 54.08]	7.04
Site B	14.20	[13.47 – 15.17]	5.99	20.82	[19.84 – 21.83]	4.77	31.02	[27.82 – 33.89]	9.79
Site C	18.05	[16.50 – 19.69]	8.83	26.22	[24.35 – 27.94]	6.85	39.80	[36.37 – 42.70]	7.95
Site D	16.01	[15.54 – 16.91]	4.29	24.58	[22.26 – 26.06]	7.73	39.57	[35.07 – 44.00]	11.28

A. 2.1c

Hand ***c*-axis**	D_{16} [mm]	95% CI [mm]	ε_{16} [± %]	D_{50} [mm]	95% CI [mm]	ε_{50} [± %]	D_{84} [mm]	95% CI [mm]	ε_{84} [± %]
Site A	11.56	[10.03 – 12.55]	10.92	18.34	[17.08 – 20.88]	10.36	33.52	[29.98 – 37.16]	10.72
Site B	9.24	[8.61 – 9.94]	7.15	14.46	[13.15 – 15.00]	6.38	22.52	[20.16 – 24.18]	8.93
Site C	11.24	[10.26 – 11.83]	6.98	16.44	[15.60 – 17.48]	5.73	28.02	[24.11 – 30.18]	10.83
Site D	10.34	[9.52 – 10.78]	6.10	15.04	[13.96 – 16.53]	8.53	24.85	[22.96 – 28.54]	11.22

Table A.2.1: Percentile values and relative uncertainties of the hand data. **a) – c)** Percentile values (D_{16}, D_{50}, D_{84}) and 95% confidence interval (CI) of all sample sites from hand data.

A.2.2a

Photo LVA (GAD)	D_{16} [mm]	95% C.I. [mm]	ε_{16} [± %]	D_{50} [mm]	95% C.I. [mm]	ε_{50} [± %]	D_{84} [mm]	95% C.I. [mm]	ε_{84} [± %]
Site A	8.80	[7.84 – 10.93]	17.56	22.33	[19.94 – 27.72]	17.42	52.97	[45.12 – 60.48]	14.50
Site B	8.13	[6.60 – 9.13]	15.54	15.46	[13.84 – 16.80]	9.58	29.42	[26.03 – 33.54]	12.76
Site C	9.66	[8.22 – 10.72]	12.94	18.00	[16.63 – 20.59]	11.00	35.24	[30.07 – 41.95]	16.85
Site D	9.29	[7.45 – 11.07]	19.48	19.67	[17.36 – 22.42]	12.86	43.43	[35.79 – 48.38]	14.50

A.2.2b

Photo LVA (GAU)	D_{16} [mm]	95% C.I. [mm]	ε_{16} [± %]	D_{50} [mm]	95% C.I. [mm]	ε_{50} [± %]	D_{84} [mm]	95% C.I. [mm]	ε_{84} [± %]
Site A	10.66	[8.24 – 11.83]	16.84	21.59	[19.10 – 24.17]	11.74	46.67	[38.28 – 53.60]	16.42
Site B	8.32	[7.26 – 9.32]	12.40	16.01	[13.86 – 17.80]	12.31	30.33	[27.97 – 33.92]	9.81
Site C	8.66	[7.40 – 9.72]	13.40	19.41	[16.89 – 22.72]	15.02	37.14	[34.24 – 42.89]	11.65
Site D	9.33	[7.79 – 11.48]	19.77	20.23	[18.04 – 23.19]	12.73	39.89	[35.28 – 44.04]	10.99

A.2.2c

Photo LVA (RAD)	D_{16} [mm]	95% C.I. [mm]	ε_{16} [± %]	D_{50} [mm]	95% C.I. [mm]	ε_{50} [± %]	D_{84} [mm]	95% C.I. [mm]	ε_{84} [± %]
Site A	8.80	[7.52 – 12.11]	26.12	21.91	[19.56 – 25.86]	14.38	46.84	[38.02 – 52.13]	15.06
Site B	7.86	[6.87 – 9.17]	14.66	15.90	[14.02 – 17.39]	10.60	28.70	[25.69 – 35.35]	16.84
Site C	7.90	[6.34 – 10.32]	25.18	19.09	[15.93 – 22.73]	17.81	35.68	[33.19 – 39.86]	9.35
Site D	8.52	[6.46 – 10.74]	25.14	19.06	[16.91 – 21.17]	11.18	42.06	[35.48 – 46.45]	13.04

A.2.2d

Photo LVA (RAU)	D_{16} [mm]	95% C.I. [mm]	ε_{16} [± %]	D_{50} [mm]	95% C.I. [mm]	ε_{50} [± %]	D_{84} [mm]	95% C.I. [mm]	ε_{84} [± %]
Site A	8.64	[6.91 – 10.75]	22.23	23.67	[19.97 – 27.17]	15.21	51.63	[41.09 – 59.86]	18.17
Site B	7.15	[6.55 – 8.69]	14.90	14.35	[12.77 – 16.26]	12.18	25.02	[21.68 – 28.51]	13.64
Site C	7.25	[6.14 – 8.29]	14.81	15.88	[14.92 – 18.78]	12.14	35.61	[30.96 – 40.87]	13.91
Site D	7.42	[5.98 – 9.60]	24.37	19.89	[17.26 – 22.87]	14.10	42.13	[34.30 – 47.15]	15.25

Table A.2.2: Percentile values and relative uncertainties of the photo data (*LVA*). **a)** – **d)**: Percentile values (*D_{16}, D_{50}, D_{84}*) and 95% confidence interval (CI) of the *LVA* (longest visible axis) from photo data of all sample sites. *GAD*: Grid-approach, distorted photos; *GAU*: Grid-approach, undistorted photos; *RAD*: Random-approach, distorted photos; *RAU*: Random-approach, undistorted photos.

A.2.3a

Photo SVA (*GAD*)	D_{16} [mm]	95% C.I. [mm]	ε_{16} [± %]	D_{50} [mm]	95% C.I. [mm]	ε_{50} [± %]	D_{84} [mm]	95% C.I. [mm]	ε_{84} [± %]
Site A	5.59	[4.87 – 7.07]	19.66	13.87	[11.83 – 16.52]	16.91	30.58	[25.60 – 36.49]	17.80
Site B	4.72	[4.17 – 5.81]	17.41	8.91	[8.30 – 9.89]	8.92	16.36	[14.44 – 20.82]	19.51
Site C	6.17	[4.86 – 6.68]	14.73	11.24	[9.93 – 12.66]	12.12	21.62	[19.20 – 26.05]	15.85
Site D	5.63	[5.03 – 6.41]	12.24	11.96	[10.88 – 13.43]	10.64	27.60	[23.68 – 29.86]	11.20

A.2.3b

Photo SVA (*GAU*)	D_{16} [mm]	95% C.I. [mm]	ε_{16} [± %]	D_{50} [mm]	95% C.I. [mm]	ε_{50} [± %]	D_{84} [mm]	95% C.I. [mm]	ε_{84} [± %]
Site A	6.07	[5.59 – 6.69]	9.03	12.24	[10.73 – 14.52]	15.48	27.53	[22.98 – 33.20]	18.56
Site B	5.15	[4.73 – 5.60]	8.48	9.60	[8.58 – 10.89]	12.03	18.97	[16.39 – 20.92]	11.92
Site C	5.13	[4.67 – 6.32]	16.03	11.80	[10.08 – 13.02]	12.46	24.50	[20.74 – 26.36]	11.46
Site D	5.62	[4.53 – 7.00]	21.97	11.44	[10.32 – 13.55]	14.12	25.37	[22.02 – 27.13]	10.05

A.2.3c

Photo SVA (*RAD*)	D_{16} [mm]	95% C.I. [mm]	ε_{16} [± %]	D_{50} [mm]	95% C.I. [mm]	ε_{50} [± %]	D_{84} [mm]	95% C.I. [mm]	ε_{84} [± %]
Site A	5.75	[4.96 – 7.34]	20.70	12.76	[11.50 – 14.80]	12.91	26.77	[23.12 – 33.53]	19.45
Site B	4.70	[4.35 – 5.11]	8.08	8.96	[8.04 – 10.32]	12.70	17.98	[15.80 – 20.48]	13.03
Site C	4.57	[3.78 – 5.58]	19.80	10.72	[9.41 – 12.18]	12.90	23.77	[20.52 – 27.35]	14.36
Site D	4.92	[3.43 – 6.50]	31.11	11.10	[9.66 – 11.79]	9.59	24.34	[20.22 – 27.93]	15.83

A.2.3d

Photo SVA (*RAU*)	D_{16} [mm]	95% C.I. [mm]	ε_{16} [± %]	D_{50} [mm]	95% C.I. [mm]	ε_{50} [± %]	D_{84} [mm]	95% C.I. [mm]	ε_{84} [± %]
Site A	5.43	[4.99 – 7.16]	19.93	12.48	[10.84 – 14.77]	15.75	27.36	[24.27 – 32.64]	15.30
Site B	4.42	[3.99 – 4.98]	11.14	8.26	[7.56 – 9.38]	11.01	15.92	[13.54 – 18.04]	14.15
Site C	4.46	[4.04 – 5.06]	11.45	10.17	[8.30 – 11.64]	16.45	21.96	[18.18 – 24.58]	14.57
Site D	4.82	[3.85 – 5.92]	21.42	11.66	[10.49 – 13.14]	11.37	26.03	[22.12 – 28.43]	12.11

Table A.2.3: Percentile values and relative uncertainties of the photo data (*SVA*). **a)** – **d)**: Percentile values (D_{16}, D_{50}, D_{84}) and 95% confidence interval (CI) of the *SVA* (shortest visible axis) from photo data of all sample sites. *GAD*: Grid-approach, distorted photos; *GAU*: Grid-approach, undistorted photos; *RAD*: Random-approach, distorted photos; *RAU*: Random-approach, undistorted photos.

Table A.2.4

Sieve data ± 5 percentiles	D_{16} [mm]	[D_{11} – D_{21}] [mm]	ε_{16} [± %]	D_{50} [mm]	[D_{45} – D_{55}] [mm]	ε_{50} [± %]	D_{84} [mm]	[D_{79} – D_{89}] [mm]	ε_{84} [± %]
Site A	10.86	[8.23 – 13.48]	24.18	35.41	[30.16 – 41.54]	16.07	102.12	[85.12 – 119.12]	16.65
Site B	7.63	[5.99 – 9.10]	20.41	17.89	[15.91 – 19.90]	11.15	31.89	[29.57 – 41.61]	18.89
Site C	6.33	[5.06 – 7.60]	19.99	15.88	[14.45 – 17.96]	11.07	30.33	[28.20 – 36.87]	14.30
Site D	8.02	[6.28 – 9.63]	20.88	19.69	[17.68 – 21.70]	10.22	39.12	[31.36 – 47.30]	20.36

Table A.2.4: Percentile values and relative uncertainties of the sieve data. Percentile values (D_{16}, D_{50}, D_{84}) and confidence range of ± 5 percentiles of all sample sites from sieve data.

2.13 Appendix B

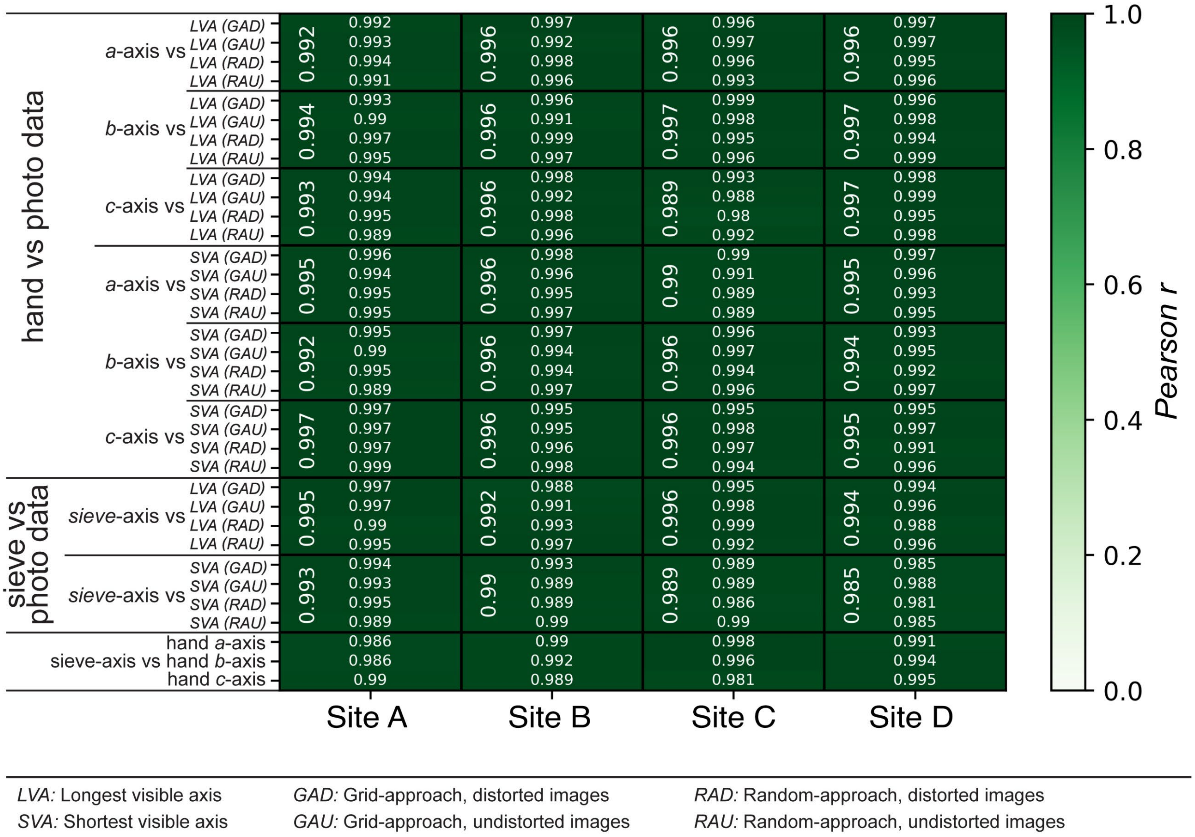

Fig. B.2.1: Pearson r-values. Colour-coded table of Pearson r-values and averages thereof (vertically oriented). Dark colours denote a good correlation (i.e., r = 1.00).

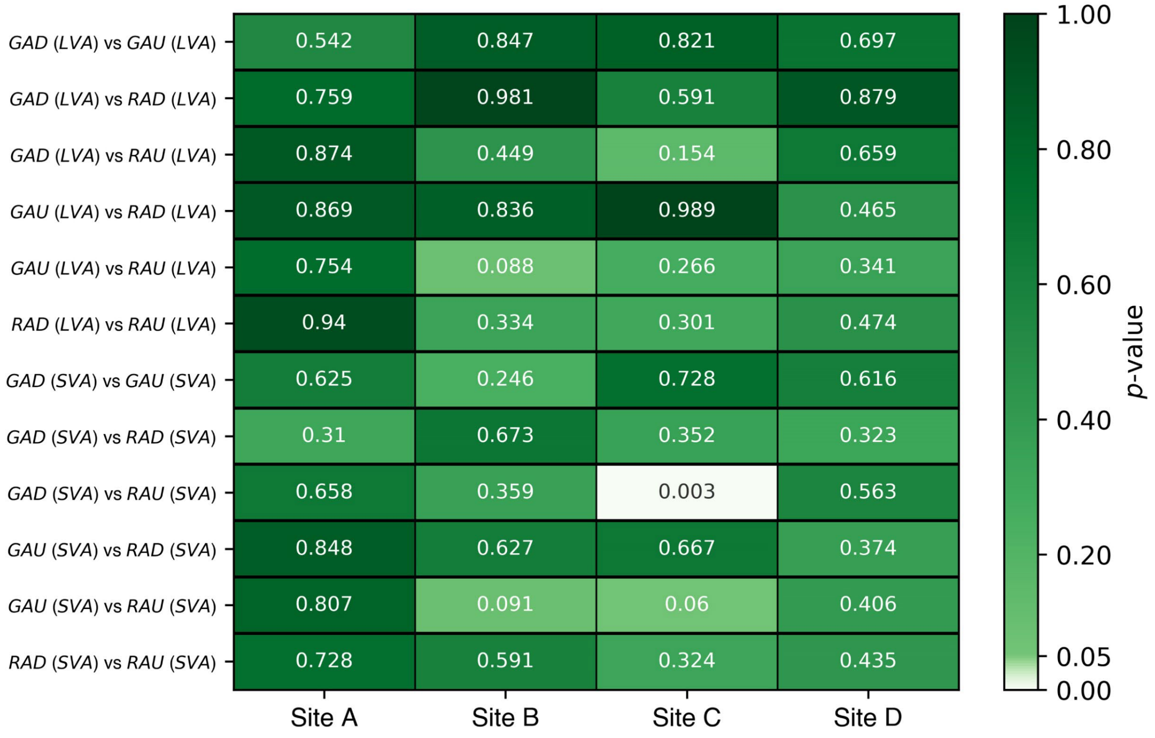

LVA: Longest visible axis
SVA: Shortest visible axis
GAD: Grid-approach, distorted images
GAU: Grid-approach, undistorted images
RAD: Random-approach, distorted images
RAU: Random-approach, undistorted images

Fig. B.2.2: KS2 *p*-values of all photo acquisition approaches. Colour-coded *p*-values based on the KS2 test (Kolmogorov-Smirnov two-sample test; see methods) with an alpha level of 0.05. Dark colours denote a good correlation (i.e., *p*-value = 1.00), light colours show a poor correlation (*p*-value = 0.00).

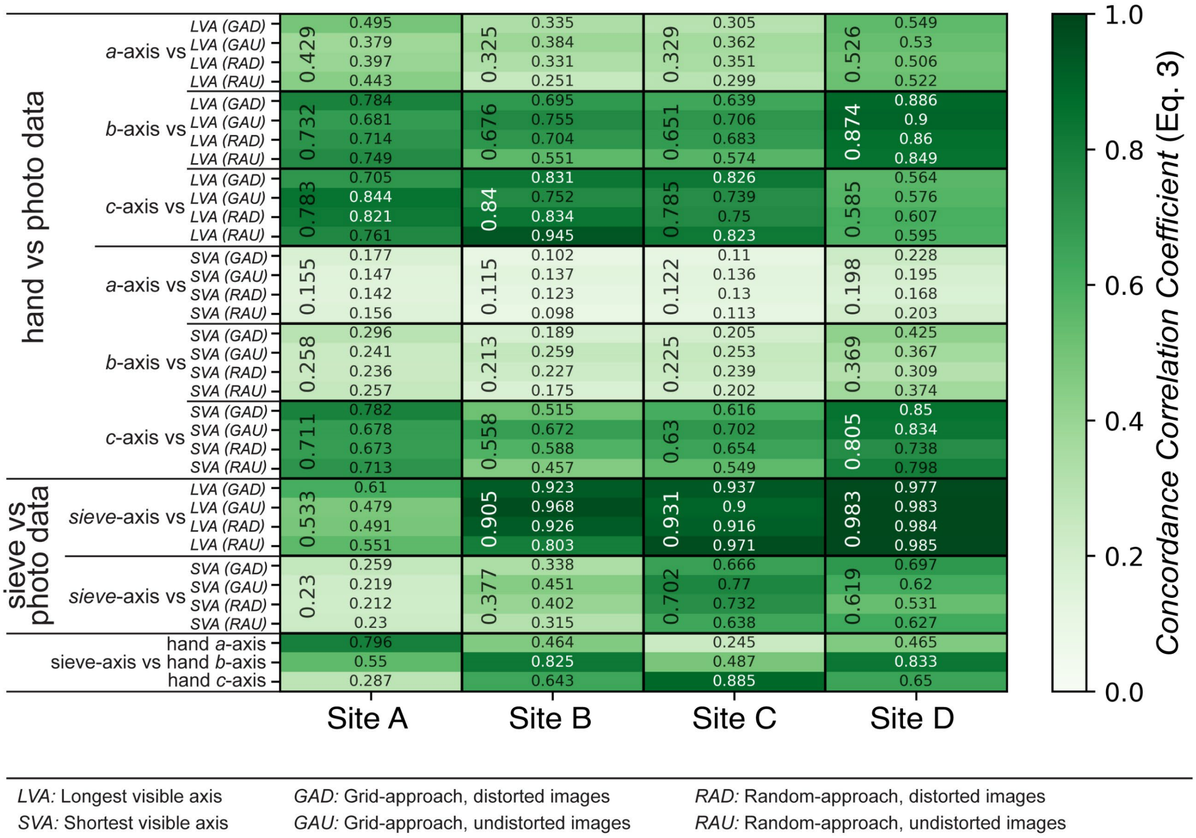

Fig. B.2.3: *CCC* values of the original datasets. Colour-coded *CCC* values (see methods) and averages thereof (vertically oriented) of the original datasets. Dark colours denote a good correlation (i.e., *CCC* = 1.00), light colours show a poor correlation (*CCC* = 0.00).

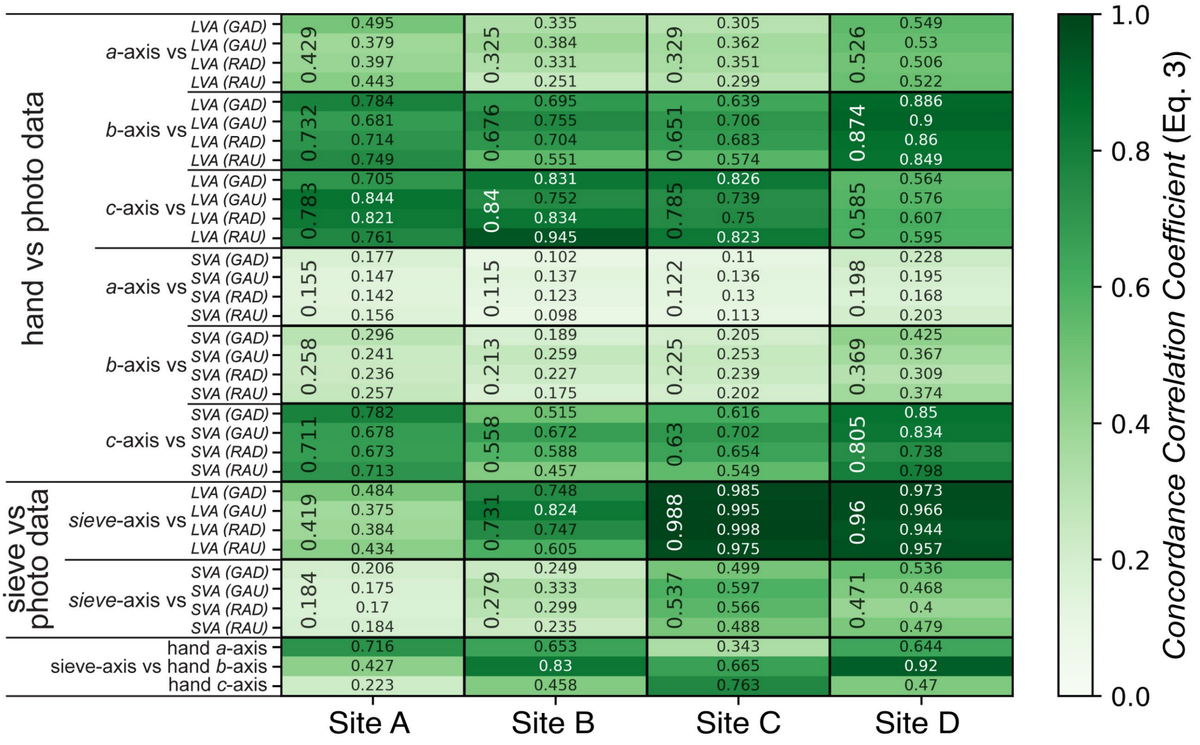

LVA: Longest visible axis *GAD:* Grid-approach, distorted images *RAD:* Random-approach, distorted images
SVA: Shortest visible axis *GAU:* Grid-approach, undistorted images *RAU:* Random-approach, undistorted images

Fig. B.2.4: *CCC* values of corrected sieve datasets. Colour-coded *CCC* values (see methods) and averages thereof (vertically oriented) of the sieve data now corrected by a factor of *Ds*/hand-*b*-axis = 0.85. Dark colours denote a good correlation (i.e., *CCC* = 1.00), light colours show a poor correlation (*CCC* = 0.00).

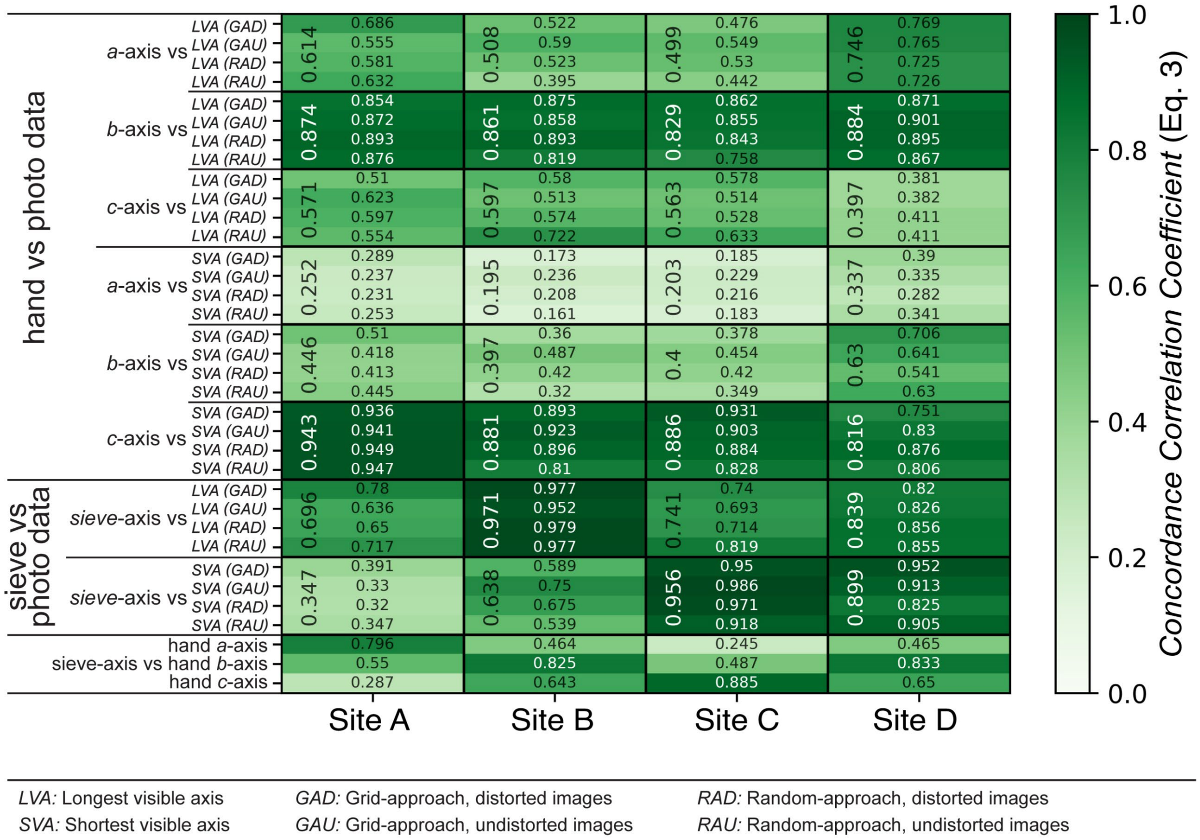

Fig. B.2.5: *CCC* values of corrected photo datasets. Colour-coded *CCC* values (see methods) and averages thereof (vertically oriented) of the photo data now corrected by a factor of *LVA*/hand-*b*-axis = 0.83 and *SVA*/hand-*c*-axis = 0.73. Dark colours denote a good correlation (i.e., *CCC* = 1.00), light colours show a poor correlation (*CCC* = 0.00).

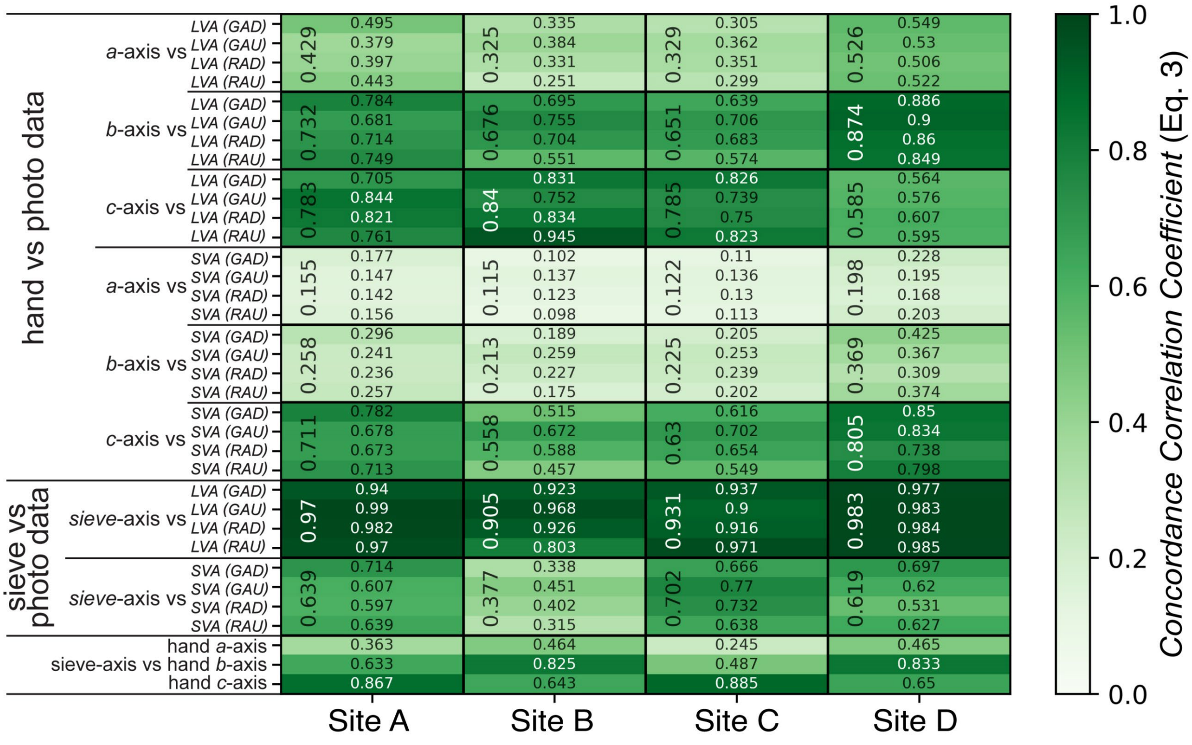

LVA: Longest visible axis
SVA: Shortest visible axis
GAD: Grid-approach, distorted images
GAU: Grid-approach, undistorted images
RAD: Random-approach, distorted images
RAU: Random-approach, undistorted images

Fig. B.2.6: *CCC* of sieve data with grains >125 mm removed. Colour-coded *CCC* values (see methods) and averages thereof (vertically oriented) of the sieve data where grain sizes > 125 mm were removed from the dataset. Dark colours denote a good correlation (i.e., *CCC* = 1.00), light colours show a poor correlation (*CCC* = 0.00).

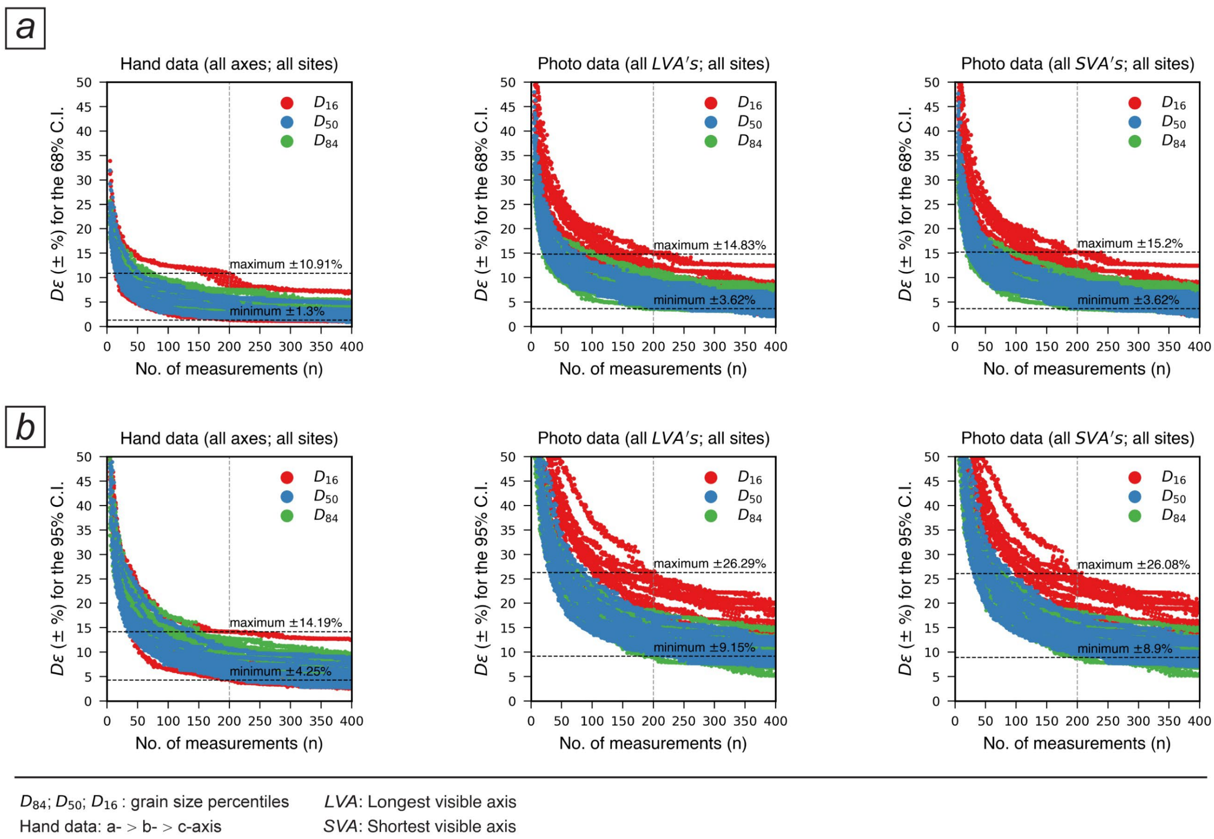

Fig. B.2.7: Uncertainties on the hand and photo data. Normalised percentile uncertainties (see methods) versus increasing number of measurements for a) the 68 % confidence interval (C.I.) and b) the 95 % C.I.. Vertical lines mark threshold for 200 measurements. Horizontal lines and related percent numbers denote the minimum and maximum uncertainty value per measuring method at n = 200, independent of the sample sites and percentiles.

3.

Quantification of sediment fluxes and intermittencies from Oligo-Miocene megafan deposits in the Swiss Molasse basin

Philippos Garefalakis*, Ariel Henrique do Prado*, Alexander C. Whittaker**, David Mair* and Fritz Schlunegger*

* University of Bern, Institute of Geological Sciences, Baltzerstrasse 1+3, 3012 Bern, Switzerland

** Department of Earth Science and Engineering, Imperial College London, South Kensington, London, SW7 2AZ, UK

The following text is status 28 June 2023. The modified version is published in Basin Research, 23 April 2024.

DOI: https://doi.org/10.1111/bre.12865

Abstract

Deposits of alluvial fans in the Swiss Molasse basin bear key information on the sedimentary dynamics of these routing systems. The architectural trends and grain sizes of the conglomerates reveal information on the sediment fluxes and thus record variations in the intermittency – a proxy for the fan's activity – which inform on the relative importance of sediment production and transport controls, i.e., tectonic or climatic processes. Here, we calculated intermittencies from sediment transport dynamics using the ratio between the long-term average and the short-term instantaneous sediment fluxes. For this, we collected grain size data from three paleo fan systems through Oligo-Miocene times where proximal-distal relationships are still preserved.

Our results show that the sediment transport dynamics vary significantly between the three fan systems, which we term the western, central, and eastern fans. The eastern fan shows a low long-term sediment flux (6.8 km^2 Myr^{-1}) which needed the fan to be active during c. 10 h yr^{-1} (intermittency factor of 1.07 x 10^{-3}). The western fan reveals a higher long-term sediment flux (17.0 km^2 Myr^{-1}) which could have accumulated during c. 16 h yr^{-1} (intermittency factor of 1.93 x 10^{-3}) thereby reflecting a less intermittent system. The central fan shows the largest long-term sediment flux (38.9 km^2 Myr^{-1}) that would require c. 55 h yr^{-1} to be deposited (intermittency factor of 6.31 x 10^{-3}) thereby representing the most active system.

By relating these characteristics to the regional exhumation history, we consider that the highly active central fan likely reflected the transient response of the Alpine surface to the break-off of the European mantle lithosphere slab, with only a minor climatic control. Contrarily, the western and eastern fans were formed during the Alpine evolution when steady-state conditions between uplift and erosion were reached and when sediment fluxes to the basin were lower.

3.1 Introduction

The formation of alluvial fans in sedimentary basins at the tip of an adjacent mountain belt is influenced by tectonic or climatic perturbations in the source area, or through adjustments of the eustatic sea level farther down-system (Blair and McPherson, 1994; Harvey et al., 2005; Ventra and Clarke, 2018). Shifts in the signals of sediment flux and water discharge, propagating from the source area into the sedimentary sink, are considered as transmitters of these processes (Allen et al., 2013; Castelltort et al., 2015; Romans et al., 2016). Changes in sediment flux can modify the distribution of the sediment's calibre along alluvial fans in basins (Jordan, 1981; Flemings and Jordan, 1990; Heller and Paola, 1992; Whittaker et al., 2011; D'Arcy et al., 2017), which is additionally controlled by the spatial distribution of accommodation space, and hence the basin's subsidence (Beaumont, 1981; Sinclair et al., 1991; Sinclair and Naylor, 2012; Brooke et al., 2018). From a stratigraphic perspective, coarse-grained conglomerate beds with sandstone and mudstone interbeds are commonly attributed to deposits of alluvial fans, or megafans if their radii exceed >10 km (Matter, 1964; Allen et al., 1991; Blair and McPherson, 1994; Schlunegger et al., 1996; Kempf et al., 1999; Harvey et al., 2005). Consequently, in such stratigraphic records, sediment flux signals are often preserved by the arrangement and the size of grains. Furthermore, information on the small-scale stacking pattern and the large-scale architecture of such deposits, paired with a chronological framework, yields the basis for quantifying the sedimentary dynamics on these fans (Bridge, 1985; Flemings and Jordan, 1989; Heller and Paola, 1992; Allen et al., 2013; Ventra and Nichols, 2014). Such stratigraphic sequences have also been identified in the Swiss Molasse basin (SMB), situated on the northern margin of the European Central Alps. This basin hosted three major large-scale dispersal systems (i.e., megafans), to which we refer for simplicity as the western, the central and the eastern fan, respectively (section 3.2.3 and Fig. 3.1).

Previous contributions have linked changes in the stacking pattern in these conglomerates and the size of grains to orogenic events in the Alpine hinterland (Allen et al., 1991; Sissingh, 1997; Schlunegger and Castelltort, 2016; Garefalakis and Schlunegger, 2018). Moreover, some authors provided first estimates on sediment fluxes, however at the scale of the entire SMB, based on the preserved mass (Hay et al., 1992) or volume of sediments (Schlunegger, 1999; Kuhlemann, 2000; Kuhlemann et al., 2001a). They found that sediment fluxes increased at c. 30 Ma and throughout the Oligocene, reaching a peak at c. 20 Ma (c. 22000 km^3 Myr^{-1}), followed by a drop, and then a short-term increase, after which sediment supply stabilised at lower values (c. 15000 km^3 Myr^{-1}) after 15 Ma. Yet, no estimates exist on the magnitude of sediment fluxes at the megafan scale in the SMB. Furthermore, we lack information on their activities – known as the intermittency. The intermittency factor can be expressed as the proportion of a year during which a system accomplishes its mean annual transport work (Dury, 1961; Parker et al., 1998; Mohrig et al., 2000; Navratil et al., 2006). Intermittent flow or intermittent sediment transport is widely recognised in modern rivers but is directly applicable to alluvial fan systems as well (Paola et al., 1992; Tucker and Slingerland, 1997; Meybeck et al., 2003; McLeod et al., 2023). Because during a bankfull discharge event, which we will use as a reference, all grains are transported at nearly the same rate (equal mobility, Paola et al., 1992), the intermittency can be a measure for the geomorphologic effectiveness of a fluvial system (Wainwright et al., 2015; Pfeiffer and Finnegan, 2018; Wickert and Schildgen, 2019; Hayden et al., 2021; Lyster et al., 2022).

Here, we estimated the long-term and short-term sediment fluxes and particularly the intermittencies of the three major megafan systems in the SMB based on stratigraphic information preserved by well-exposed sections (Fig. 3.1). Our aim is to unravel the activity of these paleo-fans, mainly because alluvial fan intermittencies are of key importance for determining how these systems record tectonic and climatic signals in the Alpine hinterland. Accordingly, a wider goal of this work is to explore how erosional-depositional mechanisms responded to the built-up of the Alpine topography, which occurred simultaneously with the construction of the target fans.

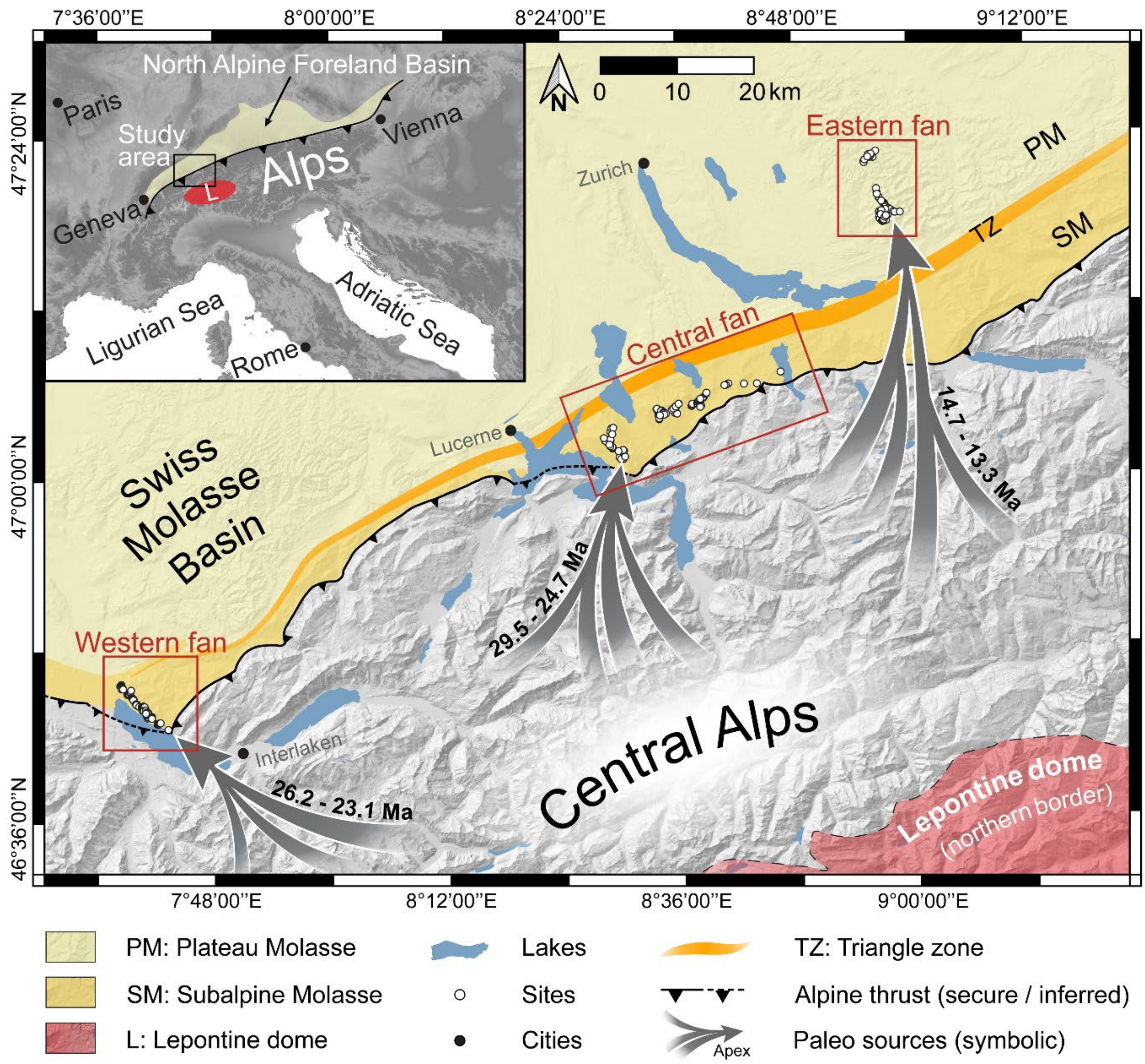

Figure 3.1: Simplified geological map of the Swiss Molasse Basin and the location of the three paleo megafan systems. The three fans were all sourced from the Central Swiss Alps throughout the Oligo- and Miocene. Sites denote locations where grain size data was collected (see also detailed geological maps of each fan system in appendix A). The underlying digital elevation model (LiDAR DEM Swiss ALTI3D; © swisstopo) shows the current topography of the Alps. The inset map shows the position of the North Alpine Foreland Basin in relation to the Alps and the present-day position of the Lepontine dome (EU-DEM v1.1 © European Union, Copernicus Land Monitoring Service 2023, European Environment Agency, EEA).

3.2 Geological setting

3.2.1 The evolution of the Central Alps and the Swiss Molasse basin

The SMB is situated to the north of the Central Alps and is bordered to the South by the basal Alpine thrust (Fig. 3.1). It formed synchronously with the build-up of the Alps between the Oligocene and the Miocene and recorded the erosional response of sediment routing systems to the different stages of the Alpine orogeny and the related topographic evolution (Beaumont, 1981; Pfiffner, 1986; Allen et al., 1991; Schlunegger and Kissling, 2022). The SMB consists of two transgressive-regressive mega-cycles, each consisting of (shallow) marine and freshwater deposits (Matter et al., 1980; Allen et al., 1991; Kuhlemann and Kempf, 2002). The Molasse basin is further subdivided into the flat-lying Plateau Molasse, which is undeformed and constitutes the SMB to a large part, and the tilted, folded and thrusted Subalpine Molasse farther to the South (Fig. 3.1). Terrestrial clastic sedimentation is recorded by the Freshwater Molasse and occurred by transverse braided systems on alluvial megafans close to the Alpine front (Stürm, 1973; Matter et al., 1980; Bürgisser, 1981; Schlunegger et al., 1996; Kempf and Matter, 1999). The Freshwater type of Molasse sedimentation yielded in the construction of stratigraphic deposits that have been analysed in detail for their sedimentological and chrono-stratigraphic properties (Matter and Weidmann, 1992; Schlunegger et al., 1993, 1997a; Kempf and Pfiffner, 2004) and for the petrology and geochemistry of individual clasts and the grain-supporting matrix (Tanner, 1944; Büchi, 1958; Stürm, 1973; Matter et al., 1980; Bürgisser, 1981; Schlunegger et al., 1997a; Bolliger, 1998; Kempf et al., 1999; Eynatten, 2003; van der Boon et al., 2018).

3.2.2 Orogenic and climatic conditions during the Oligo-Miocene

The three target fans were active during the Oligo- and Miocene, thereby reflecting the erosional evolution of the adjacent Central Alps (Pfiffner, 1986; Schlunegger et al., 1998; Kuhlemann, 2007). During Oligocene times, between c. 32 and 26 Ma, the Central Alps experienced strong topographic modifications due to rapid uplift of the orogen particularly in the Lepontine area (Fig. 3.1; Steck et al., 2013), expressed by high exhumation rates (Schlunegger and Willett, 1999; Boston et al., 2017) and large sediment fluxes (Kuhlemann et al., 2001a). Such tectonic adjustments of the orogen were explained by crustal thickening of the subsequent northward thrusting of the Alpine orogen (Beaumont et al., 1996; Schmid et al., 1996; Pfiffner et al., 2002) or by a slab break-off from the European mantle lithosphere that occurred at 32 – 30 Ma (Sinclair, 1997; Schlunegger and Castelltort, 2016; Kästle et al., 2020; Schlunegger and Kissling, 2022). Uplift related to slab break-off was considered to have initiated a transient stage in the evolution of the Alpine landscape (Garefalakis and Schlunegger, 2018), where a highly dissected terrain was formed through headward retreat of the erosional front, thereby exhuming the crystalline core of the Alps at that time. This adjustment to high uplift in the Lepontine area continued until c. 25 – 24 Ma, at which time the Alps reached a steady-state topography (Schlunegger and Kissling, 2015). At 20 Ma, the situation in the Alpine hinterland started to change again when the exhumation of the external crystalline massifs was initiated and when tectonic unroofing in the core of the Alps reached the highest rate (Schlunegger and Norton, 2013; Baran et al., 2014; Boston et al., 2017; Herwegh et al., 2017). This induced a re-organisation of the drainage network in the core of the Alps, where an orogen-normal drainage network with short streams and steep gradients (Fig. 3.2a) changed to an orogen parallel system with longer flow paths and thus shallower gradients (Fig. 3.2b; Schlunegger et al., 1998; Kühni and Pfiffner, 2001; Spiegel et al., 2001; Stutenbecker et al., 2019; Bernard et al., 2021). As a consequence, supply of sediment to the SMB started to decrease (Hay et al., 1992; Schlunegger, 1999; Kuhlemann et al., 2001b). Also at 20 Ma, syn-depositional back-thrusting along the southern margin of the Plateau Molasse resulted in the establishment of the triangle zone (Fig. 3.1; Kempf et al., 1999; Schlunegger and Mosar, 2011) and the formation of a basin-wide progressive unconformity close to the Alpine thrust (Schlunegger et al., 1997b). After a short period of a high sediment delivery to the Molasse basin between 18 – 16 Ma, the supply rates of clastic material continuously decreased (Kuhlemann et al., 2001b).

From a paleoclimate perspective, stable carbon and oxygen isotope data collected from Chattian deposits (Late Oligocene) in the Molasse basin suggest that at c. 25.5 Ma the paleoclimate possibly changed from a humid towards a warmer and drier, but probably stormier (Schlunegger and Norton, 2013), climate (Berger, 1992; Schlunegger et al., 2001; Kuhlemann and Kempf, 2002; Schlunegger and Castelltort, 2016). This is also in accordance with interpretations of the global oxygen isotope record (Zachos et al., 2001). During the Miocene, floral faunas (Mosbrugger et al., 2005) and carbon and oxygen isotope data from pedogenic carbonates (Methner et al., 2020; Krsnik et al., 2021) suggest a cooling between c. 15 and 14 Ma, right after the Mid-Miocene Climatic Optimum (at c. 17 Ma), which was also interpreted to have occurred globally (Zachos et al., 2001).

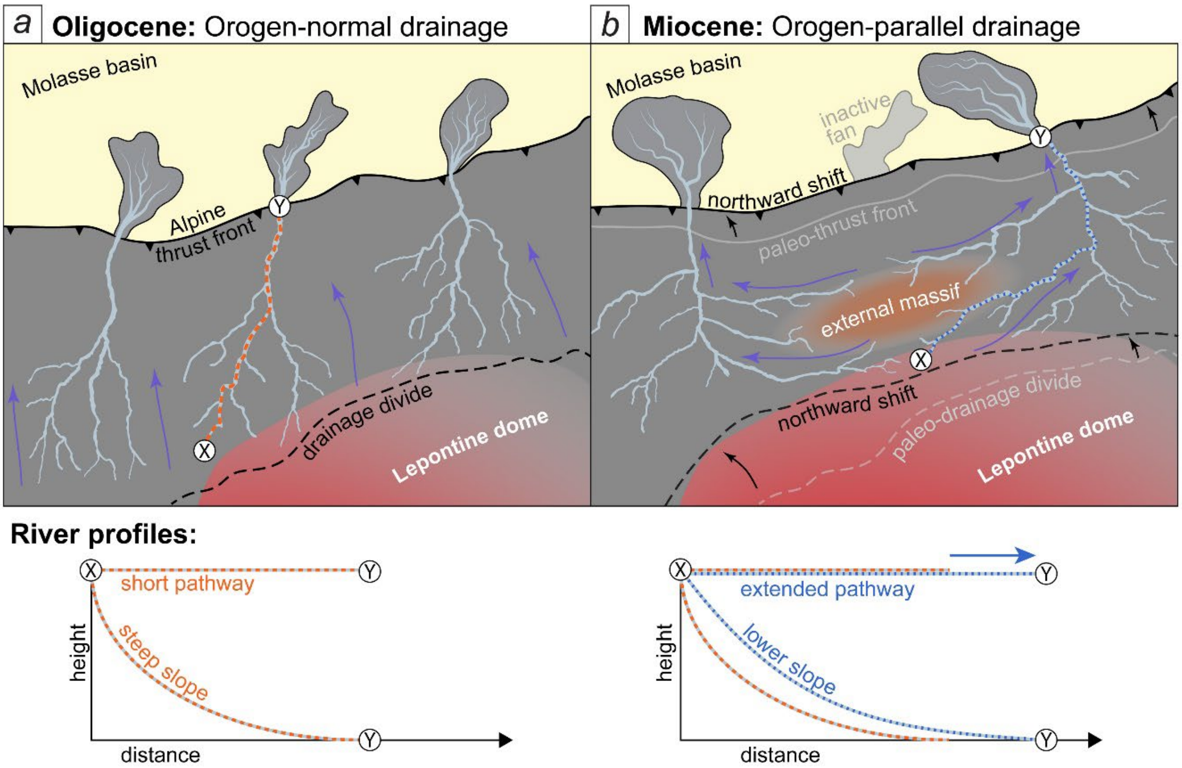

Figure 3.2: Simplified paleogeographical sketch of the drainage network in the Central Alps and the alluvial fans in the adjacent Molasse basin. **a)** During the Oligocene a drainage network, oriented normal to the Alpine strike, sourced the Central Alps (e.g., Kühni and Pfiffner, 2001; Stutenbecker et al., 2019). **b)** During the Miocene the drainage network evolved into an orogen-parallel oriented pattern, possibly influenced by the exhumation of the external massifs in the Central Alps and a northward shift of the drainage divide (e.g., Schlunegger et al., 1998; Bernard et al., 2021) This induced a re-organisation of the drainage network that experienced an extension of the pathways and a lowering of the channel slopes, respectively (e.g., Schlunegger, 1999; Spiegel et al., 2001).

3.2.3 Temporal and spatial framework of the target fans

The fan deposits have been placed into a chronological framework using magnetopolarity stratigraphies paired with micro-mammalian data collected along stratigraphic sections (Kempf et al., 1997; Schlunegger et al., 1997b; Kälin and Kempf, 2009). The westernmost section in the study area (western fan in Fig. 3.1), known as the Thun section, and its contemporaneous twin section located farther to the ENE, recorded the construction of the Blueme megafan during Oligocene times between c. 26.2 – 23.1 Ma (Schlunegger et al., 1993; 1996; Strasky et al., 2022). In the central part of the SMB (central fan in Fig. 3.1), the Rigi megafan constitutes another major depositional system, which was active c. 29.5 – 24.7 Ma ago (Schlunegger et al., 1997a, 1997c). Contemporaneous deposits farther downstream are encountered at four sections situated at the proximal basin border (Stürm, 1973; Schlunegger et al., 1997a). In the eastern part of the SMB (eastern fan in Fig. 3.1), deposits of the Hoernli megafan are exposed along two stratigraphic sections that recorded the evolution of this dispersal system (Büchi, 1958; Bürgisser, 1981; Kempf et al., 1997; Kempf and Matter, 1999; Kälin and Kempf, 2009). These deposits are younger and span the time interval between c. 14.7 – 13.3 Ma (Kempf et al., 1997; Kempf and Matter, 1999; Kälin and Kempf, 2009). Detailed geological maps and stratigraphic sections of the three fans are available in appendix A.

Proximal-distal relationships were already reconstructed as documented by earlier works based on paleo-flow and petrographic data (Stürm, 1973; Bürgisser, 1981; Schlunegger et al., 1993, 1996, 1997a; Kempf et al., 1997; Kempf and Matter, 1999; Garefalakis and Schlunegger, 2018). The position of the paleo fan apex was reconstructed based on mapping, paleo-stratigraphic restorations and measurements of discharge directions (details in appendix A). For modelling purposes, we placed the apex +3 km upstream of the location that currently exposes the most proximal deposits. We did so to compensate for the amount of tectonic erosion during the emplacement of the overlying thrust nappes (Pfiffner, 1986). This is in accordance with the outcomes of the studies that provided relatively precise positions for the paleo apex of the western (Schlunegger et al., 1993, 1996) and central fans (Stürm, 1973; Schlunegger et al., 1997a; 1997b). For the eastern fan the situation is different because large parts are not preserved (Bürgisser, 1980, 1981; Bolliger, 1998) as the basin was inverted and the Molasse sediments have been eroded since the Pliocene at the latest (Mazurek et al., 2006; Cederbom et al., 2011; Schlunegger and Mosar, 2011). Consequently, the position of the paleo apex of the eastern fan may have been located at least 3 km upstream (or even c. 10 – 15 km farther to the SE according to Bürgisser, 1980; 1981) of the most proximal location where sediments are exposed. In that context, we investigated the sensitivity of the paleo-apex' position on the outcomes of the grain size fining model (see appendix A for detailed results). Accordingly, the distance between the paleo apex and the most distal location is c. 12 km for the western, 12 vs. 24 km for the eastern, and 32 km for the central fan (Fig. 3.1).

From a sedimentological and stratigraphic perspective, the analysed deposits are similar in their large-scale architecture (Fig. 3.3). At proximal positions, the sequences are characterised by hundreds of m-thick amalgamations of several dm- to m-thick conglomerate beds, intercalated by a few m-thick sandstone and mudstone beds. Towards more distal sites, individual conglomerate beds thicken to a few meters and amalgamations thereof are rare, but the frequency of m-thick sandstone and mudstone interbeds increases. This reflects a downstream transition from a stream with braided, shallow channels towards an environment with single-thread and deep channels (Boothroyd and Ashley, 1975; Church, 2006; Huggenberger and Regli, 2009; Garefalakis and Schlunegger, 2018). At distal positions, the mudstones with reddish to yellow mottling, rootlets, and pedogenic carbonate nodules have been considered as deposits on floodplains bordering the channel belts (Stürm, 1973; Schlunegger et al., 1993, 1997a; Kempf et al., 1999; Garefalakis and Schlunegger, 2018).

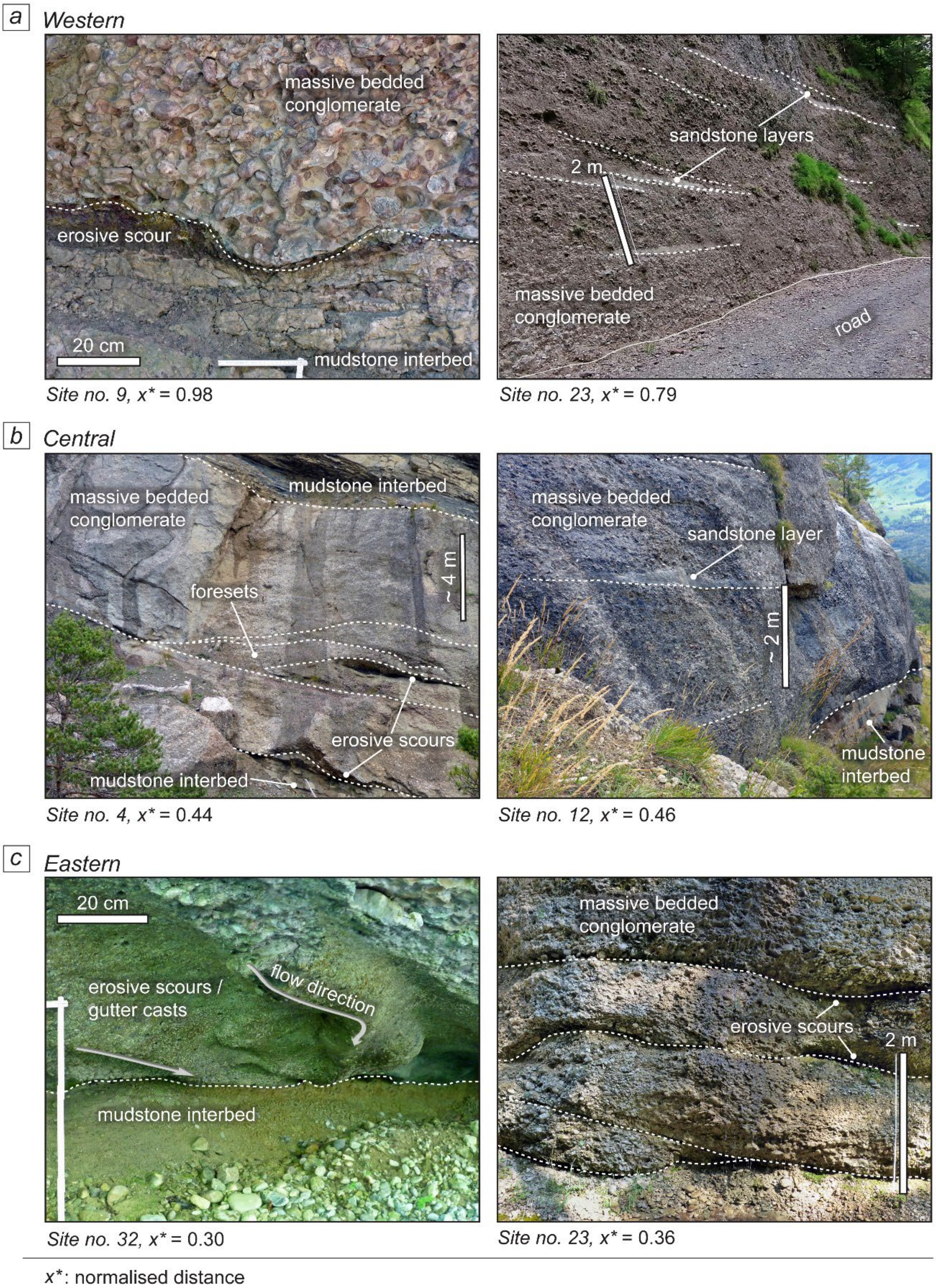

Figure 3.3: Field examples of outcrops showing conglomerate beds and sedimentary structures of the **a)** western, **b)** central and **c)** eastern fan system. Please see appendix A for the locations of these sites and appendix B for the related coordinates.

3.3 Methods

3.3.1 Revision of chronological framework

We recalibrated previously published magnetostratigraphic data through correlations to the recent Global Time Scale GTS2020 (Gradstein et al., 2020) and incorporated the results of new mapping (Hantke et al., 2022; Strasky et al., 2022) to build an updated chronological and sedimentological framework. We did so because the original temporal calibrations of the sections were either based on correlations of the magneto stratigraphic framework to the CK95 (Cande and Kent, 1995) or to the ATNTS2004 time scales (Lourens et al., 2004). However, these chronologies have partially different numerical ages than the GTS2020, particularly for the timescales of interest. The detailed chronostratigraphic revision is given in appendix A of this chapter.

3.3.2 Intermittency

We used the ratio between the long-term sediment flux ${Q_s}_A^*$, and the instantaneous bankfull bedload flux Q_b^* as a proxy for the intermittency of our target fans (Lyster et al., 2022). The dimensionless intermittency factor (I_F) is calculated as:

$$I_F = {Q_s}_A^* / {Q_b}^* \ [-] \qquad Eq. (3.1).$$

We computed ${Q_s}_A^*$ through the grain size fining model (section 3.3.3), and Q_b^* through the Meyer-Peter and Müller (1948) bedload equation (section 3.3.4). Alternatively, also in a stratigraphic framework, ${Q_s}_A^*$ could be determined using the volume of the investigated deposits as basis (Hayden et al., 2021). We also expressed the I_F in hours per year [h yr^{-1}], thereby using 365.2425 days for a year.

3.3.3 Long-term sediment flux

3.3.3.1 Principles and basic equations

Long-term sediment fluxes were calculated by applying a self-similar grain size fining model for gravel introduced by Fedele & Paola (2007). The model depends on input parameters that can be derived directly from field observations, which are: i) the down-system length of the depositional system, ii) the spatial distribution of accommodation space and its down-system decreasing rate, and iii) the grain size distribution at the apex. We then iteratively determined (through the grain size fining model) the sediment flux at the fans' apex, which reflects the long-term sediment flux ${Q_s}_A^*$. The model is ultimately derived from the Exner equation (Paola and Voller, 2005; Fedele and Paola, 2007), which bases on the principle that deposition or erosion of sediment results in a modification of the bed-surface elevation that changes in proportion to the volume of the deposited or eroded mass (Paola and Voller, 2005). Thus, it is founded on a mass-conserving sorting process (Fedele and Paola, 2007) where the balance between sediment being deposited, transported, or bypassed is maintained at any point on the fan (Fedele and

Paola, 2007; Duller et al., 2010; Armitage et al., 2011; Allen et al., 2013; Brooke et al., 2018). Additionally, it assumes that gravel grain size distributions are self-similar (i.e., the mean and standard deviation down-system decreases at the same rate). In its simplest form (details in appendix A of this chapter), the model computes the spatial distribution of sediment flux $Qs^{*}(x^{*})$:

$$Q_s{}^{*}(x^{*}) = Q_{s_A}^{*} - \left(1 - \lambda_p\right) \int_0^L r^{*}(x^{*})\, dx^{*} \; [m^3\ Myr^{-1}\ m^{-1}] \qquad Eq.(3.2).$$

Here, $Q_{s_A}^{*}$ is the unit input sediment flux at the system's apex ($x^{*} = 0$, where x^{*} is the downstream length normalised by the total depositional length L, i.e., $x^{*} = x/L$), $\lambda_p = 0.3$ is the sediment porosity and set as constant (Fedele and Paola, 2007) and r^{*} is the subsidence rate along distance (Eq. (3.7) and section 3.3.3). Following a dimensionless distance transformation (i.e., y^{*}, Eq. (S3.7) in appendix A) applied to the spatial distribution of sediment mass (i.e., Eq. (S3.4) in appendix A) and considering the principle of self-similarity (Eq. (3.5), see below), the down-system modelled grain size D_m can be calculated through:

$$D_m(x^{*}) = D_A + \varphi_A \frac{C_2}{C_1}\left(exp^{-C_1 y^{*}} - 1\right) [m] \qquad Eq.(3.3).$$

Here, D_A is the input grain size, calculated through Eq. (3.8), and φ_A its deviation, both at the apex ($x^{*} = 0$). We expressed φ_A as the product of the input grain size, D_A and the coefficient of variation, C_v, thereby following D'Arcy et al. (2017). The constants C_1 and C_2 describe how the variance in sediment supply is partitioned in downstream variations of the mean grain size (C_2) and in variations of its standard deviation at a specific site (C_1). The ratio of C_1 and C_2 can be expressed by C_v (Fedele and Paola, 2007) and thus by the ratio between the standard deviation and the mean of the grain size data ($C_v = \sigma / \bar{D}$). By modelling the spatial distribution of sediment, we also calculated the ratio between the volumes of sediment that was supplied to the system and deposited on the fan as a function of the available accommodation space. This ratio (>1: overfilled -; <1: underfilled basin) is expressed as F_E, which is the fraction of sediment in excess (D'Arcy et al., 2017):

$$F_E = \frac{Q_{s_A}^{*}}{\left(1 - \lambda_p\right) \int_0^L r^{*}(x^{*})\, dx^{*}} \; [-] \qquad Eq.(3.4).$$

As we noted above, the application of the equations assumes that grain sizes fine downstream in a self-similar way. Accordingly, the distribution of the grain size similarity variable ξ for each site is expressed through (Fedele and Paola, 2007; Brooke et al., 2018):

$$\xi = \frac{D_k - \bar{D}(x^{*})}{\sigma(x^{*})} \; [-] \qquad Eq.(3.5).$$

This variable should approximately remain constant at any downstream position of a fluvial system. Here, D_k is the size of an individual grain measured at a site, and $\bar{D}$ and σ are the mean and standard deviation of the grain size distribution at a given location $x*$. We statistically compared the similarity variables ξ of two sites at each fan using the Kolmogorov-Smirnov two-sample (KS2) test (Hodges, 1958). We tested the null hypothesis H_0 that two grain size distributions are similar and likely drawn from identical distributions at a significance level of alpha = 0.05 (i.e., 95 % confidence interval; two samples are statistically similar if the reported p-value > 0.05).

3.3.3.2 Adjustments of the grain size fining model

We applied a bootstrapping to recover possible input unit sediment fluxes and iteratively adjusted Eq. (3.2) to fit the results of Eq. (3.3) to the given conditions. The advantage of this approach is that it allows us to determine a plausible range of input sediment fluxes instead of getting one best fit only. To find the optimal modelled grain sizes through Eq. (3.3) for each of the 10^4 bootstrapping scenarios, we calculated the Root Mean Square Error (*RMSE*), thus the standard deviation of the residuals, to evaluate the difference between the modelled grain size value D_m and that of the best-fit grain size regression curve (Eq. (3.8) and section 3.3.3). For this, we kept all other parameters (i.e., D_A, φ_A, C_v, C_1, C_2, and $r*$, see equations above and section 3.3.3) fixed for a given iteration and only adjusted the input sediment flux ${Q_s}_A^*$. Conceptually, if the modelled grain size along distance is situated above the curve that best fits the regression of the downstream fining trend of grain size, and in order to minimise the *RMSE*, then the input sediment flux was decreased by an increment of 0.1; if the opposite was the case, then the input sediment flux was increased by steps of 0.1:

$$if\ D_m(x^*)\ [m] \begin{cases} > D(x^*)\ [m] \rightarrow {Q_s}_A^* - {Q_s}_A^* \cdot 0.1\ [km^2\ Myr^{-1}] \\ < D(x^*)\ [m] \rightarrow {Q_s}_A^* + {Q_s}_A^* \cdot 0.1\ [km^2\ Myr^{-1}] \end{cases} \qquad Eq. (3.6).$$

Here, D_m is the modelled grain size calculated through Eq. (3.3) and D is the best-fit grain size regression calculated through Eq. (3.8), both along downstream distance ($x*$), and ${Q_s}_A^*$ is the input unit sediment flux in [$km^2\ Myr^{-1}$]. We repeated this procedure for each of the 10^4 possibilities resulting from the bootstrapping until the *RMSE* was minimised.

3.3.3.3 Field data: Subsidence rates and grain size

Equation (3.2) requires information on the subsidence rates as input parameter. We determined these rates using information on the preserved thickness of the sedimentary units and the time interval during which they were deposited. We then approximated the total subsidence rate down the fan transect by an exponential function (Duller et al., 2010; Whittaker et al., 2011; Sinclair and Naylor, 2012; D'Arcy et al., 2017):

$$r^*(x^*) = r_A\ exp^{-\beta(x^*)}\ [m\ Myr^{-1}] \qquad Eq. (3.7).$$

Here, r_A is the subsidence rate at the apex ($x* = 0$) and β is the rate at which $r*$ decreases down-system. The resulting exponential decrease of the inferred subsidence rates are typical for a foreland basin setting (Allen et al., 1991; Sinclair and Naylor, 2012). For each fan, the subsidence pattern is based on data from two (for the western and eastern fans) and four (for the central fan) stratigraphic sequences that record the same sedimentary units along distance (appendix A). The interpolation between the sections and the extrapolation towards the apex (r_A) was done through a regression using Eq. (3.7). We additionally calculated the cross-sectional area of the accommodation space (generated through subsidence) along the projection line in 2D (appendix A) using the trapezoidal rule.

Estimates of the long-term sediment fluxes also hinges on grain size. Such data was collected on digital photos taken from outcrops. Accordingly, for each fan and at each location where outcrops >5 m^2 were accessible, we took 3-6 photos with a hand-held camera (Panasonic Lumix FT-5) at 1-1.5 m distance from the outcrops. We added a digital grid scaled to the meters stick in the photograph and measured the longest visible axis of 100 grains >2 mm that are situated beneath each grid-node following Wolman (1954) and the protocol of Garefalakis et al. (2023). We present the resulting grain size distribution at each outcrop by the median or D_{50} grain size percentile, thus the grain size at which 50% of the grains are smaller or equal to this specific size.

Finally, the downstream decrease in grain size was shown to follow an exponential function (Sternberg, 1875; Rice, 1999; Blom et al., 2016; Litty et al., 2017). We therefore approximated fining rates by fitting an exponential regression on the D_{50} of each outcrop, thereby applying the 'Sternberg-law' (Sternberg, 1875):

$$D(x^*) = D_A \, exp^{-\alpha(x^*)} \; [m] \qquad Eq. (3.8).$$

Here, D_A is the input grain size at the apex ($x^* = 0$) and α is the grain size fining rate along normalised distance x^*, which can be expressed in [% km^{-1}] (Parsons et al., 2012).

3.3.3.4 Requirements for application of the grain size fining model, and sensitivity of the model

The grain size fining model is based on some assumptions and requirements (Fedele and Paola, 2007; Duller et al., 2010; Whittaker et al., 2011), which can restrict its application. It assumes a fluvial system to be entirely depositional at any down-system location and hinges on a unimodal and self-similar grain size distribution. The model accounts only for a grain size fining controlled by selective transport and deposition, and it assumes that streamflow processes are the dominant sediment transport mechanisms. In alluvial gravel bed rivers, selective transport and deposition of the coarse-grained material has been reported to be the dominating process, whereas the effect of abrasion, such as the chemical dissolution or the mechanical particle break-down, are neglectable at the scale of alluvial fans (Parker, 1991; Ferguson et al., 1996; Hoey and Bluck, 1999; Stock et al., 2008; Duller et al., 2010; Miller et al., 2014). The mechanical particle break-down is an important mechanism in the steep headwaters of a stream only (Miller et al., 2014). More recent modifications of the model considered lateral sediment input by tributaries (e.g., Harries et al., 2019), and such models are also able to predict the dispersion of the sediment across a fan in three dimensions (D'Arcy et al., 2017). However, such modifications require either knowledge on potential tributary sources or information on the fan width. Due to the absence of evidence for sediment supply by tributaries (see discussion and appendix A) and because of a lack of constraints on the fan widths, we employed a two-dimensional model where material was supplied by one feeder channel at the fan's apex (e.g., Duller et al., 2010; Whittaker et al., 2011).

The model is designed for applications to fluvial successions covering geological timescales of $10^4 – 10^6$ years (Duller et al., 2010; Armitage et al., 2011; Parsons et al., 2012), which is appropriate for our needs. However, processes occurring at shorter intervals, such as the dynamic formation of channels that would locally influence the bed elevation, are neglected (Duller et al., 2010; Harries et al., 2019). Duller et al. (2010) also found a direct relationship between the input sediment flux, the formation rate of accommodation space, and the rates at which the sediment is distributed along the system. Accordingly, a constant sediment flux fed into a filled basin would produce a downstream fining over a long distance (i.e., low rates of α in Eq. (3.8)), if paired with a long-wavelength and low-amplitude subsidence pattern, which corresponds to slow subsidence decreasing rates (i.e., β in Eq. (3.7)). Conversely, grain sizes fine over short distances (i.e., large α) if the underlying spatial subsidence has a short-wavelength and a high-amplitude, which corresponds to a high subsidence decreasing rate. Where the sediment flux increases, relative to a fixed subsidence, the grain size fining rates become successively smaller as the basin reaches overfilled conditions (Duller et al., 2010; Whittaker et al., 2011; Parsons et al., 2012). Therefore, similarities or differences between these three variables (grain size fining rate, spatial distribution of subsidence, and input sediment flux) allow us to make first-order inferences on the mechanisms that drove the formation of alluvial fans. As such, they record either a tectonic control through high subsidence rates or an environmental control characterised by a large sediment supply.

3.3.4 Instantaneous bankfull sediment flux

Bankfull sediment fluxes, or bedload (material >2 mm) sediment transport rates per unit time and width, were calculated using a derivative of the Meyer-Peter and Müller (1948) bedload transport equation (details in appendix A):

$$Q_b{}^* = 3.97\ [(1.0 + \varepsilon)\ \tau_c{}^* - \tau_c{}^*]^{1.5}\ \left(G_S\ g\ D_{50}{}^3\right)^{0.5}\ [m^3\ s^{-1}\ m^{-1}] \qquad Eq. (3.9).$$

Here we used the constant 3.97, which is based on an improved statistical fit (Wong and Parker, 2006) of the original data by Meyer-Peter and Müller (1948), g is the gravitational acceleration (= 9.81 m s^{-2}), and G_S is the submerged specific gravity (i.e., $[(\rho_s / \rho_w) - 1] = 1.65$) using $\rho_s = 2650$ kg m^{-3} and $\rho_w = 1000$ kg m^{-3}, for the sediment and water densities, respectively. Furthermore, ε is a factor to account for lateral bank erosion (Parker, 1978; Paola and Mohrig, 1996), τ_c* is the dimensionless critical Shields-parameter (Shields, 1936), and D_{50} is the grain size percentile, respectively. For the dimensionless critical Shields-parameter τ_c* we used uniformly distributed values between 0.039 and 0.054 (Julien, 2010), thereby considering a broad range of plausible conditions controlling the incipient motion of grains with different sizes (Julien, 2010). The theoretically derived variable ε was originally set to 0.2 (Parker, 1978), but Paola and Mohrig (1996) found that a value of $\varepsilon = 0.4$ is more appropriate. We therefore used uniformly distributed values between $\varepsilon = 0.2$ and 0.4 for our calculations. For the bedload sediment flux estimates we solely used the D_{50}, first to account for the conditions during equal mobility of all grains in a channel (Paola and Mohrig, 1996; Wickert and Schildgen, 2019), and second because the MPM-equation was calibrated using the D_{50}. Therefore, any incipient motion of grains smaller than the D_{50} (that would occur prior to the movement of this percentile) is consequently neglected (Recking et al., 2012), which is an acceptable assumption (Paola and Mohrig, 1996). In addition, because we cannot get any reliable estimates on the channel widths, we are left with a two-dimensional solution only.

3.3.5 Uncertainties, error estimations and limitations

We estimated uncertainties through bootstrapping (resampling with replacement; 10^4 iterations), combined with a Monte Carlo framework where applicable (Rice and Church, 1996; Mair et al., 2022; Garefalakis et al., 2023). For instance, for the grain size data we resampled 100 grain size values D_k (measured on the photographs) and calculated the uncertainties on the D_{50} within the 95% Confidence Interval (CI). Additionally, we calculated the coefficient of determination (r^2) as a measure of how the best-fit exponential regression (Eq. (3.8)) fits the D_{50} values. For each of the outcomes we either report the mean or median value (each time indicated) along with the 95% CI in squared brackets. For a median grain size value, for instance, this would lead to $D_{50} = 22$ [17 – 25] mm. Details of the uncertainties on the various parameters are outlined in appendix A.

As will be shown, all three systems show a downstream trend in grain size but revealed a large scattering of the D_{50} at some positions – an issue which has been documented in other alluvial fan systems (e.g., Duller et al., 2010; Brooke et al., 2018). One possibility is that this variation could have been caused by a material supply from tributary sources (Rice, 1999; Harries et al., 2018). We exclude this option based on available information about the heavy mineral and clast compositions, which suggest that all systems have most likely been fed by one feeder channel only (Stürm, 1973; Bürgisser, 1981; Schlunegger et al., 1993, 1997a; Kempf et al., 1999; appendix A of this chapter). The scatter of the grain size data might thus instead reflect the consequence of the random selection of the sampling sites on the paleo-alluvial megafans, which cannot be avoided upon working with stratigraphic deposits (Duller et al., 2010; Straub et al., 2020).

Our calculations of the long-term sediment flux capture the average budget on a million-year scale. Therefore, adjustments of sediment fluxes are a consequence of shifts in tectonically induced processes, such as uplift or subsidence, or environmental controls, such as shifts in climate (Sadler, 1981; Paola and Voller, 2005; Allen et al., 2013). In contrast, such variations cannot be observed at the (temporal) scale at which we calculated the instantaneous bedload fluxes that capture larger values than the annual mean (Wainwright et al., 2015; Benavides et al., 2022; Lyster et al., 2022). In addition, bedload sediment fluxes calculated through a shear-stress approach are dependent on the competence of a river, which is a function of water depth and channel slope (details in appendices iii and v).

3.4 Results

3.4.1 Sediment accumulation and subsidence rates

At proximal positions on the western fan, 3250 ± 50 m of sediments accumulated between 24.8 – 23.1 ± 0.1 Ma, yielding an accumulation rate of 1910 ± 140 m Myr^{-1} (Thun Lakeside; Fig. S3.1, appendix A). For the same sedimentary unit, a twin section farther to the ENE (Praesserenbach; Fig. S3.1, appendix A) and thus at more distal positions recorded the accumulation of 1250 ± 50 m of sediments between 24.8 – 24.0 ± 0.1 Ma, which yields a sediment accumulation rate of 1600 ± 260 m Myr^{-1}. Accordingly, the median subsidence rate at the apex of the western fan was 2088 [1795 – 2473] m Myr^{-1} and is reduced at a median rate of 2.92 [-0.09 – 6.86] % km^{-1} down-system (Fig. 3.4a). In a cross-section and along the projection line of the fan (appendix A), the median sediment accumulation area, without considering any topography, was 18.5 [15.5 – 21.2] km^2.

The spatial distribution of accommodation space surrounding the central fan is constrained by four sections, all recording the same sedimentary unit with an age of c. 26.4 – 24.9 ± 0.25 Ma (Fig. S3.2, appendix A; Schlunegger et al., 1997a, 1997b; Engesser and Kälin, 2017). The most proximal section (Rigi; Fig. S3.2, appendix A) comprises a 1600 ± 50 m-thick suite and was accumulated at a rate of 1070.0 ± 210 m Myr^{-1}. Farther downstream, 8 km to the ENE (Rossberg; Fig. S3.2, appendix A), the same unit thins to 1485 ± 50 m, and the accumulation rate decreased to 990.0 ± 200 m Myr^{-1}. Another 6 km downstream to the East (Sattel; Fig. S3.2, appendix A), the same unit is 1040 ± 50 m thick, resulting in an accumulation rate of 695.0 ± 150 m Myr^{-1}. The last remnants of this unit, situated 7 km farther down-system (Einsiedeln; Fig. S3.2, appendix A), are only 595 ± 50 m thick, and the accumulation rate was thus less (400.0 ± 100 m Myr^{-1}). The calculated median subsidence rate at the apex was 1283 [1041 – 1552] m Myr^{-1} and was reduced at a median rate of 3.96 [2.52 – 5.62] % km^{-1} down-system (Fig. 3.4b). In a cross-section, the median depositional area (topography excluded) was 23.5 [21.4 – 25.9] km^2.

In the East, two stratigraphic sections (Toess and Hoernli; Fig. S3.3, appendix A) record the same suite spanning an age between approximately 14.6 and 13.6 ± 0.2 Ma (Kempf et al., 1997; Kälin and Kempf, 2009). At both sites, the sedimentary sequences are c. 315 m-thick and accumulated at a rate of c. 240 ± 100 m Myr^{-1} in average. Accordingly, this value corresponds to a median subsidence rate (i.e., 242 [120 – 412] m Myr^{-1}) at the apex, and the median decreasing rate of the subsidence rate was consequently 0.02 [-8.1 – 8.2] % km^{-1} (Fig. 3.4c). In a section along distance from proximal to distal, the median depositional area (topography excluded) was 2.8 [1.9 – 3.8] km^2.

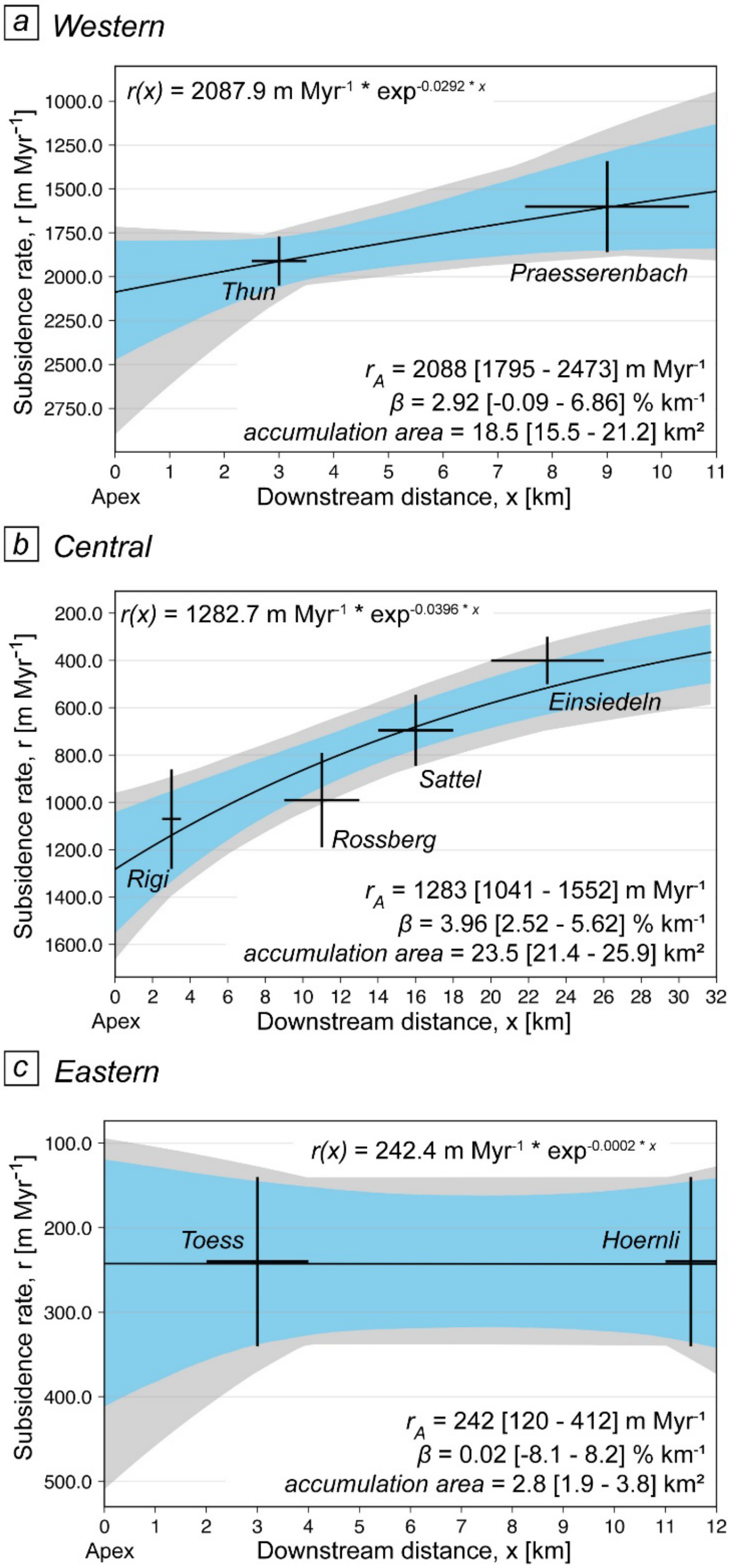

Figure 3.4: Subsidence curves of the **a)** western, **b)** central and **c)** eastern fan. The crosses represent stratigraphic sections and uncertainties in their relative position to the apex and the subsidence rates. The black line reflects the best-fit regression curve, the blue area corresponds to the 95 % CI of the exponential regression analyses, and the grey area corresponds to all possible regression scenarios thereby using 10^4 iterations. The accumulation area is the cross-sectional area calculated through the trapezoidal rule.

3.4.2 Grain size, coefficient of variation and similarity variable

For all three megafans, the grain sizes generally decrease down-system, as visible in the field (Fig. 3.5). On average, the D_{50} is approximately 51 mm for the western fan (73 sites) and 40 mm for both the central fan (84 sites) and the eastern fan (60 sites), respectively. The fining trend of the D_{50}, although clear, is not very rapid, and some sites show a spread in D_{50} values (Fig. 3.6). For the western fan, the exponential regression fit yields an approximate median input grain size of D_A = 103 [92 – 116] mm at the system's apex (Fig. 3.6a). The median value of the grain size fining rate is 9.25 [7.85 – 10.7] % km^{-1}, with the consequence that the D_{50} values are c. 30 mm at distal sites (Fig. 3.6a). For the central fan, the D_{50} values show large variations between proximal and distal positions, yet a decreasing down-system trend in grain size is detectable (Fig. 3.6b). The result is a median input grain size of D_A = 49 [47 – 51] mm at the system's apex. Approximately 14 km down-system, the sizes of the grains increase to larger values, which is then followed by a pronounced decrease. The median value of 1.4 [1.1 – 1.7] % km^{-1} for the grain size fining rate is quite low, yielding a D_{50} of c. 31 mm at distal positions (Fig. 3.6b). For the eastern fan, the D_{50} values decrease from c. 45 to 35 mm down-system at a median fining rate of 2.1 [1.2 – 2.9] % km^{-1} (Fig. 3.6c). Our fit yields a median input grain size value of D_A = 46 [43 – 49] mm at the system's apex. The cumulative distribution curves of the grain size data reflect these downstream fining trends for each fan (Fig. 3.7).

The coefficient of variation C_v for the western fan is on average C_v = 0.67 [0.57 – 0.77] and remains mostly stable (Fig. 3.8a). For the central fan, the C_v discloses a larger scatter at proximal positions but remains stable farther downstream with an overall average of C_v = 0.66 [0.56 – 0.76] (Fig. 3.8b). The eastern fan has an average C_v value of 0.63 [0.54 – 0.73] and shows a slight decreasing trend towards distal positions (Fig. 3.8c). Overall, the three fans have a very similar average C_v value of 0.65 ± 0.10, albeit some scattering of the data is observed at individual sites. This observation supports the notion that the mean and standard deviation of gravel grain sizes on these alluvial fans have a constant ratio. A similar and important observation is made for the grain size similarity variable ξ (Eq. (3.5)), when presented as cumulative distribution curves (Fig. 3.9 a, b, and c). The results show that the grain size distributions for all sites (Fig. 3.7) collapse onto self-similar curves when presented in ξ-space. Consequently, the grain size values normalised by the mean and standard deviation at a given site indeed decrease down-system at the same rate, which is reflected by the same shape of the similarity curves (Fig. 3.9 a, b, and c). The centre of the curves (i.e., 50% in Fig. 3.9) are slightly shifted to smaller ξ values and deviate from a normal distribution that is simulated for the entire fan's mean and standard deviation of the similarity data. Nevertheless, the outcomes of the KS2 test confirms that almost all distributions are similar to each other at a significance level of alpha = 0.05 (Fig. 3.9 d, e, and f). The site-to-site comparison reveals a success rate of 99.85 % for the western, 97.11 % for the central, and 98.94 % for the eastern fan, thus confirming that the ξ distributions are similar to each other (Fig. 3.9 d, e, and f).

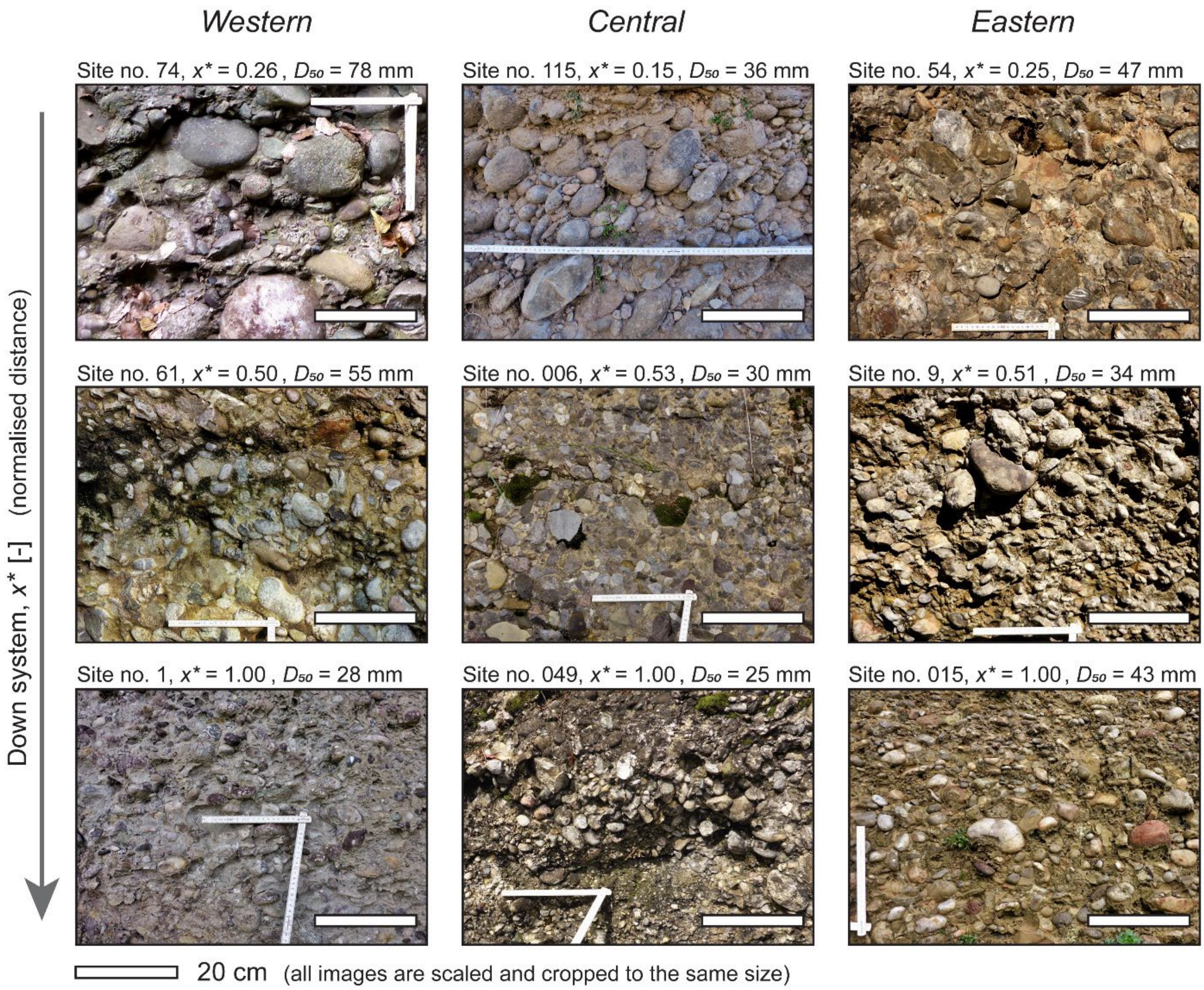

Figure 3.5: Examples of conglomerates and values of the grain size percentile D_{50} at different sites on the three fans.

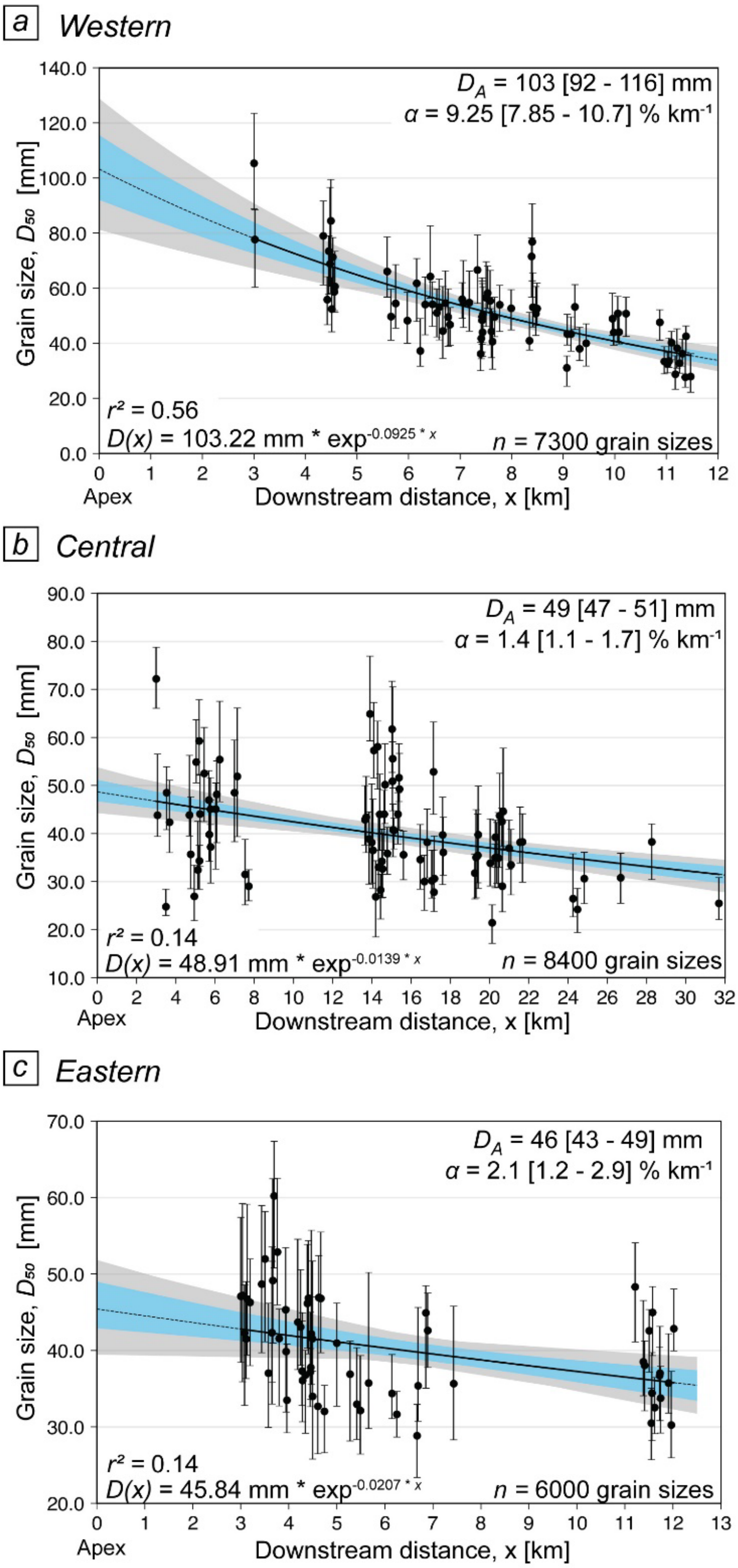

Figure 3.6: Downstream grain size trends of the **a)** western, **b)** central and **c)** eastern fan. The black dots correspond to the D_{50}, error bars show the 95 % CI of grain size values. The black line reflects the best-fit regression curve (solid = data available; dotted = extrapolated), the blue area corresponds to the 95 % CI of the exponential regression analyses, and the grey area corresponds to all possible regression scenarios thereby using 10^4 iterations. The coefficient of determination (r^2) reflects the variability between the best-fit regression and the percentile values.

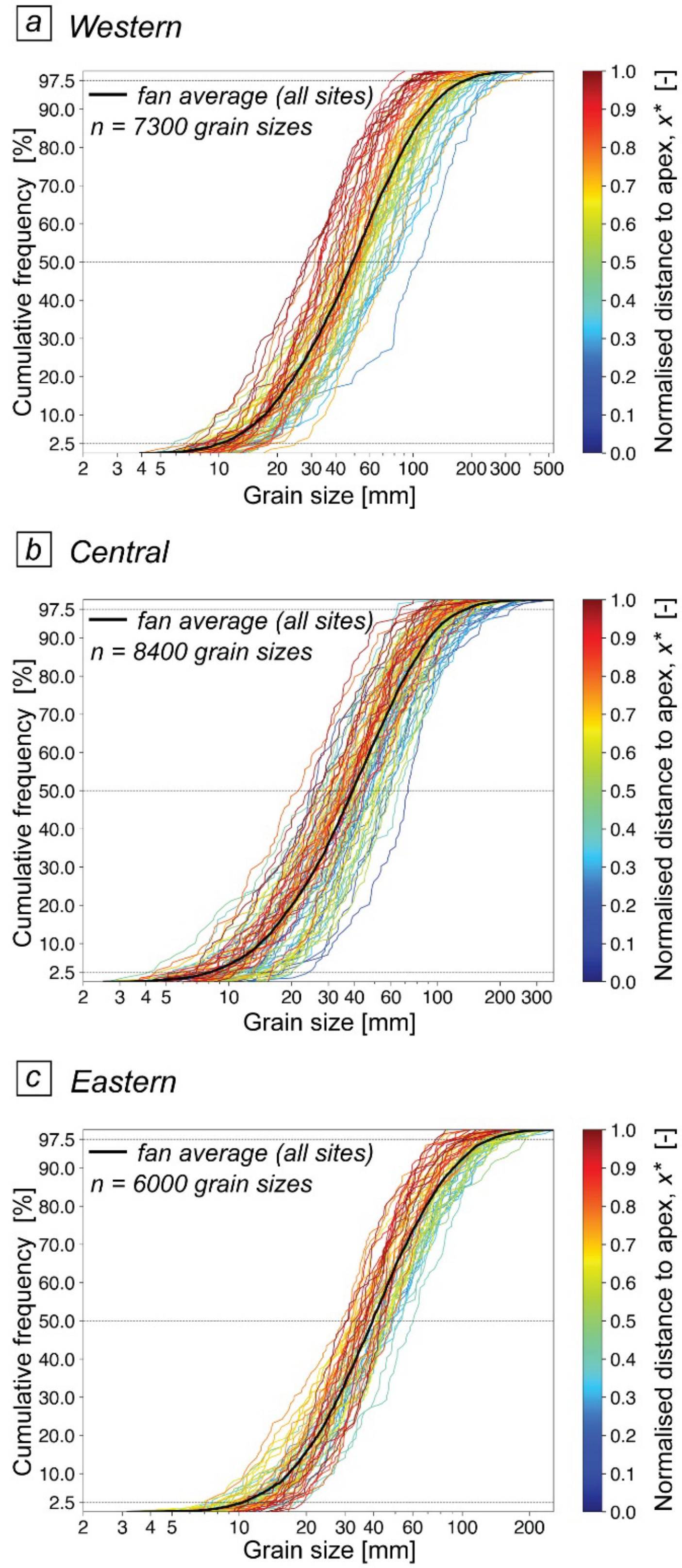

Figure 3.7: Grain size distributions of the **a)** western, **b)** central and **c)** eastern fan with respect to their relative distance to the apex. The fan average bases on the data of all individual sites. Please note the logarithmic grain size scale.

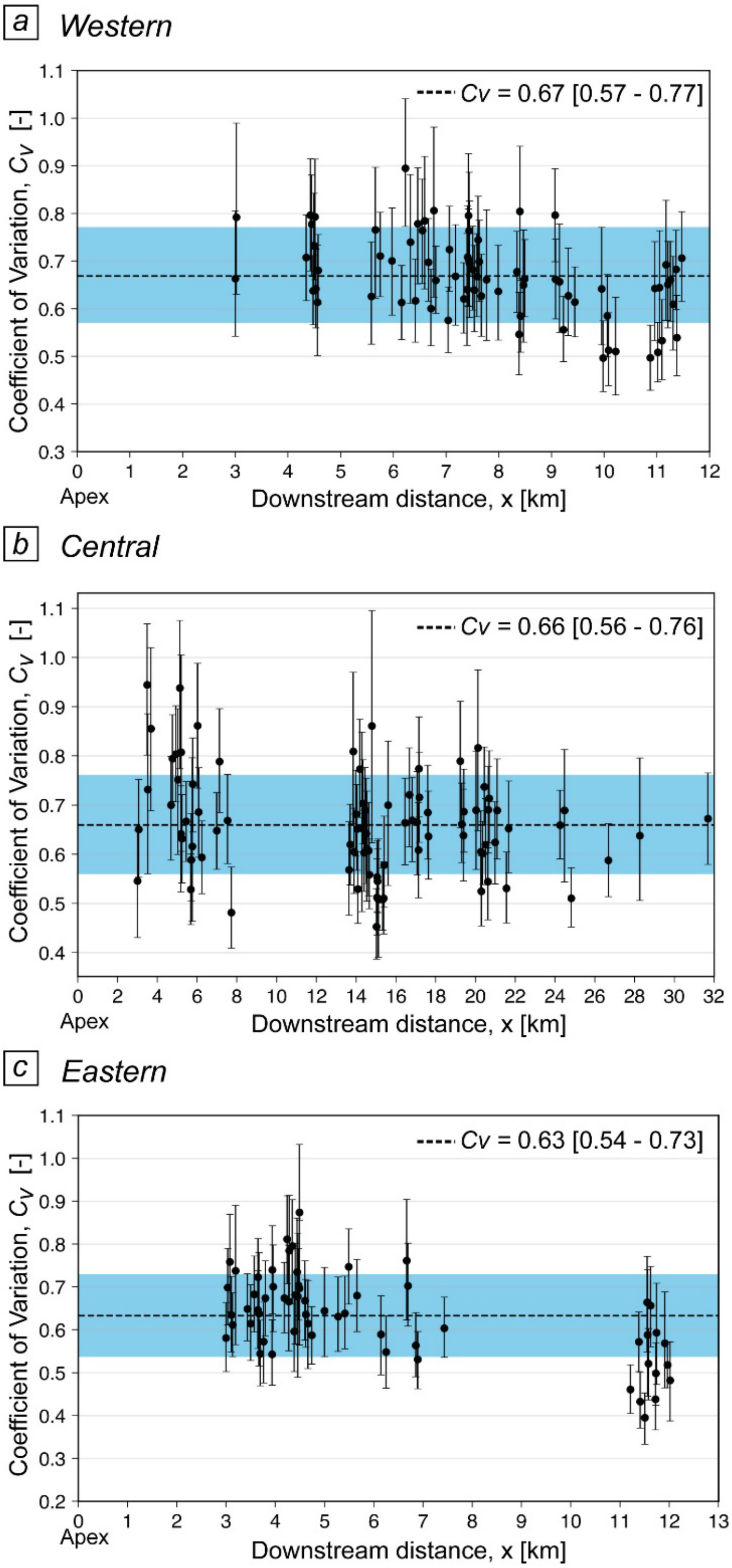

Figure 3.8: Coefficient of variation (C_v) of the **a)** western, **b)** central and **c)** eastern fan along downstream distance. The black dots correspond to the C_v, the error bars show the 95 % CI thereof. The black dotted line shows the fan average, and the blue area corresponds to the 95 % CI thereof.

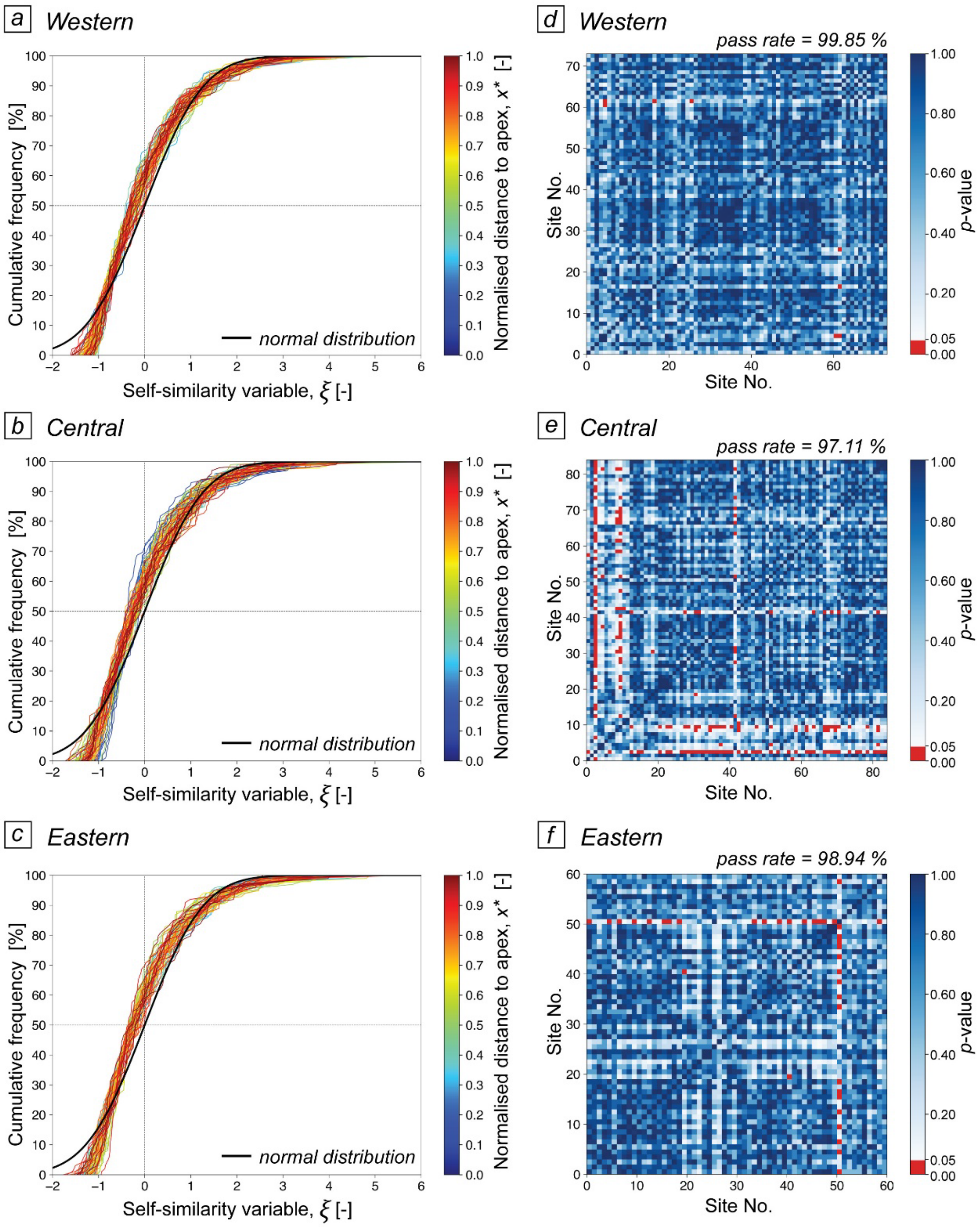

Figure 3.9: Cumulative density function of the similarity variable ξ for the **a)** western, **b)** central and **c)** eastern fan with respect to their relative distance to the apex. The black curve shows a simulated normal distribution based on the fan's average value and its standard deviation. Corresponding correlation matrices of the Kolmogorov-Smirnov two-sample test (KS2) for the **d)** western, **e)** central and **f)** eastern fan systems. Blue colours show two ξ distributions that are statistically similar if the reported p-value is larger than 0.05 (i.e., alpha level = 95 % CI), red colours show distributions that are statistically different to each other.

3.4.3 Long-term and instantaneous sediment fluxes, and fan intermittency

The existence of a self-similar distribution of grain sizes in all three fan systems (see above) allows the application of the self-similar grain size fining model (Fedele and Paola, 2007). The model results show that for the western fan, the median input sediment flux ${Q_s}_A^*$ is 17.0 [14.6 - 20.3] km^2 Myr^{-1} with a median sediment excess rate F_E = 1.19 [1.06 – 1.41]. According to the model, a median of 84 [71 – 95] % of the supplied material are deposited on the fan, while 16 [5 – 29] % are exported out of the system (Fig. 3.10a; median *RMSE* 0.0045 [0.0018 – 0.0111]). For the central fan, a median ${Q_s}_A^*$ of 38.9 [29.9 - 50.4] km^2 Myr^{-1} is necessary to successfully model the observed grain size fining rates (median *RMSE* 0.00065 [0.00023 – 0.00145]), resulting in a median sediment excess rate F_E = 2.41 [1.93 – 3.04]. The model results reveal that approximately 58 [48 – 67] % of the supplied sediment was exported out of the system, while a median of 42 [33 – 52] % was deposited on the fan (Fig. 3.10b). In the east, we obtained a median ${Q_s}_A^*$ of 6.80 [3.80 - 12.4] km^2 Myr^{-1} and a high median sediment excess rate F_E= 3.37 [2.33 – 5.64], revealing that a median 70 [57 – 82] % of the sediment was transferred out of the system, while c. 30 [18 – 43] % of the supplied material accumulated on the fan (Fig. 3.10c; median *RMSE* 0.639 [0.0935 – 2.12]*10^{-3}). Alternatively, for the eastern fan and upon considering an apex situated +15 km to the most proximal site, the model yielded a median ${Q_s}_A^*$ of 7.90 [3.20 - 21.8] km^2 Myr^{-1} and a median sediment excess rate F_E= 1.89 [1.30 – 3.61], revealing that a median 47 [23 – 72] % of the sediment was transferred out of the system.

Calculations of the bedload capacity, or instantaneous bedload fluxes, including all sites for each fan, returned median values for the bedload fluxes of approximately: Q_b^* = 8870 [3070 – 24800] km^2 Myr^{-1} for the western fan, Q_b^* = 6150 [2240 – 16500] km^2 Myr^{-1} for the central fan, and Q_b^* = 6370 [2750 – 14000] km^2 Myr^{-1} for the eastern fan. Site-specific bedload fluxes are in cases larger or smaller than the fan bulk values. In addition, the cumulative curves of the bedload fluxes, showing the bootstrapping values of each site, disclose a decreasing trend towards distal sites, albeit with some scattering of the data (Fig. 3.11). The large spread of the 95% CI is also reflected by the positive skewness of the data (Fig. 3.11) for each of the fan systems.

For each entire fan, the fan's intermittencies (or their transport activities) are: I_F = 0.0019 [0.00068 – 0.0056] for the entire western fan, which would correspond to an activity of c. 16 [6 – 49] hours per year during which channel-forming bankfull discharge occurred; I_F = 0.0063 [0.0023 – 0.018] or c. 55 [20 – 157] hours per year for the entire central fan, and I_F = 0.0011 [0.00039 – 0.0030] or c. 9 [3 – 26] hours per year for the entire eastern fan (Fig. 3.12). Alternative results for the eastern fan with a shifted paleo-fan apex position of +15 km, yielded I_F = 0.0013 [0.00036 – 0.0048] that correspond to c. 11 [3 – 42] hours per year (see appendix A for figures and details). Site-specific intermittency factors show a large spread, especially at the upper tail, where the cumulative distribution curves (generated from the bootstrapping data of each site) are right-skewed (Fig. 3.12). For all systems, the intermittency factor increases towards more distal positions (Fig. 3.12), thereby reflecting the opposite trend of the bedload fluxes (Fig. 3.11).

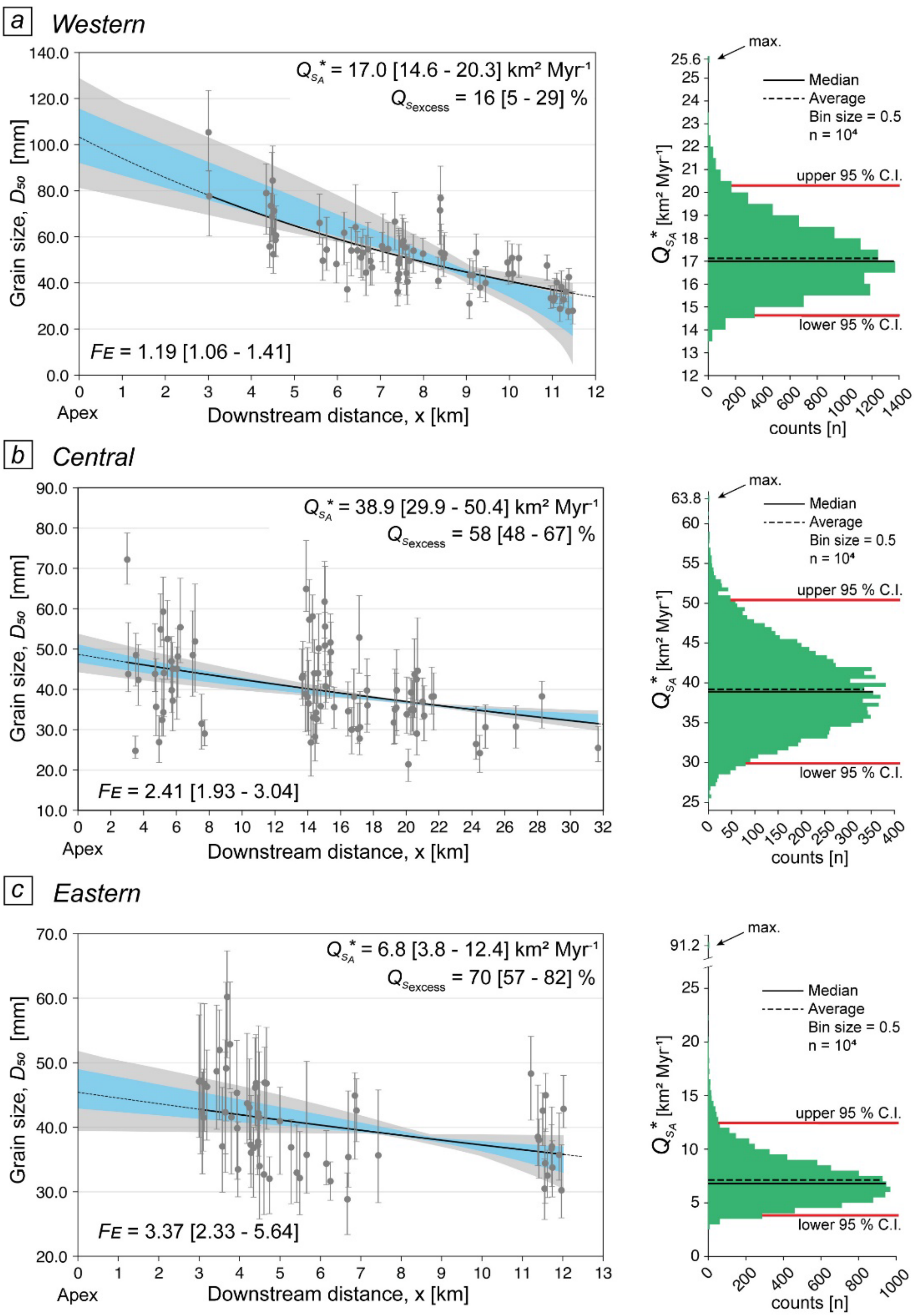

Figure 3.10: Modelled grain size fining(left) for the **a)** western, **b)** central and **c)** eastern fan for a given input sediment flux (histograms, right). The grey dots represent the D_{50} values (error bars correspond to the 95% CI), and the black line reflects the best-fit regression curve on the grain size data (solid = data available; dotted = extrapolated). The shaded blue area corresponds to the 95 % CI of the modelled grain sizes and the grey area corresponds to all possible scenarios thereby using 10^4 iterations. $Q_{S_A}^*$ = input sediment flux; F_E = sediment excess rate, $Q_{Sexcess}$ = sediment in %-excess.

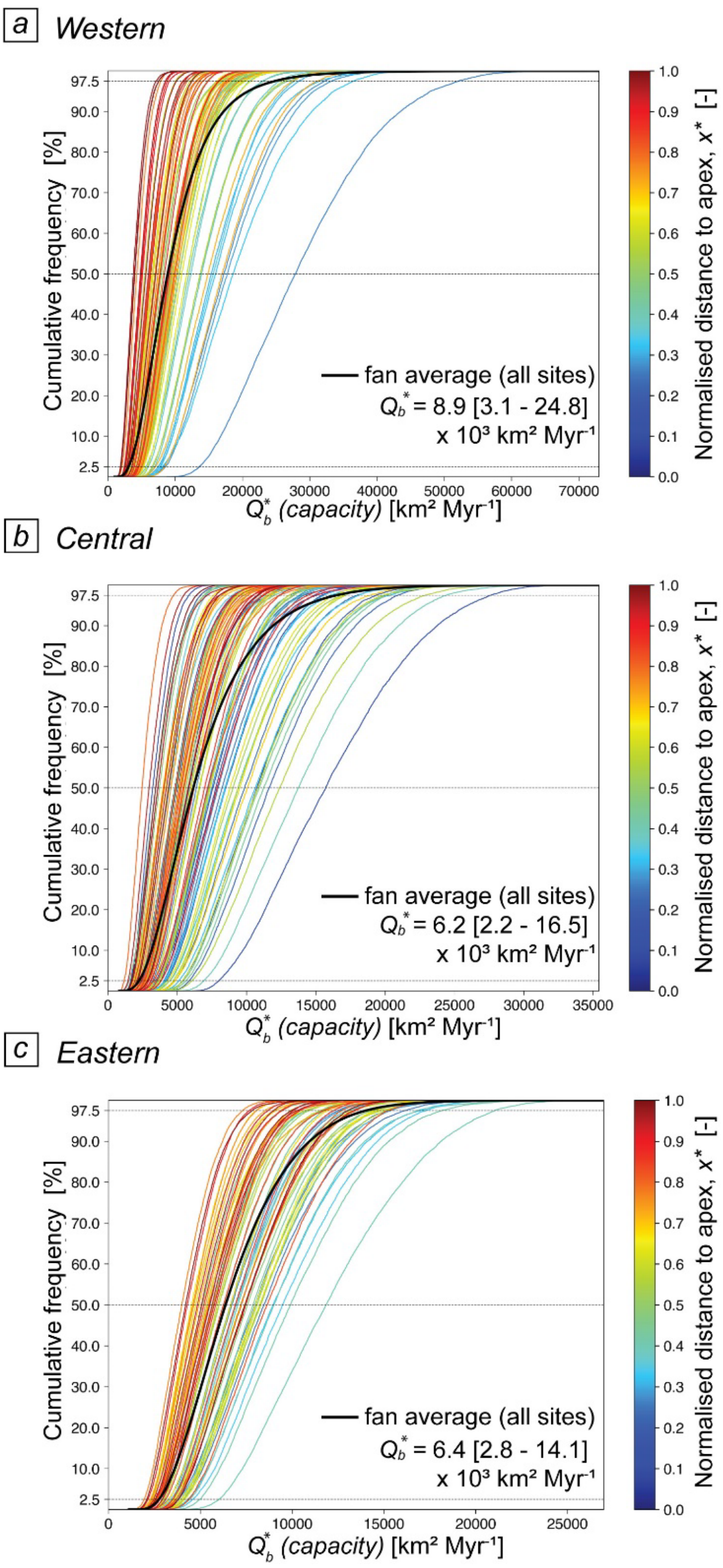

Figure 3.11: Cumulative distributions of the instantaneous bedload sediment flux Q_b^* for the **a)** western, **b)** central and **c)** eastern fan with respect to their relative distance to the apex.

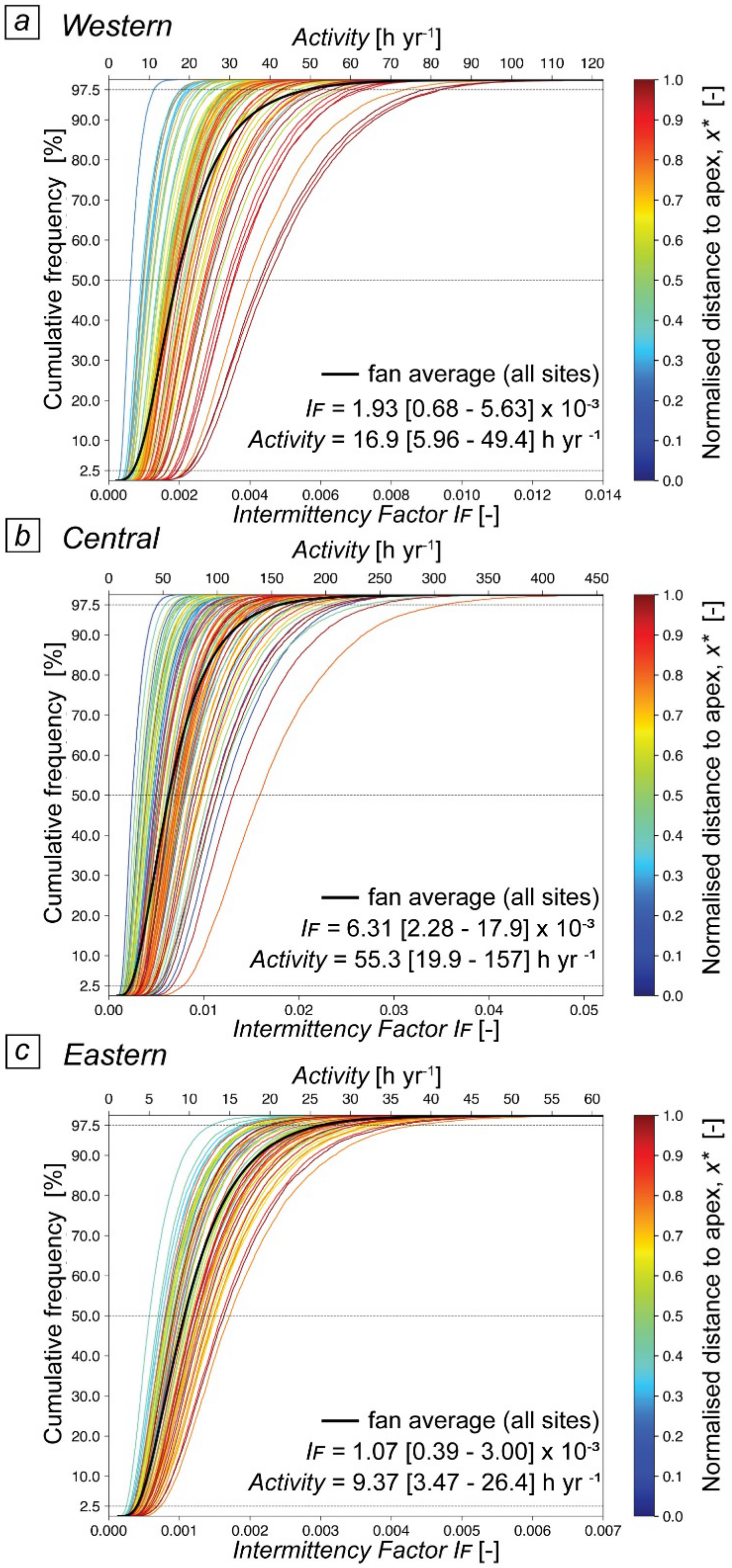

Figure 3.12: Cumulative distributions of the intermittency factors I_F for the **a)** western, **b)** central and **c)** eastern fan with respect to their relative distance to the apex. Please note the difference in magnitude for the central fan with respect to the western and eastern fan.

3.5 Interpretation & Discussion

3.5.1 Grain size trends and intermittencies of Oligo-Miocene alluvial megafans

Our results show that grain size fining occurred at each of the investigated fan systems. While the western fan revealed the most pronounced decreasing grain size trend, the results from the central and eastern fans are in the same order (Table 3.1). Despite some scattering of the grain size data, which is consistent with the variability observed for other alluvial fan systems (e.g., Whittaker et al., 2011; Brooke et al., 2018), the standard deviation decreases at the same rate as the mean of the grain size distributions if the data is collapsed into a self-similarity variable ξ (Fig. 3.9). The right-skewness of the similarity-distributions and thus the short negative tail is due to a lack of measurements < 2 mm, but could also be related to a few, but exceptionally large grains (D'Arcy et al., 2017; Harries et al., 2018). Additionally, the results of the KS2 test showed that at almost all sites the data are statistically identical to each other (at 95% CI; Fig. 3.9). The coefficients of variation C_v, which ae within the range of reported values (Fedele and Paola, 2007; Duller et al., 2010; Armitage et al., 2011; Brooke et al., 2018), revealed a similar downstream trend with an average of c. 0.65 ± 0.10 that remained approximately constant for all three systems (Fig. 3.8). The ξ and C_v values calculated from the grain size datasets suggest that the sorting of a given grain size population are approximately constant and scale-invariant at any down-system position. Consequently, these results show that alluvial fan sediments of the SMB have self-similar grain size distributions, similar to those documented for the Pobla basin of the Spanish Pyrenees and the Bermejo basin of Argentina (Whittaker et al., 2011; Harries et al., 2019) and that the underlying transport processes on each fan system was likely identical (Schlunegger et al., 2020).

Overall, the three depositional systems yielded differences in the annual long-term and instantaneous sediment fluxes, and all disclose rather low intermittency factors (Table 3.1). Amongst the three fan systems, the central fan had the highest intermittency value and was the most active one. In contrast, both the western and eastern fans had lower intermittency factors and were therefore less active (Table 3.1). Consequently, our data provides insights into the activity of these Oligo-Miocene alluvial fans for the first time and suggests that the rivers on these alluvial fans were intermittent and could move the supplied sediment within a short period.

In the following discussion, we investigate how the model outcomes (section 3.5.2) scale to independent tectonic and paleoclimatic interpretations and propose scenarios (section 3.5.3), which were possibly leading to the fan-formation that is in accordance with our intermittency values. Because for the eastern fan these outcomes do not differ significantly from the situation with a shifted apex (i.e., +15 km; appendix 3.11.1.3 and Table 3.1), we will focus in the discussion solely on the more conservative solution.

Fan systems:	Western	Central	Eastern +3km	Eastern +15km
Subsidence rate at apex r_A [m Myr^{-1}]	2088 [1795 – 2473]	1283 [1041 – 1552]	242 [120 – 412]	244 [45 – 1085]
Subsidence change rate β [% km^{-1}]	2.92 [-0.09 – 6.86]	3.96 [2.52 – 5.62]	0.02 [-8.1 – 8.2]	0.05 [-8.1 – 8.2]
Grain size at apex (input) D_A [mm]	103 [92 – 116]	49 [47 – 51]	46 [43 – 49]	59 [50 – 70]
Grain size fining rate α [% km^{-1}]	9.25 [7.85 – 10.7]	1.4 [1.1 – 1.7]	2.1 [1.2 – 2.9]	2.1 [1.2 – 2.9]
Long-term sediment flux $Q_{s_A}^{*}$ [km^2 Myr^{-1}]	17.0 [14.6 - 20.3]	38.9 [29.9 - 50.4]	6.80 [3.80 - 12.4]	7.90 [3.20 - 21.8]
Bedload sediment flux Q_b* [km^2 Myr^{-1}]	8870 [3070 – 24800]	6150 [2240 – 16500]	6370 [2750 – 14000]	6370 [2750 – 14000]
Intermittency factor I_F [-]	0.001924 [0.00068 – 0.0056]	0.006316 [0.0023 – 0.018]	0.001069 [0.00039 – 0.0030]	0.001251 [0.00036 – 0.0048]
Activity - [h yr^{-1}]	16 [6 – 49]	55 [20 – 157]	9 [3 – 26]	11 [3 – 42]

Table 3.1: Main outcomes (rounded values) of each fan system. The uncertainties correspond to the 95% CI. Please find in appendix A of this chapter the figures to the scenario where the inferred paleo-apex for the eastern fan was placed at +15 km.

3.5.2 Analyses of the model outcomes

A key question is whether the long-term sedimentation on these fans was governed primarily by tectonic or environmental boundary conditions (Hajek and Straub, 2017; Ventra and Clarke, 2018). Sensitivity analyses revealed that for a given sediment flux to the system, the grain size fining rate depends on the spatial distribution of subsidence (section 3.3.3.4; Duller et al., 2010). Particularly for the western fan, we observed a relatively high grain size fining rate paired with a relatively high subsidence decreasing rate (Table 3.1). Although these high grain size fining rates are hinting at a strong tectonic control where the basin could potentially be underfilled (Duller et al., 2010), our model outcomes suggest that the creation of accommodation space occurred nearly in pace (F_E = 1.19) with the volumes of supplied sediment (17.0 km^2 Myr^{-1}), and both mechanisms were likely balanced. For the central fan, the situation was different. There, the grain size fining rates were low, and they were paired with relatively high subsidence decreasing rates (Table 3.1). Consequently, the low grain size fining rate on the central fan was responsible for the basin to be overfilled (F_E = 2.41) and a relatively large input sediment flux (38.9 km^2 Myr^{-1}) was necessary to replicate these low grain size fining rates (Table 3.1). In the east, the subsidence decreasing rates are negligible (given a median of zero; Table 3.1), the grain size fining rates were low, and the degree of basin overfill was much higher (F_E = 3.37) compared to the other systems. We relate these observations to the low accommodation space that was created in the basin during the time the eastern system was formed. As outlined in section 3.2.2, the uplift of the triangle zone caused a decrease of the potentially available accommodation space in which the sediments could accumulate, thereby promoting the basin to be largely overfilled. We discuss in the following section how these modelling outcomes and interpretations thereof align with the climatic and tectonic history of the Central Alps and the SMB (see also section 3.2.2).

3.5.3 Tectonic versus environmental controls on the alluvial fans

The western and central fans were formed under an approximately same climate; however, according to the model, they reveal significant differences in their sediment budgets and intermittencies. If the tectonic boundary conditions were similar, we would have expected higher similarities in the model outcomes, given the same climatic boundary conditions. The eastern fan, if compared to the western and central fans, was formed under a cooler, probably also a drier, climate. Because it was documented that sediment supply rates to modern Alpine lakes were possibly higher during a cooler than a warmer climate (Glur et al., 2013), we would expect relatively large sediment supply rates and high surface dynamics during the time the eastern fan was constructed, which, however, was not the case. We, however, acknowledge that the preservation of climatic signals in stratigraphic deposits depends on the strength of the environmental parameters and on how strong these are mitigated or amplified by independent signals from other sources (Armitage et al., 2011; Whittaker, 2012; Castelltort et al., 2015). Consequently, we invoke tectonic and orogenic processes to explain the differences in the sediment fluxes and the sedimentary dynamics recorded by the deposits of the three systems. These mechanisms are elaborated in the following paragraphs.

Among the three systems, the central fan revealed evidence for the highest sediment fluxes and activity of sediment transport. As we ruled-out a distinct climate driving force, we interpret these high sediment fluxes as a consequence of the underlying tectonic boundary conditions at that time (section 3.2.2). More recently, Schlunegger and Kissling (2022) suggested that post-collisional slab break-off at c. 32 – 30 Ma, and the subsequent slab roll-back (Schlunegger and Kissling, 2015; Kissling and Schlunegger, 2018), mainly contributed to surface uplift and build of the Alpine topography. As a consequence, large sediment fluxes (Sinclair, 1997; Kuhlemann et al., 2001a) and high sediment load concentrations (Garefalakis and Schlunegger, 2018), caused the fan to rapidly prograde into the basin. Such a scenario is very likely given the short distance between the Lepontine area (figs. 3.1 and 3.2), which was the major sediment source of the central fan and which also experienced a high surface uplift rate in response to the slab break-off at that time (Schlunegger and Castelltort, 2016). We note, however, that the erosional signal of slab break-off was recorded in the central fan c. 3.6 – 5.6 Ma later. This difference in timing was interpreted by Schlunegger and Castelltort (2016) as a delayed secondary response to high surface uplift rates, conditioned by the size of the system and the pattern of exhumed bedrock.

For the western and eastern fan, our models predict smaller sediment fluxes and lower activities in comparison to the central fan. For the western fan, these lower activities possibly reflect the larger distance to the Lepontine area (Fig. 3.1). In addition, between 25 – 24 Ma and after the initial sediment pulse driven by the transient landscape adjustment to the slab break-off, the Alps reached a balance between crustal uplift and surface erosion, and thus a steady-state elevation (Schlunegger and Kissling, 2015). We use these mechanisms to explain the decrease in the fan activity after c. 25 Ma when the construction of the western fan occurred. At 20 Ma, the exhumation of the crystalline external massifs and tectonic unroofing in the core of the Alps caused a modification in the drainage network, which could have further reduced the sediment supply to the Molasse basin (section 3.2.2 and Fig. 3.2). This possibly explains why the sediment supply to the eastern fan and the sedimentary dynamics were lower compared to the other two systems (Table 3.1). Therefore, the fan intermittencies that we elaborated for the three major megafans in the SMB, possibly reflect the stratigraphic response to different sediment fluxes, driven by the tecto-geomorphic evolution of the Alpine hinterland.

3.6 Conclusions

The intermittency factor – a measure for the system's activity – can be used to determine the dynamics of sediment routing systems. We calculated such values for three Oligo-Miocene alluvial megafans in the SMB (Swiss Molasse basin). The western and central fan evolved during the Oligocene and both formed under similar climatic but different tectonic boundary conditions. Amongst these two, the central fan was a highly active system that transported sediment flux in c. 55 [20 – 157] h yr^{-1} (intermittency factor of 0.0063 [0.0023 – 0.018]), whereas the western fan needed c. 16 [6 – 49] h yr^{-1} (intermittency factor of 0.0019 [0.00068 – 0.0056]) to accomplish its annual sediment budget. We infer that the formation of the central fan was largely controlled by slab break-off tectonics of the European mantle lithosphere at c. 32 – 30 Ma. Particularly, the central fan was sourced the Lepontine dome in the Central Alps, which experienced high uplift rates at that time in response to slab break-off. In contrast, the formation of the western fan occurred some million years later, but the signal of enhanced surface erosion and large fluxes of material derived from the Alps was not recorded anymore. In the East and during the Middle Miocene, the least active system evolved during a time when the triangle zone in the SMB was formed, and when the drainage network in the Alps was reorganised. This possibly explains the low sediment supply to the eastern fan, and related to this, the relatively low activity where the supplied sediment was transported within 9 [3 – 26] h yr^{-1} (intermittency factor of 0.0011 [0.00039 – 0.0030]). Reconstructions of the sediment flux budgets and intermittencies of alluvial megafans thus not only provide insights into the evolution of the adjacent mountain belts but offer an ideal tool to unravel the dynamics of these sedimentary routing systems in the geological past. Upon applying these concepts to the Oligo-Miocene conglomerates of the Molasse foreland basin, such data provide insights onto the tectono-geomorphic evolution of the evolving Central Alps.

3.7 Author contribution

The study has been created by PG, AW and FS. PG carried out the fieldwork, collected the samples, and analysed the data with additional scientific input by all co-authors. PG prepared the manuscript and the figures with contributions from all co-authors.

3.8 Competing interests and funding sources

The authors declare that they have no conflict of interest. The authors declare the following financial interests/personal relationships which may be considered as potential competing interests: Philippos Garefalakis reports financial support was provided by the Swiss National Science Foundation (SNSF) [P1BEP2_200189].

3.9 Bibliography

Allen, P. A., Armitage, J. J., Carter, A., Duller, R. A., Michael, N. A., Sinclair, H. D., et al. (2013). The *Qs* Problem: Sediment volumetric balance of proximal foreland basin systems. Sedimentology 60, pp. 102–130. https://doi.org/10.1111/sed.12015

Allen, P. A., Crampton, S. L., and Sinclair, H. D. (1991). The inception and early evolution of the north Alpine foreland basin, Switzerland. Basin Res. 3, pp. 143–163. https://doi.org/10.1111/j.1365-2117.1991.tb00124.x

Armitage, J. J., Duller, R. A., Whittaker, A. C., and Allen, P. A. (2011). Transformation of tectonic and climatic signals from source to sedimentary archive. Nat. Geosci. 4, pp. 231–235. https://doi.org/10.1038/ngeo1087

Baran, R., Friedrich, A. M., and Schlunegger, F. (2014). The late Miocene to Holocene erosion pattern of the Alpine foreland basin reflects Eurasian slab unloading beneath the western Alps rather than global climate change. Lithosphere 6, pp. 124–131. https://doi.org/10.1130/L307.1

Beaumont, C. (1981). Foreland Basins. 291–329. https://doi.org/10.1002/9781444303810

Beaumont, C., Ellis, S., Hamilton, J., and Fullsack, P. (1996). Mechanical model for the tectonics of doubly vergent compressional orogens. Geology 24, pp. 675–678. https://doi.org/10.1130/0091-7613(1993)021<0371:MMFTTO>2.3.CO;2

Benavides, S. J., Deal, E., Rushlow, M., Venditti, J. G., Zhang, Q., Kamrin, K., et al. (2022). The Impact of Intermittency on Bed Load Sediment Transport. Geophys. Res. Lett. 49, pp. 1–18. https://doi.org/10.1029/2021GL096088

Berger, J.-P. (1992). Paléontologie de la Molasse de Suisse occidentale: Taxinomie, Biostratigraphie, Paléoecologie, Paléogéographie, Paléoclimatologie. Habilitation thesis, 405 pp. (in French).

Bernard, T., Sinclair, H. D., Gailleton, B., and Fox, M. (2021). Formation of Longitudinal River Valleys and the Fixing of Drainage Divides in Response to Exhumation of Crystalline Basement. Geophys. Res. Lett. 48, pp. 1–9. https://doi.org/10.1029/2020GL092210

Blair, T. C., and McPherson, J. G. (1994). Alluvial Fan Processes and Forms. Geomorphol. Desert Environ., pp. 354–402. https://doi.org/10.1007/978-94-015-8254-4_14

Blom, A., Viparelli, E., and Chavarrías, V. (2016). The graded alluvial river: Profile concavity and downstream fining. Geophys. Res. Lett. 43, pp. 6285–6293. https://doi.org/10.1002/2016GL068898

Bolliger, T. (1998). Age and geographic distribution of the youngest Upper Freshwater Molasse (OSM) of eastern Switzerland. Eclogae Geol. Helv. 91, pp. 321–332. https://doi.org/10.5169/seals-168426

Boothroyd, J. C., and Ashley, G. M. (1975). Processes, Bar Morphology, and Sedimentary Structures on Braided Outwash Fans, Northeastern Gulf of Alaska. Glaciofluvial Glaciolacustrine Sediment., pp. 193–222. https://doi.org/10.2110/pec.75.23.0193

Boston, K. R., Rubatto, D., Hermann, J., Engi, M., and Amelin, Y. (2017). Geochronology of accessory allanite and monazite in the Barrovian metamorphic sequence of the Central Alps, Switzerland. Lithos 286–287, pp. 502–518. https://doi.org/10.1016/j.lithos.2017.06.025

Bridge, J. (1985). Paleochannel patterns inferred from alluvial deposits: A critical evaluation. J. Sedi.. Petrol. 55, pp. 579–589. https://doi.org/10.1017/CBO9781107415324.004

Brooke, S. A. S., Whittaker, A. C., Armitage, J. J., D'Arcy, M., and Watkins, S. E. (2018). Quantifying Sediment Transport Dynamics on Alluvial Fans From Spatial and Temporal Changes in Grain Size, Death Valley, California. J. Geophys. Res. Earth Surf. 123, pp. 2039–2067.
https://doi.org/10.1029/2018JF004622

Büchi, U. P. (1958). Zur Geologie der Oberen Süsswassermolasse (OSM) zwischen Töss- und Glattal. Eclogae Geol. Helv. 51, pp. 73–105. (in German).
https://doi.org/10.5169/seals-162429

Bürgisser, Heinz, M., 1980. Zur Mittel-Miozänen Sedimentation im nordalpinen Molassebecken: Das "Appenzellergranit"-Leitniveau des Hörnli-Schuttfächers (OSM). Ph.D. Thesis, ETH Zurich, Switzerland, 196 p. (in German).
https://doi.org/10.3929/ethz-a-000218245

Bürgisser, H. M. (1981). Fazies und Paläohydrogeologie der Oberen Süsswassermolasse im Hörnli-Fächer (Nordostschweiz). Eclogae Geol. Helv. 1, pp. 19–28. (in German).
https://doi.org/10.5169/seals-165087

Cande, S. C., and Kent, D. V. (1995). Revised calibration of the geomagnetic polarity timescale for the Late Cretaceous and Cenozoic. J. Geophys. Res. 100, pp. 6093–6095.

Castelltort, S., Whittaker, A. C., and Vergés, J. (2015). Tectonics, sedimentation and surface processes: from the erosional engine to basin deposition. 1846, pp. 1839–1846.
https://doi.org/10.1002/esp.3769

Cederbom, C. E., van der Beek, P. A., Schlunegger, F., Sinclair, H. D., and Oncken, O. (2011). Rapid extensive erosion of the North Alpine foreland basin at 5-4Ma. Basin Res. 23, pp. 528–550.
https://doi.org/10.1111/j.1365-2117.2011.00501.x

Church, M. (2006). Bed Material Transport and the Morphology of Alluvial River Channels. Annu. Rev. Earth Planet. Sci. 34, pp. 325–354.
https://doi.org/10.1146/annurev.earth.33.092203.122721

D'Arcy, M., Whittaker, A. C., and Roda-Boluda, D. C. (2017). Measuring alluvial fan sensitivity to past climate changes using a self-similarity approach to grain-size fining, Death Valley, California. Sedimentology 64, pp. 388–424.
https://doi.org/10.1111/sed.12308

Duller, R. A., Whittaker, A. C., Fedele, J. J., Whitchurch, A. L., Springett, J., Smithells, R., et al. (2010). From grain size to tectonics. J. Geophys. Res. Earth Surf. 115, pp. 1–19.
https://doi.org/10.1029/2009JF001495

Dury, G. H. (1961). Bankfull discharge: An example of its statistical relationships. Int. Assoc. Sci. Hydrol. Bull. 6, pp. 48–55.
https://doi.org/10.1080/02626666109493230

Engesser, B., and Kälin, D. (2017). Eomys Helveticus N. Sp. and Eomys Schlunegger i N. Sp., two new small Eomyids of the Chattian (MP25/MP26) Subalpine Lower Freshwater Molasse of Switzerland. Foss. Impr. 73, pp. 213–224.
https://doi.org/10.1515/if-2017-0012

Eynatten, H. v. (2003). Petrography and chemistry of sandstones from the Swiss Molasse Basin: An archive of the Oligocene to Miocene evolution of the Central Alps. Sedimentology 50, pp. 703–724.
https://doi.org/10.1046/j.1365-3091.2003.00571.x

Fedele, J. J., and Paola, C. (2007). Similarity solutions for fluvial sediment fining by selective deposition. J. Geophys. Res. Earth Surf. 112, pp. 1–13.
https://doi.org/10.1029/2005JF000409

Ferguson, R., Hoey, T., Wathen, S., and Werritty, A. (1996). Field evidence for rapid downstream fining of river gravels through selective transport. Geology 24, pp. 179–182.
https://doi.org/10.1130/00917613(1996)024<0179:FEFRDF>2.3.CO;2

Flemings, P. B., and Jordan, T. E. (1990). Stratigraphic modeling of foreland basins: Interpreting thrust deformation and lithosphere rheology. Geology 18, pp. 430–434.
https://doi.org/10.1130/0091-7613(1990)018<0430:SMOFBI>2.3.CO;2

Flemings, P. B. P., and Jordan, T. E. (1989). A synthetic stratigraphic model of foreland basin development. J. Geophys. Res. Solid Earth 94, pp. 3851–3866.
https://doi.org/10.1029/JB094iB04p03851

Garefalakis, P., do Prado, A. H., Mair, D., Douillet, G. A., Nyffenegger, F., and Schlunegger, F. (2023). Comparison of three grain size measuring methods applied to coarse-grained gravel deposits. Sediment. Geol. 446, 100310.
https://doi.org/10.1016/j.sedgeo.2023.106340

Garefalakis, P., and Schlunegger, F. (2018). Link between concentrations of sediment flux and deep crustal processes beneath the European Alps. Sci. Rep.
https://doi.org/10.1038/s41598-017-17182-8

Glur, L., Wirth, S. B., Büntgen, U., Gilli, A., Haug, G. H., Schär, C., et al. (2013). Frequent floods in the European Alps coincide with cooler periods of the past 2500 years. Sci. Rep. 3, pp. 1–5.
https://doi.org/10.1038/srep02770

Gradstein, F. M., Ogg, J. G., Schmitz, M. D., and Ogg, G. M. (2020). Geologic Time Scale 2020. 1390 pp., ISBN: 9780128243602.

Hajek, E. A., and Straub, K. M. (2017). Autogenic Sedimentation in Clastic Stratigraphy. Annu. Rev. Earth Planet. Sci. 45, pp. 681–709.
https://doi.org/10.1146/annurev-earth-063016-015935

Hantke, R., Letsch, D., Felber, P., Baumeler, A., Heinz, R., Uttinger, J., et al. (2022). Blatt 1152 Ibergeregg. - Geol. Atlas Schweiz 1:25 000, Erläut. 175. (in German).
Available at: www.swisstopo.ch

Harries, R. M., Kirstein, L. A., Whittaker, A. C., Attal, M., and Main, I. (2019). Impact of recycling and lateral sediment input on grain size fining trends—Implications for reconstructing tectonic and climate forcings in ancient sedimentary systems. Basin Res. 31, pp. 866–891.
https://doi.org/10.1111/bre.12349

Harries, R. M., Kirstein, L. A., Whittaker, A. C., Attal, M., Peralta, S., and Brooke, S. (2018). Evidence for Self-Similar Bedload Transport on Andean Alluvial Fans, Iglesia Basin, South Central Argentina. J. Geophys. Res. Earth Surf. 123, pp. 2292–2315.
https://doi.org/10.1029/2017JF004501

Harvey, A. M., Mather, A. E., and Stokes, M. (2005). Alluvial Fans: Geomorphology, Sedimentology, Dynamics. Geological, 161 pp., ISBN: 1862391890.

Hay, W. W., Wold, C. N., and Herzog, J. M. (1992). “Preliminary Mass-Balance 3D Reconstructions of the Alps and the surrounding areas during the Miocene,” in Computer Graphics in Geology. Lecture Notes in Earth Sciences, 41, eds. R. Pflug and J. W. Harbaugh (Springer, Berlin), pp. 99–110.
https://doi.org/10.1007/BFb0117790

Hayden, A. T., Lamb, M. P., and McElroy, B. J. (2021). Constraining the Timespan of Fluvial Activity From the Intermittency of Sediment Transport on Earth and Mars. Geophys. Res. Lett. 48, pp. 1–13.
https://doi.org/10.1029/2021GL092598

Heller, P. L., and Paola, C. (1992). The large-scale dynamics of grain-size variation in alluvial basins, 2: Application to syntectonic conglomerate. Basin Res. 4, pp. 91–102.
https://doi.org/10.1111/j.1365-2117.1992.tb00146.x

Herwegh, M., Berger, A., Baumberger, R., Wehrens, P., and Kissling, E. (2017). Large-Scale Crustal-Block-Extrusion During Late Alpine Collision. Sci. Rep. 7, pp. 1–10.
https://doi.org/10.1038/s41598-017-00440-0

Hodges, J. L. (1958). The significance probability of the Smirnov two-sample test. Ark. för Mat. 3, pp. 469–486.
https://doi.org/10.1007/BF02589501

Hoey, T. B., and Bluck, B. J. (1999). Identifying the controls over downstream fining of river gravels. J. Sediment. Res. 69, pp. 40–50.
https://doi.org/10.2110/jsr.69.40

Huggenberger, P., and Regli, C. (2009). A Sedimentological Model to Characterize Braided River Deposits for Hydrogeological Applications. Braided Rivers, pp. 51–74.
https://doi.org/10.1002/9781444304374.ch3

Jordan, T. E. (1981). Thrust Loads and Foreland Basin Evolution, Cretaceous, Western United States. Am. Assoc. Pet. Geol. Bull. 65.
https://doi.org/10.1306/03b599f4-16d1-11d7-8645000102c1865d

Julien, P. Y. (2010). Erosion and Sedimentation. Cambridge Univ. Press 2, Cambridge, UK.
https://doi.org/10.1017/CBO9780511806049

Kälin, D., and Kempf, O. (2009). High-resolution stratigraphy from the continental record of the Middle Miocene Northern Alpine Foreland Basin of Switzerland. Neues Jahrbuch für Geol. und Paläontologie - Abhandlungen 254, pp. 177–235.
https://doi.org/10.1127/0077-7749/2009/0010

Kästle, E. D., Rosenberg, C., Boschi, L., Bellahsen, N., Meier, T., and El-Sharkawy, A. (2020). Slab break-offs in the Alpine subduction zone. Int. J. Earth Sci. 109, pp. 587–603.
https://doi.org/10.1007/s00531-020-01821-z

Kempf, O., Bolliger, T., Kälin, D., Engesser, B., and Matter, A. (1997). “New Magnetostratigraphic Calibration of Early to Middle Miocene Mammal Biozones of the North Alpine Foreland Basin,” in Actes du Congrès BIochrom’97, eds. J. Aguilar, S. Legendre, J. Michaux, and B. Mammalienne, pp. 547–561.

Kempf, O., and Matter, A. (1999). Magnetostratigraphy and depositional history of the Upper Freshwater Molasse (OSM) of eastern Switzerland. Eclogae Geol. Helv. 92, pp. 97–103.
https://doi.org/10.5169/seals-168650

Kempf, O., Matter, A., Burbank, D. W., and Mange, M. (1999). Depositional and structural evolution of a foreland basin margin in a magnetostratigraphic framework: The eastern Swiss Molasse Basin. Int. J. Earth Sci. 88, pp. 253–275.
https://doi.org/10.1007/s005310050263

Kempf, O., and Pfiffner, O. A. (2004). Early Tertiary evolution of the North Alpine Foreland Basin of the Swiss Alps and adjoining areas. Basin Res. 16, pp. 549–567.
https://doi.org/10.1111/j.1365-2117.2004.00246.x
Kissling, E., and Schlunegger, F. (2018). Rollback Orogeny Model for the Evolution of the Swiss Alps. Tectonics 37, pp. 1097–1115.
https://doi.org/10.1002/2017TC004762
Krsnik, E., Methner, K., Campani, M., Botsyun, S., Mutz, S. G., Ehlers, T. A., et al. (2021). Miocene high elevation in the Central Alps. Solid Earth 12, pp. 2615–2631.
https://doi.org/10.5194/se-12-2615-2021
Kuhlemann, J. (2000). Post-Collisional Sediment Budget of Circum-Alpine Basins (Central Europe). Mem. Di Sci. Geol. Padova 52, pp. 1–93.
Kuhlemann, J. (2007). Paleogeographic and paleotopographic evolution of the Swiss and Eastern Alps since the Oligocene. Glob. Planet. Change 58, pp. 224–236.
https://doi.org/10.1016/j.gloplacha.2007.03.007
Kuhlemann, J., Frisch, W., Dunkl, I., and Székely, B. (2001a). Quantifying tectonic versus erosive denudation by the sediment budget: the Miocene core complexes of the Alps. Tectonophysics 330, pp. 1–23.
https://doi.org/10.1016/S0040-1951(00)00209-2
Kuhlemann, J., Frisch, W., Dunkl, I., Szekely, B., and Spiegel, C. (2001b). Miocene shifts of the drainage divide in the Alps and their foreland basin. Z. Geomorph. N. F. 45, pp. 239–265.
https://doi.org/10.1127/zfg/45/2001/239
Kuhlemann, J., and Kempf, O. (2002). Post-Eocene evolution of the North Alpine Foreland Basin and its response to Alpine tectonics. Sediment. Geol. 152, pp. 45–78.
https://doi.org/10.1016/S0037-0738(01)00285-8
Kühni, A., and Pfiffner, O. A. (2001). Drainage patterns and tectonic forcing: A model study for the Swiss Alps. Basin Res. 13, pp. 169–197.
https://doi.org/10.1046/j.1365-2117.2001.00146.x
Litty, C., Schlunegger, F., and Viveen, W. (2017). Possible threshold controls on sediment grain properties of Peruvian coastal river basins. Earth Surf. Dyn. 5, pp. 571–583.
https://doi.org/10.5194/esurf-5-571-2017
Lourens, L. J., Hilgen, F. J., Laskar, J., Shackleton, N. J., and Wilson, D. (2004). "The Neogene Period," in A Geologic Time Scale 2004, eds. F. M. Gradstein, J. G. Ogg, and A. G. Smith (Cambridge University Press, Cambridge), 409-440.
Lyster, S. J., Whittaker, A. C., Farnsworth, A., and Hampson, G. J. (2022). Constraining flow and sediment transport intermittency in the geological past. Geol. Soc. Am. Bull.
https://doi.org/10.1130/B36873.1
Mair, D., do Prado, A. H., Garefalakis, P., Lechmann, A., and Schlunegger, F. (2022). Grain size of fluvial gravel bars from close-range UAV imagery – uncertainty in segmentation-based data. Earth Surf. Dynam. 10, pp. 953–973.
https://doi.org/doi.org/10.5194/esurf-10-953-2022
Matter, A. (1964). Sedimentologische Untersuchungen im östlichen Napfgebiet (Entlebuch - Tal der Grossen Fontanne, Kt. Luzern). Eclogae Geol. Helv. 57, pp. 315–429. (in German).
Matter, A., Homewood, P., Caron, C., Rigassi, D., van Stuijvenberg, J., Weidmann, M., et al. (1980). "Flysch and Molasse of western and central Switzerland," in Geology of Switzerland: A Guide Book. Part B Geological Excursions, eds. P. Homewood and R. Trümpy (Basel: Wepf & Co), pp. 261–293.
Matter, A., and Weidmann, M. (1992). Tertiary sedimentation in the Swiss Molasse: An overview. Eclogae Geol. Helv. 85, pp. 776–777.
https://doi.org/10.5169/seals-167041
Mazurek, M., Hurford, A. J., and Leu, W. (2006). Unravelling the multi-stage burial history of the Swiss Molasse Basin: Integration of apatite fission track, vitrinite reflectance and biomarker isomerisation analysis. Basin Res. 18, pp. 27–50.
https://doi.org/10.1111/j.1365-2117.2006.00286.x
McLeod, J. S., Wood, J., Lyster, S. J., Valenza, J. M., Spencer, A. R. T., and Whittaker, A. C. (2023). Quantitative constraints on flood variability in the rock record. Nat. Com. 14, pp. 1–12.
https://doi.org/10.1038/s41467-023-38967-8
Methner, K., Campani, M., Fiebig, J., Löffler, N., Kempf, O., and Mulch, A. (2020). Middle Miocene long-term continental temperature change in and out of pace with marine climate records. Sci. Rep. 10.
https://doi.org/10.1038/s41598-020-64743-5
Meybeck, M., Laroche, L., Dürr, H. H., and Syvitski, J. P. M. (2003). Global variability of daily total suspended solids and their fluxes in rivers. Glob. Planet. Change 39, pp. 65–93.
https://doi.org/10.1016/S0921-8181(03)00018-3
Miller, K. L., Szabó, T., Jerolmack, D. J., and Domokos, G. (2014). Quantifying the significance of abrasion and selective transport for downstream fluvial grain size evolution. J. Geophys. Res. F Earth Surf. 119, pp. 2412–2429.
https://doi.org/10.1002/2014JF003156

Mohrig, D., Heller, P. L., and Lyons, W. J. (2000). Interpreting avulsion process from ancient alluvial sequences: Guadalope-Matarranya system (northern Spain) and Wasatch Formation (western Colorado). Geol. Soceity Am. Bull. 112, pp. 1787–1803.
https://doi.org/10.1130/0016-7606(2000)112<1787:IAPFAA>2.0.CO;2

Mosbrugger, V., Utescher, T., and Dilcher, D. L. (2005). Cenozoic continental climatic evolution of Central Europe. Proc. Natl. Acad. Sci. U. S. A. 102, pp. 14964–14969.
https://doi.org/10.1073/pnas.0505267102

Navratil, O., Albert, M.-B., Hérouin, E., and Gresillon, J.-M. (2006). Determination of bankfull discharge magnitude and frequency: Comparison of methods on 16 gravel-bed river reaches. Earth Surf. Process. Landforms 31, pp. 1345–1363.
https://doi.org/10.1002/esp

Paola, C., Heller, P. L., and Angevinet, C. L. (1992). The Large Scale Dynamics Of Grain Size Variation In Alluvial Basins, 1: Theory. Basin Res. 4, pp. 73–90.
https://doi.org/10.1111/j.1365-2117.1992.tb00145.x

Paola, C., and Mohrig, D. (1996). Palaeohydraulics revisited: Palaeoslope estimation in coarse-grained braided rivers. Basin Res. 8, pp. 243–254.
https://doi.org/10.1046/j.1365-2117.1996.00253.x

Paola, C., and Voller, V. R. (2005). A generalized Exner equation for sediment mass balance. J. Geophys. Res. Earth Surf. 110, pp. 1–8.
https://doi.org/10.1029/2004JF000274

Parker, G. (1978). Self-formed straight rivers with equilibrium banks and mobile bed. Part 2. The gravel river. J. Fluid Mech. 89, pp. 127–146.
https://doi.org/10.1017/S0022112078002505

Parker, G. (1991). Selective sorting and abrasion of river gravel. I: Theory. J. Hydraul. Eng. 117, pp. 131–147.
https://doi.org/10.1061/(ASCE)0733-9429(1991)117:2(131)

Parker, G., Paola, C., Whipple, K. X., and Mohrig, D. (1998). Alluvial Fans Formed by Channelized Fluvial and Sheet Flow. I: Theory. pp. 985–995.
https://doi.org/10.1061/(ASCE)0733-9429(1998)124:10(996)

Parsons, A. J., Michael, N. A., Whittaker, A. C., Duller, R. A., and Allen, P. A. (2012). Grain-size trends reveal the late orogenic tectonic and erosional history of the south-central Pyrenees, Spain. J. Geol. Soc. London. 169, pp. 111–114.
https://doi.org/10.1144/0016-76492011-087

Pfeiffer, A. M., and Finnegan, N. J. (2018). Regional Variation in Gravel Riverbed Mobility, Controlled by Hydrologic Regime and Sediment Supply. Geophys. Res. Lett. 45, pp. 3097–3106.
https://doi.org/10.1002/2017GL076747

Pfiffner, O. A. (1986). Evolution of the north Alpine foreland basin in the Central Alps (Switzerland). Spec. Publs int. Ass. Sediment. 8, pp. 219–228.
https://doi.org/10.1002/9781444303810.ch11

Pfiffner, O. A., Schlunegger, F., and Buiter, S. J. H. (2002). The Swiss Alps and their peripheral foreland basin: Stratigraphic response to deep crustal processes. Tectonics 21, pp. 1-16.
https://doi.org/10.1029/2000TC900039

Recking, A., Liébault, F., Peteuil, C., and Jolimet, T. (2012). Testing bedload transport equations with consideration of time scales. Earth Surf. Process. Landforms 37, pp. 774–789.
https://doi.org/10.1002/esp.3213

Rice, S. P. (1999). The nature and controls on downstream fining within sedimentary links. J. Sediment. Res. 69, pp. 32–39.
https://doi.org/10.2110/jsr.69.32

Rice, S. P., and Church, M. (1996). Sampling surficial fluvial gravels; the precision of size distribution percentile sediments. J. Sediment. Res. 66, pp. 654–665.
https://doi.org/10.2110/jsr.66.654

Romans, B. W., Castelltort, S., Covault, J. A., Fildani, A., and Walsh, J. P. (2016). Environmental signal propagation in sedimentary systems across timescales. Earth-Science Rev. 153, pp. 7–29.
https://doi.org/10.1016/j.earscirev.2015.07.012

Sadler, P. M. (1981). Sediment Accumulation Rates and the Completeness of Stratigraphic Sections. J. Geol. 89, pp. 569–584. Available at: www.jstor.com/stable/30062397

Schlunegger, F. (1995). Magnetostratigraphie und fazielle Entwicklung der Unteren Süsswassermolasse zwischen Aare und Limmat. Unpubl. PhD Thesis, University of Bern, Switzerland, pp. 185. (in German).

Schlunegger, F. (1999). Controls of surface erosion on the evolution of the Alps: Constraints from the stratigraphies of the adjacent foreland basins. Int. J. Earth Sci. 88, pp. 285–304.
https://doi.org/10.1007/s005310050265

Schlunegger, F., Burbank, D. W., Matter, A., Engesser, B., and Mödden, C. (1996). Magnetostratigraphic calibration of the Oligocence to Middle Miocene (30-15 Ma) mammal biozones and depositional sequences of the Swiss Molasse Basin. Eclogae Geol. Helv. 89, pp. 753–788.
https://doi.org/10.5169/seals-168650
Schlunegger, F., and Castelltort, S. (2016). Immediate and delayed signal of slab breakoff in Oligo/Miocene Molasse deposits from the European Alps. Sci. Rep. 6, 31010.
https://doi.org/10.1038/srep31010
Schlunegger, F., Delunel, R., and Garefalakis, P. (2020). Short communication: Field data reveal that the transport probability of clasts in Peruvian and Swiss streams mainly depends on the sorting of the grains. Earth Surf. Dyn. 8, pp. 717–728.
https://doi.org/10.5194/esurf-8-717-2020
Schlunegger, F., Jordan, T. E., and Klaper, E. M. (1997a). Controls of erosional denudation in the orogen on foreland basin evolution: The Oligocene central Swiss Molasse Basin as an example. Tectonics 16, pp. 823–840.
https://doi.org/10.1029/97TC01657
Schlunegger, F., and Kissling, E. (2015). Slab rollback orogeny in the Alps and evolution of the Swiss Molasse basin. Nat. Commun. 6, 8605.
https://doi.org/10.1038/ncomms9605
Schlunegger, F., and Kissling, E. (2022). Slab Load Controls Beneath the Alps on the Source-to-Sink Sedimentary Pathways in the Molasse Basin. Geosci. 12.
https://doi.org/10.3390/geosciences12060226
Schlunegger, F., Leu, W., and Matter, A. (1997b). Sedimentary sequences, seismic facies, subsidence analysis, and evolution of the Burdigalian Upper Marine Molasse Group, central Switzerland. AAPG Bull. 81, pp. 1185–1207.
https://doi.org/10.1306/522B4A19-1727-11D7-8645000102C1865D
Schlunegger, F., Matter, A., Burbank, D. W., and Klaper, E. M. (1997c). Magnetostratigraphic constraints on relationships between evolution of the central Swiss Molasse basin and Alpine orogenic events. GSA Bull. 109, pp. 225–241.
https://doi.org/10.1130/0016-7606(1997)109<0225:MCORBE>2.3.CO;2
Schlunegger, F., Matter, A., and Mange, M. A. (1993). Alluvial fan sedimentation and structure of the southern Molasse Basin margin, Lake Thun area, Switzerland. Eclogae Geol. Helv. 86, pp. 717–750.
https://doi.org/10.5169/seals-167260
Schlunegger, F., Melzer, J., and Tucker, G. E. (2001). Climate, exposed source-rock lithologies, crustal uplift and surface erosion: A theoretical analysis calibrated with data from the Alps/North Alpine foreland basin system. Int. J. Earth Sci. 90, pp. 484–499.
https://doi.org/10.1007/s005310100174
Schlunegger, F., and Mosar, J. (2011). The last erosional stage of the Molasse Basin and the Alps. Int. J. Earth Sci. 100, pp. 1147–1162.
https://doi.org/10.1007/s00531-010-0607-1
Schlunegger, F., and Norton, K. P. (2013). Headward retreat of streams in the Late Oligocene to Early Miocene Swiss Alps. Sedimentology 60, pp. 85–101.
https://doi.org/10.1111/sed.12010
Schlunegger, F., Slingerland, R. L., and Matter, A. (1998). Crustal thickening and crustal extension as controls on the evolution of the drainage network of the central Swiss Alps between 30 Ma and the present: Constraints from the stratigraphy of the North Alpine Foreland Basin and the structural evolution of the. Basin Res. 10, pp. 197–212.
https://doi.org/10.1046/j.1365-2117.1998.00063.x
Schlunegger, F., and Willett, S. D. (1999). Spatial and temporal variations in exhumation of the central Swiss Alps and implications for exhumation mechanisms. Geol. Soc. Spec. Publ. 154, pp. 157–179.
https://doi.org/10.1144/GSL.SP.1999.154.01.07
Schmid, S. M., Pfiffner, O. A., Froitzheim, N., Schönborn, G., and Kissling, E. (1996). Geophysical-geological transect and tectonic evolution of the Swiss-Italian Alps. Tectonics 15, pp. 1036–1064.
https://doi.org/10.1029/96TC00433
Shields, A. (1936). Anwendung der Ähnlichkeitsmechanik und der Turbulenzforschung auf die Geschiebebewegung. Preuss. Versuchsanstalt für Wasserbau und Schiffbau 26.
Sinclair, H. D. (1997). Flysch to Molasse transition in peripheral foreland basins: The role of the passive margin versus slab breakoff. Geology 25, pp. 1123–1126.
https://doi.org/10.1130/0091-7613(1997)025<1123:FTMTIP>2.3.CO;2
Sinclair, H. D., Coakley, B. J., Allen, P. A., and Watts, A. B. (1991). Simulation of Foreland Basin Stratigraphy Using A Diffusion Model Of Mountain Belt Uplift And Erosion: An Example From The Central Alps, Switzerland. 10, pp. 599–620.
https://doi.org/10.1029/90TC02507
Sinclair, H. D., and Naylor, M. (2012). Foreland basin subsidence driven by topographic growth versus plate subduction. Bull. Geol. Soc. Am. 124, pp. 368–379.
https://doi.org/10.1130/B30383.1

Sissingh, W. (1997). Tectonostratigraphy of the North Alpine Foreland Basin: Correlation of Tertiary depositional cycles and orogenic phases. Tectonophysics 282, pp. 223–256.
https://doi.org/10.1016/S0040-1951(97)00221-7

Spiegel, C., Kuhlemann, J., Dunkl, I., and Frisch,Paleogeography and catchment evolution in a mobile orogenic belt: The Central Alps in Oligo-Miocene times. Tectonophysics 341, pp. 33–47.
https://doi.org/10.1016/S0040-1951(01)00187-1

Steck, A., Della Torre, F., Keller, F., Pfeifer, H. R., Hunziker, J., and Masson, H. (2013). Tectonics of the Lepontine Alps: Ductile thrusting and folding in the deepest tectonic levels of the Central Alps. Swiss J. Geosci. 106, pp. 427–450.
https://doi.org/10.1007/s00015-013-0135-7

Sternberg, H. (1875). Untersuchungen über Längen- und Querprofil geschiebeführender Flüsse. Zeitschrift für Bauwes. 25, pp. 483–506. (in German).
Available at: https://digital.zlb.de/viewer/image/15239363_1875/262/

Stock, J. D., Schmidt, K. M., and Miller, D. M. (2008). Controls on alluvial fan long-profiles. Bull. Geol. Soc. Am. 120, pp. 619–640.
https://doi.org/10.1130/B26208.1

Strasky, S., Schlunegger, F., Hänni, R., Häuselmann, P., Mojon, A., and Schwizer, B. (2022). Blatt 1208 Beatenberg. - Geol. Atlas Schweiz 1:25 000, Erläut. 170-171.
Available at: www.swisstopo.ch

Straub, K. M., Duller, R. A., Foreman, B. Z., and Hajek, E. A. (2020). Buffered, incomplete, and shredded: The challenges of reading an imperfect stratigraphic record. J. Geophys. Res., 93.
https://doi.org/10.1029/2019JF005079

Stürm, B. (1973). Die Rigi Schüttung - Sedimentpetrographie, Sedimentologie, Palaeogeographie, Tektonik. Unpubl. PhD Thesis, Univ. Bern, 96 pp.

Stutenbecker, L., Tollan, P. M. E., Madella, A., and Lanari, P. (2019). Miocene basement exhumation in the Central Alps recorded by detrital garnet geochemistry in foreland basin deposits. Solid Earth Discuss., pp. 1–26.
https://doi.org/10.5194/se-2019-98

Tanner, H. J. (1944). Beitrag zur Geologie der Molasse zwischen Ricken und Hörnli. Mitteilungen der Thurgauischen Naturforschenden Gesellschaft 33, pp. 1–108.
https://doi.org/10.5169/seals-593971

Tucker, G. E., and Slingerland, R. L. (1997). Drainage basin responses to climate change. Water Resour. Res. 33, pp. 2031–2047.
https://doi.org/10.1029/97WR00409

van der Boon, A., Beniest, A., Ciurej, A., Gaździcka, E., Grothe, A., Sachsenhofer, R. F., et al. (2018). The Eocene-Oligocene transition in the North Alpine Foreland Basin and subsequent closure of a Paratethys gateway. Glob. Planet. Change 162, pp. 101–119.
https://doi.org/10.1016/j.gloplacha.2017.12.009

Ventra, D., and Clarke, L. E. (2018). Geology and geomorphology of alluvial and fluvial fans: current progress and research perspectives. Geol. Soc. London, Spec. Publ. 440, pp. 1–21.
https://doi.org/10.1144/sp440.16

Ventra, D., and Nichols, G. J. (2014). Autogenic dynamics of alluvial fans in endorheic basins: Outcrop examples and stratigraphic significance. Sedimentology 61, pp. 767–791.
https://doi.org/10.1111/sed.12077

Wainwright, J., Parsons, A. J., Cooper, J. R., Gao, P., Gillies, J. A., Mao, L., et al. (2015). The concept of transport capacity in geomorphology. Rev. Geophys. 53, pp. 1155–1202.
https://doi.org/10.1002/2014RG000474

Whittaker, A. C. (2012). How do landscapes record tectonics and climate? Lithosphere 4, pp. 160–164.
https://doi.org/10.1130/RF.L003.1

Whittaker, A. C., Duller, R. A., Springett, J., Smithells, R. A., Whitchurch, A. L., and Allen, P. A. (2011). Decoding downstream trends in stratigraphic grain size as a function of tectonic subsidence and sediment supply. pp. 1363–1382.
https://doi.org/10.1130/B30351.1

Wickert, A. D., and Schildgen, T. F. (2019). Long-profile evolution of transport-limited gravel-bed rivers. Earth Surf. Dyn. 7, pp. 17–43.
https://doi.org/10.5194/esurf-7-17-2019

Wolman, M. G. (1954). A method of sampling coarse river-bed material. Trans. Am. Geophys. Union 35, 951–956.
https://doi.org/10.1029/TR035i006p00951

Wong, M., and Parker, G. (2006). Reanalysis and Correction of Bed-Load Relation of Meyer-Peter and Müller Using Their Own Database. J. Hydraul. Eng. 132, pp. 1159–1168.
https://doi.org/10.1061/(asce)0733-9429(2006)132:11(1159)

Zachos, J. C., Pagani, H., Sloan, L., Thomas, E., and Billups, K. (2001). Trends, rhythms, and aberrations in global climate 65 Ma to present. Science (80). 292, pp. 686–693.
https://doi.org/10.1126/science.1059412

3.10 Appendix A

Appendix A summarizes the sedimentary facies of the analysed sections, gives insights into the equations of the self-similar grain size fining model and provides the equations to calculate the instantaneous bedload sediment flux. In addition, Appendix A comprises the approach on how to measure channel depths from stratigraphic deposits and how to calculate the paleoslope. Furthermore, Appendix A provides an overview of the used variables and parameters, summarised in a table.

3.10.1 Sedimentary facies and age models of the stratigraphic sections

The stratigraphic framework along with the age model is based on published information and combined with own observations for each of the investigated megafan deposits. In the field, we analysed the stacking pattern at the outcrop scale. We used the morphology and the arrangement of individual conglomerate, sandstone or mudstone beds as criteria and investigated the preserved sedimentary structures therein, such as cross-beds or erosional scours. This allowed us to analyse flow paths, and, in combination with the arrangement or imbrication of individual clast, we updated the paleodischarge direction as proposed from data in the literature. These analyses also provided the basis for the chronological correlation between the various sections. We additionally recalibrated published magnetostratigraphic data of the three fan systems through correlations to the recent Global Time Scale GTS2020 (Gradstein et al., 2020).

3.10.1.1 Western fan

Sedimentary facies

The c. 3250 m-thick Thun section (Schlunegger et al., 1993, 1996), to which we refer for simplicity reasons to as deposits of the western fan (Thun Lakeside section; Figs. S3.1a and S3.1b), runs along Lake Thun and chronicles the deposits of the Blueme alluvial fan system (Schlunegger et al., 1993). These Oligocene coarse-grained fluvial deposits constitute the Thun Formation (Schlunegger et al., 1993, 1996), which is part of the Lower Freshwater Molasse group (German abbreviation: USM, ‘Untere Suesswasser Molasse’). The Thun Fm (Fig. S3.1b) is divided into an upper and lower part based on characteristic lithological properties. The lower part, which is referred to as the Huenibach conglomerate, is c. 550 m-thick and consists of alternations of several meters-thick conglomerate and sandstone beds with intercalated mudstone (silt and clay) interbeds that are a few meters thick (Fig. S3.1b). The conglomerate beds consist of rounded and sub-rounded grains embedded in a sandy matrix. Sedimentary structures in these beds, such as cross-beds, are only locally preserved, while the majority of the conglomerates are massive-bedded. Occasionally, imbrications and erosional scours are visible. Petrological analyses (Schlunegger et al., 1993; Strasky et al., 2022) revealed that the Huenibach conglomerate consists of up to 60 – 70% of crystalline clasts, of which 1/3 are red granites, whereas the rest (30 – 40% of the total) have a sedimentary origin (cherts, limestones, dolomites, sandstones). The upper part of the Thun Fm is referred to as the Gunten Quarzite conglomerate, which is c. 2700 m-thick at the site where we analysed the section (Fig. S3.1b). There, the frequency and thickness of individual conglomerate beds increases up-section (Schlunegger et al., 1993; Strasky et al., 2022). The majority of the conglomerate beds are massive bedded, but occasionally cross- and horizontal-bedding and erosional scours at their base also occur. In contrast to the Huenibach unit, the Gunten Quarzite conglomerate contains quartzite clasts (10 – 30%; Schlunegger et al., 1993; Strasky et al., 2022). Therefore, the Huenibach and Gunten Quarzite units can be distinguished based on petrographic information. Our own clasts counts at 19 locations confirmed this (Tab. S3.1). We used our revised age model of the Thun Fm (see below) together with its thickness at proximal (Thun/Thunersee/Lake Thun section, c. 3250 m thick) and distal positions (Praesserenbach section, c. 1280 m thick; Figs. S3.1a and b) to estimate proximal-distal trends in the sediment accumulation rates.

Unit (mapped)	Distance from apex [m]	Site	Red Granite	Crystalline (general)	Dolomite	Sandstone	Limestone (bright)	Limestone (siliceous, dark)	Quarzite	Vein Quartz	Conglomerate	Total counts
Gunten Quarzit conglomerate	5973	60	-	18	-	1	24	21	32	4	-	100
	6156	59	-	27	-	-	27	24	20	2	-	100
	6322	58	3	21	-	1	17	32	26	-	-	100
	6461	57	5	22	-	1	19	28	25	-	-	100
	6711	54	4	24	-	-	19	18	33	2	-	100
	8466	26	9	16	1	2	17	28	27	-	-	100
	8491	25	5	24	-	-	12	37	19	3	-	100
	9066	24	3	29	-	-	16	35	14	1	2	100
	9151	22	4	24	1	2	32	18	16	3	-	100
	9441	19	6	22	-	2	15	31	23	1	-	100
	9953	15	4	21	-	-	6	30	18	21	-	100
	9978	14	10	34	-	2	6	32	9	6	1	100
Huenibach conglomerate	10057	17	3	30	3	6	13	27	7	11	-	100
	10083	16	3	40	2	2	10	31	3	9	-	100
	10872	7	7	39	1	4	8	29	3	7	2	100
	11098	5	5	31	2	4	14	35	5	4	-	100
	11255	3	4	21	1	5	18	40	4	6	1	100
	11364	2	4	18	-	2	14	43	7	12	-	100
	11470	1	10	27	-	2	18	33	6	4	-	100

Table S3.1: Lithological clast counts at the western fan in the Thun formation (see Fig. S3.1a for locations of the individual sites).

Age model

We used the magneto- and biostratigraphic data of the Praesserenbach section (Schlunegger et al., 1996; Strasky et al., 2022) situated 6 km to the ENE of the Thun Lakeside section to constrain our age model (i.e., Magneto-stratigraphic section in Fig. S3.1a). To this end, we focused on the Thun Fm, which is only c. 1300 m thick at the Praesserenbach section, where the local Magnetic Polarity Stratigraphy (MPS) was established (Schlunegger et al., 1996; Strasky et al., 2022; Fig. S3.1b). We considered the original corelation of the individual reversals (Schlunegger et al., 1996) to the global magneto chrons. Yet we used the most recent temporal calibration (GTS2020 of Gradstein et al., 2020) for assigning numerical ages to the global MPTS (Magneto Polarity Time Scale). As a first consequence, the base of the Thun Fm is 24.8 ± 0.05 Ma old, and the top of the same unit has a numerical age of 24.0 ± 0.05 Ma (Fig. S3.1b). Accordingly, the Thun Fm along the Praesserenbach section spans an age interval between 24.8 – 24.0 ± 0.05 Ma and comprises 1280 ± 50 m of sediments (Fig. S3.1b). This yields a sediment accumulation rate of 1600 ± 260 m/Myr. As a second consequence of this correlation, the topmost unit of the Praesserenbach section (i.e., Gitzischoepf conglomerate) has an age of 23.1 ± 0.05 Ma (Schlunegger et al., 1996).

The 3250 m-thick Thun Fm exposed along the Thun Lakeside section has not been dated numerically, and no information on micro mammal faunas are available there. We therefore projected the ages established for the Praesserenbach section onto the sedimentary suite exposed along Lake Thun because both sections record the identical development of the petrofacies (Schlunegger et al., 1993, 1996; Strasky et al., 2022). Accordingly, while the base of the Thun FM appears to be isochronous as revealed by mapping (Roger Heinz, pers. comm. 2022), an assignment of an age for the top of this unit is not straightforward, because of heterochronous facies relationships (Schlunegger et al., 1993). Yet, mapping has shown that the Honegg Marls and the Gitzischoepf conglomerates, both of which are exposed along the Praesserenbach section (Fig. S3.1b), are time equivalent to the top of the Thun Fm farther west (Roger Heinz, pers. comm. 2022). Therefore, for the deposits along the Lake Thun, we assign an age of 24.8 and 23.1 ± 0.05 Ma to the base and the top of the Thun Fm, respectively (Fig. S3.1b). Because the Thun Fm along the Thun Lakeside section is 3250 ± 50 m thick, the sediment accumulation rates were 1910 ± 140 m/Myr.

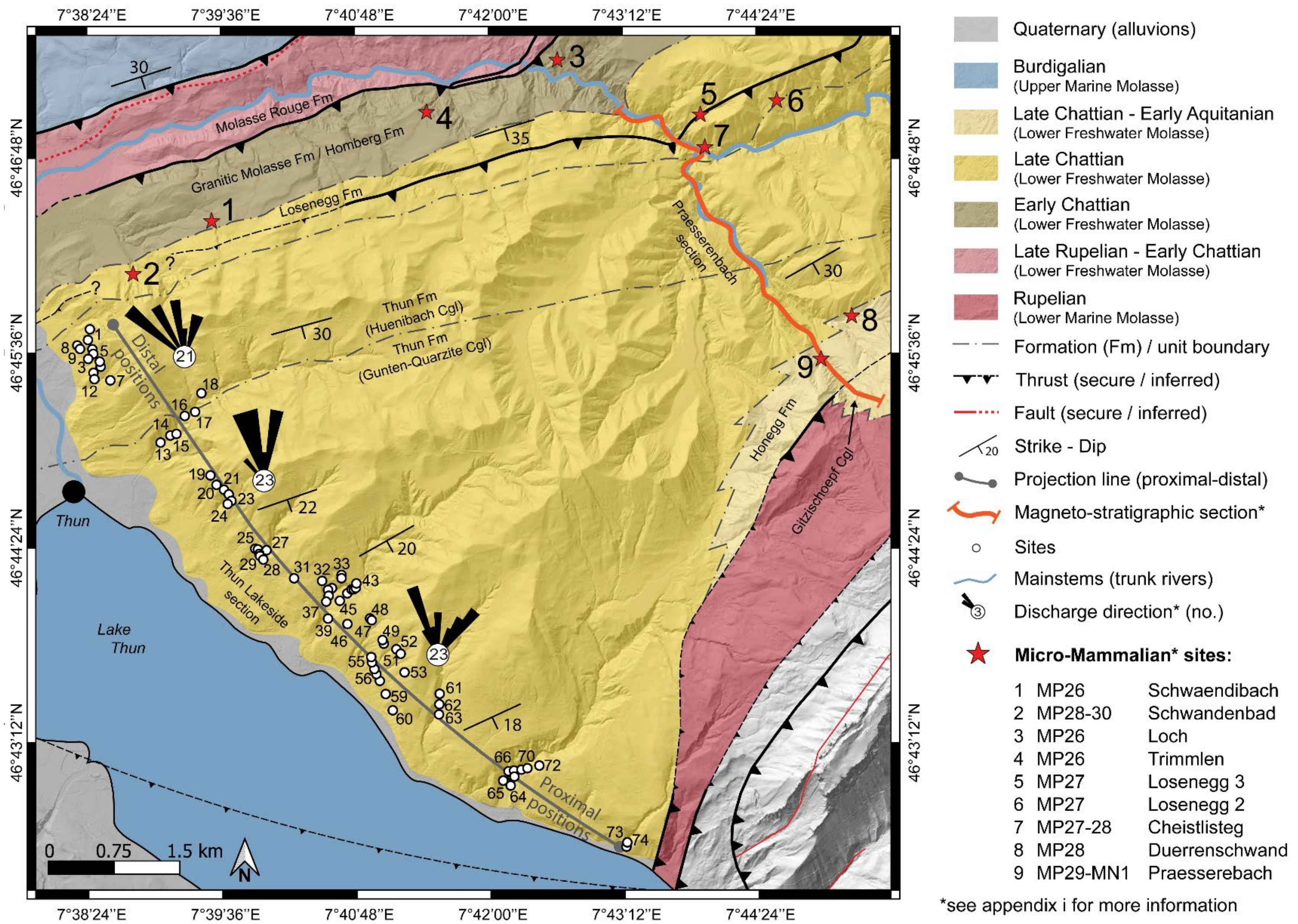

Figure S3.1a: Simplified geological map of the western fan and the surrounding area. Appendix i corresponds to appendix A of this thesis' chapter.

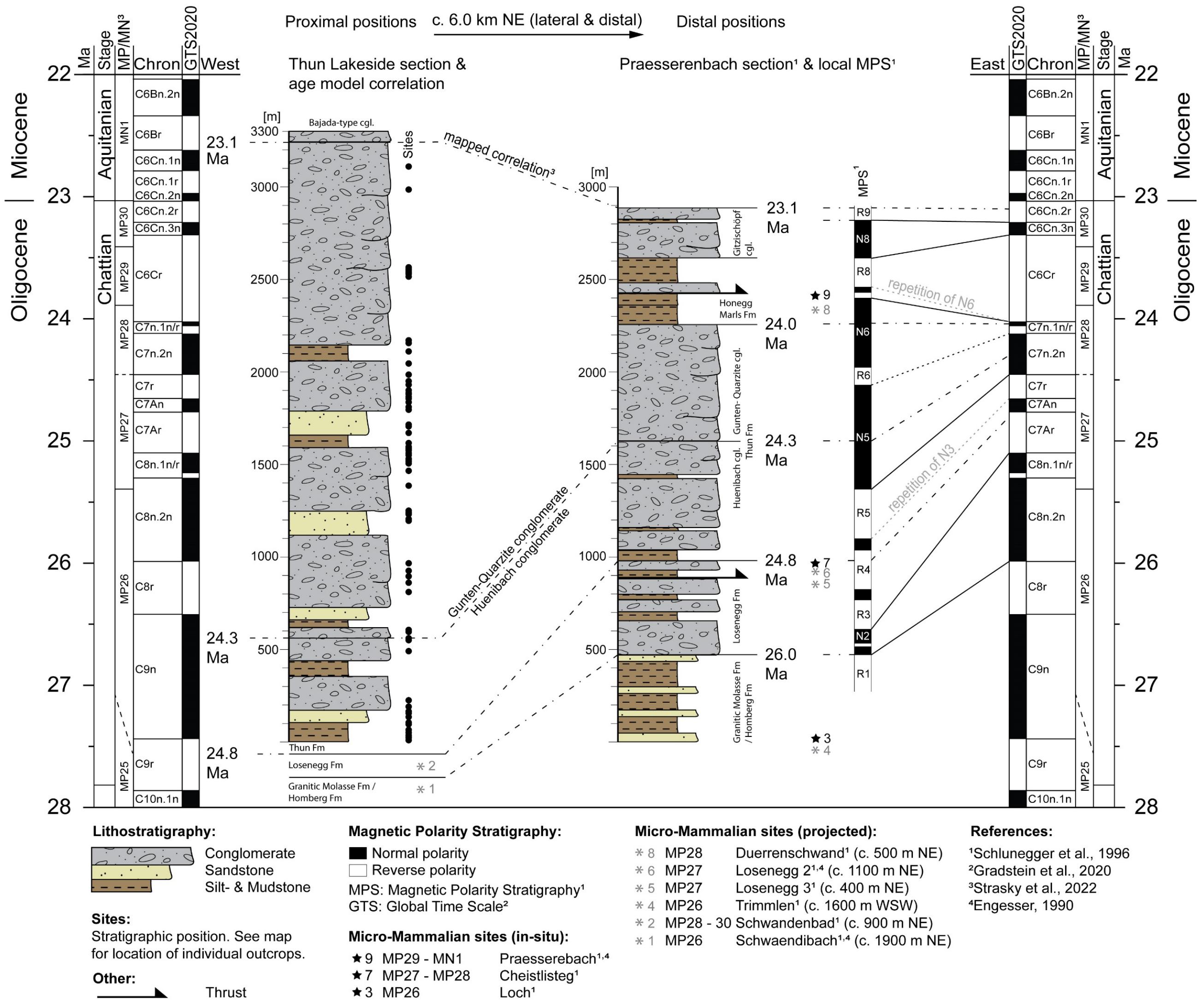

Figure S3.1b: Chronostratigraphic framework of the western fan deposits.

3.10.1.2 Central fan

Sedimentary facies

The central alluvial megafan was constructed by the Rigi dispersal system (Stürm, 1973; Schlunegger et al., 1997b, 1997a), and the resulting deposits are part of the Lower Freshwater Molasse group (German abbreviation: USM, 'Untere Suesswasser Molasse'). The most complete and dated stratigraphic section (the Rigi section; i.e., the magneto-stratigraphic section in Fig. S3.2a) is a 4000 m-thick suite of sediments spanning a time interval between 29.5 and 24.0 Ma during the Oligocene (Schlunegger et al., 1997b). The sediments encountered along the Rigi-section can be traced 30 km down-system and they crop out along 4 additional stratigraphic sections (Schlunegger et al., 1997a; Figs. S3.2a and S2b). The central fan deposits consist of several lithostratigraphic units (Fig. S3.2b), of which we selected the upper part referred to as the Bunte Rigi conglomerate for our analysis. We selected this unit because its base can be easily identified in the field by the first appearance of granite clasts (Stürm, 1973; Schlunegger et al., 1997b). At proximal positions, this unit consist of an amalgamation of several tens of meters thick conglomerate beds that are occasionally intercalated by a few dm- to m-thick sandstone and mudstone beds. Towards distal parts, individual conglomerate beds thin to few meters and alternate with several m-thick sandstone and mudstone interbeds. The conglomerate beds consist of rounded to sub-rounded clasts, embedded in a sandy matrix. They are mostly massive-bedded and occasionally display low-angular cross-beds, erosional scours at their base and fining-up trends towards the top of individual conglomerate beds (Stürm, 1973; Schlunegger et al., 1997a; Garefalakis and Schlunegger, 2018). In the lower half of the target unit (between 1700 to 2800 m of Rigi section, Fig. S3.2b), approximately 80 – 90 % of the clasts are of sedimentary origin (sandstone, dolomite, limestone, and chert clasts), and the rest (10 – 20 %) consists of red granites and radiolarites (Schlunegger et al., 1997b). The increase of the sandstone clasts towards the top could be explained by a material supply through a paleotributary system. However, an approximately constant composition of the heavy minerals within the sandstones (Stürm, 1973), of which zircons constitute c. 80 % to the bulk of the Bunte Rigi conglomerate unit, suggests that the sediments were supplied and dispersed on the fan by a single system (Stürm, 1973; Schlunegger et al., 1997b). The top of the Bunte Rigi conglomerate is defined where the mudstone interbeds of the overlying Scheidegg unit become more frequent and thicker (Fig. S3.2b; Schlunegger et al., 1997b). The occurrence of red granite clasts was then used as criteria to trace the target unit (i.e., the Bunte Rigi conglomerate unit) from distal to more proximal positions (Schlunegger et al., 1997a, 1997b). Accordingly, the Bunte Rigi unit is approximately 1600 ± 50 m thick along the Rigi section, from where the thickness decreases to 1485 ± 50 m along the Rossberg, 1040 ± 50 m along the Sattel and finally to 595 ± 50 m along the Einsiedeln section (Fig. S3.2b).

Age model

The chronological framework of the central fan is based on the local Magnetic Polarity Stratigraphy (MPS) established along the Rigi section (i.e., the magneto-stratigraphic section in Fig. S3.2a). We employed the correlation of the MPS to the global MPTS as proposed by Schlunegger et al. (1997b) but considered the most recent calibration of the magneto-chrons to the GTS2020 by Gradstein et al. (2020) instead. Accordingly, the base of the Bunte Rigi conglomerate unit has an age of 26.4 ± 0.05 Ma, whereas the top of this unit spans most likely the time interval between 25.1 and 24.7 Ma (Fig. S3.2b). We note that due to sample gaps particularly in the upper part of the section, it was not possible to determine a more precise age for the top of this unit (Schlunegger et al., 1997b). Therefore, Schlunegger et al. (1997b) considered the possibility of additional polarity shifts from normal to reversed ones where the sampling density is low (grey polarities in MPS, Fig. S3.2b). As an example, a solution where the top of the MPS would correlate with C7n.2n would imply the occurrence of a hiatus, for which no evidence has been presented so far in the literature (Stürm, 1973; Schlunegger et al., 1997a, 1997b; Garefalakis and Schlunegger, 2018). We are thus left with a large age range for the top of the Bunte Rigi conglomerate unit. But for simplicity we used an average of 24.9 ± 0.2 Ma, which we then extrapolated towards more distal sites (Rossberg, Sattel and Einsiedeln sections, Fig. S3.2a and b). Note that the proposed age model is consistent with ages offered by two micro-mammalian fauna sites at the base of the Rossberg (Engesser and Kälin, 2017) and Sattel (Hantke et al., 2022) sections, which we projected onto our profiles (Fig. S3.2b). Accordingly, our target unit spans a time interval that is approximately 1.5 ± 0.25 Ma long, and it thins from c. 1600 m at the apex to approximately 600 m towards the ENE (see above and Fig. S3.2b). This yields sediment accumulation rates of approximately 1070 ± 210 m Myr^{-1} for the Rigi section, 990 ± 200 m Myr^{-1} for the Rossberg section, 695 ± 150 m Myr^{-1} for the Sattel section, and 400 ± 100 m Myr^{-1} for the Einsiedeln section.

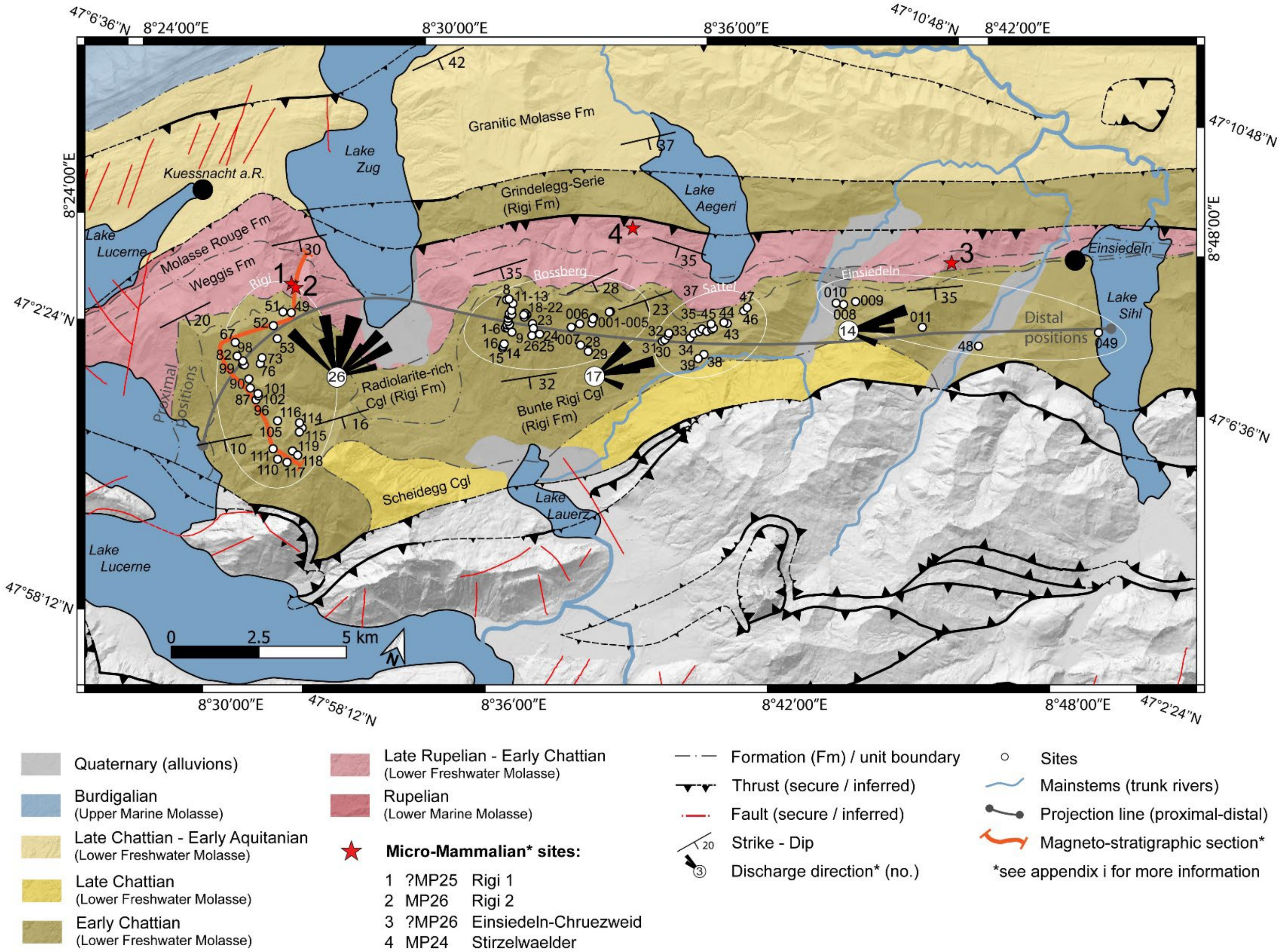

Figure S3.2a: Simplified geological map of the central fan and the surrounding area. Appendix i corresponds to appendix A of this thesis' chapter.

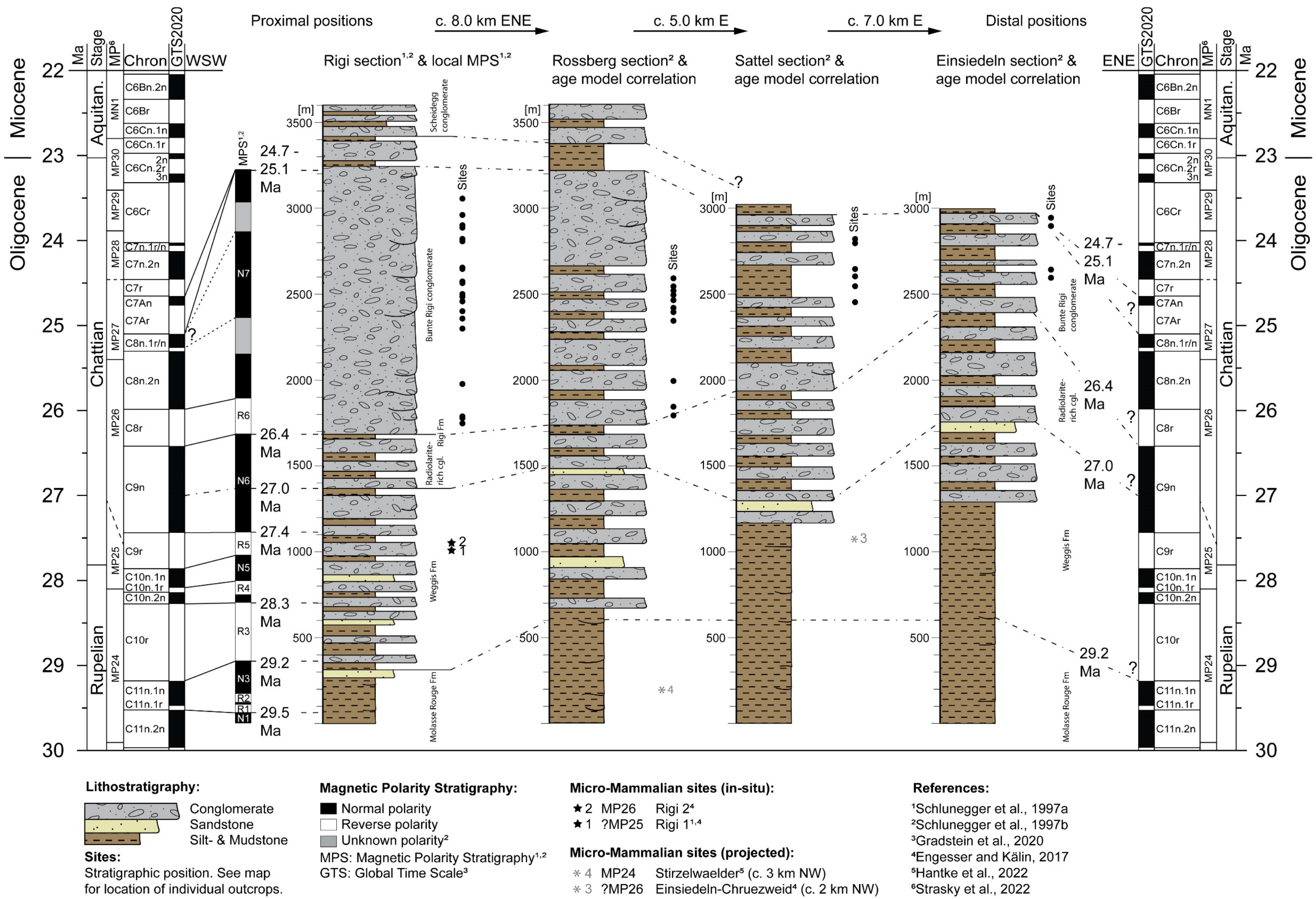

Figure S3.2b: Chronostratigraphic framework of the central fan deposits.

3.10.1.3 Eastern fan

Sedimentary facies

In the east, the deposits of the Hoernli alluvial megafan are encountered along two sections (Hoernli and Toess profiles), which are part of the Upper Freshwater Molasse group (German abbreviation: OSM, 'Obere Suesswasser Molasse') deposited during Miocene times (Figs. S3a and S3b). The Hoernli section, representing the sediments at more distal positions (i.e., the magneto-stratigraphic section in Fig. S3.3a and see below), was dated by magneto-polarity investigations and built the basis for the chronological framework (Kempf et al., 1997; Kälin and Kempf, 2009). Approximately 9 km farther to the South, the Toess section comprises the same sedimentary units as encountered at the Hoernli but in a more proximal position. Amongst others, Hottinger et al. (1970) defined four sedimentary units at the Hoernli, which are from the bottom to the top the Oehniger, Toesswald, Hoernligubel, and Hoenrligipfel units (Fig. S3.3b). The lowermost Oehniger unit is characterised by an alternation of several m-thick mudstone and a few m-thick sandstone beds, occasionally intercalated with dm- to m-thick conglomerate beds. Therefore, only a few sites were available where grain size measurements could be conducted (Fig. S3.3b). Along the Hoernli profile, the transition to the overlying Toesswald unit is very sharp. It is characterised by several m-thick conglomerate beds, forming amalgamations of a few tens of meters. The mudstone interbeds are only m-thick and occur occasionally (Fig. S3.3b). The conglomerate beds of this unit consist of rounded to sub-rounded clasts within a sandy matrix. In these beds, massive-bedding dominates over cross-bedding. Clast counts revealed that c. 60 – 80 % of the material is of sedimentary origin (limestones, sandstones, dolomites, radiolarites, breccias), whereas crystalline clasts are subordinate (Tanner, 1944). Heavy mineral analyses of this unit revealed a high abundance of epidote (70 – 90 %), which are successively replaced by apatite and staurolite towards the top of the Toesswald unit (Füchtbauer, 1964). The change to the overlying Hoernligubel and -gipfel units is characterized by an increase in dolomite and limestone clasts (c. 10 – 20, locally up to 50 % and c. 30% respectively), with a minor contribution by crystalline constituents (c. 5 – 10 %; Tanner, 1944). The Hoernligubel and - gipfel units are commonly combined into one single unit, mainly because the Hoernligubel unit is made up of a c. 20 m-thick mudstone bed that is prominently exposed at the Hoernli section only (Hottinger et al., 1970; Wyss and Hofmann, 1999). Within this mudstone bed, the occurrence of the c. 1.5 – 2 m-thick Hoernli-Breccia, located at c. 990 m a.s.l. (Fig. S3.3b) was interpreted as a mass flow deposit (Bolliger, 1998). The Hoernli-Breccia thins out to a few dm towards more distal sites. The overlying Hoernligipfel unit is characterised by massive, several m-thick conglomerate beds, occasionally intercalated by mudstone and sandstone beds. Here, we focussed our study on the Toesswald unit because along the Hoernli section, its lower and upper bounds are defined by well-visible changes in the stratigraphic architecture.

Along the proximal Toess section, the stratigraphic architecture of the aforementioned units is very similar, which first hampers a distinct subdivision into units and particularly complicates a correlation to the Hoernli section. This was also why Bürgisser (1981) introduced an alternative stratigraphic scheme (H1, H2, and H3) based on lithotypes. Yet, our own mapping has shown that it was impossible to extrapolate these lithotypes from the Hoernli to the Toess area. However, because conglomerate packages are well visible in the 2 m resolution digital elevation model (LiDAR DEM Swiss ALTI3D; © swisstopo), we traced the base and the top of the Toesswald unit from the Hoernli to the Toess area using existing geological maps and the LiDAR DEM as a basis. In this context, we benefitted from the fact that both sections are situated in the Plateau Molasse and that only a gently northward dipping anticline separates both sections (Fig. S3.3a). This finally results in nearly the same thickness of c. 240 ± 50 m for this unit along both sections (Fig. S3.3b).

Age model

Kempf et al. (1997) and Kälin and Kempf (2009) presented an age model for the Hoernli section, which is based on magnetopolarity stratigraphic and biostratigraphic constraints. This yielded a numerical age of c. 14.9 – 13.3 Ma for the entire Hoernli section, of which the unit of interest (Toesswald unit; see above) has an age between c. 14.6 and 13.6 Ma (Fig. S3.3b), respectively. While the age of the Toesswald unit is well constrained at the Hoernli (Kälin and Kempf, 2009, Fig. S3.3b), a correlation with the more proximal suite is hampered because neither a mammal site nor a magnetostratigraphic data are available. Therefore, we base our age assignment on the mapping and bed-by-bed tracing on the LiDAR DEM as outlined in the section above. Given this chronological framework for the Toesswald unit, which covers c. 1.0 ± 0.2 Ma, we calculated a sediment accumulation rate of c. 240 m Myr^{-1} on average for both sites, albeit with a considerable uncertainty of ± 100 m Myr^{-1}.

The position of the paleo apex and implications for the model

The point where the alluvial megafans entered the Molasse basin is of particular interest for the grain size fining model as it defines the position where accumulation of sediment started. In that context, the paleo apex' position constrains the accommodation space, and placing its position has implications for defining the wavelength and magnitude at which subsidence occurs. For simplicity, we considered the apex for any fan to be situated 3 km farther upstream from the most proximal site. However, that of the eastern fan may well have been located 10 – 15 km farther to the SE (Bürgisser, 1981; section 3.2.3 in main text). We therefore applied large uncertainties in constraining the subsidence pattern at the apex for the eastern fan (see above). The results of the subsidence distribution for a now extrapolated position of the apex +15 km farther to the SE show that the range of possible subsidence rates at the apex largely increased, i.e., R_A = 244 [44 – 1085] m Myr^{-1} (Fig. S3.4a). Upon applying the grain size fining model (see e.g., section 3.10.2) we do not see a major shift in the results of the grain size fining model. The necessary sediment flux to replicate the extrapolated grain size regression is in median ${Q_s}_A^*$ of 7.90 [3.20

- 21.8] km^2 Myr^{-1} and a median sediment excess rate F_E = 1.89 [1.30 – 3.61], revealing that a median 47 [23 – 72] % of the sediment was transferred out of the system, while c. 53 [28 – 77] % of the supplied material accumulated on the fan (Fig. S3.4b). Using the same instantaneous bedload sediment fluxes (see results in main text), we obtained intermittency factors of I_F = 0.00124 [0.00036 – 0.0048] that correspond to c. 11 [3 – 42] hours per year (Fig. S3.4c). These outcomes are in good agreement with the results if an apex at +3 km is considered (see results in main text; e.g., Table 3.1) and therefore do not alter the main conclusion.

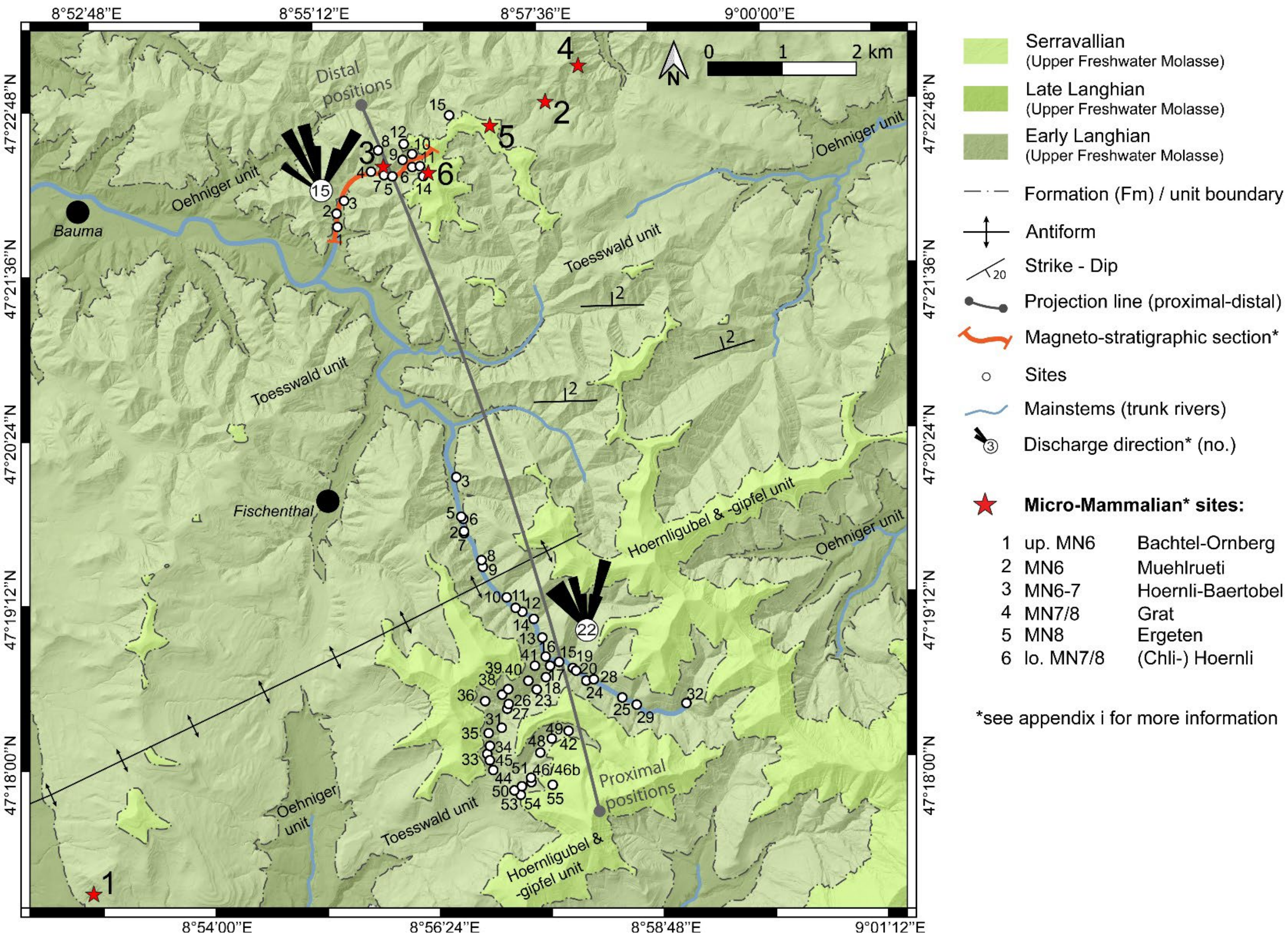

Figure S3.3a: Simplified geological map of the eastern fan and the surrounding area. Appendix i corresponds to appendix A of this thesis' chapter.

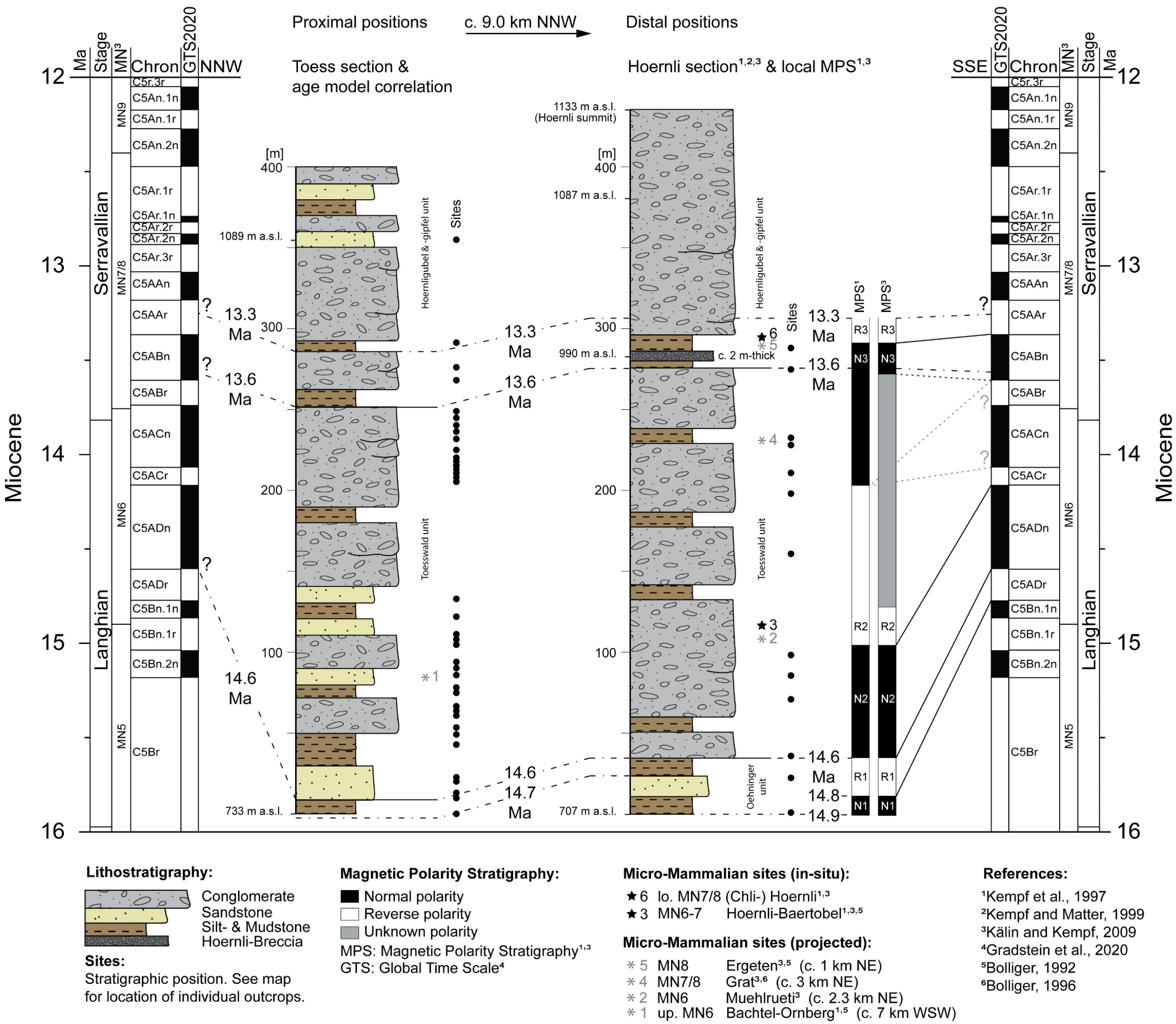

Figure S3.3b: Chronostratigraphic framework of the eastern fan deposits.

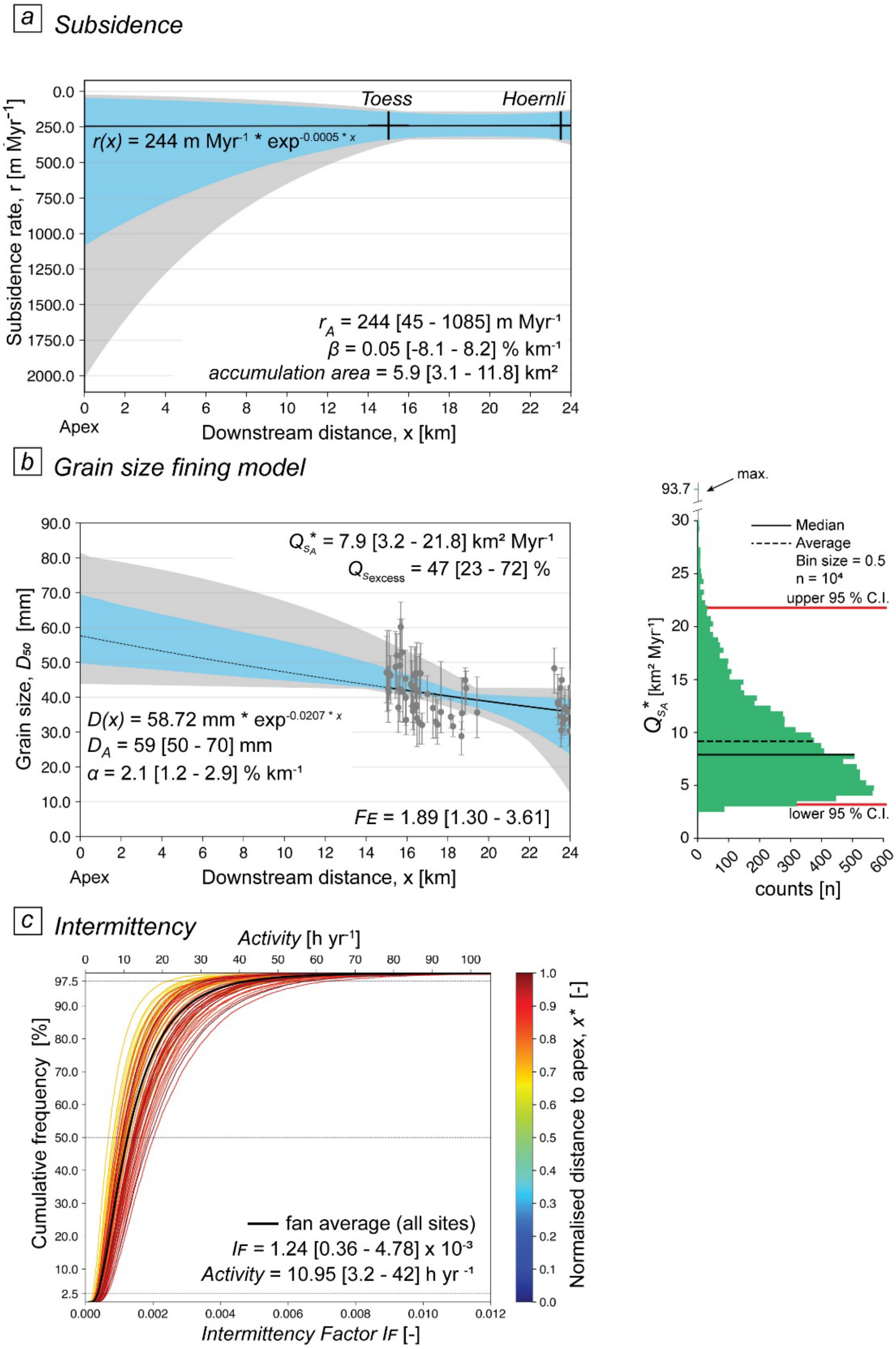

Figure S3.4: Results from the eastern fan for the **a)** subsidence pattern, **b)** grain size fining model and **c)** intermittency calculations, if an appendix +15 km to the most proximal site is considered. **a)**: The black line reflects the best-fit exponential regression, the blue area corresponds to the 95 % CI of the regression analyses, and the grey area corresponds to all possible regression scenarios thereby using 10^4 iterations. The accumulation area in is the cross-sectional area calculated through the trapezoidal rule. **b):** The grey dots represent the D_{50} values (error bars correspond to the 95% CI) and the black line reflects the best-fit regression curve on the grain size data (solid = data available; dotted = extrapolated). The shaded blue area corresponds to the 95 % CI of the modelled grain sizes from the grain size fining model and the grey area corresponds to all possible scenarios thereby using 10^4 iterations. $Q_{s_A}^*$ = input sediment flux; F_E = sediment excess rate, $Q_{Sexcess}$ = sediment in %-excess.

3.10.2 Self-similar grain size fining model

Derivation of the model

The grain size fining model introduced by Fedele and Paola (2007) requires four input parameters that are: i) the down-system length of the depositional system, ii) the distribution of the local subsidence and its down-system decreasing rate, and iii) the grain size distribution at the apex of the fan system, expressed by the input grain size D_A. As a fourth parameter, an estimate of the unit sediment flux ${Q_s}_A^*$ at the apex, here in [km^2 Myr^{-1}], is needed. Here, we used an inversion of the model thereby iteratively determining these long-term sediment fluxes. From the three parameters, the down-system length and the subsidence pattern can easily be extracted by analysing the sections of interest, given that a chronological framework is provided (see section 3.10.1). The third parameter, the input grain size, depends on the grain size fining rate along distance, which can be expressed as an exponential function following the 'Sternberg-law' (Sternberg, 1875):

$$D(x^*) = D_A \, exp^{-\alpha(x^*)} \; [m] \qquad Eq. (S3.1).$$

Here, x^* is the normalised down-system length, D_A is the input grain size at length $x^* = 0$, that can be considered the apex of the system, and α is the grain size fining rate along the normalised distance, respectively. The parameters D_A and α can be retrieved by approximating the grain size fining along x^* with an exponential function. For the grain size fining we used the D_{50} as representation at each location because this percentile best characterizes the bulk grain size distribution, particularly during equal mobility conditions (Paola and Mohrig, 1996; Wickert and Schildgen, 2019). To be more conservative, we applied a bootstrapping on the D_{50} values and modelled 10^4 possible solutions of both grain size fining functions and related input grain size. We then used these 10^4 values of D_A and α for further calculations.

As a requirement for the grain size fining model, the distribution of the sediment size has to be self-similar (Fedele and Paola, 2007). In other words, when the grain size distribution is collapsed into the similarity variable ξ, the mean and the standard deviation of the sediment at the surface and in the substrate decrease down-system both at the same rate. Consequently, the grain size distribution at any site has the same shape, if normalised, as follows:

$$\xi = \frac{D_k - \overline{D}(x^*)}{\sigma(x^*)} \; [-] \qquad Eq. (S3.2).$$

Here, D_k is an individual grain size value, $\overline{D}$ and σ are the mean and standard deviation of the grain size distribution at a given location along a stream with a normalised down-system length x^*, respectively. This assumption is incorporated in the self-similar grain size fining model (Paola and Voller, 2005; Fedele and Paola, 2007) that is based on a constant critical Shields number of 1.4 multiplied by the dimensionless critical shear stress τ_c* (see section 3.10.3) and on the inference of threshold conditions for sediment transport during bankfull discharge. The underlying principle of the grain size fining model is a variation of the Exner sediment mass balance where the material is either in transport or stored in the substrate (Paola and Voller, 2005; Fedele and Paola, 2007). In this concept, aggradation and, thus, deposition of sediment yields adjustments of the bed-surface elevation that increases proportionally to the deposited mass. If the material is re-entrained and the bed degrades, the bed-surface elevation also decreases in proportion to the mass in transport (Paola and Voller, 2005). This mass-conserving principle, in combination with knowledge of the available accommodation space, as revealed by the subsidence pattern, thus allows to predict how much of the sediments are deposited or extracted downstream (Fedele and Paola, 2007; Allen et al., 2013; Brooke et al., 2018). This balance between processes governing extraction and deposition of sediment along down-system distance can be expressed as:

$$\frac{df}{dx^*} = f\left[R^*\left(1-\frac{1}{J}\right)-\frac{1}{J}\frac{dJ}{dx^*}\right]\ [-] \qquad Eq.(S3.3).$$

Here, J is the relative mobility of the sediment, where $J > 1$ likely indicates that a sediment with a given calibre is in transport, whereas $J < 1$ expresses that the same sedimentary particle becomes deposited or remains in the substrate (Fedele and Paola, 2007; Brooke et al., 2018). It reflects the proportion of sediment in transport p and the fraction of it in the substrate f as $J = p/f$ (as a function of normalised down-system length x^*). Because J also behaves in a self-similar way downstream, J and f can be expressed as a function of ξ (Fedele and Paola, 2007; Duller et al., 2010; D'Arcy et al., 2017; Brooke et al., 2018). R^* in Eq. (*S3.3*) quantifies the dimensionless distribution of sediment mass down-system, expressed as:

$$R^*(x^*) = \left(1-\lambda_p\right) L\,\frac{r^*(x^*)}{Q_s{}^*(x^*)}\ [-] \qquad Eq.(S3.4),$$

where $\lambda_p = 0.3$ is the sediment porosity (Fedele and Paola, 2007), L is the total down-system length, while Qs^* is the spatial variation in unit sediment flux and r^* is the subsidence rate both along distance x^*. As a simplification, we express the subsidence rate along distance by an exponential function (Duller et al., 2010; Whittaker et al., 2011; D'Arcy et al., 2017):

$$r^*(x^*) = r_A\, exp^{-\beta(x^*)}\ [m\ Myr^{-1}] \qquad Eq.(S3.5).$$

Here, r_A is the subsidence rate at the apex where $x^* = 0$ and β is the decreasing rate at which r^* decreases down-system (x^*). Examples have shown that such a function corresponds well to the distribution of accommodation space in foreland basins (Allen et al., 1991; Sinclair and Naylor, 2012). Section 3.10.1 (appendix A) describes how we determined the subsidence rates for our fans of interest. The rate of sediment being extracted along distance $Qs^*(x^*)$ can then be defined as the difference between the input sediment flux ${Q_s}_A^*$ per unit channel width and the deposited volume of sediment. This volume is integrated along distance L, along which sediment accumulation occurs:

$$Q_s^*(x^*) = {Q_s}_A^* - (1 - \lambda_p) \int_0^L r^*(x^*)\, dx^* \; [m^3\ Myr^{-1}\ m^{-1}] \qquad Eq. (S3.6).$$

The underlying assumption here is that any change of bed elevation is taking place at relatively short timescales and changes thereof evolve and diminish spontaneously. Therefore, these short-term perturbations in the long-term sediment flux are considered negligible (Fedele and Paola, 2007; Duller et al., 2010; Harries et al., 2019). To model the grain size deposited in the substrate, *f*, we applied a dimensionless distance transformation $y^*(x^*)$ (Fedele and Paola, 2007) that integrates the spatial distribution of sediment mass in the down-system direction:

$$y^*(x^*) = \int_0^{x^*} R^*(x^*)\, dx^* \; [-] \qquad Eq. (S3.7).$$

The removal of sediment mass, which is expressed as R^*, scales proportionally to the grain size fining rates recovered from Eq. (*S3.1*). Therefore it is possible to model the size D_m of a grain as a function of y^* along distance x^* (Fedele and Paola, 2007):

$$D_m(x^*) = D_A + \varphi_A \frac{C_2}{C_1}\left(exp^{-C_1 y^*} - 1\right) [m] \qquad Eq. (S3.8).$$

Here, D_A is the input grain size and φ_A its deviation at the apex where $x^* = 0$, expressed as $\varphi_A = D_A * C_V$ (coefficient of variation; see below), thereby following D'Arcy et al. (2017). As outlined above, we applied a bootstrapping approach with 10^4 iterations on Eq. (*S3.1*), thereby recovering numerous possible solutions of the Sternberg-law and thus for the input grain size D_A. Fedele and Paola (2007) introduced the coefficients C_1 and C_2, which describe the relative partitioning of the variance in sediment supply. While C_1 scales to the standard deviation at a location, C_2 scales to the down-system change of the mean grain size (Fedele and Paola, 2007). The aforementioned authors thus found that the ratio between the standard deviation σ and the mean grain size $\overline{D}$, defined as the coefficient of variation C_v, is equivalent to the ratio between C_1 and C_2. Furthermore, they showed that for fluvial gravels, the C_v remains approximately constant along distance (Fedele and Paola, 2007). Because values for C_1 have already been determined on a theoretical basis and since values for C_v can be extracted from our dataset, it is possible to compute values for C_2, which is needed as an input for the model (Eq. (*S3.8*)), using the following relationships:

$$C_v = \frac{C_1}{C_2} = \frac{\sigma(x^*)}{\overline{D}(x^*)} \; [-] \qquad Eq. (S3.9).$$

Here, the median value of C_v was determined for each site by bootstrapping (10^4 iterations on each individual grain size distribution). The C_v value at the scale of the entire fan is then the average of the individual site-specific median C_v values. For further calculations, we considered a uniform distribution within the 95 % CI averaged for the entire fan. The coefficient of variation C_v for each target fan is c. 0.65 ± 0.10 (see results). Additionally, our C_v values are within those reported in other studies that typically range between c. 0.55 and 0.90 (Fedele and Paola, 2007; Duller et al., 2010; Armitage et al., 2011; Brooke et al., 2018). Similarly, the value of C_1. has been shown to lie between c. 0.50 and 0.90 (Fedele and Paola, 2007; Duller et al., 2010; Armitage et al., 2011), but values ranging between 0.70 and 0.80 or an average value of 0.75 have been commonly applied in previous studies (Fedele and Paola, 2007; Armitage et al., 2011; Whittaker et al., 2011; D'Arcy et al., 2017). Therefore, and being slightly more conservative, we assigned values to C_1 that are uniformly distributed between 0.60 and 0.90. This is consistent with the results of sensitivity analyses on this variable, which showed that different values of C_1 do not significantly influence the modelled downstream grain size fining rates (Duller et al., 2010).

<u>Previous applications</u>

The grain size fining model has been successfully applied to stratigraphic deposits in the Spanish Pyrenees, supporting the idea that shifts in tectonically induced subsidence rates, variations in sediment flux, and related changes of erosion rates are recorded by these sediments (Duller et al., 2010; Whittaker et al., 2011; Parsons et al., 2012; Allen et al., 2013). Some of these applications also revealed large input grain sizes and fining rates for four proximal-distal timelines within the Montsor conglomerates (Pobla Basin, Spanish Pyrenees). The results additionally implied that these large values are inversely scaled to the length of the systems (Duller et al., 2010; Whittaker et al., 2011). Additionally, the model was applied to Holocene deposits in Death Valley, USA, where grain size fining rates and shifts in sediment fluxes were related to climatic perturbations (D'Arcy et al., 2017). A related work conducted in the same area could show that these environmental changes were also reflected in a modification of the relative mobility of a given grain size (Brooke et al., 2018). Other applications and modifications of the grain size fining model, with a focus on modern alluvial fans in the Iglesia basin, Argentine Andes, could show that variations of sediment flux were controlled by a combination of lateral sediment input from tributary catchments and recycling of previously deposited material (Harries et al., 2019).

3.10.3 Instantaneous bedload sediment flux

Principles and basic equations

Sediment transport occurs as bedload if coarse particles (>2 mm) are rolling, sliding and/or saltating along the riverbed (Baker and Ritter, 1975; Dade and Friend, 1998; Recking, 2015). The model of non-dimensional bedload transport proposed by Meyer-Peter and Müller (1948; known as the MPM-equation) bases on the inference that sediment is entrained in proportion to the shear stress at the channel bed (or competence of a stream), which itself is expressed as the basal shear stress τ_b (Baker and Ritter, 1975; Church, 2006; Rice and Church, 2010):

$$\tau_b = \rho_w \, g \, R_h \sin(\gamma) \; [Pa] \qquad Eq.(S3.10).$$

Here, ρ_w is the water density (1000 kg m^{-3}), g is the gravity of Earth (9.81 m s^{-2}), and γ is the gradient of the riverbed, respectively. For small angles, i.e., <1°, sin(γ) approximates to tan(γ). Furthermore, R_h is the hydraulic radius, which is approximated by the depth of the flow for wide channels that exceed a width to depth ratio > 20 (Tinkler, 1982, 1997; Tucker and Slingerland, 1997), particularly during bankfull discharge.

It has been proposed that a grain of a particular size, e.g. the D_{50} grain size percentile, is entrained if the drag force of the flow, expressed by the basal shear stress (Eq. *S3.10*), exceeds a critical value and thus overcomes the submerged weight of a grain (Church, 2006). This is defined as the dimensionless shear stress τ^* or Shields-stress (Shields, 1936):

$$\tau^* = \frac{\rho_w \, g \, d_{bf} \, S}{(\rho_s - \rho_w) \, g \, D_{50}} \; [-] \qquad Eq.(S3.11).$$

Here, d_{bf} is the channel depth during bankfull discharge (see section 3.10.5 and appendix B for channel depth measurements), S (in RAD) is the channel slope that substitutes sin(γ) (Julien, 2010; Wickert and Schildgen, 2019), D_{50} is the grain size percentile, and ρ_s and ρ_w are the sediment and water densities, respectively. The dimensionless submerged specific gravity of Quartz can be expressed as $G_S = [(\rho_s./\ \rho_w) - 1] = 1.65$, which is close to values of natural sediments with $\rho_s = 2650$ kg m^{-3} and $\rho_w = 1000$ kg m^{-3} for the sediment and water densities, respectively.

Following Shields (1936), grains are mobilized if $\tau^* = \tau_c^*$. Here, τ_c^* is the dimensionless critical shear stress, which is the boundary shear stress needed for the incipient transport of a single grain, commonly referred to as the critical Shields-parameter (Shields, 1936). Additionally, during bankfull discharge, which is the underlying assumption here, shear stresses exceed the critical Shields-parameter by a constant multiple (Parker, 1978; Paola and Mohrig, 1996; Pfeiffer et al., 2017; Schlunegger and Garefalakis, 2018; Wickert and Schildgen, 2019), which is expressed in the following way:

$$\tau^* = \frac{d_{bf}\, S}{G_S\, D_{50}} = (1.0 + \varepsilon)\, \tau_c{}^* \, [-] \qquad Eq.(S3.12).$$

Here ε is a variable, that considers (for a steady flow with a given water discharge) how much water depth changes when the channel width increases or decreases downstream (Parker, 1978). It thus bases on the equilibrium-channel hypothesis where the shear stress in the channel's centre cannot overcome a threshold without widening the river by lateral erosion (Parker, 1978; Engelder and Pelletier, 2013). This variable has a theoretical value of $\varepsilon = 0.2$ (Parker, 1978), but Paola and Mohrig (1996) suggested using $\varepsilon = 0.4$ instead. We thus employed a uniformly distributed range between both values to consider all possibilities for our calculations.

Note that a variety of Shields-parameters have been reported for gravel-bed rivers for bedload transport (Petit et al., 2015). Here, we used a uniformly distributed range (Julien, 2010; Schlunegger et al., 2020) between 0.039 and 0.054 for τ_c*, which appears appropriate for material between ≥ 2 mm ($\tau_c* = 0.039$; Julien, 2010) and < 128 mm ($\tau_c* = 0.054$; Julien, 2010). This range of Shields-parameters also includes the dependency of the critical shear stress on the local slopes (Müller et al., 2005; Parker et al., 2007; Lamb et al., 2008) and was reported for natural gravelly-bed rivers (Wilcock, 1993; Julien, 2010; Bunte et al., 2013; Petit et al., 2015).

Bedload sediment flux equation

We used the MPM-equation (Meyer-Peter and Müller, 1948) to compute the volumetric bedload sediment transport rate per unit time and unit channel width, denoted as the instantaneous unit bedload sediment flux Q_b^*. The MPM-equation was calibrated in the laboratory and has been widely applied in both flume-experiments and on natural-datasets (Church, 2006; Huang, 2010; Wickert and Schildgen, 2019; Ancey, 2020b, 2020a). In its simplest form, it can be expressed as the dimensionless bedload transport rate q_b^*:

$$q_b{}^* = C(\tau^* - \tau_c{}^*)^{1.5} \, [-] \qquad Eq.(S3.13).$$

The dimensionless bedload transport rate q_b^* can also be expressed as the Einstein number (Einstein, 1950):

$$q_b{}^* = \frac{Q_b{}^*}{(\, G_S\, g\ \ D_{50}{}^3\,)^{0.5}} \, [-] \qquad Eq.(S3.14),$$

Therefore, the combination of equations *S3.13* and *S3.14* yields an expression that allows to calculate the unit bedload sediment flux Q_b^*:

$$Q_b{}^* = 3.97\, (\tau^* - \tau_c{}^*)^{1.5} \left(G_S\, g\, D_{50}{}^3\right)^{0.5} \, [m^3\, s^{-1}\, m^{-1}] \qquad Eq.(S3.15).$$

Here, we set for C = 3.97 [-] as re-calibrated by Wong and Parker (2006) using the original dataset of Meyer-Peter and Müller (1948) as basis. Substitution of τ^* in equation *S3.15* by the expression derived from equation *S3.12* results in an expression where Q_b^* solely depends (among other given variables) on the grain size D_{50}:

$$Q_b{}^* = 3.97\ [(1.0+\varepsilon)\ \tau_c{}^* - \tau_c{}^*]^{1.5}\ \left(G_S\ g\ D_{50}{}^3\right)^{0.5}\ [m^2\ s^{-1}] \qquad Eq. (S3.16).$$

Here, g is the gravitational force (9.81 m s^{-2}), G_S is the dimensionless submerged specific gravity of Quartz (1.65), D_{50} is the grain size percentile, τ_c* the Shields-parameter, and ε is the erosional correction factor, respectively. We calculated the unit bedload sediment flux Q_b^* using a combined bootstrapping and Monte Carlo approach and propagated each of the variables ε, τ_c*, and D_{50} over 10^4 times and report the fan's averaged time-transgressive median Q_b^* value together with the 95% confidence interval.

Yet, among other (theoretically and empirically derived) variables, our derivation of the bedload equation solely depends on the grain size, mainly because we did not estimate paleo slopes in another way than using a shear-stress approach (see also section 3.10.5 for details on the paleo slope calculations). Nevertheless, the MPM-equation, on which our approach bases, has been proven to replicate field-based measurements of bedload fluxes in recent rivers (Parker, 1990; Wilcock and Crowe, 2003; Gray and Simões, 2008; Gao, 2011; Petit et al., 2015). In addition, the related concepts were also considered to interpret grain size and channel depth information from stratigraphic records (Brewer et al., 2020; Sharma et al., 2023).

3.10.4 Uncertainties and error estimations

We reported the mean or median value (each time indicated) along with the 95% Confidence Interval (CI) in squared brackets (e.g., D_{50} = 22 [17 – 25] mm). The errors were calculated as followed.

For the calculations of errors on the subsidence rate, we used the uncertainties arising from the age models and the inferred sediment accumulation rates, and we considered uniform distributions between the maximum and minimum accumulation rates for each section (section 3.10.1). We then calculated a range of plausible subsidence patterns by applying a Monte Carlo simulation on these values. This was done through a regression analysis on the values resulting from Eq. (3.7) or Eq. (S3.5).

For the grain size data, we resampled with replacement 100 grain size values D_k (measured on the photographs) and calculated the uncertainties on the D_{50} within a given confidence interval by bootstrapping 10^4 scenarios. We then incorporated these values into the equations, which we used for calculating the input grain size D_A, thereby considering the results of a regression analysis applied to the outcome of Eq. (3.8) or Eq. (S3.1). For estimating the C_v values, we calculated the median along with the 95% CI for each site, and we report the averages thereof for each entire fan.

For calculating the uncertainties on the unit bedload sediment fluxes Q_b^*, we used the grain size values from the bootstrapping in combination with the results of the Monte Carlo error estimation. We accomplished this for ε and τ_c using uniformly distributed values (details in appendices ii and iii). Uncertainties on the long-term sediment fluxes were also calculated and propagated following these procedures. Because we only get the fan-average long-term sediment flux but have estimates on the bedload fluxes for each individual outcrop, we calculated the intermittency factors through bootstrapping. For this, we resampled both results (long-term and instantaneous sediment fluxes) for each site, and we calculated their ratios (Eq. 3.1 in main text).

3.10.5 Channel depth and paleoslope

Information on grain size, in combination with measurements of bankfull flow depth, was used to make first-order estimates on the local paleoslope of the target channels (Paola and Mohrig, 1996; Long, 2021). Information on paleoslopes is required for paleo-hydrological and -geomorphological analyses of the depocenters (e.g., Castelltort, 2018; Long, 2021) and allow estimates on the paleoelevation of the adjacent mountain range (Schlunegger and Kissling, 2015; Krsnik et al., 2021; Lyster et al., 2021).

Channel depth

Estimates of the water depth *h* during bankfull discharge, the conditions used as reference in this work, are accomplished by using the thicknesses of preserved channel deposits (Bridge, 1985; Paola and Mohrig, 1996; Long, 2021). While this approach works well for single-thread channels, the same task is more complicated for braided river deposits because of the amalgamation of channel fills and gravel bars (Blair and McPherson, 1994, 2009; Harvey et al., 2005). In a braided system, the depth of a channel can be constrained by the height of bordering longitudinal bars (Miall, 1985). Such bars overlay an erosive base and are topped by sand layers, both of which we found recorded in the stratigraphy (e.g., Fig. 3.3). We, therefore, used such constraints to determine the depth of channels during bankfull discharge (Miall, 1976; Bridge, 1985; Paola and Borgman, 1991; Paola and Mohrig, 1996; Long, 2021). Alternatively, bankfull flow depths can be constrained by the height of low-angular cross-beds, as they form at the margin of lateral bars or at the confluence between tributary and main channels (Mohrig et al., 2000; Long, 2021). Yet, the height of these bars only yields minimum estimates for flow depths during bankfull discharge. As reported for preserved gravel bars of braided river systems, either thickness measurements underestimate the *average* water depth by a factor of c. 0.6 to 0.7 (Paola and Borgman, 1991). This would consequently be c. 0.7 to 0.8 if an uncertainty of +10% is added to the field measurements, thereby considering the thickness contribution where the conglomerate beds are decompacted (Kuhlemann et al., 2001; Long, 2021). Therefore, the thickness of gravel bars measured in the field likely reflects the situation during bankfull discharge, which generally exceed the average water depth.

We identified such arrangements in the field and consequently measured the thickness defined by these features at 4 – 6 places at each outcrop. We then took the average as a reference for the channel depth during bankfull flow and considered a decompaction contribution of +10%. To account for potential uncertainties that would yield an under- or overestimation of bankfull conditions (e.g., because of local scours), we considered ±15% uncertainties to the decompacted thickness upon bootstrapping 10^4 values.

The resulting channel depths show an increasing trend toward distal positions for all three fan systems (Fig. S3.5). In the western fan, channel depths of 27 sites increase linearly (r^2 = 0.46) from c. 1 to 3 m (Fig. S3.5a) with an overall fan average of d_{bf} = 1.58 [1.36 – 1.81] m. Similarly, channel depths at the central fan (32 sites) also increase linearly (r^2 = 0.69) down-system from c. 1 to 3 m, with a slightly larger overall average of d_{bf} = 1.91 [1.63 – 2.18] m (Fig. S3.5b). In the eastern fan (14 sites), channel depths increase linearly (r^2 = 0.51) towards distal positions from c. 1.5 to 2.5 m, with an average of d_{bf} = 1.64 [1.41 – 1.87] m. Note that channel depth values at the most distal position display a large scatter (Fig. S3.5c).

Paleoslope

For the calculation of paleoslopes we followed Paola and Mohrig (1996) that based their derivation on a threshold shear stress approach, which they applied to gravel-bed rivers. For this, we followed the approach outlined in section 3.10.3 and solved Eq. (*S3.11*) for channel slope *S:*

$$S = \frac{(1.0 + \varepsilon)\left[\left({}^{\rho_s}/_{\rho_w}\right) - 1\right] D_{50}\, \tau_c{}^*}{d_{bf}} \; [RAD;\ m/m] \qquad Eq.(S3.18).$$

Here, we substituted the dimensionless shear stress τ^* with the critical Shields-parameter τ_c^* because we considered the conditions of initial sediment entrainment (threshold approach), which occurs if $\tau^* = \tau_c^*$ (see also section 3.10.3). For constraining the D_{50} and d_{bf} (decompacted bankfull channel depths; see above), we used the 10^4 values resulting from the bootstrapping. For constraining the other variables, i.e., ε, and τ_c^*, we propagated 10^4 values through a combined bootstrapping and Monte Carlo simulation, solving for *S*. We then report the median along with the 95% confidence interval for each location of all fan systems.

The resulting slopes for all three fan systems reveal a linearly decreasing trend in the down-system direction. The western fan shows a pronounced decrease of *S* from c. 0.50 to 0.10° (c. 0.0087 to 0.0017 m m^{-1}), averaging at *S* = 0.20 [0.15 – 0.28]° (Fig. S3.6a; r^2 = 0.56). The slopes at the central system decrease from c. 0.25 to 0.05° (c. 0.0044 to 0.00087 m m^{-1}), with an average of *S* = 0.16 [0.12 – 0.22]° (Fig. S3.6b; r^2 = 0.46). Similarly, the slopes at the eastern fan reveal a decreasing trend from c. 0.22 to 0.12° (c. 0.0038 to 0.0021 m m^{-1}) with an average around *S* = 0.16 [0.12 – 0.22]° (Fig. S3.6c; r^2 = 0.44).

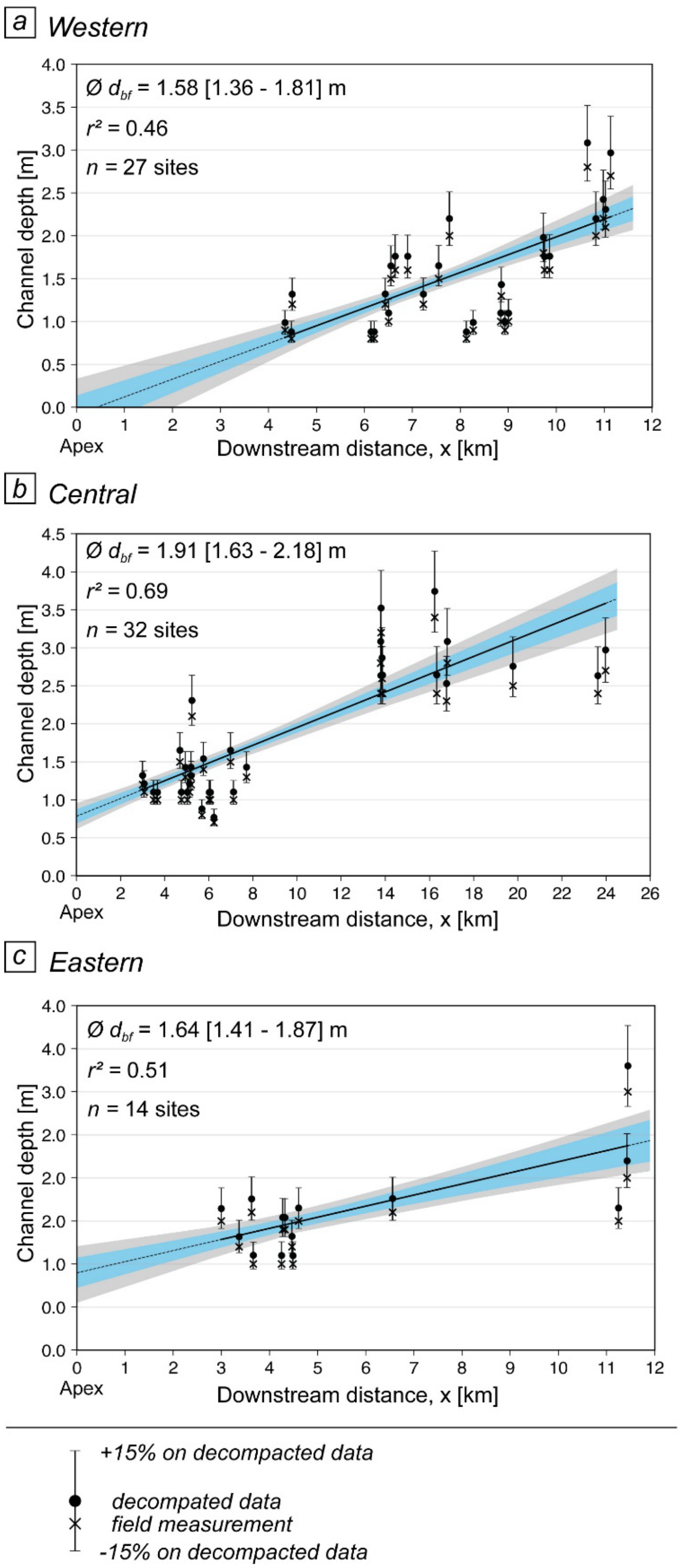

Figure S3.5: Results of channel depth measurements for the ***a)*** western, ***b)*** central and ***c)*** eastern fan systems. The black line reflects the best-fitting linear regression curve, the blue area corresponds to the 95 % CI of the regression analyses, and the grey area corresponds to all possible regression scenarios of 10^4 iterations.

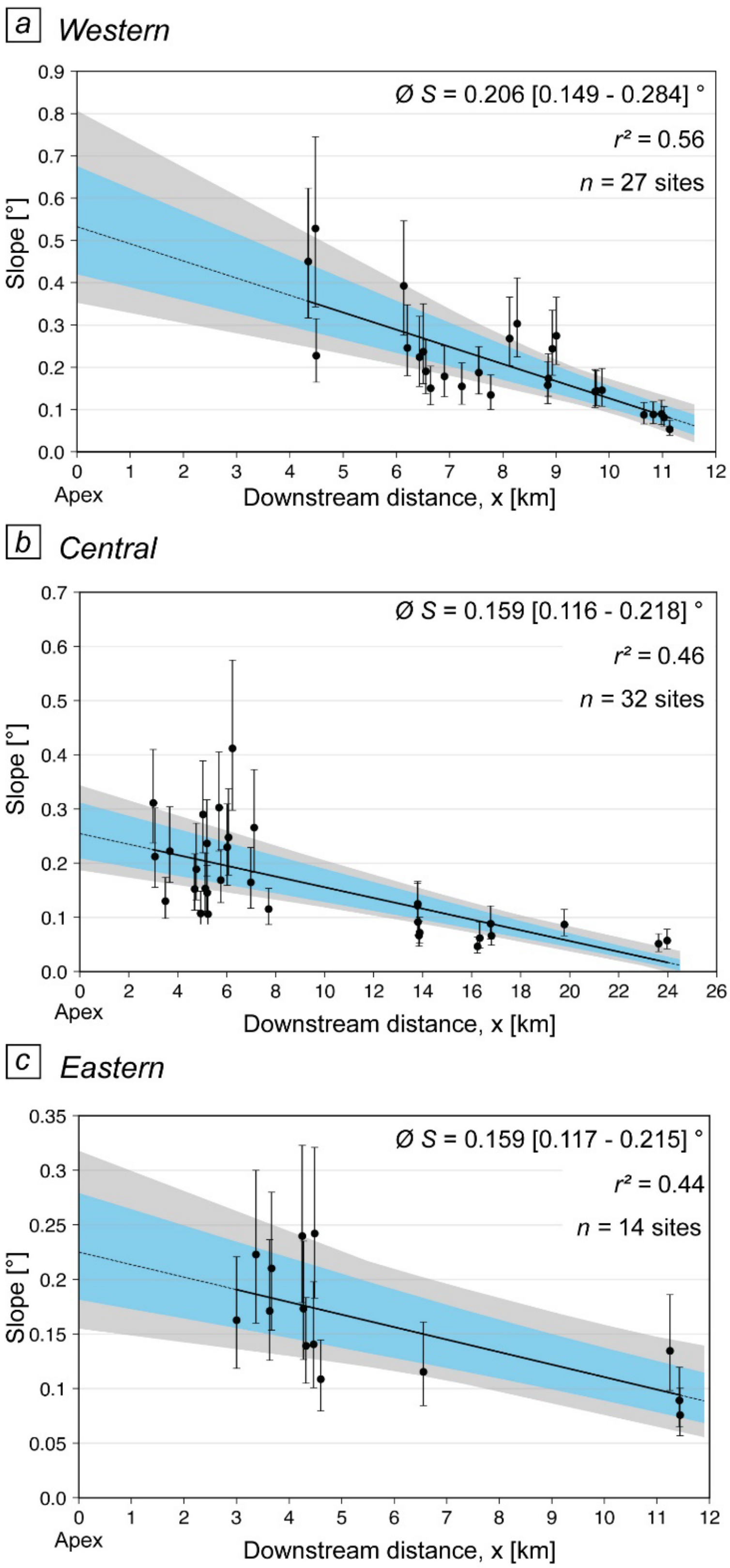

Figure S3.6: Slope calculations for the **a)** western, **b)** central and **c)** eastern fan systems. Error bars denote the 95 % CI of each calculated slope value. The black line reflects the best-fitting linear regression curve, the blue area corresponds to the 95 % CI of the regression analyses, and the grey area corresponds to all possible regression scenarios of 10^4 iterations.

3.10.6 Variables and parameters

Parameter	Description	Value / Unit* / Equation	Key reference
C_1	Downstream partitioning of variance of a gravel supply expressed by its standard deviation	0.60 – 0.90 / [-] / Eq. (3.3; S3.9)	Fedele & Paola, 2007; Duller et al., 2010; Armitage et al., 2011
C_2	Downstream partitioning of variance of a gravel supply expressed by its mean grain size	$C_2 = C_1/C_v$ / [-] / Eq. (3.3; S3.9)	Fedele & Paola, 2007; Duller et al., 2010; Armitage et al., 2011
C_v	Coefficient of variation	$C_v = \sigma/\bar{D}$ / [-] / Eq. (S3.9)	
$\bar{D}$	Mean / Average grain size	[m] / Eq. (3.5; S3.2)	
$D(x^*)$	Spatial distribution of grain size	[m] / Eq. (3.8; S3.1)	Sternberg, 1875
D_A	Input grain size at the apex (x^* = 0)	[m] / Eq. (3.3: 3.8; S3.1)	Sternberg, 1875
D_{50}	Grain size where 50% of the sediment is smaller or equal than this grain size	[m] / Eq. (3.9)	
D_k	Individual grain size value	[m] / Eq. (3.8; S3.1)	
D_m	Modelled grain size	[m] / Eq. (3.3; 3.6; S3.8)	Fedele & Paola, 2007
d_{bf}	Bankfull channel depth	[m] / Eq. (S3.11)	
F_E	Fraction of sediment in excess: F_E = 1: filled; > 1: overfilled; < 1: underfilled basin	[-] / Eq. (3.4)	D'Arcy et al., 2017
f	Fraction of a given sediment size being in the substrate	[-] / Eq. (S3.3)	Fedele & Paola, 2007
g	Earth gravity	9.81 / [m s^{-2}] / Eq. (3.9; S3.16)	
G_S	Dimensionless submerged specific gravity = [(ρ_s / ρ_w) - 1]	1.65 / [-] / Eq. (3.9; S3.12)	
h; h_{bf}	Water depth; during bankfull discharge	[m]	
I_F	Intermittency factor; $I_F = Qs_A^* / Q_b^*$	[-] / Eq. (3.1)	Paola et al., 1992
J	Relative mobility function	[-] / Eq. (*S3.3*)	Fedele & Paola, 2007
L	Total down-system length	[m] / Eq. (3.2)	
p	Fraction of a given sediment size in transport	[-] / Eq. (S3.3)	Fedele & Paola, 2007
q_b^*	Einstein number or dimensionless bedload transport rate	[-] / Eq. (S3.13, S3.14)	Einstein, 1950
Q_b^*	Instantaneous bedload sediment flux per unit channel width (i.e., unit bedload flux or unit capacity)	[m^3 s^{-1} m^{-1}] / Eq. (3.9; S3.16)	Meyer-Peter & Müller, 1948; Einstein, 1950; Wong & Parker, 2006
$Qs^*(x^*)$	Spatial distribution of long-term sediment flux per unit channel width (i.e., unit sediment flux)	[m^3 Myr^{-1} m^{-1}] / Eq. (3.3; S3.6)	Fedele & Paola, 2007

Parameter	Description	Value / Unit* / Equation	Key reference
Qs_A^*	Long-term input sediment flux per unit channel width at the fan's apex (x^* = 0)	[m^3 Myr^{-1} m^{-1}] / Eq. (3.2; 3.4; *S3.6*)	Fedele & Paola, 2007
$r^*(x^*)$	Spatial distribution of subsidence	[m Myr^{-1}] / Eq. (3.2; 3.4; 3.8)	Fedele & Paola, 2007; Duller et al., 2010
$R^*(x^*)$	Spatial distribution of sediment mass	[-] / Eq. (*S3.4*)	Fedele & Paola, 2007
r_A	Subsidence rate at the apex (x^* = 0)	[m Myr^{-1}] / Eq. (3.7)	Fedele & Paola, 2007; Duller et al., 2010
R_h	Hydraulic radius, i.e., d_{bf} for wide rivers	[m]	Tinkler, 1982
S	Paleoslope, channel gradient	RAD [m m^{-1}] / Eq. (S3.18)	Paola & Mohrig, 1996
x	Down-system distance	[m]	
x^*	Normalised down-system distance	[-]	Fedele & Paola, 2007
y^*	Transformation of x^*	[-] / Eq. (3.3; S3.7)	Fedele & Paola, 2007
α	Grain size fining rate / decreasing rate	[m^{-1}] / Eq. (3.8; S3.1)	Sternberg, 1875
β	Subsidence decreasing rate	[m^{-1}] / Eq. (3.7)	Fedele & Paola, 2007; Duller et al., 2010
ε	Correction factor for lateral channel erosion	0.2 – 0.4 / [-] / Eq. (3.9; S3.12)	Parker, 1978; Paola & Mohrig, 1996
λ_p	Sediment porosity	0.3 / [-] / Eq. (3.2; 3.4; S3.6)	Fedele & Paola, 2007
ρ_s	Sediment density	2650 / [kg m^{-3}]	Julien, 2010
ρ_w	Water density	1000 / [kg m^{-3}]	Julien, 2010
σ	Standard deviation of a given grain size; $\sigma(x^*)$ along (normalised) distance	[m] / Eq. (3.3; 3.5; S3.10)	Fedele & Paola, 2007
τ_b	Basal shear stress	[Pa] / Eq. (S3.10)	Julien, 2010
τ^*	Dimensionless shear stress / Shields-stress	[-] / Eq. (3.9; S3.11)	Shields, 1936; Julien, 2010
τ_c^*	Critical dimensionless shear stress / Shields-parameter	0.039 – 0.054 / [-] / Eq. (3.9; S3.12)	Shields, 1936; Julien, 2010
φ_A	Deviation of the input grain size at the apex (x^* = 0)	$\varphi_A = D_A*C_v$, / [m] / Eq. (3.3; S3.9)	D'Arcy et al., 2017
ξ	Similarity variable	[-] / Eq. (3.5; S3.2)	Fedele & Paola, 2007

*Units are reported as used for calculations and might differ from the units expressed in the text and figures.

3.10.7 Bibliography to Appendix A

Allen, P. A., Armitage, J. J., Carter, A., Duller, R. A., Michael, N. A., Sinclair, H. D., et al. (2013). The *Qs* Problem: Sediment volumetric balance of proximal foreland basin systems. Sedimentology 60, pp. 102–130. https://doi.org/10.1111/sed.12015

Allen, P. A., Crampton, S. L., and Sinclair, H. D. (1991). The inception and early evolution of the north Alpine foreland basin, Switzerland. Basin Res. 3, pp. 143–163. https://doi.org/10.1111/j.1365-2117.1991.tb00124.x

Ancey, C. (2020a). Bedload transport: a walk between randomness and determinism. Part 1. The state of the art. J. Hydraul. Res. 58, pp. 1–17. https://doi.org/10.1080/00221686.2019.1702594

Ancey, C. (2020b). Bedload transport: a walk between randomness and determinism. Part 2. Challenges and prospects. J. Hydraul. Res. 58, pp. 18–33. https://doi.org/10.1080/00221686.2019.1702595

Armitage, J. J., Duller, R. A., Whittaker, A. C., and Allen, P. A. (2011). Transformation of tectonic and climatic signals from source to sedimentary archive. Nat. Geosci. 4, pp. 231–235. https://doi.org/10.1038/ngeo1087

Baker, V. R., and Ritter, D. F. (1975). Competence of rivers to transport coarse bedload material. Bull. Geol. Soc. Am. 86, pp. 975–978. https://doi.org/10.1130/0016-7606(1975)86<975:CORTTC>2.0.CO;2

Blair, T. C., and McPherson, J. G. (1994). Alluvial Fan Processes and Forms. Geomorphol. Desert Environ., pp. 354–402. https://doi.org/10.1007/978-94-015-8254-4_14

Blair, T. C., and McPherson, J. G. (2009). “Processes and forms of alluvial fans,” in Geomorphology of Desert Environments, pp. 413–467. https://doi.org/10.1007/978-1-4020-5719-9_14

Bolliger, T. (1998). Age and geographic distribution of the youngest Upper Freshwater Molasse (OSM) of eastern Switzerland. Eclogae Geol. Helv. 91, pp. 321–332. https://doi.org/10.5169/seals-168426

Brewer, C. J., Hampson, G. J., Whittaker, A. C., Roberts, G. G., and Watkins, S. E. (2020). Comparison of methods to estimate sediment flux in ancient sediment routing systems. Earth-Science Rev. 207. https://doi.org/10.1016/j.earscirev.2020.103217

Bridge, J. (1985). Paleochannel Paterns Inferred from alluvial Deposits: A Critical Evaluation. J. Sediment. Petrol. 55, pp. 579–589. https://doi.org/10.1017/CBO9781107415324.004

Brooke, S. A. S., Whittaker, A. C., Armitage, J. J., D’Arcy, M., and Watkins, S. E. (2018). Quantifying Sediment Transport Dynamics on Alluvial Fans From Spatial and Temporal Changes in Grain Size, Death Valley, California. J. Geophys. Res. Earth Surf. 123, pp. 2039–2067. https://doi.org/10.1029/2018JF004622

Bunte, K., Abt, S. R., Swingle, K. W., Cenderelli, D. A., and Schneider, J. M. (2013). Critical Shields values in coarse-bedded steep streams. Water Resour. Res. 49, pp. 7427–7447. https://doi.org/10.1002/2012WR012672.

Castelltort, S. (2018). Empirical relationship between river slope and the elongation of bars in braided rivers: A potential tool for paleoslope analysis from subsurface data. Mar. Pet. Geol. 96, pp. 544–550. https://doi.org/10.1016/j.marpetgeo.2018.05.008

Church, M. (2006). Bed Material Transport and the Morphology of Alluvial River Channels. Annu. Rev. Earth Planet. Sci. 34, pp. 325–354. https://doi.org/10.1146/annurev.earth.33.092203.122721

Church, M., and Kellerhals, R. (1978). On the statistics of grain size variation along a gravel river. Can. J. Earth Sci. 15, pp. 1151–1160. https://doi.org/10.1139/e78-121

D’Arcy, M., Whittaker, A. C., and Roda-Boluda, D. C. (2017). Measuring alluvial fan sensitivity to past climate changes using a self-similarity approach to grain-size fining, Death Valley, California. Sedimentology 64, pp. 388–424. https://doi.org/10.1111/sed.12308

Dade, W. B., and Friend, P. F. (1998). Grain-size, sediment-transport regime, and channel slope in alluvial rivers. J. Geol. 106, pp. 661–675. https://doi.org/10.1086/516052

Duller, R. A., Whittaker, A. C., Fedele, J. J., Whitchurch, A. L., Springett, J., Smithells, R., et al. (2010). From grain size to tectonics. J. Geophys. Res. Earth Surf. 115, pp. 1–19. https://doi.org/10.1029/2009JF001495

Einstein, H. A. (1950). The Bed-Load Function for Sediment Transportation in Open Channel Flows. Soil Conserv. Serv., pp. 1–31.

Engelder, T. M., and Pelletier, J. D. (2013). Autogenic cycles of channelized fluvial and sheet flow and their potential role in driving long-runout gravel progradation in sedimentary basins. Lithosphere 5, pp. 343–354. https://doi.org/10.1130/L274.1

Fedele, J. J., and Paola, C. (2007). Similarity solutions for fluvial sediment fining by selective deposition. J. Geophys. Res. Earth Surf. 112, pp. 1–13. https://doi.org/10.1029/2005JF000409

Füchtbauer, H. (1964). Sedimentpetrographische Untersuchungen in der älteren Molasse nördlich der Alpen. Eclogae Geol. Helv. 57, pp. 157–298. (in German)

Gao, P. (2011). An equation for bed-load transport capacities in gravel-bed rivers. J. Hydrol. 402, pp. 297–305. https://doi.org/10.1016/j.jhydrol.2011.03.025

Garefalakis, P., and Schlunegger, F. (2018). Link between concentrations of sediment flux and deep crustal processes beneath the European Alps. Sci. Rep. https://doi.org/10.1038/s41598-017-17182-8

Gradstein, F. M., Ogg, J. G., Schmitz, M. D., and Ogg, G. M. (2020). Geologic Time Scale 2020. 1390 pp., ISBN: 9780128243602.

Gray, J. R., and Simões, F. J. M. (2008). Estimating Sediment Discharge. Sediment. Eng., pp. 1067–1088. https://doi.org/10.1061/9780784408148.apd

Hantke, R., Letsch, D., Felber, P., Baumeler, A., Heinz, R., Uttinger, J., et al. (2022). Blatt 1152 Ibergeregg. - Geol. Atlas Schweiz 1:25 000, Erläut. 175. (in German)
Available at: www.swisstopo.ch

Harries, R. M., Kirstein, L. A., Whittaker, A. C., Attal, M., and Main, I. (2019). Impact of recycling and lateral sediment input on grain size fining trends—Implications for reconstructing tectonic and climate forcings in ancient sedimentary systems. Basin Res. 31, pp. 866–891. https://doi.org/10.1111/bre.12349

Harvey, A. M., Mather, A. E., and Stokes, M. (2005). Alluvial Fans: Geomorphology, Sedimentology, Dynamics. Geological, 161 pp., ISBN: 1862391890.

Hottinger, L., Matter, A., Nabholz, W., and Schindler, C. (1970). Erläuterungen - Landeskarte 1093 Hörnli - 1970. Erläuterungen Kartenblatt. (in German)
Available at: www.swisstopo.ch

Huang, H. Q. (2010). Reformulation of the bed load equation of Meyer-Peter and Müller in light of the linearity theory for alluvial channel flow. Water Resour. Res. 46, pp. 1–11. https://doi.org/10.1029/2009WR008974

Julien, P. Y. (2010). Erosion and Sedimentation. Cambridge Univ. Press 2, Cambridge, UK. https://doi.org/10.1017/CBO9780511806049

Kälin, D., and Kempf, O. (2009). High-resolution stratigraphy from the continental record of the Middle Miocene Northern Alpine Foreland Basin of Switzerland. Neues Jahrbuch für Geol. und Paläontologie - Abhandlungen 254, pp. 177–235. https://doi.org/10.1127/0077-7749/2009/0010

Kempf, O., Bolliger, T., Kälin, D., Engesser, B., and Matter, A. (1997). "New Magnetostratigraphic Calibration of Early to Middle Miocene Mammal Biozones of the North Alpine Foreland Basin," in Actes du Congrès BIochrom'97, eds. J. Aguilar, S. Legendre, J. Michaux, and B. Mammalienne, pp. 547–561.

Krsnik, E., Methner, K., Campani, M., Botsyun, S., Mutz, S. G., Ehlers, T. A., et al. (2021). Miocene high elevation in the Central Alps. Solid Earth 12, pp. 2615–2631. https://doi.org/10.5194/se-12-2615-2021

Kuhlemann, J., Frisch, W., Dunkl, I., and Székely, B. (2001). Quantifying tectonic versus erosive denudation by the sediment budget: the Miocene core complexes of the Alps. Tectonophysics 330, pp. 1–23. https://doi.org/10.1016/S0040-1951(00)00209-2

Lamb, M. P., Dietrich, W. E., and Venditti, J. G. (2008). Is the critical shields stress for incipient sediment motion dependent on channel-bed slope? J. Geophys. Res. Earth Surf. 113, pp. 1–20. https://doi.org/10.1029/2007JF000831

Long, D. G. F. (2021). Trickling down the paleoslope: an empirical approach to paleohydrology. Earth-Science Rev. 220, 103740. https://doi.org/10.1016/j.earscirev.2021.103740

Lyster, S. J., Whittaker, A. C., Hampson, G. J., Hajek, E. A., Allison, P. A., and Lathrop, B. A. (2021). Reconstructing the morphologies and hydrodynamics of ancient rivers from source to sink: Cretaceous Western Interior Basin, Utah, USA. Sedimentology 68, pp. 2854–2886. https://doi.org/10.1111/sed.12877

Meyer-Peter, E., and Müller, R. (1948). Formulas for Bed-Load Transport. Proc. 2nd Meet. Int. Assoc. Hydraul. Res., pp. 39–64. https://doi.org/1948-06-07

Miall, A. D. (1976). Palaeocurrent and palaeohydrologic analysis of some vertical profiles through a Cretaceous braided stream deposit, Banks Island, Arctic Canada. Sedimentology 23, pp. 459–483.
https://doi.org/10.1111/j.1365-3091.1976.tb00063.x

Miall, A. D. (1985). Architectural-element analysis: A new method of facies analysis applied to fluvial deposits. Earth Sci. Rev. 22, pp. 261–308.
https://doi.org/10.1016/0012-8252(85)90001-7

Mohrig, D., Heller, P. L., and Lyons, W. J. (2000). Interpreting avulsion process from ancient alluvial sequences: Guadalope-Matarranya system (northern Spain) and Wasatch Formation (western Colorado). GSA Bull. 112, pp. 1787–1803.
https://doi.org/10.1130/0016-7606(2000)112<1787:IAPFAA>2.0.CO;2

Müller, E. R., Pitlick, J., and Nelson, J. M. (2005). Variation in the reference Shields stress for bed load transport in gravel-bed streams and rivers. Water Resour. Res. 41, pp. 1–10.
https://doi.org/10.1029/2004WR003692

Paola, C., and Borgman, L. (1991). Reconstructing random topography from preserved stratification. Sedimentology 38, pp. 553–565.
https://doi.org/10.1111/j.1365-3091.1991.tb01008.x

Paola, C., and Mohrig, D. (1996). Palaeohydraulics revisited: Palaeoslope estimation in coarse-grained braided rivers. Basin Res. 8, pp. 243–254.
https://doi.org/10.1046/j.1365-2117.1996.00253.x

Paola, C., and Voller, V. R. (2005). A generalized Exner equation for sediment mass balance. J. Geophys. Res. Earth Surf. 110, pp. 1–8.
https://doi.org/10.1029/2004JF000274

Parker, G. (1978). Self-formed straight rivers with equilibrium banks and mobile bed. Part 2. The gravel river. J. Fluid Mech. 89, pp. 127–146.
https://doi.org/10.1017/S0022112078002505

Parker, G. (1990). Surface-based bedload transport relation for gravel rivers. J. Hydraul. Res. 28, pp. 417–436.
https://doi.org/10.1080/00221689009499058

Parker, G., Wilcock, P. R., Paola, C., Dietrich, W. E., and Pitlick, J. (2007). Physical basis for quasi-universal relations describing bankfull hydraulic geometry of single-thread gravel bed rivers. J. Geophys. Res. Earth Surf. 112, pp. 1–21.
https://doi.org/10.1029/2006JF000549

Parsons, A. J., Michael, N. A., Whittaker, A. C., Duller, R. A., and Allen, P. A. (2012). Grain-size trends reveal the late orogenic tectonic and erosional history of the south-central Pyrenees, Spain. J. Geol. Soc. London. 169, pp. 111–114.
https://doi.org/10.1144/0016-76492011-087

Petit, F., Houbrechts, G., Peeters, A., Hallot, E., Van Campenhout, J., and Denis, A. C. (2015). Dimensionless critical shear stress in gravel-bed rivers. Geomorphology.
https://doi.org/10.1016/j.geomorph.2015.09.008

Pfeiffer, A. M., Finnegan, N. J., and Willenbring, J. K. (2017). Sediment supply controls equilibrium channel geometry in gravel rivers. Proc. Natl. Acad. Sci. U. S. A. 114, pp. 3346–3351.
https://doi.org/10.1073/pnas.1612907114

Recking, A. (2015). Bedload transport in rivers: From the flume to the field.
Available at: https://hal.science/tel-02292527v1

Rice, S. P., and Church, M. (2010). Grain-size sorting within river bars in relation to downstream fining along a wandering channel. Sedimentology 57, pp. 232–251.
https://doi.org/10.1111/j.1365-3091.2009.01108.x

Schlunegger, F., Burbank, D. W., Matter, A., Engesser, B., and Mödden, C. (1996). Magnetostratigraphic calibration of the Oligocence to Middle Miocene (30-15 Ma) mammal biozones and depositional sequences of the Swiss Molasse Basin. Eclogae Geol. Helv. 89, pp. 753–788.
https://doi.org/10.5169/seals-168650

Schlunegger, F., Delunel, R., and Garefalakis, P. (2020). Short communication: Field data reveal that the transport probability of clasts in Peruvian and Swiss streams mainly depends on the sorting of the grains. Earth Surf. Dyn. 8, pp. 717–728.
https://doi.org/10.5194/esurf-8-717-2020

Schlunegger, F., and Garefalakis, P. (2018). Clast imbrication in coarse-grained mountain streams and stratigraphic archives as indicator of deposition in upper flow regime conditions. Earth Surf. Dyn. 6.
https://doi.org/10.5194/esurf-6-743-2018

Schlunegger, F., Jordan, T. E., and Klaper, E. M. (1997a). Controls of erosional denudation in the orogen on foreland basin evolution: The Oligocene central Swiss Molasse Basin as an example. Tectonics 16, pp. 823–840.
https://doi.org/10.1029/97TC01657

Schlunegger, F., and Kissling, E. (2015). Slab rollback orogeny in the Alps and evolution of the Swiss Molasse basin. Nat. Commun. 6, pp. 1–10.
https://doi.org/10.1038/ncomms9605

Schlunegger, F., Matter, A., Burbank, D. W., and Klaper, E. M. (1997b). Magnetostratigraphic constraints on relationships between evolution of the central Swiss Molasse basin and Alpine orogenic events. GSA Bull. 109, pp. 225–241.
https://doi.org/10.1130/0016-7606(1997)109<0225:MCORBE>2.3.CO;2

Schlunegger, F., Matter, A., and Mange, M. A. (1993). Alluvial fan sedimentation and structure of the southern Molasse Basin margin, Lake Thun area, Switzerland. Eclogae Geol. Helv. 86, pp. 717–750.
https://doi.org/10.5169/seals-167260

Sharma, N., Whittaker, A. C., Watkins, S. E., Valero, L., Verité, J., Puigdefàbregas, C., et al. (2023). Water discharge variations control fluvial stratigraphic architecture in the middle Eocene Escanilla formation, Spain. Sci. Rep. 13, 1–14.
https://doi.org/10.1038/s41598-023-33600-6

Shields, A. (1936). Anwendung der Ähnlichkeitsmechanik und der Turbulenzforschung auf die Geschiebebewegung. Preuss. Versuchsanstalt für Wasserbau und Schiffbau 26. (in German)

Sinclair, H. D., and Naylor, M. (2012). Foreland basin subsidence driven by topographic growth versus plate subduction. Bull. Geol. Soc. Am. 124, pp. 368–379.
https://doi.org/10.1130/B30383.1

Sternberg, H. (1875). Untersuchungen über Längen- und Querprofil geschiebeführender Flüsse. Zeitschrift für Bauwes. 25, pp. 483–506. (in German)
Available at: https://digital.zlb.de/viewer/image/15239363_1875/262/

Strasky, S., Schlunegger, F., Hänni, R., Häuselmann, P., Mojon, A., and Schwizer, B. (2022). Blatt 1208 Beatenberg. - Geol. Atlas Schweiz 1:25 000, Erläut. 170-171. (in German)
Available at: www.swisstopo.ch

Stürm, B. (1973). Die Rigi Schüttung - Sedimentpetrographie, Sedimentologie, Palaeogeographie, Tektonik. Unpubl. PhD Thesis, Univ. Bern, 96 pp. (in German)

Tanner, H. J. (1944). Beitrag zur Geologie der Molasse zwischen Ricken und Hörnli. Mitteilungen der Thurgauischen Naturforschenden Gesellschaft 33, pp. 1–108. (in German)

Tinkler, K. J. (1982). Avoiding Error When Using the Manning Equation.

Tinkler, K. J. (1997). Critical flow in rockbed streams with estimated values for Manning's n. Geomorphology.
https://doi.org/10.1016/s0169-555x(97)00011-1

Tucker, G. E., and Slingerland, R. L. (1997). Drainage basin responses to climate change. Water Resour. Res. 33, pp. 2031–2047.
https://doi.org/10.1029/97WR00409

Whittaker, A. C., Duller, R. A., Springett, J., Smithells, R. A., Whitchurch, A. L., and Allen, P. A. (2011). Decoding downstream trends in stratigraphic grain size as a function of tectonic subsidence and sediment supply. pp. 1363–1382.
https://doi.org/10.1130/B30351.1

Wickert, A. D., and Schildgen, T. F. (2019). Long-profile evolution of transport-limited gravel-bed rivers. Earth Surf. Dyn. 7, pp. 17–43.
https://doi.org/10.5194/esurf-7-17-2019

Wilcock, P. R. (1993). Critical shear stress of natural sediments. J. Hydraul. Eng. 119, pp. 491–505.
https://doi.org/10.1061/(ASCE)0733-9429(1993)119:4(491)

Wilcock, P. R., and Crowe, J. C. (2003). Surface-based Transport Model for Mixed-Size Sediment. J. Hydraul. Eng. 129, pp. 120–128.
https://doi.org/10.1061/ASCE0733-94292003129:2120

Wong, M., and Parker, G. (2006). Reanalysis and Correction of Bed-Load Relation of Meyer-Peter and Müller Using Their Own Database. J. Hydraul. Eng. 132, pp. 1159–1168.
https://doi.org/10.1061/(asce)0733-9429(2006)132:11(1159)

Wyss, R., and Hofmann, F. (1999). Molasse im Thurgau. Mitteilungen der Thurgauischen Naturforschenden Gesellschaft 55.
https://doi.org/10.5169/seals-594089

3.11 Appendix B

Appendix B contains tables with the locations of each site of the three proximal-distal sequences and the values for the D_{50} grain size percentile and the channel depth measurements. The coordinates are based on the Swiss coordinate reference system CH1903+ (LV95).

Site	X-Coord. (CH1903+)	Y-Coord. (CH1903+)	Z-Coord. (Altitude m a.s.l.)	D50 [mm]	Distance from Apex [m]	Normalised distance from Apex [-]
73	2621531.5	1173143.8	568.8	105.43	3000.00	0.26
74	2621541.2	1173193.8	576.2	77.70	3018.10	0.26
72	2620537.7	1174070.3	721.8	79.06	4343.65	0.38
71	2620401.8	1174039.9	663.7	55.90	4423.34	0.39
64	2620210.7	1173841.2	586.4	73.48	4449.55	0.39
70	2620333.5	1174023.3	641.2	68.91	4476.01	0.39
69	2620253.0	1173943.9	629	84.50	4490.81	0.39
68	2620227.0	1173951.2	601.3	52.48	4509.55	0.39
67	2620249.0	1174013.0	601.7	71.33	4527.60	0.39
65	2620125.8	1173898.7	601.9	58.72	4558.68	0.40
66	2620186.0	1174004.5	599.4	60.65	4571.23	0.40
63	2619393.6	1174654.1	697.6	66.07	5583.38	0.49
62	2619397.2	1174769.6	716.7	49.75	5657.32	0.49
61	2619401.2	1174889.1	774.5	54.48	5748.80	0.50
60	2618866.2	1174700.7	624.4	48.25	5973.20	0.52
59	2618785.3	1174886.7	646.1	61.76	6155.81	0.54
53	2619000.6	1175134.0	820.5	37.28	6224.86	0.54
58	2618718.0	1175036.2	659.5	54.08	6322.25	0.55
52	2618956.3	1175345.7	840.4	64.29	6419.24	0.56
57	2618678.8	1175113.8	666.9	54.21	6460.82	0.56
51	2618906.8	1175397.6	842.8	51.07	6547.54	0.57
56	2618656.6	1175170.9	676.7	53.16	6591.86	0.57
55	2618628.2	1175247.6	683.5	44.51	6662.94	0.58
54	2618620.4	1175308.3	692.9	54.64	6711.24	0.59
50	2618763.4	1175460.6	836.2	49.54	6766.76	0.59
49	2618749.4	1175502.1	837.1	46.78	6804.05	0.59
48	2618625.8	1175728.4	813.3	56.05	7036.45	0.61
47	2618606.6	1175748.6	814	54.67	7063.18	0.62
46	2618348.4	1175686.0	747	54.83	7177.56	0.63
39	2618127.0	1175747.1	637.2	66.63	7334.64	0.64
43	2618443.8	1176096.5	713.3	36.21	7395.68	0.64
37	2618134.4	1176007.6	654.9	58.23	7533.74	0.66
42	2618420.2	1176081.6	736.6	41.78	7408.80	0.65
45	2618262.0	1175950.3	743.9	48.42	7422.95	0.65
41	2618396.2	1176079.1	734.5	49.65	7425.14	0.65
40	2618347.0	1176035.3	756.1	44.05	7434.59	0.65
44	2618450.6	1176148.7	716.7	50.54	7443.12	0.65
38	2618106.7	1175940.7	649.4	56.58	7503.68	0.65
35	2618172.8	1176094.7	692.7	55.42	7581.37	0.66
34	2618281.4	1176208.1	745.3	44.31	7607.97	0.66
36	2618127.4	1176075.1	683.6	40.66	7625.16	0.66
33	2618281.4	1176245.1	752.1	49.65	7666.52	0.67
32	2618059.9	1176177.2	748.4	54.00	7765.58	0.68
31	2617740.5	1176207.3	740.5	52.68	7987.64	0.70

Table B.4.1: Locations of sites and grain size values (D50) of western fan (Thun Lakeside / Lake Thun section).

Site	X-Coord. (CH1903+)	Y-Coord. (CH1903+)	Z-Coord. (Altitude m a.s.l.)	D50 [mm]	Distance from Apex [m]	Normalised distance from Apex [-]
28	2617389.5	1176420.8	699.2	40.98	8343.77	0.73
29	2617351.3	1176462.3	656.8	71.59	8384.58	0.73
27	2617426.2	1176527.2	689.7	76.87	8397.80	0.73
30	2617343.5	1176485.8	659.6	53.14	8410.43	0.73
26	2617327.2	1176536.2	693.1	50.77	8466.11	0.74
25	2617297.0	1176544.9	693.5	52.67	8490.66	0.74
24	2616982.6	1177055.2	757.5	31.09	9066.17	0.79
23	2617025.6	1177090.7	772.3	43.45	9076.19	0.79
22	2616995.4	1177164.8	776.8	43.38	9151.26	0.80
21	2616941.0	1177217.2	788.7	53.23	9224.81	0.80
20	2616855	1177274.2	795.1	38.06	9316.84	0.81
19	2616786.2	1177380.6	809.5	40.03	9440.80	0.82
15	2616398.5	1177854.3	623.4	48.93	9952.61	0.87
14	2616328.9	1177836.5	629.8	43.94	9977.89	0.87
17	2616611.0	1178106.5	686	50.89	10057.24	0.88
16	2616493.1	1178059.7	684.3	44.07	10082.90	0.88
18	2616683.4	1178319.2	780.8	50.82	10216.73	0.89
7	2615645.0	1178465.6	753.3	47.63	10872.05	0.95
12	2615462.9	1178479.2	692.9	33.44	10959.49	0.96
11	2615452.4	1178551.7	686.1	32.46	11019.07	0.96
6	2615534.0	1178621.3	740.8	33.56	11049.53	0.96
5	2615524.0	1178679.3	736	40.23	11098.26	0.97
10	2615392.4	1178710.4	673.6	28.76	11171.97	0.97
4	2615449.9	1178767.8	731	38.26	11206.60	0.98
3	2615438.9	1178820.8	734.3	32.82	11254.70	0.98
9	2615298.6	1178824.3	658.7	36.22	11307.92	0.99
2	2615389.0	1178926.8	728.8	27.74	11364.26	0.99
8	2615267.6	1178864.3	653	42.53	11379.94	0.99
1	2615411.3	1179048.8	719.4	27.95	11469.90	1.00

Table B.4.1 (continued): Locations of sites and grain size values (D_{50}) of western fan (Thun Lakeside / Lake Thun section).

Site	X-Coord. (CH1903+)	Y-Coord. (CH1903+)	Z-Coord. (Altitude m a.s.l.)	Channel depth [m]	Distance from Apex [m]	Normalised distance from Apex [-]
72	2620379.5	1173845.3	721.8	0.90	4343.65	0.39
69	2620249.6	1173939.2	629	0.80	4476.49	0.40
68	2620229.1	1173954.1	601.3	1.20	4495.23	0.40
59	2618913.1	1175028.9	646.1	0.80	6137.19	0.55
53	2618909.3	1175032.4	820.5	0.80	6206.24	0.56
56	2618704.5	1175222.4	676.7	1.20	6433.83	0.58
55	2618652.3	1175272.6	683.5	1.00	6504.91	0.58
54	2618617.9	1175305.7	692.9	1.50	6553.21	0.59
49	2618588.0	1175334.4	837.1	1.60	6641.58	0.60
47	2618388.9	1175530.0	814	1.60	6900.69	0.62
43	2618126.2	1175798.6	713.3	1.20	7228.58	0.65
32	2617904.6	1176036.4	748.4	1.50	7548.09	0.68
31	2617746.1	1176212.2	740.5	2.00	7770.14	0.70
28	2617491.5	1176507.1	699.2	0.80	8126.27	0.73
25	2617393.6	1176623.9	693.5	0.90	8268.59	0.74
24	2617046.1	1177098.6	757.5	1.00	8844.10	0.79
23	2617043.3	1177102.8	772.3	1.30	8854.12	0.80
22	2616999.1	1177167.3	776.8	0.90	8929.19	0.80
21	2616957.4	1177228.4	788.7	1.00	9002.74	0.81
15	2616487.9	1177915.4	623.4	1.80	9730.11	0.87
14	2616474.0	1177935.7	629.8	1.60	9755.39	0.88
16	2616422.3	1178011.3	684.3	1.60	9860.23	0.89
7	2615963.3	1178683.1	753.3	2.80	10648.51	0.96
6	2615855.4	1178840.9	740.8	2.00	10824.09	0.97
4	2615760.4	1178980.0	731	2.20	10979.14	0.99
3	2615732.2	1179021.2	734.3	2.10	11027.24	0.99
2	2615666.9	1179116.7	728.8	2.70	11134.15	1.00

Table B.4.2: Locations of sites and channel depths of western fan (Thun Lakeside / Lake Thun section).

Section	Site	X-Coord. (CH1903+)	Y-Coord. (CH1903+)	Z-Coord. (Altitude m a.s.l.)	D50 [mm]	Distance from Apex [m]	Normalised distance from Apex [-]
Rigi	117	2680880.0	1208486.5	1475.40	72.20	3000.00	0.09
	110	2680597.0	1208479.5	1433.40	43.81	3067.52	0.10
	111	2680374.0	1208711.5	1455.80	24.80	3490.63	0.11
	118	2681096.0	1208782.5	1544.00	48.54	3525.31	0.11
	119	2680915.0	1208843.5	1534.10	42.36	3678.80	0.12
	105	2680221.0	1209506.5	1463.30	43.86	4690.42	0.15
	115	2680915.0	1209416.5	1511.90	35.67	4760.26	0.15
	96	2679439.0	1209858.0	1344.80	26.93	4936.65	0.16
	114	2680950.0	1209555.5	1507.10	54.90	5034.13	0.16
	102	2679469.0	1209984.5	1446.40	32.43	5129.05	0.16
	116	2680828.0	1209664.5	1500.40	59.31	5191.21	0.16
	101	2679433.0	1210042.5	1459.50	34.34	5202.32	0.16
	87	2679172.0	1210116.5	1353.00	44.09	5235.20	0.17
	90	2679044.0	1210344.0	1425.00	52.54	5450.35	0.17
	95	2678738.0	1210675.5	1457.40	46.97	5685.21	0.18
	99	2678785.0	1210679.5	1483.20	39.81	5710.65	0.18
	82	2678509.0	1210843.5	1450.00	45.08	5761.69	0.18
	98	2678707.0	1210769.5	1492.50	37.24	5776.35	0.18
	67	2678324.0	1211191.5	1590.90	45.11	6026.71	0.19
	76	2679200.0	1210867.5	1406.50	48.16	6081.36	0.19
	73	2679192.0	1211042.5	1366.70	55.40	6240.15	0.20
	53	2679414.0	1211703.5	1580.60	48.54	6989.52	0.22
	52	2679183.5	1212011.5	1678.60	51.91	7129.77	0.22
	51	2679306.0	1212472.5	1502.30	31.50	7531.99	0.24
	49	2679537.0	1212535.5	1545.20	29.03	7720.78	0.24

Table B.4.3: Locations of sites and grain size values (D_{50}) of central fan (Rigi section).

Section	Site	X-Coord. (CH1903+)	Y-Coord. (CH1903+)	Z-Coord. (Altitude m a.s.l.)	D50 [mm]	Distance from Apex [m]	Normalised distance from Apex [-]
Rossberg	7	2685180.5	1214980.0	1511.80	42.88	13640.30	0.43
	8	2685238.0	1215022.0	1522.60	43.43	13702.25	0.43
	1	2685422.0	1214216.0	1137.80	38.92	13857.68	0.44
	4	2685402.0	1214495.0	1254.10	64.92	13897.04	0.44
	15	2685543.0	1213649.5	989.60	38.17	13987.72	0.44
	2	2685438.0	1214310.0	1171.30	36.54	14048.46	0.44
	5	2685394.0	1214588.5	1295.70	57.33	14090.33	0.44
	14	2685542.0	1213701.0	1011.70	26.85	14187.69	0.45
	6	2685387.0	1214632.5	1315.50	58.09	14291.72	0.45
	3	2685431.0	1214411.0	1215.00	33.02	14329.11	0.45
	16	2685543.5	1213775.0	1029.60	44.00	14395.12	0.45
	9	2685474.0	1214234.0	1156.30	28.27	14436.68	0.46
	12	2685416.0	1214743.0	1369.70	34.25	14505.34	0.46
	13	2685387.0	1214940.5	1459.00	32.66	14534.85	0.46
	10	2685498.0	1214344.0	1206.20	44.04	14626.00	0.46
	11	2685463.5	1214636.0	1333.60	50.18	14667.01	0.46
	27	2685637.0	1214164.0	1198.30	35.86	14784.21	0.47
	22	2685788.0	1214743.0	1376.60	61.77	15018.24	0.47
	20	2685820.0	1214686.0	1361.20	50.90	15041.53	0.47
	21	2685805.0	1214795.0	1401.70	55.58	15054.63	0.48
	19	2685840.0	1214723.0	1374.80	40.78	15080.42	0.48
	18	2685869.0	1214776.0	1397.00	40.64	15116.48	0.48
	23	2686107.0	1214592.0	1302.30	44.03	15328.75	0.48
	26	2686205.0	1214267.0	1216.00	51.63	15383.48	0.49
	24	2686178.0	1214474.0	1274.70	49.27	15402.93	0.49
	25	2686400.0	1214382.0	1238.40	35.61	15604.43	0.49
	007	2687178.6	1214876.1	1302.80	34.58	16455.54	0.52
	006	2687372.9	1215048.2	1329.30	30.01	16678.26	0.53
	28	2687602.0	1214487.0	1132.10	38.20	16817.51	0.53
	29	2687871.0	1214394.0	1082.10	30.21	17056.44	0.54
	001	2687691.8	1215184.9	1320.00	52.87	17136.13	0.54
	002	2687677.9	1215313.1	1363.30	27.83	17154.54	0.54
	003	2687691.0	1215352.5	1352.90	30.65	17177.53	0.54
	004	2688050.8	1215651.3	1424.90	39.74	17599.56	0.56
	005	2688076.3	1215677.5	1429.30	36.08	17630.21	0.56

Table B.4.3 (continued): Locations of sites and grain size values (D_{50}) of central fan (Rossberg section).

Section	Site	X-Coord. (CH1903+)	Y-Coord. (CH1903+)	Z-Coord. (Altitude m a.s.l.)	D50 [mm]	Distance from Apex [m]	Normalised distance from Apex [-]
Sattel	30	2689755.5	1215387.5	868.70	31.78	19239.34	0.61
	31	2689809.0	1215449.5	859.00	35.03	19308.61	0.61
	32	2689853.5	1215596.5	864.80	35.47	19391.57	0.61
	33	2689854.0	1215666.5	873.70	39.77	19410.99	0.61
	34	2690468.5	1215740.0	793.40	33.83	20028.60	0.63
	35	2690524.5	1215899.0	787.40	21.45	20129.15	0.64
	36	2690648.5	1216003.0	776.60	34.99	20278.68	0.64
	39	2690888.5	1215271.5	804.30	39.23	20293.43	0.64
	37	2690701.0	1216103.0	770.60	35.06	20369.38	0.64
	38	2690999.5	1215441.5	815.60	34.89	20445.56	0.65
	40	2690853.5	1216084.0	802.40	43.72	20507.46	0.65
	45	2690896.0	1216327.0	790.80	42.50	20623.95	0.65
	41	2690965.0	1216188.0	820.60	29.07	20646.50	0.65
	42	2690998.0	1216236.5	829.70	44.62	20692.27	0.65
	44	2691223.0	1216488.0	870.40	36.97	20991.23	0.66
	43	2691325.5	1216497.5	860.40	33.47	21091.68	0.67
	46	2691643.0	1216994.5	838.10	38.21	21554.57	0.68
	47	2691701.0	1217120.0	892.90	38.26	21665.89	0.68
Einsiedeln	010	2694041.4	1218105.2	967.80	26.45	24251.40	0.77
	008	2694252.9	1218139.2	1005.90	24.23	24475.99	0.77
	009	2694547.9	1218332.3	1093.90	30.63	24821.52	0.78
	011	2696588.8	1218297.5	1211.70	30.80	26680.72	0.84
	48	2698276.0	1218342.0	918.70	38.29	28263.37	0.89
	049	2701361.0	1219875.5	892.70	25.49	31691.79	1.00

Table B.4.3 (continued): Locations of sites and grain size values (D_{50}) of central fan (Sattel and Einsiedeln sections).

Section	Site	X-Coord. (CH1903+)	Y-Coord. (CH1903+)	Z-Coord. (Altitude m a.s.l.)	Channel depth [m]	Distance from Apex [m]	Normalised distance from Apex [-]
Rigi	117	2678482.6	1208014.1	1475.4	1.20	3000	0.09
	110	2678466.9	1208097.9	1433.4	1.10	3067.5231	0.10
	111	2678408.4	1208532.4	1455.8	1.00	3490.6261	0.11
	119	2678395.9	1208701.5	1534.1	1.00	3676.1668	0.12
	105	2678448.0	1209776.5	1463.3	1.50	4687.7889	0.15
	115	2678457.3	1209834.3	1511.9	1.00	4757.6204	0.15
	96	2678498.5	1210051.5	1344.8	1.30	4934.0159	0.16
	114	2678509.5	1210101.8	1507.1	1.00	5031.4993	0.16
	102	2678535.0	1210210.6	1446.4	1.10	5126.4105	0.16
	116	2678547.0	1210258.6	1500.4	1.30	5188.5786	0.16
	101	2678550.6	1210272.3	1459.5	1.21	5199.6805	0.16
	87	2678552.1	1210278.0	1353	2.10	5232.5692	0.17
	95	2678680.5	1210695.9	1457.4	0.77	5682.0918	0.18
	82	2678707.1	1210769.3	1450	1.40	5756.7529	0.18
	67	2678793.8	1210987.1	1590.9	1.00	6017.2775	0.19
	76	2678814.7	1211035.1	1406.5	1.00	6071.9225	0.19
	73	2678885.0	1211188.9	1366.7	0.70	6230.7166	0.20
	53	2679242.2	1211817.3	1580.6	1.50	6980.4876	0.22
	52	2679312.4	1211919.9	1678.6	1.00	7120.3431	0.22
	49	2679690.8	1212395.5	1545.2	1.30	7709.7528	0.24
Rossberg	4	2685418.2	1214397.7	1254.1	2.80	13782.477	0.43
	5	2685425.6	1214399.0	1295.7	2.40	13796.098	0.44
	6	2685425.9	1214399.0	1315.5	3.20	13802.774	0.44
	12	2685472.0	1214406.7	1369.7	2.60	13846.431	0.44
	13	2685475.8	1214407.3	1459	2.40	13875.934	0.44
	29	2687758.8	1214868.7	1082.1	3.40	16233.659	0.51
	002	2687781.7	1214874.1	1363.3	2.40	16326.125	0.52
	004	2688221.9	1214978.3	1424.9	2.30	16770.685	0.53
	005	2688252.1	1214986.0	1429.3	2.80	16801.331	0.53
	45	2691070.6	1215793.3	790.8	2.50	19781.984	0.62
	008	2694681.7	1217171.0	1005.9	2.40	23629.269	0.75
	009	2694999.8	1217311.8	1093.9	2.70	23974.793	0.76

Table B.4.4: Locations of sites and channel depths of central fan (Rigi and Rossberg sections).

Section	Site	X-Coord. (CH1903+)	Y-Coord. (CH1903+)	Z-Coord. (Altitude m a.s.l.)	D50 [mm]	Distance from Apex (m)	Normalised distance from Apex [-]
Töss	54	2714667.9	1239456.0	1025.40	47.10	3000.00	0.25
	55	2715099.5	1239592.3	1089.30	47.22	3032.62	0.25
	53	2714581.0	1239516.8	1003.20	42.30	3078.78	0.26
	50	2714683.6	1239571.8	982.50	41.53	3107.31	0.26
	46	2714811.6	1239627.8	972.70	46.73	3131.14	0.26
	51	2714806.6	1239688.8	972.40	46.29	3191.55	0.27
	44	2714295.8	1239791.4	958.60	48.70	3433.28	0.29
	48	2714931.6	1240027.4	965.60	51.99	3500.88	0.29
	45	2714249.6	1239924.0	952.80	37.05	3572.98	0.30
	49	2715086.6	1240217.4	1010.40	42.34	3646.89	0.30
	32	2716905.8	1240697.2	866.60	42.33	3648.44	0.30
	33	2714215.6	1240008.4	951.30	49.15	3665.78	0.31
	42	2715312.8	1240322.0	978.50	60.22	3692.39	0.31
	34	2714251.2	1240117.4	947.30	52.90	3762.04	0.31
	29	2716234.0	1240676.4	843.30	41.58	3797.50	0.32
	35	2714233.2	1240289.8	946.00	45.34	3933.25	0.33
	25	2716039.0	1240772.4	840.40	39.87	3939.60	0.33
	31	2714410.2	1240363.8	856.00	33.49	3957.05	0.33
	27	2714485.4	1240619.4	844.20	43.73	4184.78	0.35
	26	2714504.4	1240684.4	843.70	43.10	4242.80	0.35
	28	2715654.2	1241018.4	821.40	37.33	4274.16	0.36
	24	2715552.8	1241000.4	842.50	36.08	4283.11	0.36
	23	2714883.8	1240881.4	826.30	36.79	4344.01	0.36
	36	2714186.4	1240722.4	944.50	46.15	4383.05	0.36
	38	2714416.0	1240811.2	943.60	46.85	4406.56	0.37
	20	2715414.8	1241134.8	814.20	37.18	4444.29	0.37
	39	2714498.2	1240885.2	942.50	37.79	4455.64	0.37
	18	2715007.8	1241046.8	811.90	42.18	4469.39	0.37
	40	2714769.8	1240998.2	943.00	41.54	4491.22	0.37
	19	2715371.2	1241170.8	814.10	34.01	4492.38	0.37
	17	2715063.8	1241199.8	805.60	32.70	4602.91	0.38
	15	2715185.8	1241252.8	806.60	46.93	4621.04	0.38
	41	2714858.8	1241201.2	944.20	46.83	4664.19	0.39
	16	2715004.0	1241325.2	797.20	32.06	4739.46	0.39
	13	2714958.8	1241582.4	794.10	40.96	4999.06	0.42
	14	2714843.0	1241834.4	787.40	36.91	5276.07	0.44
	12	2714689.0	1241931.4	784.20	32.99	5412.95	0.45
	11	2714597.2	1241984.2	776.80	32.17	5489.55	0.46
	10	2714477.2	1242125.2	776.00	35.75	5658.90	0.47

Table B.4.5: Locations of sites and grain size values (D_{50}) of eastern fan (Töss section).

Section	Site	X-Coord. (CH1903+)	Y-Coord. (CH1903+)	Z-Coord. (Altitude m a.s.l.)	D50 [mm]	Distance from Apex (m)	Normalised distance from Apex [-]
Töss	9	2714154.0	1242538.2	753.40	34.39	6146.16	0.51
	8	2714137.0	1242629.2	753.90	31.66	6249.44	0.52
	7	2713901.0	1242992.4	746.10	28.85	6666.60	0.55
	2	2713900.0	1243019.4	745.50	35.40	6692.60	0.56
	6	2713892.0	1243185.4	742.60	44.93	6853.03	0.57
	5	2713863.2	1243216.0	733.70	42.61	6890.61	0.57
	3	2713797.0	1243751.2	754.80	35.67	7432.01	0.62
Hörnli	1	2712190.5	1247131.7	707.50	48.34	11212.87	0.93
	2	2712179.0	1247310.7	729.30	38.53	11383.15	0.95
	14	2713349.0	1247816.8	995.10	38.06	11409.06	0.95
	3	2712280.0	1247485.2	743.20	42.59	11506.04	0.96
	11	2713305.0	1247953.8	936.60	30.51	11550.60	0.96
	5	2712932.5	1247815.3	805.30	34.44	11561.89	0.96
	6	2713200.5	1247941.3	868.70	44.99	11577.19	0.96
	7	2712820.0	1247831.3	792.70	32.54	11619.52	0.97
	9	2713071.0	1248038.3	905.70	36.73	11717.67	0.98
	4	2712644.0	1247878.3	778.30	37.04	11730.17	0.98
	10	2713200.5	1248116.8	907.20	33.76	11740.59	0.98
	12	2713086.5	1248253.3	982.20	35.75	11907.34	0.99
	8	2712740.0	1248165.8	918.50	30.26	11963.88	1.00
	15	2713699.0	1248641.0	938.70	42.87	12015.85	1.00

Table B.4.5 (continued): Locations of sites and grain size values (D_{50}) of eastern fan (Töss and Hörnli sections).

Section	Site	X-Coord. (CH1903+)	Y-Coord. (CH1903+)	Z-Coord. (Altitude m a.s.l.)	Channel depth (m)	Distance from Apex (m)	Normalised distance from Apex
Töss	46	2715591.9	1239817.5	967.50	1.50	3131.14	0.26
	48	2715502.5	1240176.8	960.50	1.20	3500.88	0.29
	34	2715436.9	1240427.6	949.10	1.60	3762.04	0.31
	29	2715427.0	1240465.3	838.60	1.00	3797.50	0.32
	36	2715278.5	1241028.4	951.10	1.00	4383.05	0.36
	38	2715272.1	1241051.1	930.70	1.40	4406.56	0.37
	39	2715258.9	1241098.4	940.40	1.40	4455.64	0.37
	17	2715218.3	1241243.1	817.60	1.20	4602.91	0.38
	15	2715213.4	1241260.5	802.50	1.00	4621.04	0.38
	16	2715181.4	1241374.9	794.70	1.50	4739.46	0.39
	2	2714620.7	1243248.6	739.30	1.60	6692.60	0.56
Hörnli	2	2712999.7	1247652.7	734.70	1.50	11383.15	0.95
	5	2712932.0	1247815.1	794.80	2.00	11561.89	0.96
	6	2712927.0	1247827.3	863.40	3.00	11577.19	0.96

Table B.4.6: Locations of sites and channel depths of eastern fan (Töss and Hörnli sections).

4.

Trends of grain size and relative mobility of Oligo-Miocene megafan deposits in the Swiss Molasse

Philippos Garefalakis*

* University of Bern, Institute of Geological Sciences, Baltzerstrasse 1+3, 3012 Bern, Switzerland

The following text is status 11 October 2023. The modified version is published in the Journal of Sedimentary Research, 23 May 2025. The authors of the published article are: Philippos Garefalakis; Fritz Schlunegger; Ariel Henrique do Prado; David Mair and Alexander C. Whittaker.

DOI: https://doi.org/10.2110/jsr.2024.058

Abstract

The Swiss Molasse Basin, situated north to the Central European Alps, documents the tectono-geomorphological evolution of both, the foreland basin and the adjacent mountain belt. In this study, we analysed grain size data preserved in long-term records of coarse-grained stratigraphic sections in the Swiss Molasse, and we explored these regarding the competence of the paleostreams to transfer the supplied material, expressed as the relative mobility function J.

We applied the concept of self-similarity and relative mobility to this dataset through calculating the self-similarity variable ξ, which corresponds to a normalisation of the grain size data, and we estimated the critical grain size that is likely in transport or preferentially stored in the substrate (i.e., the values for the relative mobility function solved for the case where $J = 1$). Because tectonic processes in the source area, sediment supply and climate conditions significantly changed during the time conglomerate sedimentation occurred, we anticipated large differences in grain size through time.

We find that the values of the D_{50} and D_{84} grain size percentiles scatter around an average of 40 and 80 mm, respectively, and that they do not show statistically significant shifts through time. In addition, a statistical analysis of the underlying grain size distributions GSDs of all analysed sections (a total of 15, and c. 50’000 measured grains) revealed that the GSDs are similar to each other, and they follow a normal distribution after the data was normalised thereby applying the concept of the self-similarity. Finally, the results of the solutions for the relative mobility function for $J = 1$ revealed that the rivers feeding the fans preferentially entrained particles with grain sizes smaller than 12 mm, whereas coarser-grained material was preferentially deposited on the fan.

We then related the grain size values with the tectonic evolution in the Alpine hinterland, the supply rates of the sediment to the basin, and the climatic conditions at the time the material was deposited. This comparison did not disclose obvious correlations at the scale of the basin. This suggests that grain size datasets are not fully conclusive for inferring shifts in the mechanisms driving the evolution of the Alps and the Molasse basin at the large scale, but they do record the fluvial dynamics on the fans such as selective deposition and entrainment.

4.1 Introduction

Alluvial fans, forming at the tip of an evolving mountain range, and their sedimentary deposits made up of coarse-grained fluvial material, have been widely recognised as recorders of the tectono-geomorphological and climatic conditions in the source areas as well as in the sedimentary basin (Duller et al., 2010; Jerolmack and Paola, 2010; Armitage et al., 2011; Whittaker, 2012; Hajek and Straub, 2017). The size and shape of alluvial fans is controlled by allogenic and autogenic processes, which in turn also influence the built-up of the resulting fluvial stratigraphic successions (Harvey et al., 2005; Glotzbach et al., 2010; Ventra and Nichols, 2014). Changes in the allo- and autogenic driving mechanisms exert a control on the sediment transport dynamics and particularly on water- and sediment-fluxes, which not only influence the large-scale architecture of the adjacent foreland basin, but also the alluvial fan morphometry (DeCelles and Giles, 1996; Whipple et al., 1998; Schlunegger and Castelltort, 2016). Amongst the various parameters, the size of grains and the underlying grain size distribution (GSD) are considered as ideal recorders of these sediment transport dynamics (Paola et al., 1992; Parker et al., 2007; Allen et al., 2013) and thus serve as indicators for the underlying environmental conditions (Tucker and Slingerland, 1997; Wainwright et al., 2015; Romans et al., 2016; Ventra and Clarke, 2018). The related concepts are partly based on results of flume experiments (Meyer-Peter and Müller, 1948; Paola and Mohrig, 1996; Wong and Parker, 2006) and that were applied to alluvial fan stratigraphies. As such, they have offered a simple but effective way to estimate paleo-hydraulics based solely on grain size datasets (Whittaker et al., 2011; Litty et al., 2016; Schlunegger and Garefalakis, 2018). This is also the case for the coarse-grained fluvial deposits in the Swiss Molasse Basin (SMB), situated north to the Central Alps (Fig. 4.1), where alluvial fans have been intensively explored from various perspectives, including estimates of sediment supply and transport dynamics. For instance, sediment fluxes have been established at both the scale of the entire SMB (Hay et al., 1992; Schlunegger, 1999; Kuhlemann, 2000; Kuhlemann et al., 2001; Schlunegger et al., 2001) and at that of individual dispersal systems (Garefalakis et al., 2023b, submitted). In the same sense, stratigraphic trends, changes in the stacking pattern of individual sections (Allen et al., 1991; Sissingh, 1997; Schlunegger and Kissling, 2022) together with shifts in grain sizes, both at the basin and the local scales (Kempf, 1998; Schlunegger and Castelltort, 2016; Garefalakis and Schlunegger, 2018), have been linked to orogenic processes at the Alpine front and in the Central Alps. However, we lack a holistic view on these processes, which particularly includes information on how changes in the GSDs are linked to the evolution of the Alpine hinterland from a tectonic and climatic perspective. One way to accomplish this is by applying the concept of relative mobility (Fedele and Paola, 2007). The relative mobility of grains can be considered as a quantitative measure for the sediment transport dynamics of a fluvial system (Fedele and Paola, 2007; D'Arcy et al., 2017; Brooke et al., 2018; Harries et al., 2018), and such data is considered to record the combined effect of a tectonic and climatic driving force, both operating at local and regional scales. The related concepts are deviated from the self-similar grain size fining model (section 4.3), and base on the principle where selective deposition or transportation of grains with a particular size results in the built up of stratigraphic successions with distinct characteristics (Fedele and Paola, 2007; Duller et al., 2010).

Fedele and Paola (2007) defined the relative mobility function J as the ratio between the fraction of material that is in transport p, and the fraction in the substrate f, both for a given GSD:

$$J = {}^{p}/_{f} \ [-] \qquad Eq. (4.1).$$

Thus, for the case of $J = 1$, a specific grain size has the same frequency in both underlying GSDs of p and f (D'Arcy et al., 2017; Brooke et al., 2018; Harries et al., 2018). These frequencies of the GSDs can be assumed to represent the probability of a given grain size that is, for $J = 1$, both in transport and stored in the substrate at the same time (Armitage et al., 2011; Whittaker et al., 2011; Brooke et al., 2018). Consequently, and in a practical sense, in case that $J > 1$, the probability of transport occurrence of the same sediment particle is higher; however, if $J < 1$, the probability of deposition and storage exceeds that of transport (more details in section 4.3).

In this study, we applied the concept of relative mobility to 15 stratigraphic sections (section 4.2.2) made up of alluvial fan deposits encountered in the SMB (Fig. 4.1). The analysed sections are located along the thrust front of the Central Alps of Switzerland and cover the time span between c. 31 and 13 Ma. We particularly aimed at estimating how the relative mobility changed through time and space. In doing so, we established a database where the size of c. 50 000 grains was individually measured. We statistically analysed the GSDs determined from these deposits for their self-similar behaviour and modelled the relative mobility (section 4.3) at the scale of an entire stratigraphic section and thus of an individual dispersal system. In this context, we are particularly interested on how capable, in terms of relative mobility, the dispersal systems on these alluvial fans were to entrain a given grain size through time. We will then link our outcomes to the climatic and tectonic evolution of the Central Alps and the SMB.

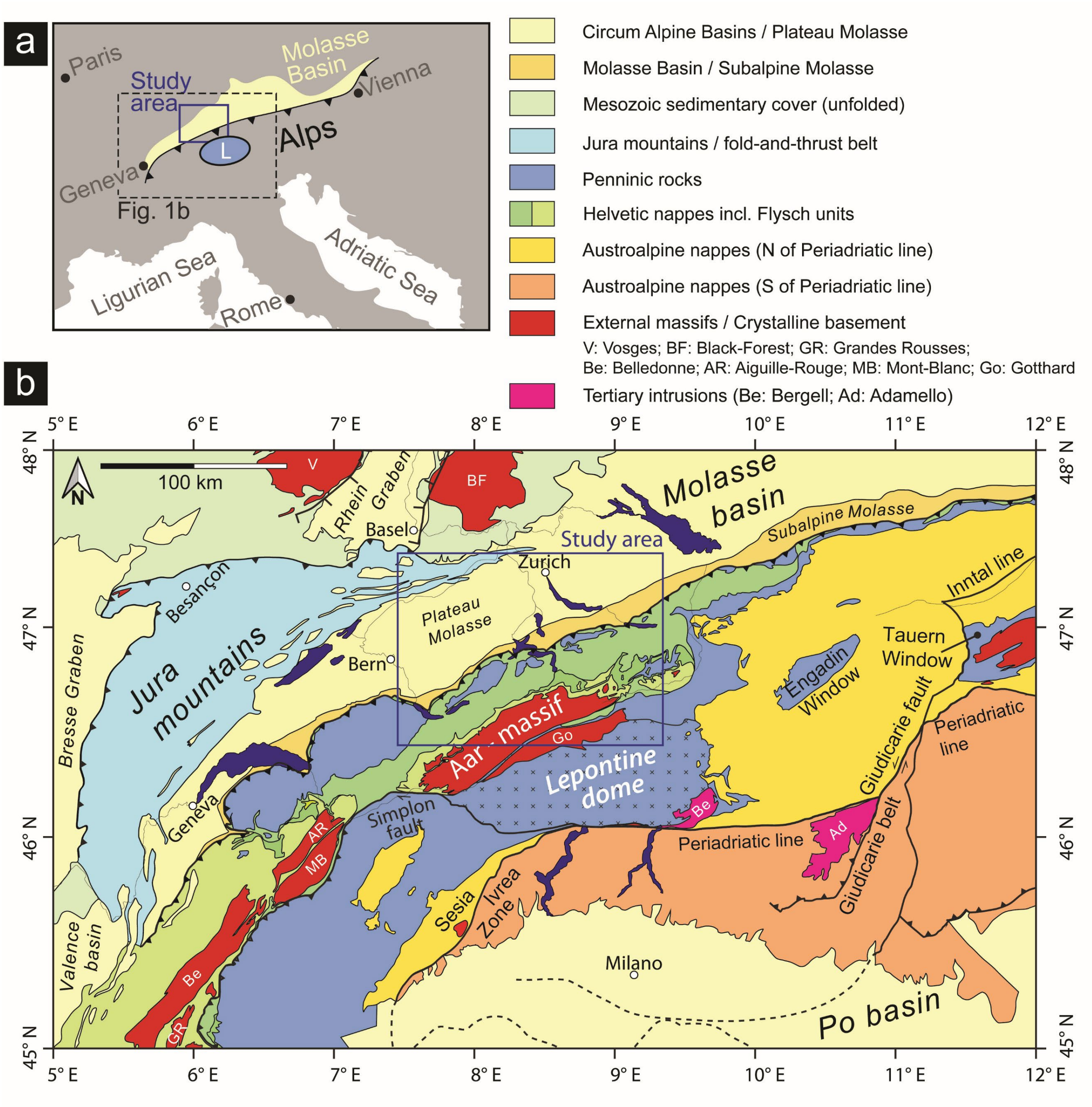

Figure 4.1: Simplified geological map of the study area. **a)** The Molasse Basin, north to the European Alps, and the oval marks the approximate position of the Lepontine Dome (marked with an L; see also Lepontine Dome in Fig. b). **b)** Simplified paleogeographical units in the Alps (mod. After Schmid et al., 2004; Schlunegger & Kissling, 2022).

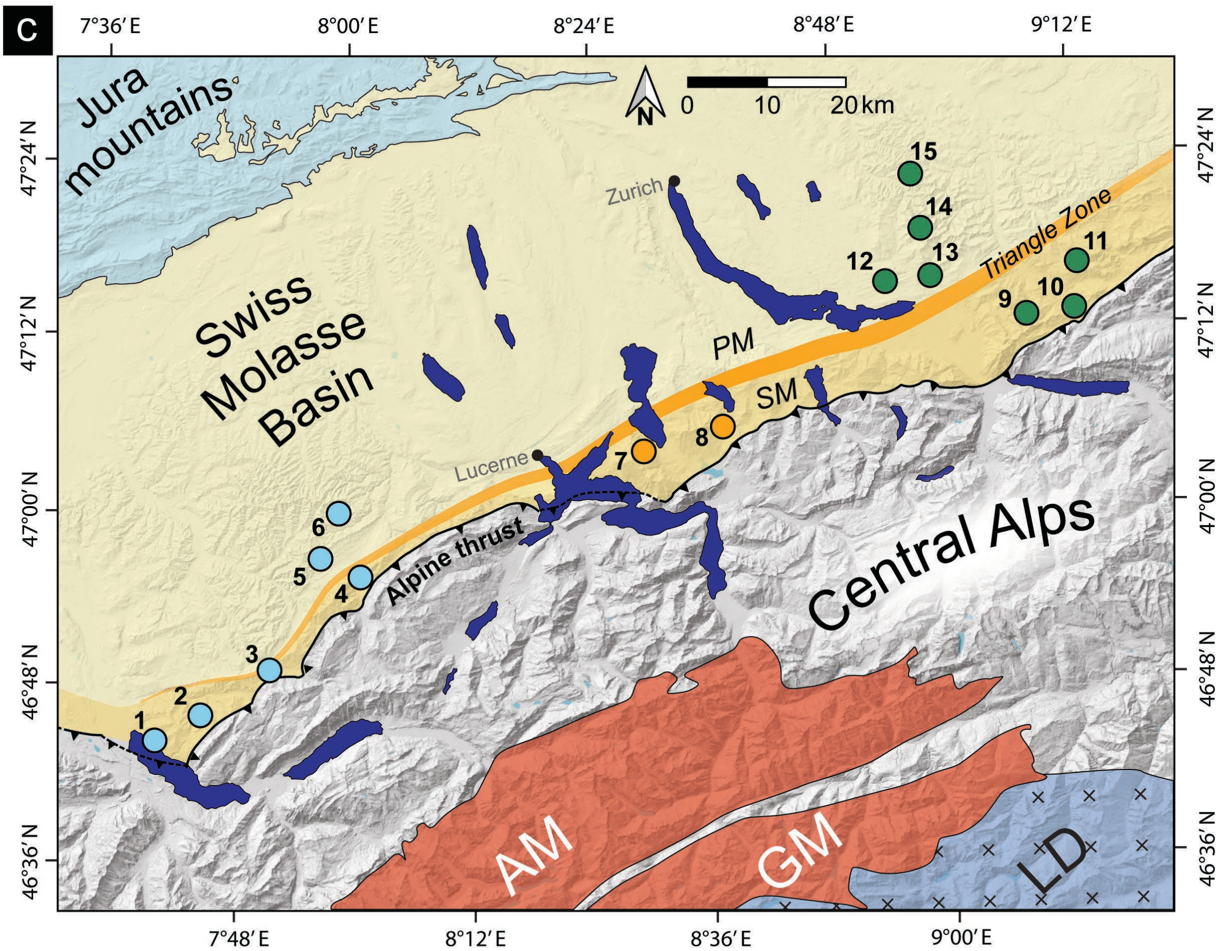

Legend:

PM: Plateau Molasse
SM: Subalpine Molasse
AM: Aar massif
GM: Gotthard massif
LD: Lepontine Dome
Lakes
Cities

Stratigraphic sections:

West		Central		East	
1	Lake Thun	**7**	Rigi	**9**	Steintal
2	Prässerenbach	**8**	Rossberg	**10**	Thur
3	Honegg			**11**	Necker
4	Emme			**12**	Jona
5	Schwändigraben			**13**	Goldingen
6	Fontannen			**14**	Töss
				15	Hörnli

Figure 4.1 (continued): c) Study area (see Fig. 4.1a and 4.1b for its position) and the location of the stratigraphic sections analysed in this study. The underlying digital elevation model (LiDAR DEM Swiss ALTI3D; © swisstopo) shows the present-day topography of the Central Alps, the Molasse basin and the Jura mountains.

4.2 Geological setting of study area

4.2.1 Evolution of the Swiss Molasse Basin and the Central Alps

The SMB is made up of clastic sediments that accumulated during Oligo-Miocene times. The basin is subdivided into the undeformed and flat-lying Plateau Molasse at distal positions relative to the Alpine orogen, and the tilted, folded and thrusted Subalpine Molasse adjacent to the Alpine front (figs. 4.1b and c). The formation of the SMB occurred contemporaneously with the development of the Central Alps. The sediment routing systems in the SMB, therefore, acted as recorders of the erosional history of the Alpine hinterland (Allen et al., 1991; Pfiffner et al., 2002; Schlunegger and Kissling, 2022). At the scale of the entire SMB, the deposits form two large-scale transgressive-regressive mega-cycles (Matter et al., 1980; Sinclair et al., 1991). Each cycle records a shallowing-upward sequence and encompasses the transition from marine to terrestrial conditions (Pfiffner, 1986; Kuhlemann and Kempf, 2002). The latter sediments are referred to as the Lower and Upper Freshwater Molasse (USM; OSM; conventional German abbreviations). The Freshwater Molasse records the occurrence of braided streams on alluvial megafans that were oriented perpendicular to the Alpine front and that were sourced the Central Alps (Schlunegger et al., 1997a; Kempf and Pross, 2005). The formation of these megafans in the SMB is closely linked to the tectonic evolution of the adjacent Alpine hinterland (section 4.2.3). Likewise, it was proposed that the sediment also recorded changes in the paleoclimate (section 4.2.4).

4.2.2 Stratigraphic sections as recorders of alluvial fan sedimentation

Over the course between c. 31 to 13 Ma, freshwater sedimentation yielded in the construction of several hundred of m-thick stratigraphic sections, which in general reveal coarsening- and thickening-upward trends and recorded the deposition on alluvial megafans where the depocenters prograded towards more distal positions (Stürm, 1973; Bürgisser, 1981; Matter and Weidmann, 1992; Schlunegger et al., 1997a; Kempf and Matter, 1999). At least for some of the sections (i.e., Lake Thun, Prässerenbach, Necker; see below), such observations were inferred to have rooted in the advancement of the basal Alpine thrust towards the north (Schlunegger et al., 1993; Kempf, 1998). A progradation of the depocenters, for all sections, is also supported by the change in the sedimentary facies up-section, where alternations of conglomerate beds with sandstone- and mudstone-beds at the lower part of the sections give way to amalgamations of conglomerate beds where finer-grained deposits become less frequent (Hantke, 1980; Matter et al., 1980; Schlunegger et al., 1996; Kempf et al., 1999; Garefalakis and Schlunegger, 2018). These conglomerates are made-up of rounded and sub-rounded clasts of fluvial origin, embedded within a sandy matrix (Stürm, 1973; Bürgisser, 1980; Schlunegger and Castelltort, 2016; Garefalakis and Schlunegger, 2018). In summary, higher, and generally younger, stratigraphic levels are related to a more proximal-situated depositional facies, while lower and older stratigraphic levels are associated with a more distally situated environment.

The 15 stratigraphic sections analysed in this study are situated along strike the present-day Alpine front and are encountered in the western, central and eastern SMB (Fig. 4.1c). The analysed sections have been the focus of previous studies and were explored for their compositional and sedimentological properties (Büchi, 1958; Bürgisser, 1981; Matter and Weidmann, 1992; Schlunegger et al., 1997c; Kempf et al., 1999; Eynatten, 2003; van der Boon et al., 2018). They have been dated in the framework of numerous paleontological and magnetostratigraphic studies that were in the western and central (Schlunegger et al., 1996, 1997a; Kälin and Kempf, 2009; Engesser and Kälin, 2017) and the eastern basin (Kempf et al., 1997; Kempf and Matter, 1999; Kälin and Kempf, 2009). The age constraints are based on correlations of the magnetostratigraphic polarities and biostratigraphic data with the CK95 (Cande and Kent, 1995), the ATNTS2004 (Gradstein et al., 2004) or the ATNTS2012 age models (Vandenberghe et al., 2012).

4.2.2.1 Sections in the western SMB

In the west (Fig. 4.1c), we analysed 6 stratigraphic sections, which are named: Emme, Honegg, Prässerenbach, Lake Thun, Schwändigraben and Fontannen. The Emme section recorded the construction of the Beichlen dispersal system (c. 31 – 29 Ma), and the conglomerate beds mainly comprise siliceous limestones and dolomite clasts, amongst sandstone and crystalline particles (Schlunegger et al., 1996, 1998). Farther to the SE (Fig. 4.1c), the Lake Thun, Prässerenbach and Honegg sections recorded the proximal-distal suite of the Honegg-Blueme dispersal system. The conglomerate beds comprise a variety of crystalline and sedimentary clasts, with abundant siliceous limestone constituents (Schlunegger et al., 1996, 1998). The Lake Thun (c. 24.8 – 23.1 Ma) and Prässerenbach (c. 26.5 – 22.5 Ma) sections are made up of material that was deposited at proximal positions in the basin, whereas the Honegg section (c. 28.3 – 24.3 Ma), situated farther to the NE, chronicles the accumulation on a more distal position of the Honegg-Blueme fan (Schlunegger et al., 1996, 1998). After c. 24 Ma, the Honegg-Blueme dispersal system eventually transitioned into the Napf paleoriver recorded by the composite sections Schwändigraben (c. 18.5 – 16.5 Ma) and Fontannen (c. 16.7 – 14.7 Ma).

4.2.2.2 Sections in the central SMB

In the central part of the SMB (Fig. 4.1c), we analysed 2 stratigraphic sections. These are the Rigi and Rossberg sections (both c. 29.5 – 24.7 Ma), of which the Rossberg is a composite of three individual sections (i.e., Rossberg, Sattel and Einsiedeln section; see for details e.g., Schlunegger et al., 1997a or Garefalakis et al., 2023b, submitted). The Rigi and Rossberg sections comprise the proximal-distal suite of the Rigi dispersal system. The related conglomerate beds comprise limestone, siliceous limestone and dolomite clasts at the base of both sections, which are partly replaced by sandstone and crystalline clasts towards the top (Schlunegger et al., 1997a, 1998).

4.2.2.3 Sections in the eastern SMB

In the east (Fig. 4.1c), we measured grain sizes along 7 sections, which are called: Thur, Steintal, Necker, Goldingen, Jona, Hörnli and Töss. The Thur and Steintal sections (both c. 31 – 27 Ma) comprise the deposits of the Speer alluvial fan system at proximal (Steintal) and more distal (Thur) locations (Kempf et al., 1999). The conglomerate beds are mainly made up of sedimentary clasts, where limestones dominate over sandstone constituents (Kempf et al., 1999). The Speer dispersal system transitioned into the Kronberg alluvial fan, the sediments of which are recorded in the uppermost part of the Necker section (c. 24.7 – 20.2 Ma). The deposits of the Kronberg system mainly comprise sedimentary clasts (limestone and sandstone particles), and crystalline clasts are less frequent (Kempf et al., 1999). The Goldingen, Jona, Hörnli and Töss sections (c. 20 – 13 Ma) all recorded deposition on the Hörnli alluvial fan (Kempf et al., 1997). Due to the exposure conditions, we focused our analysis on the coarse-grained sediments that are exposed along the Goldingen (c. 21 – 18 Ma) and the slightly younger Jona sections (c. 17 – 14 Ma) where the proximal facies of the Hörnli dispersal system is exposed. At more distal sites, contemporaneous sediments are encountered along the Hörnli and Töss sections (both c. 15 – 13 Ma). Petrographic analyses revealed that the conglomerate beds of the Hörnli fan mainly comprise limestone, sandstone and crystalline clasts, the latter of which become less frequent towards the top of the sections (Kempf et al., 1999).

For a detailed summary of the depositional evolution and the descriptions of these stratigraphic sections and related dispersal systems, the reader is referred to the aforementioned references. The stratigraphic sections along with the chronological framework are provided in appendix A of this chapter. As an overview of the sections, Figure 4.2 provides an overview of their age ranges (Fig. 4.2a) and their thicknesses (Fig. 4.2b).

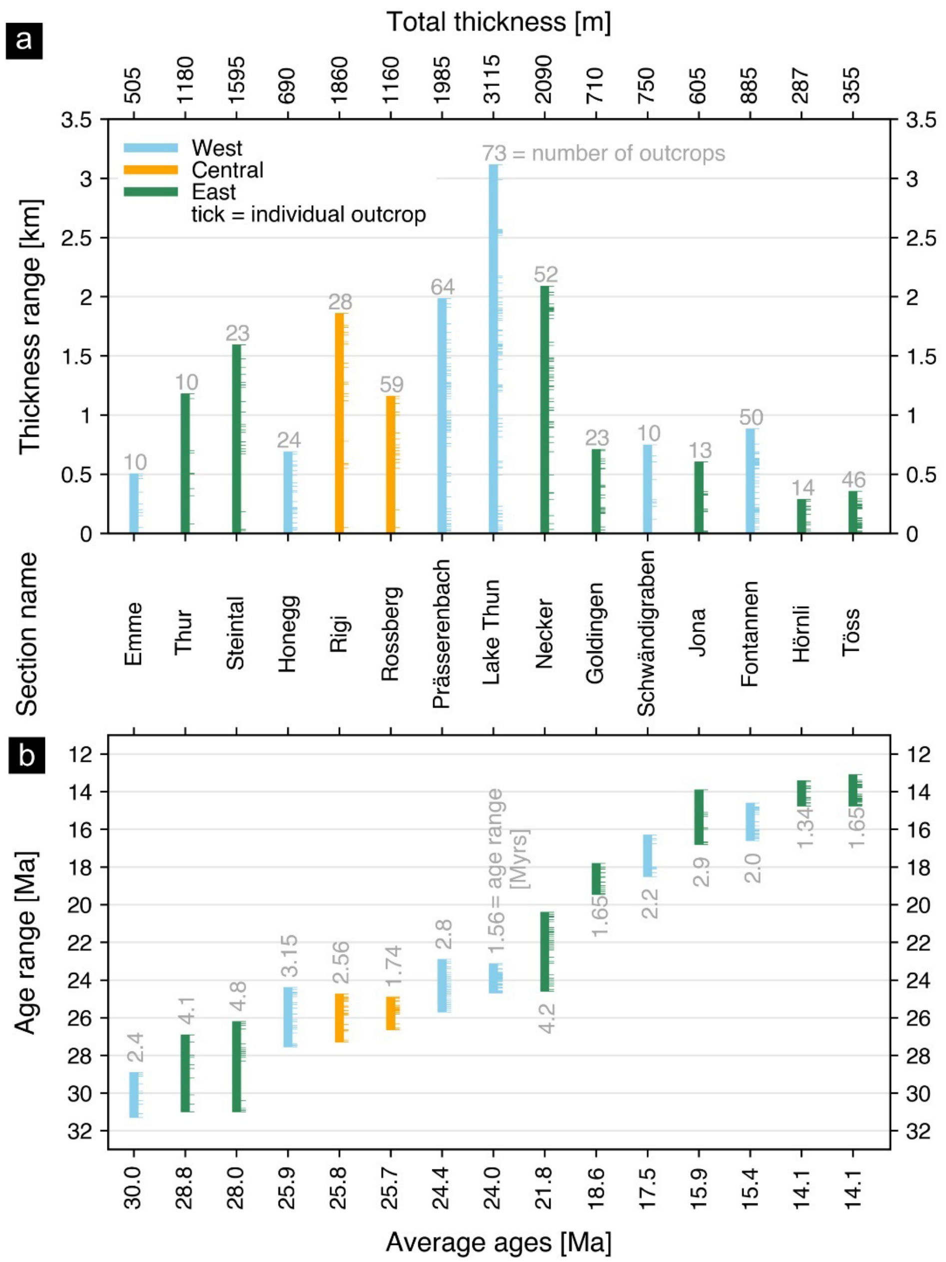

Figure 4.2: Thicknesses and age ranges of the stratigraphic sections, arranged along their increasing average ages. **a)** Variations in the thicknesses of individual sections, the total sections' thicknesses and the number of analysed outcrops (tick marks represent the relative positions of the outcrops in the stratigraphic sections); and **b)** age ranges and the average ages of the analysed sections (tick marks are related to ages of the outcrops in the stratigraphic sections). See inset in a) for legend.

4.2.3 Tectonic evolution of the Alps

Between c. 32 and 26 Ma (Rupelian to Chattian), the Central Alps, which were the main source of the deposits in the SMB (Kuhlemann and Kempf, 2002), experienced high exhumation rates (Schlunegger and Willett, 1999; Boston et al., 2017) due to the rapid tectonic uplift in the Lepontine area that is situated in the core of the Alps (Fig. 4.1). This uplift initiated a transient stage in the topographic evolution of the Alpine hinterland, where the landscape changed from an elevated plateau at c. 30 Ma to a highly dissected terrain after 25 Ma (Schlunegger and Kissling, 2015; Garefalakis and Schlunegger, 2018). Fluvial incision occurred through headward retreat from the orogenic front into the crystalline core of the Alps and rapid erosion resulted in large sediment fluxes. The volume of supplied sediments continuously increased form c. 2000 km^3 Myr^{-1} prior to 30 Ma, to c. 15000 km^3 Myr^{-1} thereafter, as recorded by the SMB (Hay et al., 1992; Schlunegger, 1999; Kuhlemann, 2000; Kuhlemann et al., 2001; Schlunegger et al., 2001). Around 25 – 22 Ma (late Chattian to Aquitanian), the Central Alps were considered to have reached a steady-state topography (Schlunegger and Kissling, 2015). This was also the time when the largest sediment fluxes of c. 15000 – 22000 km^3 Myr^{-1} occurred. At the same time, the uplift and exhumation of the external crystalline massifs was initiated in the Central Alps (Herwegh et al., 2017; e.g., Fig. 4.1b). This was also the time when the area surrounding the Lepontine dome (figs. 4.1b and c) experienced the highest exhumation rates, which was accomplished by tectonic erosion through slip along the Simplon fault zone (Schlunegger, 1999; Boston et al., 2017). The resulting exposure of lithologies with a higher erosional resistance resulted in a northward shift of the drainage divide. This in turn caused a re-organisation of the drainage pattern in the Central Alps, thereby establishing an orogen parallel drainage network with long flow paths (Schlunegger et al., 1998; Kühni and Pfiffner, 2001; Spiegel et al., 2001; Stutenbecker et al., 2019). In addition, around 20 Ma, a marine transgression occurred in the SMB (Allen et al., 1985; Schlunegger et al., 1997b; Jost et al., 2016; Garefalakis and Schlunegger, 2019) and a triangle-zone was established at the southern border of the Plateau Molasse through syn-depositional back-thrusting (Kempf et al., 1999; Pfiffner et al., 2002; Schlunegger and Mosar, 2011). During this time, the sediment supply to the basin decreased to c. 12000 km^3 Myr^{-1} (Hay et al., 1992; Schlunegger, 1999; Kuhlemann, 2000; Kuhlemann et al., 2001; Schlunegger et al., 2001). Around 18 – 16 Ma, terrestrial conditions in the entire SMB were established again (Kuhlemann and Kempf, 2002). This occurred together with a rapid increase in sediment supply to c. 16000 km^3 Myr^{-1}. Then the supplies decreased to a constant value of c. 12000 km^3 Myr^{-1}.

4.2.4 Paleoclimate

The Central Alps and the SMB underwent various climatic conditions during their evolution. Globally, the period between c. 32 and 27 Ma was characterised by a relatively stable and cold paleoclimate, as revealed by the relatively high values of the oxygen isotope record ($\delta^{18}O$; Zachos et al., 2001). This is consistent with paleoclimate interpretation that base on calcareous seeds of charophytes collected in the SMB (Berger, 1992; Schlunegger et al., 2001). Following this period, the global oxygen isotope record indicates a shift towards smaller values and thus warmer conditions (Zachos et al., 2001), which is referred to the Late Oligocene Warming Event (LOWE). Slightly later, around c. 25.5 Ma, a shift towards a warmer and drier, possibly also stormier (Schlunegger and Norton, 2013) climate was interpreted from stable carbon and oxygen isotope data collected in the SMB (Berger, 1992; Schlunegger et al., 2001). Following the LOWE, the Oligo-Miocene Transition (OMT) at c. 23 Ma marks the transition towards a cold period, albeit of a short duration only (Zachos et al., 2001). During the Miocene, temperatures increased between c. 17 – 15 Ma. This rise corresponds to the Miocene Climate

Optimum (MCO) and is documented in both, the global records (Zachos et al., 2001) and in the carbon and oxygen isotopes collected from pedogenic carbonates in the SMB (Methner et al., 2020; Krsnik et al., 2021). This shift towards a warmer climate is also recorded in the record of floral faunas in the Molasse basin (Mosbrugger et al., 2005). Eventually, the MCO was followed by a cooling event around c. 14 Ma, also recorded globally as well as in the deposits of the SMB (Zachos et al., 2001; Methner et al., 2020; Krsnik et al., 2021).

4.3 Grain size fining and the self-similarity model

Grain size fining in fluvial systems is primarily driven by selective deposition of the material (Parker, 1991; Ferguson et al., 1996; Stock et al., 2008), whereas abrasion only plays a major role particularly in the steep headwaters (Miller et al., 2014). Based on field studies, it was shown that the fining can be approximated by an exponential function (Sternberg, 1875; Ferguson et al., 1996; Blom et al., 2016), for which both the mean and the standard deviation of a grain size distribution (GSD) decrease at the same rate downstream. Therefore, a GSD normalised by these two variables will remain approximately constant at any downstream position of a fluvial system along which grain size fining occurs. This normalised GSD can be expressed by the self-similarity variable ξ (Fedele and Paola, 2007):

$$\xi = \frac{D_k - \bar{D}(x^*)}{\sigma(x^*)} \; [-] \qquad Eq. (4.2).$$

Here, D_k is an individual grain size, $\bar{D}$ and σ are the mean and sample standard deviation of the GSD, all at a downstream site expressed by the normalised distance x^* with respect to the length of the depositional system. The assumption of a self-similar GSD builds the basis for the grain size fining model proposed by Fedele & Paola (2007), which allows to estimate the volume of sediments that is deposited or extracted downstream of a fluvial system. Therefore, although the self-similarity grain size fining model was tailored to systems where proximal-distal relationships are still preserved, we are left with the assumption that the analysed stratigraphic sections record such a trend if analysed up-section (see section 4.2.2 for justification).

The grain size fining model itself is derived from the Exner sediment mass balance where material is either in transport or stored in the substrate (Paola and Voller, 2005; Fedele and Paola, 2007). Generally, the model considers changes in the hydraulic conditions, such as adjustments of the riverbed slope, shifts in the critical shear stress required for sediment entrainment or the self-regulatory controls on the river width. However, because these mechanisms are less significant for longer timescales, in our case millions of years, these are set as constant in a modelling framework (Parker, 1991; Fedele and Paola, 2007; Duller et al., 2010). As a consequence, grain size trends on alluvial megafans are to a first-order controlled by the subsidence rate and pattern of a foreland basin, and by the rate at which sediment was supplied to the basin. In this context, for a given sediment supply, a low-subsidence rate promotes the occurrence of a low grain size fining trend, whereas a high-subsidence rate will be reflected by a higher rate at which the supplied material fines downstream (Duller et al., 2010; Armitage et al., 2011). Consequently, the spatially averaged GSD is characterised by coarser-grained material for a system where subsidence rates are low, because a large portion of the particles are transferred out of the system. In contrast a system with high-subsidence rates yields in a finer-grained material, because most of the particles are stored at more proximal positions on the fan, and only a few and relatively small grains reach the outlet of the fan. In addition, large volumes of supplied sediments to an alluvial fan tend to result in a decrease of the fining rates along distance, thereby yielding GSDs characterised by larger grains, and vice versa respectively (Hoey and Bluck, 1999; Blom et al., 2016).

Grain size data can be used to estimate the relative mobility of the supplied material once it has reached the fan surface. For coarse-grained material where the particle size is larger than 2 mm, Fedele and Paola (2007) proposed a solution to calculate the relative mobility function J. Its derivation bases on the observation that the mobilisation of coarse-grained material occurs if grain-size dependent thresholds during bankfull discharge conditions are exceeded (Paola et al., 1992; Bunte et al., 2004; Parker et al., 2007; Wickert and Schildgen, 2019). An important assumption of the grain size fining model is that the J-values (Eq. 4.1) have a self-similar distribution (Fedele and Paola, 2007; Duller et al., 2010; D'Arcy et al., 2017; Brooke et al., 2018). Therefore, the relative mobility function J can be expressed as a function of ξ (Eq. 4.2) as follows:

$$J(\xi) = a_g * exp^{-b_g * \xi} + c_g \, [-] \qquad Eq. (4.3).$$

The parameters a_g, b_g and c_g (all > 0) describe the shape of the relative mobility function for the case of gravel-sized particles (subscript g) and characterise the incipient motion of these (Fedele and Paola, 2007). Here, the parameter a_g quantifies the mobility of all grain sizes of a given GSD (if a_g increases, the particle mobility increases with grain size), b_g influences the rate of the relative mobility (if b_g increases, particles with larger sizes become less mobile than smaller particles), and c_g describes the minimum probability at which grains of all sizes are transported (if $c_g > 1$, then all grains are likely in transport). This is the case because c_g describes the asymptote of the falling limb of the similarity function (Fedele and Paola, 2007; Brooke et al., 2018; Harries et al., 2018). These three parameters are based on the assumption that sediment entrainment occurs if flow-specific threshold conditions are exceeded (e.g., shear stress; see above), and they depend on the transformation of particle size into ξ (Eq. 4.2). Previous studies with a scope on fluvially transported material showed that the parameters a_g, b_g and c_g lay within the range of 0.1 – 0.9 for a_g, 0.2 – 3.0 for b_g and 0.01 – 0.5 for c_g (Fedele and Paola, 2007; Duller et al., 2010; D'Arcy et al., 2017; Brooke et al., 2018; Harries et al., 2018). Related to this, Harries et al. (2018) modelled the relative mobility function for three alluvial fans in the Central Argentine Andes. They documented the values of the aforementioned parameters are different depending on whether they are calculated in a normal-space or in a logarithmic-space. Especially parameter c_g tends to be close to 0 when the calculations are accomplished on the log-transformed data. Furthermore, as also shown by Brooke et al. (2018), the parameters a_g and b_g are sensitive to the distribution of the ξ values, hereafter ξ-distribution, where distributions with a low standard deviation and small peaks will yield best-fit values for largely different a_g and b_g values.

4.4 Methods: Data collection and calculations

4.4.1 Revised chronological framework

The previously established age models of the analysed sections (section 4.2.2) have comparatively different numerical ages. Therefore, we recalibrated the original magneto polarity stratigraphies to the recent Global Time Scale GTS2020 (Gradstein et al., 2020) and considered new mapping results in the study area (Hantke et al., 2022; Strasky et al., 2022) to harmonise the age model for all sections. The revised age model for the Lake Thun, Töss, Hörnli, Rigi and Rossberg (including the Sattel and Einsiedeln) sections have been taken from Garefalakis et al. (2023b, submitted). For each section, the calibration of the magnetostratigraphic polarities to the GTS2020 is given in appendix A of this chapter, Table S4.1 indicates which age model (original or revised) has been considered for the recalibration.

4.4.2 Grain size data and logarithmic transformation

The grain size data was collected on digital photos (Panasonic Lumix FT-5) taken from accessible outcrops of conglomerates. On each photograph (3-6 per outcrop >5 m^2), taken at a distance of 1-1.5 m, the longest visible axes of 100 grains >2 mm were measured with ImageJ (Rasband, 1997) using a grid-based Wolman point count approach (Wolman, 1954). This was accomplished following the measuring protocol of Garefalakis et al. (2023a). The grain size data of the Lake Thun, Töss, Hörnli, Rossberg sections (which includes the data of the Sattel and Einsiedeln sections) were taken from Garefalakis et al., (2023b; submitted), and the data of the Rigi section was taken from Garefalakis and Schlunegger (2018), respectively.

Clasts transported by fluvial processes were shown to follow a logarithmic-/log-normal or a gamma distribution (Friedman, 1962; Church and Kellerhals, 1978; Vaz and Fortes, 1988; Armitage et al., 2011). A log-transformation of the data has implications on the tails of the underlying distribution and lessens the skew of these when compared to a distribution where no transformation is applied (Wilcock et al., 2009). More important, because the calculation of the self-similarity variable ξ (Eq. 4.2) implicitly bases on the assumption that the grain size data follows a normal distribution (Fedele and Paola, 2007; Duller et al., 2010; Armitage et al., 2011; Brooke et al., 2018), we transformed the obtained GSDs into a natural log-space (ln(GSD)) to achieve a normal distribution of the datasets. Please note that the log-transformation was only applied on the grain size data and not on the self-similarity variables that we calculated from these. Therefore, we refer to the log-transformed ξ data as $\xi(ln(\text{GSD}))$.

4.4.3 Statistical tests

We tested whether the original non-transformed and the log-transformed grain size datasets as well as the ξ values are normally distributed. This was accomplished using the Shapiro-Wilk (*SW*) test (Shapiro and Wilk, 1965; Shapiro et al., 1968). We additionally used the Kolmogorov-Smirnov two-sample (*KS2*) test (Hodges, 1958) to show that the GSD expressed by the self-similarity variable ξ have a statistically higher similarity. The null-hypothesis H_0 states i) for the *SW*-test that the data is likely normally distributed, and ii) for the *KS2*-test that two pairs of datasets are similar and likely drawn from identical distributions. For both tests, the H_0 cannot be rejected if the p-value is larger than 0.05 (i.e., significance level α = 5% equivalent to the 95 % confidence level.). Please note, the p-value of the *SW*-test is accurate if the sample size does not exceed 5000 (Shapiro and Wilk, 1965). Because 4 sections exceed this number (i.e., Rossberg, Prässerenbach, Lake Thun and Necker; see results), we additionally report the *SW*-statistics for these. In these cases, the data is likely normally distributed if the *SW*-statistics tends to approach 1.

4.4.4 Calculation of the fraction in the substrate

The optimal values for the parameters a_g, b_g and c_g were determined upon finding a best-fit between the model results of f (the fraction in the substrate, Eq. 4.1) and our ξ dataset within the 95 % C.I. (confidence interval). For this, we used the analytical solution of Fedele and Paola, 2007 as basis and followed the approaches of D'Arcy et al. (2017) and Brooke et al. (2018). As a first step, f can be expressed as a function of ξ:

$$f(\xi) = C * exp^{-\Phi(\xi)} \; [-] \qquad Eq. (4.4).$$

The integration constant C can be calculated using equations 4.8 and 4.9 (see below), and the exponent $\Phi(\xi)$ is the integral of $\varphi(\xi)$:

$$\Phi(\xi) = -\int \varphi(\xi)\, d\xi \; [-] \qquad Eq. (4.5),$$

where $\varphi(\xi)$ is:

$$\varphi(\xi) = \frac{1}{C_1 * \left(1 + \frac{C_2}{C_1} * \xi\right)} * \left(1 - \frac{1}{J}\right) - \frac{J'}{J} \; [-] \qquad Eq. (4.6).$$

Here, J is the relative mobility function (Eq. 4.1 and 4.3) and J' its derivative with respect to the self-similarity variable ξ (i.e., $J' = dJ(\xi) / d\xi$; Fedele & Paola, 2007). The variables C_1 and C_2 describe how the variance in sediment supply differs along distance, expressed as downstream variations of the mean grain size (C_2) and as site-specific variations of the standard deviation (C_1). Values for C_1 were determined on a theoretical and analytical basis and typically range between c. 0.55 and 0.90 (Fedele and Paola, 2007; Duller et al., 2010; Armitage et al., 2011; D'Arcy et al., 2017). The ratio of C_1 and C_2 can be expressed by the coefficient of variation C_v (Fedele and Paola, 2007; Eq. 4.7), calculated from the grain size dataset (see section 4.4.2). This then allows to determine the values for C_2:

$$C_v = \frac{C_1}{C_2} = \frac{\sigma}{\overline{D}} \; [-] \rightarrow C_2 = \frac{C_1}{C_v} \; [-] \qquad Eq. (4.7).$$

Here, σ and $\overline{D}$ are the sample standard deviation and the mean grain size of a particular GSD, respectively. The relative mobility function J follows the assumption that mass is preserved during selective deposition or transport, which thus excludes the occurrence of abrasion (Fedele and Paola, 2007). Following this principle, the integration constant C (Eq. 4.4) can be determined by:

$$\int_{-\infty}^{\infty} f(\xi)\, d\xi = C * \int_{-\infty}^{\infty} exp^{-\Phi(\xi)} d\xi = 1 \; [-] \qquad Eq. (4.8),$$

and solved for C:

$$C = \frac{1}{\int_{-\infty}^{\infty} exp^{-\Phi(\xi)} d\xi} \; [-] \qquad Eq. (4.9).$$

Given the above-mentioned functions, we finally determined the optimal parameters a_g, b_g and c_g of the relative mobility function $J(\xi)$ (Eq. 4.3) within a 95 % C.I.. This can be achieved by calculating the probability density of the self-similarity variable ξ to which $f(\xi)$ (Eq. 4.4) was fitted using least square regressions. For the calculations of the probability density we used 0.5-ξ binning intervals (Duller et al., 2010; Whittaker et al., 2010; D'Arcy et al., 2017; Brooke et al., 2018; Harries et al., 2018). After numerically solving the relative mobility function with the best-fit parameters, we calculated the values of the relative mobility function for $J = 1$, which is considered to be a crucial measure for the system's capability to transport a given grain size (see introduction). We did the calculations for both, the ξ-distribution and the bulk GSD of the entire system. For the latter we report the outcomes of J against a dimensional grain size D_k [mm], after all calculations using Equations (4.1) to (4.9) are done in log-space (see section 4.4.2), thereby using a reformulation of Eq. 4.2 as follows:

$$ln(D_k(\xi)) = ln(\xi)_{BT\ median} \cdot ln(\sigma)_{system} + ln(\overline{D})_{system} \; [-]$$
$$e^{[ln(D_k(\xi))]} = D_k(\xi) \; [\mathrm{mm}] \qquad Eq. (4.10).$$

For this, we used for ξ the values from the BT (bootstrapping, see below), for estimating the mean grain size $\overline{D}$ and the sample standard deviation σ we used for each individual site of a section the overall average $\overline{D}$ and σ values, all calculated by using the log-transformed data. Finally, we back-transformed the results from log-space (dimensionless [-]) into dimensional grain size values (in [mm]). In the figures, we only present the sections' median solutions along with the 95 % C.I. for the sake of clarity.

4.4.5 Uncertainty estimations and calculations

For all calculations and computation of the related uncertainties, we applied a bootstrapping (*BT*) and resampled 100 grain size values with replacement to simulate 10^4 scenarios. We then report the median values along with the 95 % C.I. in square brackets where applicable (e.g., for a grain size: D_{50} = 15 [12 – 17] mm). For the sake of completeness, we also show the GSD of all sections, including the average, the D_{50} and the D_{84} grain size percentiles for all sites and for the entire system (i.e., the bulk GSD). To account for the large variability in grain size values measured for each section, we applied the same *BT* to the bulk GSD for the calculations of the relative mobility function (see equations above). Consequently, for the calculations of ξ (Eq. 4.2) and the related probability distributions and for each iteration scenario, we used the resampled grain size dataset from which we then computed $f(\xi)$ (Eq. 4.4). Also for each scenario and using the same re-sampled grain size values, we determined the values for C_v that is used for the calculation of the variable C_2 (Eq. 4.7). For this, we combined the *BT* with a Monte-Carlo framework and used uniformly distributed values between 0.60 and 0.90 for the variable C_1. We justify this approach, because a small value of C_1 is appropriate for systems with limited down-system changes in grain sizes, whereas for a system with a rapid grain size fining larger values of C_1 should be considered (e.g., Brooke et al., 2018). Because we cannot derive grain size fining rates from our stratigraphic sections, we assign this plausible range to the C_1 values.

The calculations of the statistical tests shown in the related figures are based on the median GSD and the ξ-distribution, for each section. We approximated these distributions by calculating for the grain size datasets, which base on 100 measurements per outcrop (see section 4.4.2), or the values of the corresponding self-similarity variable ξ (in 0.5-bins for the probability density distributions) each time the median value of each ordinal number in increasing order (i.e., the median of all first, second, third etc. values of the grain size measurements of all outcrops of a section). We justify this approach, because the distribution of the bulk grain size data (bulk GSD) or that of the bulk ξ values (bulk ξ-distributions) can be biased by extreme values (e.g., maximum grain size values) and by the number of samples (see e.g., Fig. 4.4 for number of measured grains per section). In addition, we calculated the median instead of the average, because grain size datasets tend to follow a log-normal distribution and thus do not fulfil the criteria of a symmetric distribution (see section 4.4.2). For the sake of completeness, the statistical tests based on the bulk data (statistical outliers included) are shown in appendix B of this chapter.

4.5 Results and Interpretation

4.5.1 Accumulation rates of the stratigraphic sections

Given the thickness and age dataset (e.g., Fig. 4.2), we calculated the sediment accumulation rate for each section with an estimated uncertainty of ± 20 %. The accumulation rates scatter between c. 200 and 2000 m Myr^{-1}, with a long-term average of 500 m Myr^{-1} (Fig. 4.3c). Through time, we observe a slow increase in these rates from 200 – 300 m Myr^{-1} between c. 30 and 26 Ma (Emme to Honegg). The sediment accumulation rates further increase to 500 – 700 m Myr^{-1} between c. 26 –22 Ma (Rigi to Necker), with the highest accumulation rates calculated for the Thun Lake section (2000 m Myr^{-1}) at c. 24 Ma (Fig. 4.3c). Thereafter, between c. 19 – 14 Ma, the rates slowly decrease from c. 400 m Myr^{-1} to values scattering around 200 – 300 m Myr^{-1} (Fig. 4.3c).

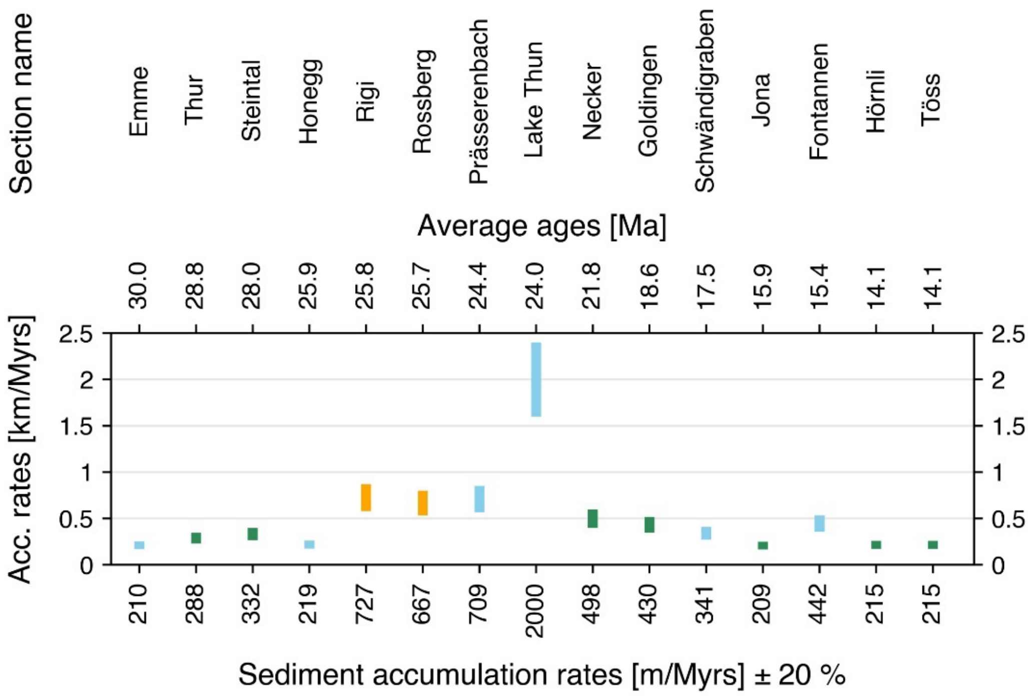

Figure 4.3: Calculated sediment accumulation rates of the stratigraphic sections, illustrated with ± 20 % of uncertainties and ordered against increasing average section age.

4.5.2 Grain sizes, self-similarity values, and evolution through time

We measured a total of 49900 grains along the 15 sections. The number of measured grains per section ranges between 1000 and 7300 (Fig. 4.4a; i.e., 100 grains per outcrop). The grain size values, shown as regular box-whisker-plots (extremes not shown) and ordered against increasing average ages (Fig. 4.3b), range between >2 mm and 90 – 160 mm (Fig. 4.4a). The values of the 25th and 75th grain size percentiles (interquartile-range) range from 20 to 80 mm for all sections and reveals a similar scatter as the uppermost whiskers through time (Figs. 4.4a). The grain size average and percentile values, which are determined from the bulk GSD of each section, show an irregular pattern through time. The average per section ranges from c. 40 to 60 mm with an overall average of around 49 mm (Fig. 4.4a). The D_{50} ranges from c. 30 to 50 mm, with an overall average of 40 mm, whereas the sizes of the D_{84} scatter between c. 60 – 100 mm with an average of 80 mm (Fig. 4.4a). The maximum measured grain sizes range form c. 170 to 530 mm, and the values neither follow the pattern of the upper whiskers nor that of the indicated grain size percentiles (not shown; see appendix B of this chapter for values of the maximum grain sizes per section).

The GSD, the average values and the percentiles based on the bulk grain size dataset and for all sections do not disclose a clear trend through time (Fig. 4.4a). Yet, there exist time spans during which the average grain size, the D_{50}, and especially the D_{84} appear to increase and decrease over shorter periods. For instance, between c. 29 and 26 Ma (i.e., Thur, Steintal, Honegg), the sizes of the D_{50}, and D_{84} percentiles show a decrease from c. 45 to 33 mm and from c. 85 to 62 mm, respectively. Thereafter, between c. 26 and 24 Ma (i.e., Rossberg, Prässerenbach, Lake Thun), the D_{50} increases to 49 mm, and the D_{84} to 100 mm. Finally, between c. 24 and 18.5 Ma (until Goldingen), the values for the same percentiles decrease to c. 40 mm and 70 mm (for the D_{50}, and D_{84}, respectively), after which they scatter between c. 60 and 80 mm until c. 14 Ma (Fig. 4.3a and 4.4a). However, these aforementioned trends of increasing and decreasing grain size percentile values are within uncertainties (95 % C.I.) and thus not significant. Therefore, the data likely suggest a random scatter of the bulk grain size percentiles through the entire observed geological time.

The transformation of the grain size data into self-similarity values ξ (dimensionless; Eq. 4.2), based on the bulk grain size data of each section, yields the expected normalisation of the data (Fig. 4.4b). Expressed as regular box-whisker-plots, the ξ-values range between c. -3 – 3, and the interquartile-range lays between -0.6 – 0.6 (Fig. 4.4b). The values of the ξ-percentiles are very similar to each other, ranging between c. -0.01 – 0.11 for the ξ_{50} (with an overall average of c. 0.05). Likewise, the ξ_{84} values range between 0.98 – 1.02 and average around 1 (Fig. 4.4b). The ξ-transformation reveals that the bulk grain size datasets of all sections are self-similar to each other. This behaviour is not only observed at the scale of an entire section, but also at that of an individual outcrops (see figs. SB4.8 and SB4.9 in appendix B of this chapter).

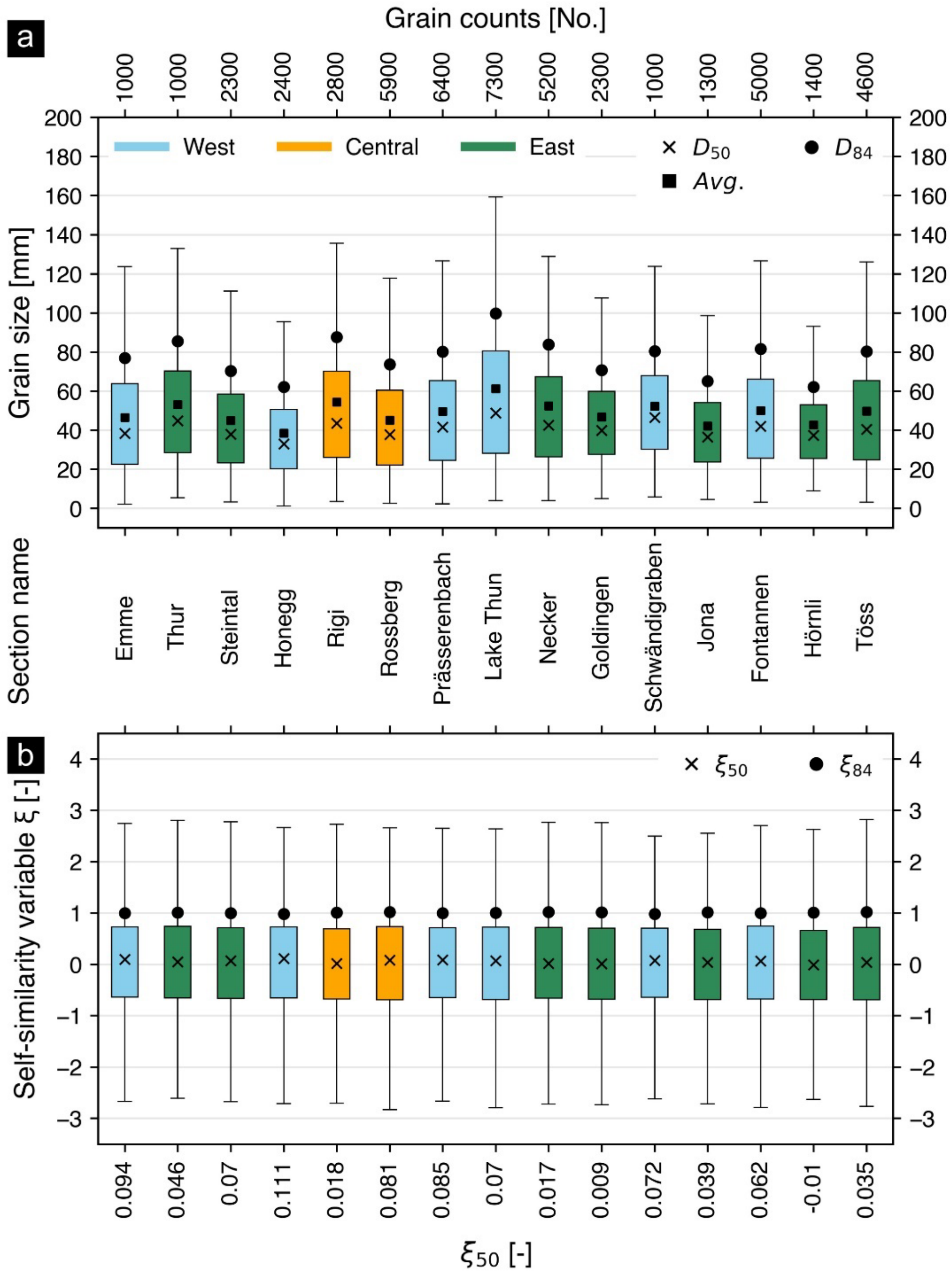

Figure 4.4: Grain size distributions and self-similarity variable distributions. The **a)** bulk GSD and **b)** ξ-distributions of the analysed sections expressed as box-whisker-plots. The boxes comprise the interquartile range (i.e., 25th to 75th percentiles). The values of the self-similarity variable ξ were calculated using Eq. 4.2.

4.5.3 Frequency distributions and statistical tests

The cumulative frequency curves of the sections' median GSD (section 4.4.5) have a larger spread between each other particularly for the values above the D_{50} (Fig. 4.5a). In addition, the GSD are right-skewed towards larger and left-skewed towards smaller grain sizes (Fig. 4.5a). When applying a natural-logarithm transformation to the grain size data, the resulting values yield a more evenly distributed cumulative distribution at both tails, thereby revealing that the skewed tails are not a relic of the sampling technique, but that the GSD's indeed follow a log-normal distribution (Fig. 4.5b). This is supported by the larger similarity between the simulated normal distribution (from the bulk average and bulk sample standard deviation of all sections; Figs. 4.5a and 4.5b) and by the outcomes of the *SW*-test (see below).

The transformation of the data into the self-similarity variable ξ yields distributions where all frequency curves collapse on the same curve, and which disclose a high similarity to the simulated normal distribution (Fig. 4.5c). However, the right-skewed upper tail and left-skewed lower tail still discloses that the underlying GSD follows a log-normal distribution (Fig. 4.5c). Upon calculating the self-similarity variable of the log-transformed grain size data i.e., $\xi(ln(\text{GSD}))$, the cumulative frequency curves perfectly match the simulated normal distribution and the skews in the tails are nearly absent (Fig. 4.5d). This is observed not only at the scale of an entire sections, but also for individual sites at each section (see appendix B of this chapter for figures).

We applied the *KS2* test to explore whether the median GSD and the median *ln*(GSD) datasets are similar to each other. The results show that c. 87 % of the sections are statistically similar to each other at the 95 % C.I. (Fig. 4.6a). The large scatter of the *p*-values, expressing a higher similarity when close to 1, confirms that the GSD are not completely congruent. This is already shown by the cumulative curves (figs. 4.5a and 4.5b). Likewise, the application of the *KS2* test to the self-similarity variable ξ shows that the various sections and their underlying median distributions are 100 % similar to each other (Fig. 4.6b). While all cross-comparisons yield *p*-values above the threshold of 0.05 (i.e., the 95 % C.I.), only a few cross-comparisons yield *p*-values that are slightly below 1 (Fig. 4.6b). The corresponding *KS2* test results of the $\xi(ln(\text{GSD}))$ data also disclose a similarity of 100 % if cross-compared across all sections, whereas all *p*-values are very close to 1 (Fig. 4.6c). Alternatively, the statistical tests can be applied to the bulk GSD and ξ-distributions, which consequently yield largely different values. In case of the *KS2* test, its application to the bulk GSD and *ln*(GSD) datasets reveal a similarity of only c. 16 %. If we apply this test to the values after the ξ transformation, then the results disclose a similarity of c. 77 %, and for the $\xi(ln(\text{GSD}))$ data the outcomes yield the highest similarity of c. 94 % (see Fig. SB4.2 in appendix B of this chapter).

We also applied the *SW* test to explore whether the median GSD and median ξ-distributions follow a normal distribution. The results show that none of the data is normally distributed (0 %; Fig. 4.7a). This is also illustrated in the cumulative distributions, where both, the median GSD and ξ distribution diverge from the simulated normal distribution (figs. 4.5a and 4.5b). A transformation into log-space largely improves the *SW* test results to 100 % and reveals that both, the median *ln*(GSD) and $\xi(ln(\text{GSD}))$ datasets follow a normal distribution at the 95 % C.I. (figs. 4.7b and 4.7c). Moreover, the *p*-values of the $\xi(ln(\text{GSD}))$ datasets are slightly higher than those of the *ln*(GSD) datasets. For sections where > 5000 grain sizes were measured, we additionally report the *SW*-statistics, which are in all cases

> 0.98 and thus close to 1 (figs. 4.7b and 4.7c). We then applied the *SW* test for exploring whether the grain size and ξ values of the bulk datasets are normally distributed. The results show that the bulk GSDs and ξ-distributions are not normally distributed (0 %). However, the log-transformed datasets *ln*(GSD) and ξ(*ln*(GSD)) of the bulk distributions revealed that c. 20 % follow a normal distribution (see Fig. SB4.3 in appendix B of this chapter). This is not surprising, because in this case the simulated normal distribution is based on the overall mean and standard deviation values calculated from the bulk population of all sections and therefore includes statistical outliers, such as very coarse grain sizes (see also section 4.5.2)

Given these results and regarding their median distributions, the grain size data of the various sections are in average self-similar to each other, independent of the ages of the explored deposits and the positions of the sections and the related sites in the basin. For all sections, a better statistical similarity is reached when the unmodified median GSD is transformed into the median ξ-distribution, that is based on the self-similarity variable ξ values. This suggest that on average, the values that characterise the variations in grain sizes, and thus the mean and the standard deviations, are proportional to each other through time and for all locations in the basin. The statistical highest similarity, however, is reached after a log-transformation of the data (Fig. 4.6c and Fig. SB4.2 in appendix B of this chapter). This also yields the highest probability that the data is normally distributed (Fig. 4.7c and Fig. SB4.3. in appendix B of this chapter). Therefore, for the following calculations of the relative mobility function, which requires similarity and implicitly assumes a normal distribution of the data, we considered the ξ(*ln*(GSD)) dataset only. Please note that we used the bulk dataset for the related calculations (section 4.4.5).

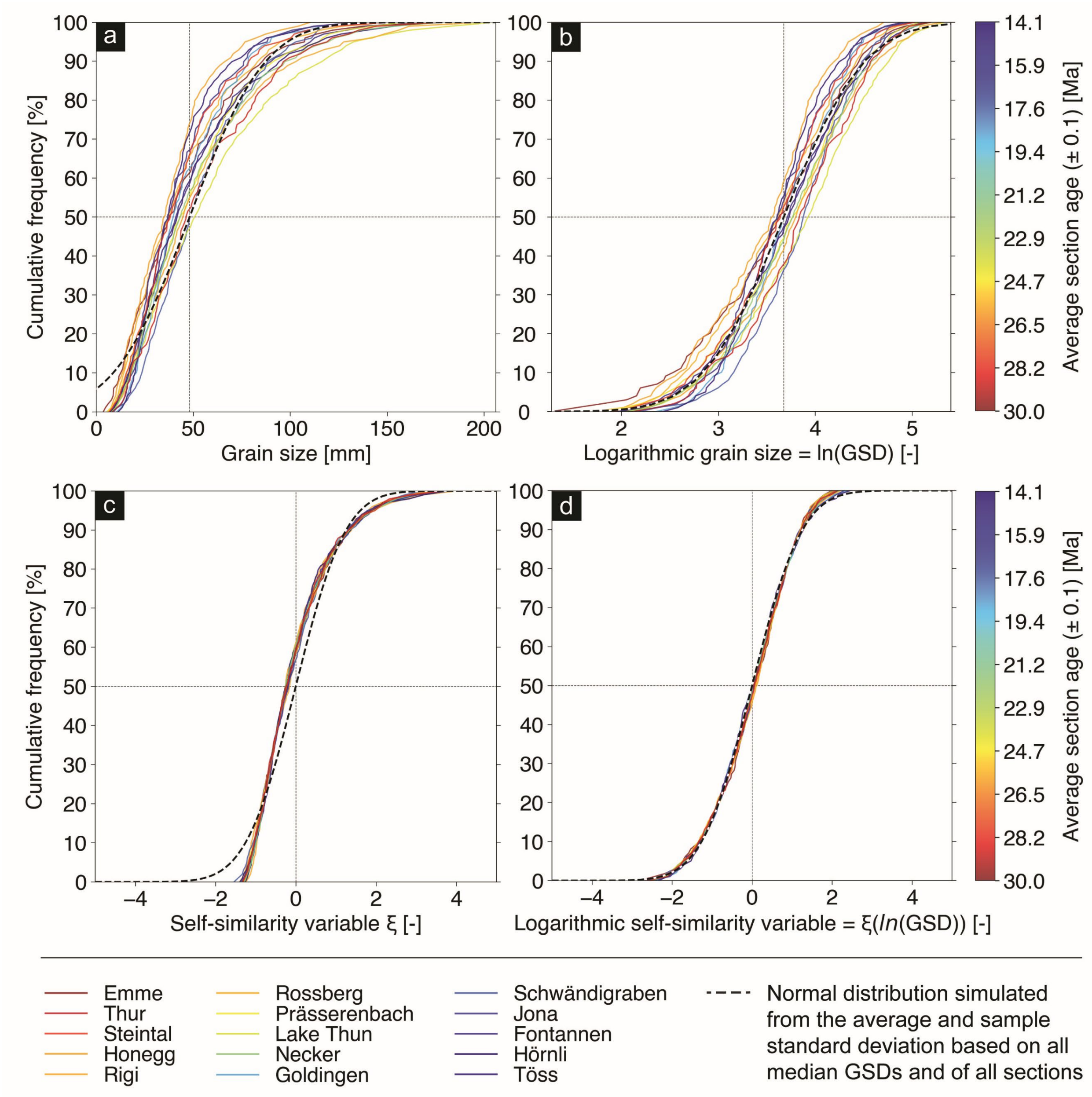

Figure 4.5: The cumulative distribution functions for each section of the **a)** median GSD and **b)** median log-transformed GSD, and **c)** median ξ and **d)** median ξ values calculated from the log-transformed GSD. Please see the section 4.4.5 for the calculation of the median distributions. The dotted black line indicates a simulated normal distribution of the data for all sections. The horizontal lines in each figure mark the position of the 50th percentile of this normal distribution, and the vertical line mark the value of the 50th percentile along the x-axis. Please find the corresponding figures with the bulk data of each section in appendix B (Fig. SB4.1) of this chapter.

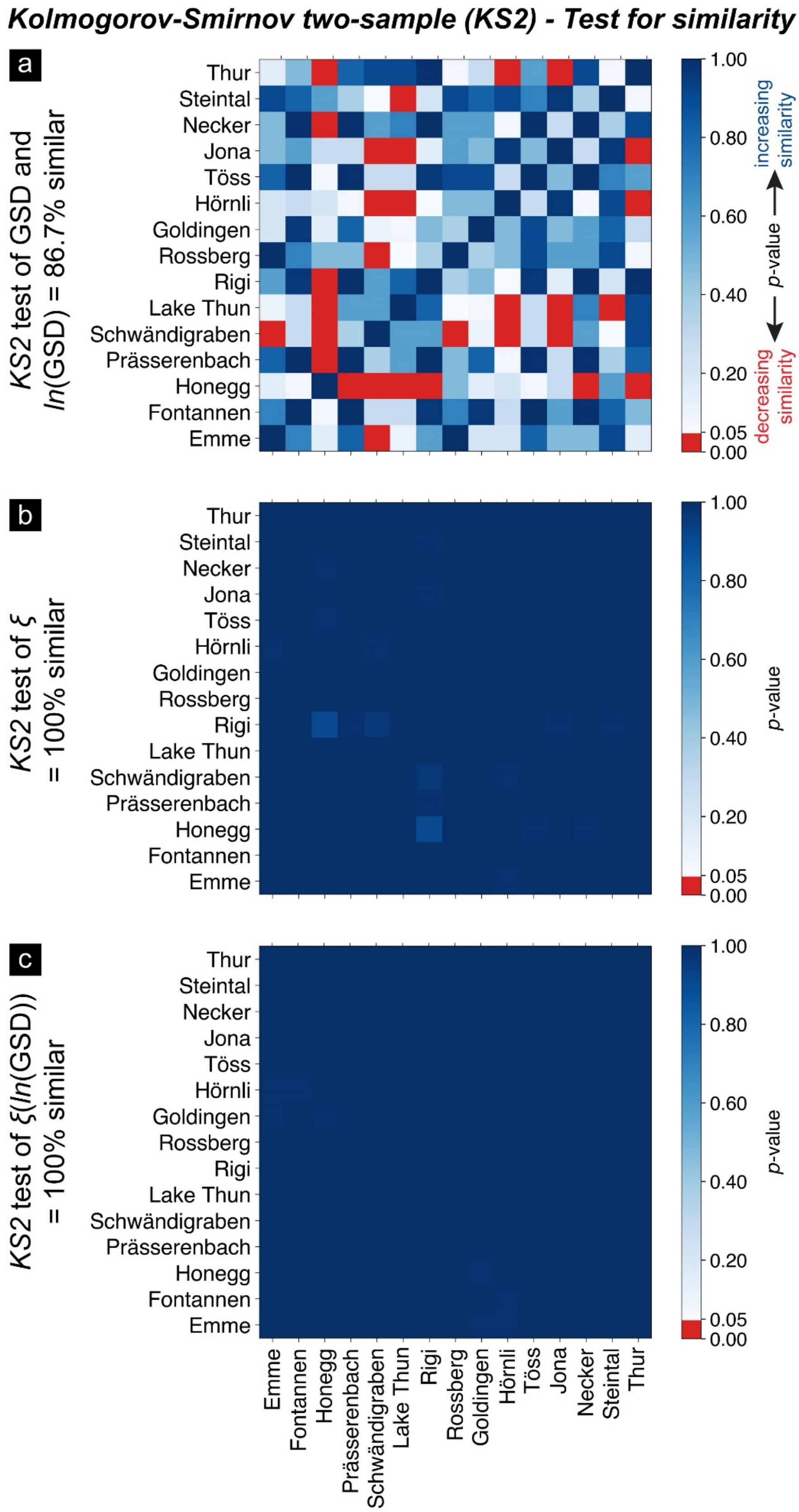

Figure 4.6: The results of the Kolmogorov-Smirnov two-sample (*KS2*) test for similarity for **a)** the GSD and the log-transformed GSD, **b)** the self-similarity variable ξ and **c)** the ξ values calculated on the log-transformed GSD. The results are based on the median GSDs and ξ-distributions (see methods). The tests were computed at the 95 % C.I. (i.e., significance level of α = 0.05). Please find the corresponding figures with the bulk data of each section in appendix B (Fig. SB4.2) of this chapter.

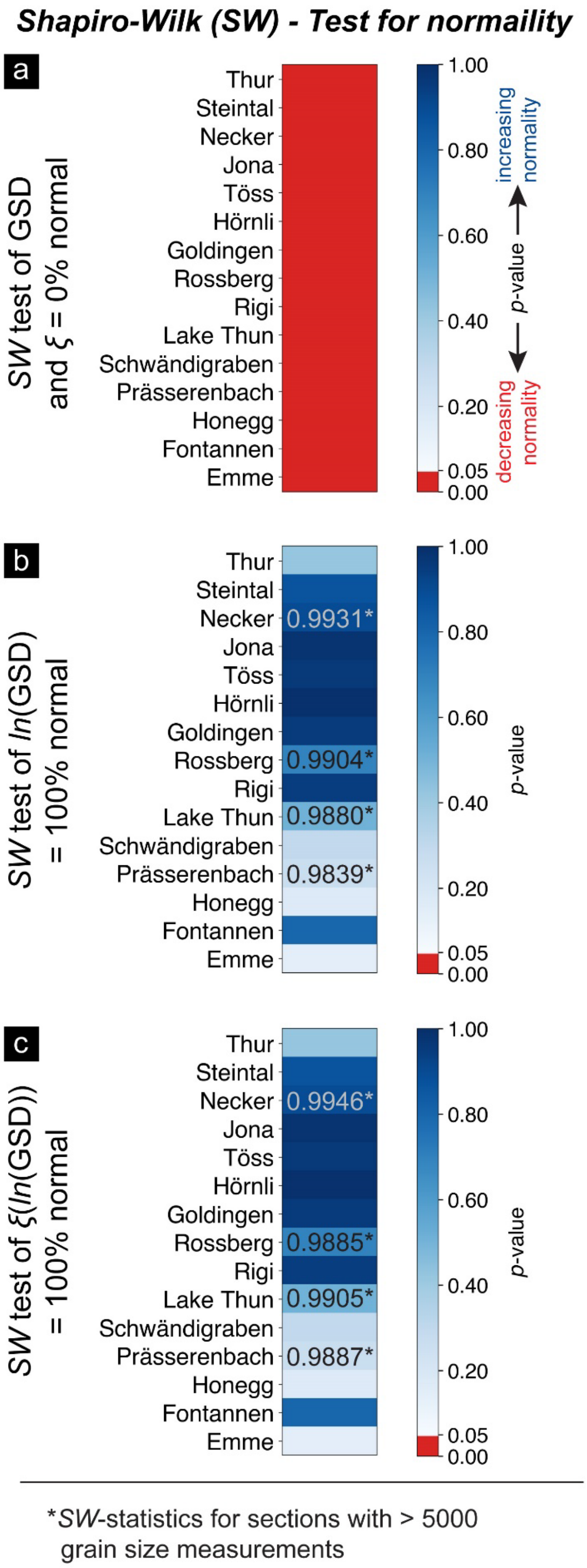

Figure 4.7: The results of the Shapiro-Wilk (*SW*) test for normality for **a)** the GSD and self-similarity variable ξ-distributions, **b)** the log-transformed GSD, and **c)** the ξ data calculated on the log-transformed GSD. The results are based on the median GSD and ξ-distributions (see methods). The tests were computed at the 95 % C.I. (i.e., significance level of α = 0.05). Please find the corresponding figures with the bulk data of each section in appendix B (Fig. SB4.3) of this chapter.

4.5.4 Modelling the relative mobility

We computed the solutions for the relative mobility function J based on the $\xi(ln(\text{GSD}))$ data for all stratigraphic sections. We did so upon modelling the best-fit solutions between the modelled $f(\xi)$ and the $\xi(ln(\text{GSD}))$ data. Please note, that for the calculations of the values that arise from the relative mobility function J and related (dimensionless) variables (C_V, C_1, C_2) and parameters (a_g, b_g, c_g; see 4.3.4 and 4.3.5) we considered the bulk GSD, thereby included potential statistical outliers, and transformed into log-space.

Our calculations for C_V, which is an input variable for the model, yielded values between c. 0.14 and 0.22 with an overall average of around 0.18 (Fig. 4.8a). Our calculations for C_2 yielded values between c. 3.4 and 5.3 with an average of c. 4.2 (Fig. 4.8a). Values of C_2 were calculated using our C_V values (see above) and fixed values for C_1. Hence, we considered values that are uniformly distributed between the range of 0.6 and 0.9, with an average of 0.75 (Fig. 4.8a). For both, C_V and C_2, we observed no significant trends, as the data largely scatter within 95 % C.I. (Fig. 4.8a). Only the Hörnli section yielded C_V values and related uncertainties that are different to those of some of the other sections (Fig. 4.8a). The modelling of the outcomes of the relative mobility function J for each section considers the broad variability of the input variables C_V, C_1, and C_2 (Fig. 4.8a). The range of the model output parameters fall between 0.23 – 0.27 for a_g, 0.67 – 0.79 for b_g, and are close to 0 (i.e., $2\text{x}10^{-16}$) for c_g (Fig. 4.8b). These outcomes for a_g and b_g lay within the range proposed by Harries et al., (2018) also calculated in log-space (section 4.1.1), however, these authors have fixed c_g at a value of 0.01. When plotted against increasing average ages of the sections, the parameters a_g and b_g vary within the given uncertainties (95 % C.I.; Fig. 4.8b).

The best-fit solutions of $f(\xi)$ together with the 95 % C.I. is plotted against the median of the $\xi(ln(\text{GSD}))$ distributions and the spread of the bulk data for each section (Fig. 4.9). When expressed by the median of our modelled $f(\xi)$ outcomes, the related curves (blue curves in Fig. 4.9) are slightly above the peak frequencies of the overall median ξ-distributions for all sections (black dotted curves in Fig. 4.9). Likewise, the left- and right-tails of the modelled median $f(\xi)$ curves are also situated above of the median ξ-distributions. In contrast, the median $f(\xi)$ curves tend to yield smaller frequencies at the positions of the left- and the right-shoulders of the median ξ distributions (Fig. 4.9). Overall, the modelled median $f(\xi)$ curves are in good agreement with the spread of the bulk ξ-distributions (i.e., ξ_{System} in Fig. 4.9). Given the high similarity between the model outcomes across all sections, each of the individual best-fit solutions all collapse on the same curve (Fig. 4.10).

We additionally tested how changes in the three parameters, a_g, b_g and c_g, of the relative mobility function have to be adjusted to fit different shapes of ξ-distributions. Our sensitivity analyses showed that symmetrical distributions with smaller peaks require smaller values for b_g and larger values for c_g. In contrast, ξ-distributions with higher peaks require larger values for b_g and smaller values for c_g. A combination of right-skewed ξ-distributions with low peaks are better approximated by large values of a_g, whereas left-skewed distributions with high peaks generally require small values of a_g. The specific combination of a_g, b_g and c_g, together with the individual solutions for C_V and C_2, might therefore create numerous best-fit solutions which is accommodated by the spread of the 95 % C.I. of these parameters (Fig. 4.8).

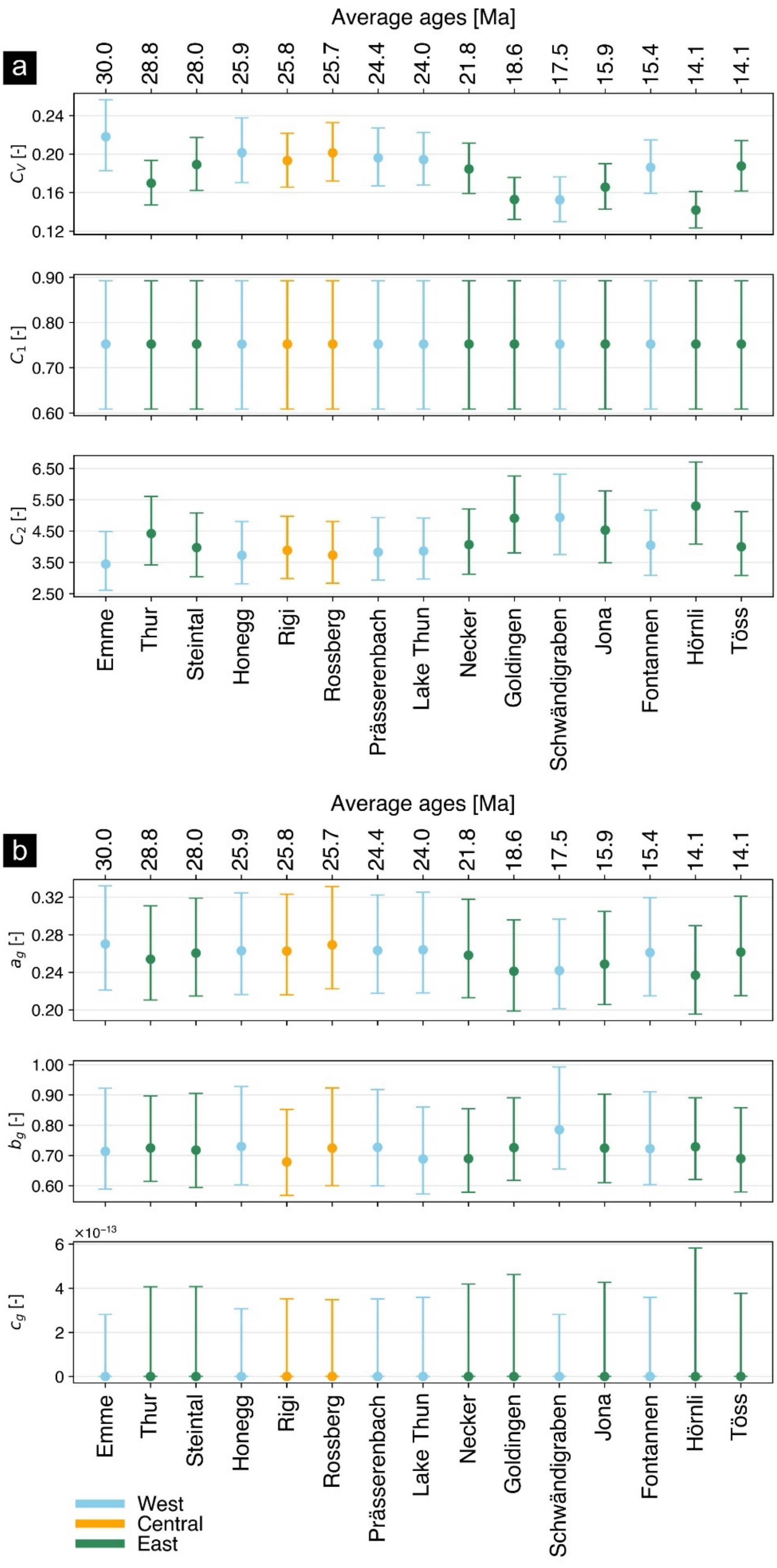

Figure 4.8: Results of the modelling variables and parameters illustrated as range-plots of **a)** the modelling input variables C_V, C_1 and C_2 and **b)** the modelling outcome parameters a_g, b_g and c_g for calculations of the relative mobility function. The spread of the uncertainties represents the 95 % C.I., and the data is arranged as increasing average age of the analysed sections. Please note the scientific notation for the parameter c_g.

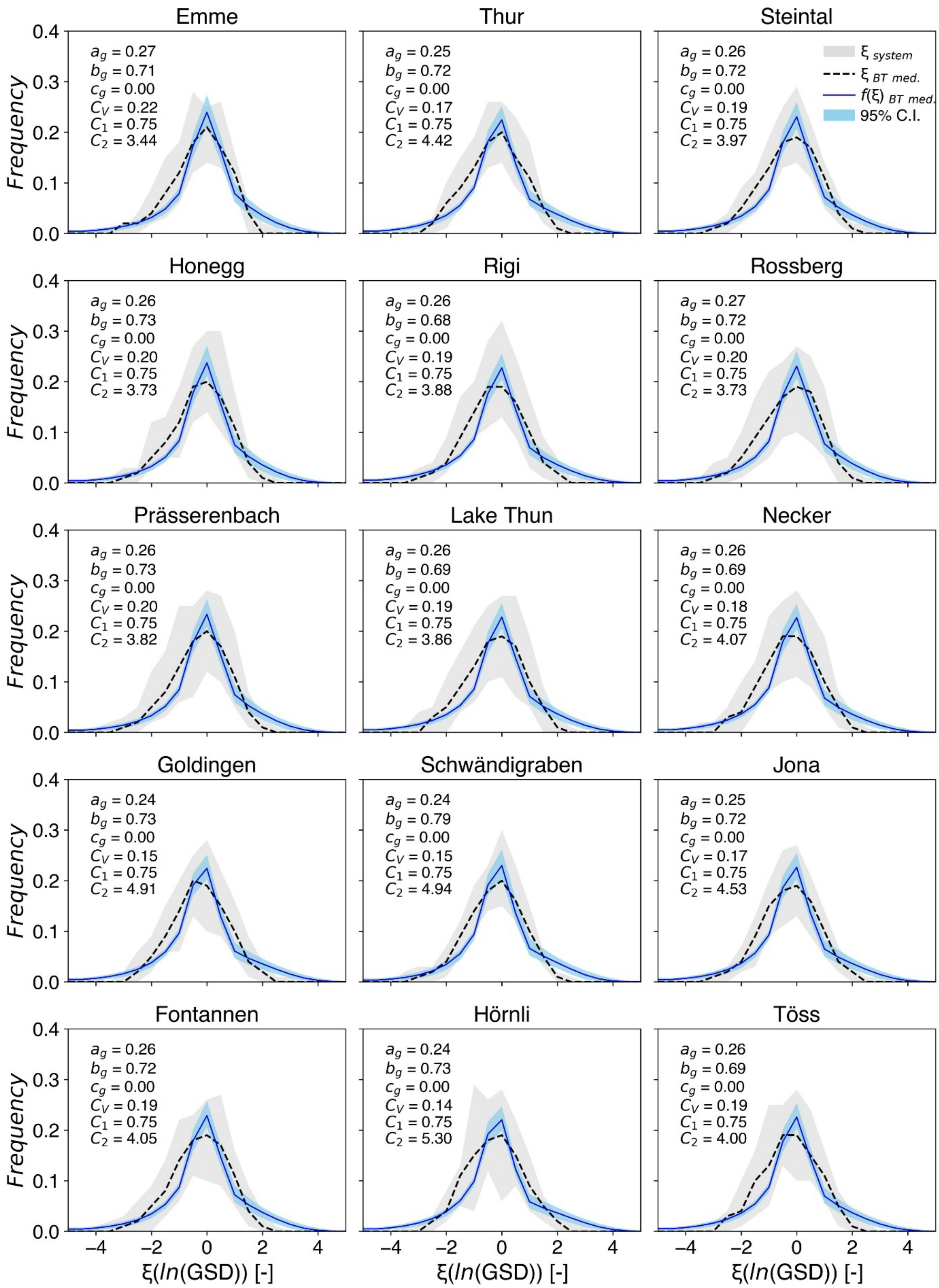

Figure 4.9: Solutions of the curve-fitting for the fraction of the material in the substrate as a function of ξ(*ln*(GSD)). The values of the model variables and parameters (top-left in each plot) are rounded to two decimals. For the related uncertainties, please see Fig. 4.8. Please note, for visualisation purposes and the sake of clarity, we only showed the median ξ and *f*(ξ) distributions as curves and the bulk data as gray-shaded regions (see also Fig. SB4.10. in appendix B of this chapter). Please find the related legend in the uppermost right plot.

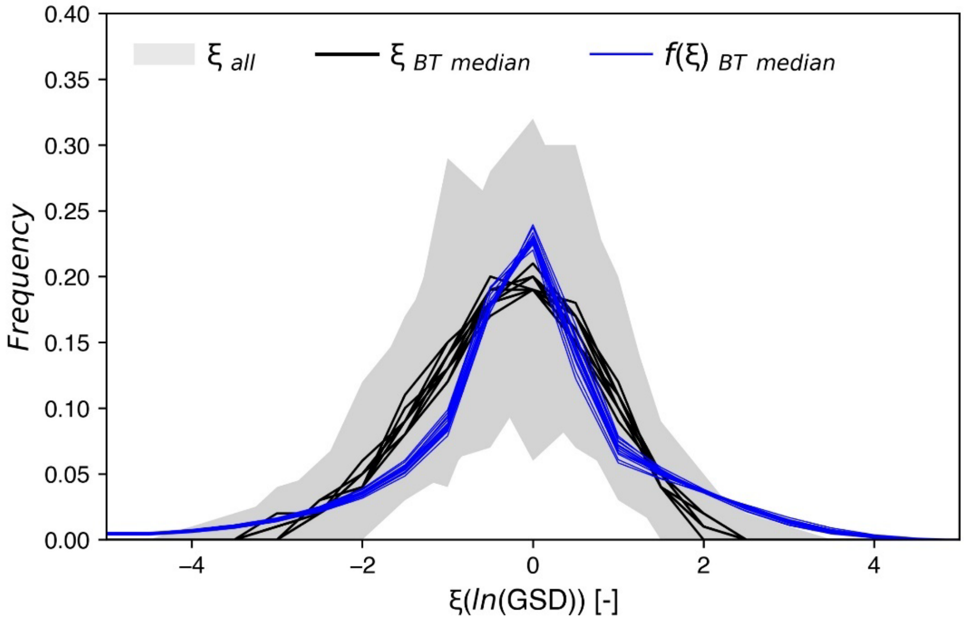

Figure 4.10: Solutions of the curve-fitting for the fraction of the material in the substrate as a function of ξ*(ln*(GSD)) for all sections (median curves only). The gray-coloured shaded area (ξ_{all}) represents the spread of all ξ-distributions of all sections. The individual solution for each section is shown in Fig. 4.9.

4.5.5 Solutions of the relative mobility function

Based on the model outcomes for $f(\xi)$ and the fitting to the $\xi(ln(\mathrm{GSD}))$ data, which yielded the results for the related parameters, a_g, b_g and c_g, we calculated the values for the relative mobility function J (Eq. 4.3) as a function of the $\xi(ln(\mathrm{GSD}))$ distributions for all sections. Given the high-similarity between the model-input variables (C_V, C_2), the values for $J(\xi(ln(\mathrm{GSD})))$ revealed a congruent pattern (Fig. 4.11a). The uncertainties expressed by the 95 % C.I. largely overlap between the values characterising the individual sections. This suggests that there are no significant differences between all sections (Fig. 4.11a). In particular, values for the case where $J = 1$ and for the $\xi(ln(\mathrm{GSD}))$ distributions, range between -1.97 and -1.80 with an overall average of c. -1.89 (inset in Fig. 4.11a). The back-transformation of non-dimensional $\xi(ln(\mathrm{GSD}))$ into dimensional grain size values (Eq. 4.10) reveals a similar pattern, where the 95 % C.I. generally overlap between the various sections (Fig. 4.11b). For the case where $J = 1$ and for the back-transformed grain size data, the corresponding critical grain size values range between c. 8 and 16 mm with an overall average around 12 mm (inset in Fig. 4.11b; see also Fig. SB4.5 in appendix B of this chapter). If compared to the relative mobility of the D_{50} or the D_{84}, then these specific percentiles have a c. 75 % or 88 % higher probability of being in the substrate than being in transport (i.e., the intersection at J for the grain size values of D_{50} and D_{84}). Therefore, the relative mobility of particles at all sections is relatively low.

When plotted against increasing average ages for the analysed sediments (per section), the values of $\xi(ln(\mathrm{GSD}))$ at $J = 1$ do not show a significant trend through time, as these largely scatter around the associated uncertainties (Fig. 4.12a). The cross-comparison of the back-transformed grain size values for the case where $J = 1$ revealed that all critical grain size values show variations through time, yet these values largely scatter around the associated uncertainties, and therefore apparent trends are not significant (Fig. 4.12b). Upon comparing the outcomes of the $\xi(ln(\mathrm{GSD}))$ values at $J = 1$ to the results of other studies, we observe that our calculations are within the same range of values and their associated uncertainties. For instance, Harries et al. (2018) reported values between approximately -0.3 and -1.5 for their modelled $J(\xi)$ values for the case where $J = 1$ (uncertainties included), where the underlying ξ datasets were also transformed into log-space.

4.5.6 Summary of relevant results

The statistical analyses of the grain size datasets collected from 15 stratigraphic sections revealed no significant trend of grain size variations through geological time. Such a pattern, particularly for the D_{50} and D_{84} values, becomes visible if the bulk grain size data per stratigraphic sections are considered. Albeit some apparent trends, the median values of these percentiles scatter around the related uncertainties (Fig. 4.4a). The transformation of the GSD into the self-similarity variable ξ yielded a similarity of 100 % for the data of all sections (median ξ and $\xi(ln(\mathrm{GSD}))$ distributions; Fig. 4.6b). Moreover, our data suggests that grain sizes measured from fluvial deposits indeed follow a log-normal distribution, which emphasises the necessity of applying a logarithmic transformation to the data. In fact, the ξ values calculated from the median *ln*(GSD) not only yield a similarity of 100 % of this data (Fig. 4.6c), it also discloses that underlying datasets follow a normal distribution (100 %; Fig. 4.7c), if compared to the non-transformed median GSD and ξ-distributions (Fig. 4.7a).

By applying the concept of relative mobility on our log-transformed data, notably by considering for each section the entire grain size dataset (bulk GSD), we were able to calculate the values of the relative mobility function J, which solutions for the case where $J = 1$ allow to estimate the critical grain size of particles that are either preferentially transported or deposited. We found that for all stratigraphic sections, the analytical solutions of J, for both the $\xi(ln(\text{GSD}))$ and the back-transformed grain size values, largely overlap within their uncertainties (i.e., 95 % C.I.; Fig. 4.11a and b). Finally, for the values calculated from the relative mobility function for the case where $J = 1$ (the situation where a particle with a critical grain size is equally in transport or deposited) and based on the back-transformed grain size values, the related outcomes range between 8 and 16 mm (Fig. 4.12b). The solutions also revealed that the D_{50} and D_{84} have a c. 75 and 88 % higher probability, respectively, of being stored in the substrate.

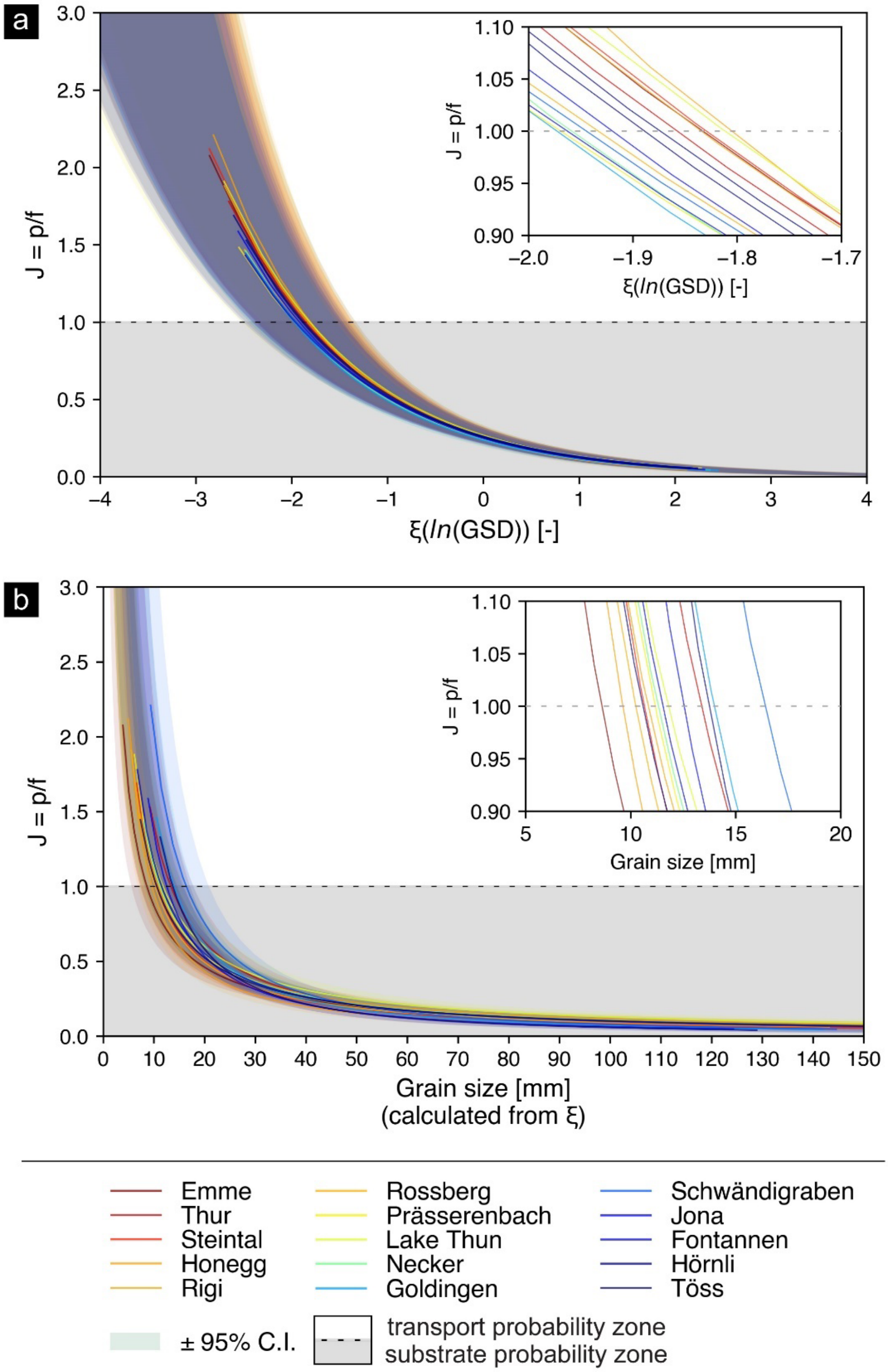

Figure 4.11: The solutions for the relative mobility function *J* (see Eq. 4.10) as a function of **a)** *ξ*(*ln*(GSD)) and **b)** the back-transformed dimensional grain size for all sections. For the sake of clarity, the insets in a) and b) do not show the uncertainty envelopes.

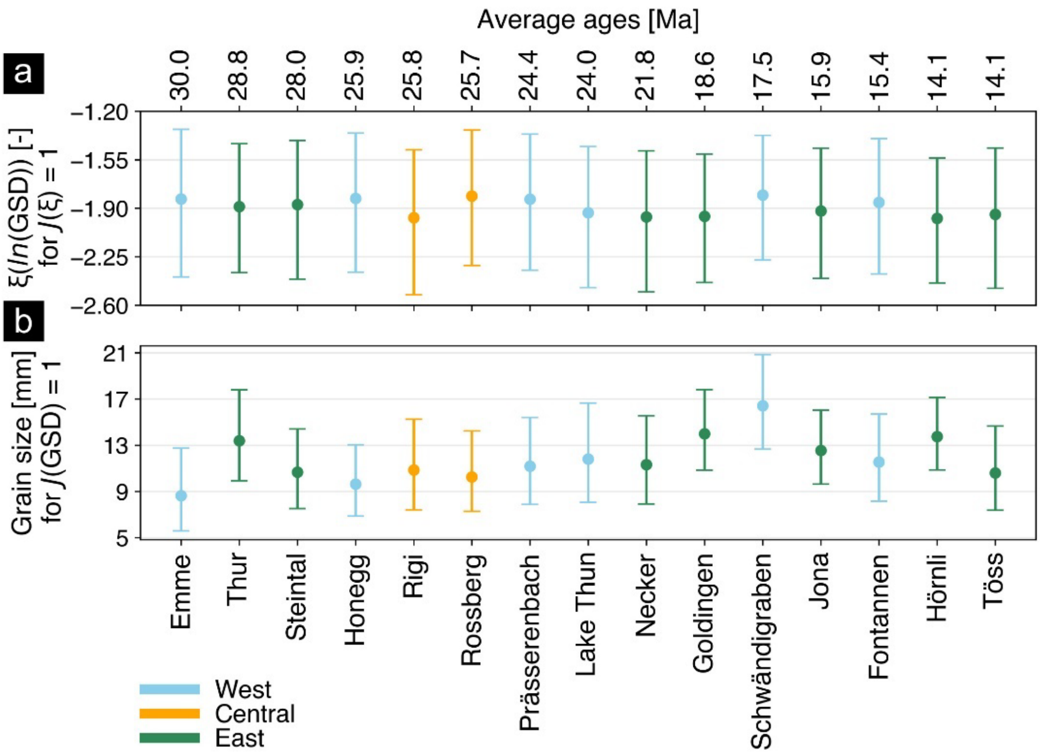

Figure 4.12: The solution values of the relative mobility function *J* (see Eq. 4.10) for the case where *J* = 1 and for **a)** the *ξ(ln*(GSD)) and **b)** the back-transformed dimensional grain size. The spread of the uncertainties represents the 95 % C.I., and the data is arranged in increasing average section age.

4.6 Discussion

4.6.1 Biases related to sampling strategies

To investigate the long-term temporal variations in grain size values across multiple stratigraphic sections, we have collapsed our GSD into a single dataset for each entire section. Accordingly, we did not collect grain size data along a proximal-distal transect. However, since most concepts applied in this work (section 4.3) base on proximal-distal relationships of sediment transport and deposition, our results and the resulting conclusions could be biased. One way to avoid such a bias would be the consequent collection of grain size data at sites that have a fixed location in relation to a specific point, e.g., the inferred apex of a system. However, this is possible for a few sections only, which are the Lake Thun, Rigi, and Necker sections. For the other sections, it is not possible to estimate the upstream distance to e.g., the Alpine border at the time the sediments were deposited, or such estimates would be associated with large uncertainties. However, for the aforementioned sections where the locations of the fans' apices were mapped (Schlunegger et al., 1997a; Kempf et al., 1999), the sedimentation was documented to have been influenced by a material supply through high-concentrated flows such as debris flows and mudflows. The mechanisms related to such mass movement processes violate the concepts of the applied models which base on the entrainment and transport of clasts through fluvial processes. This is the major reason why we collapsed the entire grain size dataset into a single GSD or grain size value characterising an entire section, where the deposits at different stratigraphic positions were likely deposited at spatially different locations on the paleo fans, in order to exploring possible controls on the long-term temporal patterns of grain size.

4.6.2 Relationships between changes in climate, sedimentary supply and grain size

Our results suggest no significant trend for our grain size data (GSD, specific grain sizes and the ξ-distributions). Likewise, no temporal changes are identified for the variables and parameters characterising the relative mobility function and the results for the case where $J = 1$, as all values largely scatter around a similar median value and within the related uncertainties. Because climate conditions, sediment supply and tectonic processes in the Alps have experienced large changes during the time (sections 4.2.3 and 4.2.4) as the coarse-grained material accumulated, we would expect that they would be related to corresponding shifts in grain size signals recorded in the SMB. In particular, the apparent increase in the median D_{84} and D_{50} values of the bulk GSD observed for the sections that chronicle the basin evolution between c. 28 to 21 Ma could be interpreted as the combined response to the Late Oligocene warming (LOWE; Fig. 4.13) and the increase in sediment supply to the basin. Likewise, the subsequent decrease in the grain size values could reflect the response to the oscillations in paleoclimate and particularly to the nearly contemporaneous decrease in sediment supply to the basin (Fig. 4.13). Whereas we cannot fully exclude such correlations and controls, the aforementioned changes in the granulometric properties of the Molasse sediments occur within uncertainties and are therefore statistically not significant.

4.6.3 Possible controls of tectonic processes, and relative mobility

The controls of tectonic processes on the development of grain size were documented at the scale of individual sections. In particular, as outlined in section 4.2.2, the trends towards coarser grained material from the base to the top of the Lake Thun, Prässerebach, Rigi and Necker sections were considered to have been controlled by thrusting at the Alpine front or/and by the increased supply of sediments. At the scale of the entire Alps, tectonic controls on changes in grain size patterns have not been explored in detail. Yet changes in sediment flux and shifts in the petrographic compositions of the conglomerates were related to large-scale tectonic processes. These include: i) the occurrence of the slab break-off at 32 – 30 Ma and the corresponding legacy, which was used to explain the rise in sediment supply between 30 – 22 Ma; ii) the tectonic unroofing of the Lepontine dome; and iii) the rise of the external massifs and the related change in the drainage pattern in the Alps from orogen-normal to orogen-parallel. The combination of the latter two mechanisms was invoked to explain the drop in sediment supply starting at 22 Ma and the subsequent transgression of the Burdigalian seaway at 20 Ma (Allen et al., 1985). Because of the proposed link between material supply and tectonic processes, and since we tentatively considered a corresponding response in the grain size datasets, such controls cannot be fully discarded. But similar to section 4.6.2, we note that the changes in the granulometric properties of the Molasse sediments as illustrated in Figure 4.13 occur within uncertainties.

The ambiguity in interpreting the temporal evolution of the grain size data (section 4.6.2 and above) is mainly rooted in the possible bias explained in section 4.6.1. Here, the solutions of the relative mobility function, particularly for the case when $J = 1$, where the probability of transport and deposition is the same, offers a solution as the underlying concept accounts for proximal-to-distal effects and upon normalising the grain size datasets (section 4.3). Indeed, our data implies that the values for the critical grain sizes are constant through time and measure c. 12 mm on average, irrespective about the time when the sediments were deposited, and the location where sedimentation accumulation occurred. This suggests that the mechanisms of selective transport and deposition have not changed significantly in the Molasse despite different climate conditions and various supply rates of material.

4.6.4 Steady-state conditions?

In a broader sense, it is surprising to see these low variations in grain sizes at the basin scale, where the values possibly do change through time, but where the shifts occurred within uncertainties. It may be that variations in the rates at which sediment was supplied to the basin might have been overprinted by local effects including e.g., sorting processes thereby averaging grain sizes on the long-term. Although short term perturbations (i.e., $<10^4$ years) are more likely controlled by such autogenic processes (Einsele et al., 1991; Hinderer, 2012; Hajek and Straub, 2017), recent studies showed that these self-organised mechanisms can also take place at longer time scales ($>10^6$ years), and therefore result in a dilution or even ‘shredding’ of the signals that have an allogenic driving force (Jerolmack and Paola, 2010; Wang et al., 2011; Paola, 2016; Romans et al., 2016; Straub et al., 2020). Therefore, any initial grain sizes, which were either coarser or finer, might have been buffered and averaged out throughout the long-term formation of the alluvial fans. Accordingly, signals related to external (allogenic) controlling forces might only be preserved in the stratigraphy if their amplitude is much larger than those of autogenic processes.

Alternatively, because selective extraction of grains into the stratigraphy is controlled by the combined effect of sediment supply and the formation of accommodation space, as explicitly implemented in the models (section 4.3), changes in grain size could be inferred to estimate how the ratio between these variables changed through time. For instance, for a given sediment supply, a low-subsidence rate promotes the occurrence of a low grain size fining trend, whereas a high-subsidence rate will be reflected by a higher rate at which the supplied material fines downstream (Duller et al., 2010; Armitage et al., 2011; Garefalakis et al., 2023b, submitted). In our case, however, trends in the grain size values occur within uncertainties and are therefore not statistically significant. This would suggest that at the basin scale, the supply of sediment occurred nearly in equilibrium with the rate at which accommodation space is generated. This invokes a mechanism where the basin formation and the built of the Alpine topography through subduction tectonics, and the erosional unloading of the Alps driven by environmental controls, occurred at steady state at least between 31 and 13 Ma when conglomerates accumulated. We thus suggest that such specific combinations likely occurred in the SMB, especially given the observed time range of c. 18 Myrs. However, the transgression of the peripheral sea at 20 Ma is not fully in line with such a view because the related shift from terrestrial to shallow marine conditions and the associated backstepping of the megafans (Schlunegger and Norton, 2015) was considered to have occurred because of a reduction sediment supply to the basin. Therefore, it possible that the sedimentary facies could be more sensitive to changes in the dominant driving mechanisms than grain size alone. This also reveals that grains and their sizes offer most likely not the best proxies for inferring tectonic and environmental controls on the sedimentation mechanisms at the basin scale.

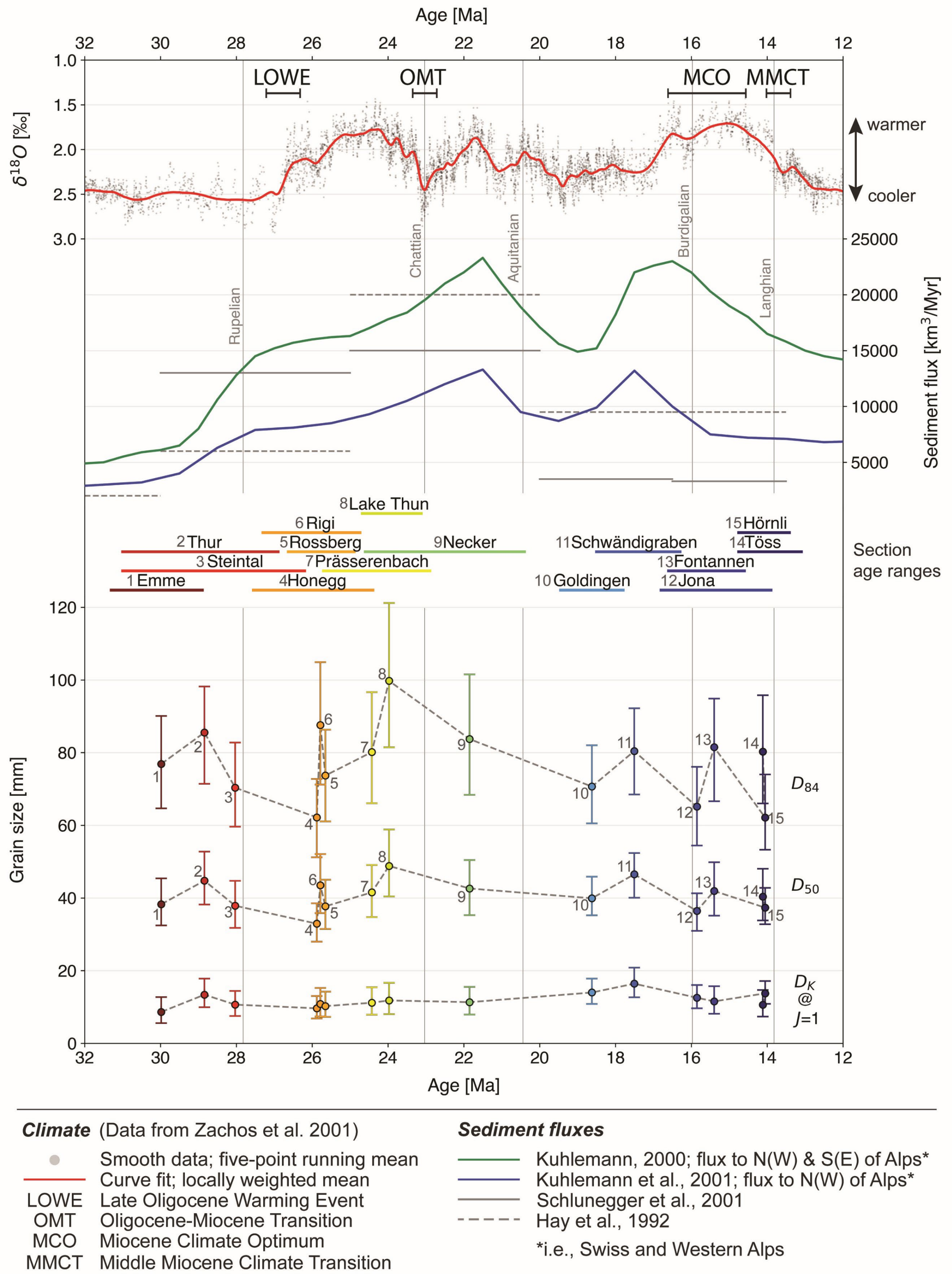

Figure 4.13: Grain sizes versus proxies for climate and tectonics. Compilation of proxies for the climate, expressed by the oxygen isotope record ($\delta^{18}O$), and the sediment flux estimates, thereby reflecting the tectono-geomorphological evolution of the Central Alps. The vertical lines mark the end of the corresponding geological stage (according to the ICS; International Commission on Stratigraphy). The age ranges of the sections indicate the uncertainty spread of the related grain size values along time. The positions of the grain size values (scatter dots) are aligned with the average section ages. The numbers 1-15 beside the section names and corresponding D_{84} and D_{50} values are for reference purposes. The dotted lines show a connection between the median grain size values.

4.7 Conclusion

We analysed long-term records of coarse-grained stratigraphic sections according to their grain size trends. We also explored the records regarding the competence of the paleostreams to transfer the supplied material, expressed as the relative mobility. For this, we focused on 15 stratigraphic sections recording alluvial megafan sedimentation in the Swiss Molasse Basin (SMB) during c. 18 Myrs throughout Oligo-Miocene times. At these sections, we measured the size of c. 50000 grains, and we statistically analysed the underlying grain size distributions (GSD). We applied the concept of self-similarity and relative mobility to this dataset, and we estimated the critical grain size of a particle that is likely in transport or preferentially stored in the substrate ($J = 1$). Because tectonic processes in the source area, sediment supply and climate conditions significantly changed during the time conglomerate sedimentation occurred, we anticipated large differences in the grain size through time.

Statistical tests (Kolmogorov-Smirnov two-sample test for similarity and Shapiro-Wilk test for normality) revealed that the underlying GSD are neither similar to each other nor do they follow a simulated normal distribution. Transformation of the grain size data into the self-similarity variable ξ (which is a normalisation by the local mean and standard deviation of each outcrop and for each grain size value; Fedele & Paola, 2007), yielded ξ-distributions that are 100 % similar across all sections. To achieve normality of the ξ-distributions, which is implicitly assumed in the self-similarity model, we transformed our GSD into logarithmic-space. The results showed that these log-transformed ξ-distributions (i.e., the $\xi(ln(\text{GSD}))$ data), are normally distributed and, as outlined above, 100% similar to each other. Given that the conditions of the model were satisfied (similarity and normality), we calculated the solutions for the relative mobility function J for each section, using the $\xi(ln(\text{GSD}))$ data and for the case where $J = 1$. The results suggest that the grain sizes data of all 15 sections were likely similar and infer the occurrence of a comparable relative mobility of the sedimentary material. In average, the rivers feeding the fans preferentially entrained grain sizes smaller than 12 mm, whereas coarser-grained material was preferentially stored in the substrate. In addition, the analysis of the GSD revealed that the values of the D_{50} and D_{84} grain size percentiles scatter around an average of c. 40 and 80 mm, respectively, thereby revealing no significant trend through time as these values lay within uncertainties expressed by the 95 % Confidence Interval (C.I.).

A comparison of the grain size values with i) the tectonic evolution in the hinterland, ii) the supply rates of the sediment to the basin, and iii) the climatic conditions at the time the material was deposited did not disclose obvious correlations at the scale of the basin. It is thus possible that the formation rate of accommodation space occurred in pace with the supply rates of sediment, with the consequence that, at the scale of the entire basin, the grain sizes were nearly constant through time. If changes in grain size did occur, they were too small to be statistically significant. However, the transgression of the peripheral sea at 20 Ma and the associated backstepping of the megafans were considered to have occurred because of a reduction of sediment supply to the Molasse basin. While such shifts in external driving forces are recorded by the development of the sedimentary facies at the basin scale, the granulometric properties of grains are possibly not fully sensitive to these and are therefore not fully conclusive for inferring shifts in the mechanisms driving the evolution of the Alps and the Molasse basin.

4.8 Author contribution

The study has been created by PG, Fritz Schlunegger and Alexander C. Whittaker. PG carried out the fieldwork, collected the samples, and analysed the data with additional scientific input by Ariel Henrique do Prado, David Mair, Alexander C. Whittaker, and Fritz Schlunegger. PG prepared the manuscript and the figures with contributions from Fritz Schlunegger. The manuscript is in preparation and has not been sent to the co-authors yet.

4.9 Funding sources

Philippos Garefalakis reports financial support was provided by the Swiss National Science Foundation (SNSF) [P1BEP2_200189].

4.10 Bibliography

Allen, P. A., Armitage, J. J., Carter, A., Duller, R. A., Michael, N. A., Sinclair, H. D., et al. (2013). The *Qs* Problem: Sediment volumetric balance of proximal foreland basin systems. Sedimentology 60, pp. 102–130. https://doi.org/10.1111/sed.12015

Allen, P. A., Crampton, S. L., and Sinclair, H. D. (1991). The inception and early evolution of the north Alpine foreland basin, Switzerland. Basin Res. 3, pp. 143–163. https://doi.org/10.1111/j.1365-2117.1991.tb00124.x

Allen, P. A., Mange-Rajetky, M. A., Matter, A., and Homewood, P. (1985). Dynamic paleogeography of the open Burdigalian seaway, Swiss Molasse Basin. Eclogae Geol. Helv. 78, pp. 351–381. https://doi.org/10.5169/seals-165661

Armitage, J. J., Duller, R. A., Whittaker, A. C., and Allen, P. A. (2011). Transformation of tectonic and climatic signals from source to sedimentary archive. Nat. Geosci. 4, pp. 231–235. https://doi.org/10.1038/ngeo1087

Beaumont, C. (1981). Foreland Basins. pp. 291–329. https://doi.org/10.1002/9781444303810

Berger, J.-P. (1992). Paléontologie de la Molasse de Suisse occidentale: Taxinomie, Biostratigraphie, Paléoecologie, Paléogéographie, Paléoclimatologie. Habilitation thesis, 405 pp. (in French)

Blom, A., Viparelli, E., and Chavarrías, V. (2016). The graded alluvial river: Profile concavity and downstream fining. Geophys. Res. Lett. 43, pp. 6285–6293. https://doi.org/10.1002/2016GL068898

Boston, K. R., Rubatto, D., Hermann, J., Engi, M., and Amelin, Y. (2017). Geochronology of accessory allanite and monazite in the Barrovian metamorphic sequence of the Central Alps, Switzerland. Lithos. 286–287, pp. 502–518. https://doi.org/10.1016/j.lithos.2017.06.025

Brooke, S. A. S., Whittaker, A. C., Armitage, J. J., D'Arcy, M., and Watkins, S. E. (2018). Quantifying Sediment Transport Dynamics on Alluvial Fans From Spatial and Temporal Changes in Grain Size, Death Valley, California. J. Geophys. Res. Earth Surf. 123, pp. 2039–2067. https://doi.org/10.1029/2018JF004622

Büchi, U. P. (1958). Zur Geologie der Oberen Süsswassermolasse (OSM) zwischen Töss- und Glattal. Eclogae Geol. Helv. 51, pp. 73–105. (in German) https://doi.org/10.5169/seals-162429

Bunte, K., Abt, S. R., Potyondy, J. P., and Ryan, S. E. (2004). Measurement of Coarse Gravel and Cobble Transport Using Portable Bedload Traps. J. Hydraul. Eng. 130, pp. 879–893. https://doi.org/10.1061/(asce)0733-9429(2004)130:9(879)

Bürgisser, H. M. (1980). Zur Mittel-Miozänen Sedimentation im nordalpinen Molassebecken: Das "Appenzellergranit"-Leitniveau des Hörnli-Schuttfächers (OSM). PhD Thesis, ETH Zürich, Switzerland. pp. 196. (in German) https://doi.org/10.3929/ethz-a-010782581

Bürgisser, H. M. (1981). Fazies und Paläohydrogeologie der Oberen Süsswassermolasse im Hörnli-Fächer (Nordostschweiz). Eclogae Geol. Helv. 1, pp. 19–28. (in German)
https://doi.org/10.5169/seals-165087

Cande, S. C., and Kent, D. V. (1995). Revised calibration of the geomagnetic polatiry timescale for the Late Cretaceous and Cenozoic. J. Geophys. Res. 100, pp. 6093–6095.

Castelltort, S., Whittaker, A. C., and Vergés, J. (2015). Tectonics, sedimentation and surface processes: from the erosional engine to basin deposition. Earth Surf. Process. Landforms, 1846, pp. 1839–1846.
https://doi.org/10.1002/esp.3769

Church, M., and Kellerhals, R. (1978). On the statistics of grain size variation along a gravel river. Can. J. Earth Sci. 15, pp. 1151–1160.
https://doi.org/doi.org/10.1139/e78-121

D'Arcy, M., Whittaker, A. C., and Roda-Boluda, D. C. (2017). Measuring alluvial fan sensitivity to past climate changes using a self-similarity approach to grain-size fining, Death Valley, California. Sedimentology 64, pp. 388–424.
https://doi.org/10.1111/sed.12308

DeCelles, P. G., and Giles, K. A. (1996). Foreland basin systems. Basin Res. 8, pp. 105–123.
https://doi.org/10.1046/j.1365-2117.1996.01491.x

Duller, R. A., Whittaker, A. C., Fedele, J. J., Whitchurch, A. L., Springett, J., Smithells, R., et al. (2010). From grain size to tectonics. J. Geophys. Res. Earth Surf. 115, pp. 1–19.
https://doi.org/10.1029/2009JF001495

Einsele, G., Ricken, W., and Seilacher, A. (1991). Cycles and Events in Stratigraphy. Berlin: Springer-Verlag.

Engesser, B., and Kälin, D. (2017). Eomys Helveticus N. Sp. and Eomys Schlunegger N. Sp., two new small Eomyids of the Chattian (MP25/MP26) Subalpine Lower Freshwater Molasse of Switzerland. Foss. Impr. 73, pp. 213–224.
https://doi.org/10.1515/if-2017-0012

Eynatten, H. v. (2003). Petrography and chemistry of sandstones from the Swiss Molasse Basin: An archive of the Oligocene to Miocene evolution of the Central Alps. Sedimentology 50, pp. 703–724.
https://doi.org/10.1046/j.1365-3091.2003.00571.x

Fedele, J. J., and Paola, C. (2007). Similarity solutions for fluvial sediment fining by selective deposition. J. Geophys. Res. Earth Surf. 112, pp. 1–13.
https://doi.org/10.1029/2005JF000409

Ferguson, R., Hoey, T., Wathen, S., and Werritty, A. (1996). Field evidence for rapid downstream fining of river gravels through selective transport. Geology 24, pp. 179–182.
https://doi.org/10.1130/00917613(1996)024<0179:FEFRDF>2.3.CO;2

Friedman, G. M. (1962). On Sorting, Sorting Coefficients, and the Lognormality of the Grain-Size Distribution of Sandstones. J. Geol. 70, pp. 737–753.
https://www.jstor.org/stable/30066373

Garefalakis, P., and Schlunegger, F. (2018). Link between concentrations of sediment flux and deep crustal processes beneath the European Alps. Sci. Rep. 8, 183.
https://doi.org/10.1038/s41598-017-17182-8

Garefalakis, P., and Schlunegger, F. (2019). Tectonic processes, variations in sediment flux, and eustatic sea level recorded by the 20-Myr old Burdigalian transgression in the Swiss Molasse basin. Solid Earth 10, pp. 2045–2072.
https://doi.org/10.5194/se-10-2045-2019

Garefalakis, P., do Prado, A. H., Mair, D., Douillet, G. A., Nyffenegger, F., and Schlunegger, F. (2023a). Comparison of three grain size measuring methods applied to coarse-grained gravel deposits. Sediment. Geol. 446, 100310. doi:
https://doi.org/10.1016/j.sedgeo.2023.106340

Garefalakis, P., do Prado, A. H., Whittaker, A. C., Mair, D., and Schlunegger, F. (2023b). Quantification of sediment fluxes and intermittencies from Oligo-Miocene megafan deposits in the Swiss Molasse basin. Submitted to Basin Research (28 June 2023). *See Chapter 3 of this thesis.*

Glotzbach, C., Reinecker, J., Danišík, M., Rahn, M., Frisch, W., and Spiegel, C. (2010). Thermal history of the central Gotthard and Aar massifs, European Alps: Evidence for steady state, long-term exhumation. J. Geophys. Res. Earth Surf. 115.
https://doi.org/10.1029/2009JF001304

Gradstein, F. M., Ogg, J. G., and Smith, A. G. S. (2004). A Geologic Time Scale 2004 - The Neogene Period. Cambridge University Press. ISBN: 0521786738.

Gradstein, F. M., Ogg, J. G., Schmitz, M. D., and Ogg, G. M. (2020). A Geologic Time Scale 2020. ISBN: 9780128243602.

Hajek, E. A., and Straub, K. M. (2017). Autogenic Sedimentation in Clastic Stratigraphy. Annu. Rev. Earth Planet. Sci. 45, pp. 681–709.
https://doi.org/10.1146/annurev-earth-063016-015935

Hantke, R. (1980). Die Obere Süsswassermolasse der Schweiz, ihr Paläorelief und ihre stratigraphische Fortsetzung in die Vogesen-Schüttung. Vierteljahrsschrift der Naturforschenden Gesellschaft Zürich 125, pp. 365–374. (in German) Available at: https://www.ngzh.ch/publikationen/vjs/125/4

Hantke, R., Letsch, D., Felber, P., Baumeler, A., Heinz, R., Uttinger, J., et al. (2022). Blatt 1152 Ibergeregg. - Geol. Atlas Schweiz 1:25 000, Erläut. 175. (in German)
Available at: www.swisstopo.ch

Harries, R. M., Kirstein, L. A., Whittaker, A. C., Attal, M., Peralta, S., and Brooke, S. (2018). Evidence for Self-Similar Bedload Transport on Andean Alluvial Fans, Iglesia Basin, South Central Argentina. J. Geophys. Res. Earth Surf. 123, pp. 2292–2315.
https://doi.org/10.1029/2017JF004501

Harvey, A. M., Mather, A. E., and Stokes, M. (2005). Alluvial fans: Geomorphology, sedimentology, dynamics - Introduction. A review of alluvial-fan research. Geol. Soc. Spec. Publ. 251, pp. 1–7.
https://doi.org/10.1144/GSL.SP.2005.251.01.01

Hay, W. W., Wold, C. N., and Herzog, J. M. (1992). "Preliminary Mass-Balance 3D Reconstructions of the Alps and the surrounding areas during the Miocene," in Computer Graphics in Geology. Lecture Notes in Earth Sciences, 41, eds. R. Pflug and J. W. Harbaugh (Springer, Berlin), pp. 99–110.
https://doi.org/10.1007/BFb0117790

Herwegh, M., Berger, A., Baumberger, R., Wehrens, P., and Kissling, E. (2017). Large-Scale Crustal-Block-Extrusion During Late Alpine Collision. Sci. Rep. 7, 413.
https://doi.org/10.1038/s41598-017-00440-0

Hinderer, M. (2012). From gullies to mountain belts: A review of sediment budgets at various scales. Sediment. Geol. 280, pp. 21–59.
https://doi.org/10.1016/j.sedgeo.2012.03.009

Hodges, J. L. (1958). The significance probability of the Smirnov two-sample test. Ark. för Mat. 3, pp. 469–486.
https://doi.org/10.1007/BF02589501

Hoey, T. B., and Bluck, B. J. (1999). Identifying the controls over downstream fining of river gravels. J. Sed. Res. 69, pp. 40–50.
https://doi.org/10.2110/jsr.69.40

Jerolmack, D. J., and Paola, C. (2010). Shredding of environmental signals by sediment transport. Geoph. Res. Lett. 37, pp. 1-5.
https://doi.org/10.1029/2010GL044638

Jost, J., Kempf, O., and Kälin, D. (2016). Stratigraphy and palaeoecology of the Upper Marine Molasse (OMM) of the central Swiss Plateau. Swiss J. Geosci. 109, pp. 149–169.
https://doi.org/10.1007/s00015-016-0223-6

Kälin, D., and Kempf, O. (2009). High-resolution stratigraphy from the continental record of the Middle Miocene Northern Alpine Foreland Basin of Switzerland. Neues Jahrb. für Geol. und Paläontologie - Abhandlungen 254, pp. 177–235.
https://doi.org/10.1127/0077-7749/2009/0010

Kempf, O. (1998). Magnetostratigraphy and facies evolution of the Lower Freshwater Molasse (USM) of eastern Switzerland. Unpubl. PhD thesis, University of Bern, Switzerland. pp. 283.

Kempf, O., Bolliger, T., Kälin, D., Engesser, B., and Matter, A. (1997). "New Magnetostratigraphic Calibration of Early to Middle Miocene Mammal Biozones of the North Alpine Foreland Basin," in Actes du Congrès BIochrom'97, eds. J. Aguilar, S. Legendre, J. Michaux, and B. Mammalienne, pp. 547–561.

Kempf, O., and Matter, A. (1999). Magnetostratigraphy and depositional history of the Upper Freshwater Molasse (OSM) of eastern Switzerland. Eclogae Geol. Helv. 92, pp. 97–103.
https://doi.org/10.5169/seals-168650

Kempf, O., Matter, A., Burbank, D. W., and Mange, M. (1999). Depositional and structural evolution of a foreland basin margin in a magnetostratigraphic framework: The eastern Swiss Molasse Basin. Int. J. Earth Sci. 88, pp. 253–275.
https://doi.org/10.1007/s005310050263

Kempf, O., and Pross, J. (2005). The lower marine to lower freshwater Molasse transition in the northern Alpine foreland basin (Oligocene; central Switzerland-south Germany): Age and geodynamic implications. Int. J. Earth Sci. 94, pp. 160–171.
https://doi.org/10.1007/s00531-004-0437-0

Krsnik, E., Methner, K., Campani, M., Botsyun, S., Mutz, S. G., Ehlers, T. A., et al. (2021). Miocene high elevation in the Central Alps. Solid Earth 12, pp. 2615–2631.
https://doi.org/10.5194/se-12-2615-2021

Kuhlemann, J. (2000). Post-Collisional Sediment Budget of Circum-Alpine Basins (Central Europe). Mem. Di Sci. Geol. Padova 52, pp. 1–93.

Kuhlemann, J., Frisch, W., Dunkl, I., and Székely, B. (2001). Quantifying tectonic versus erosive denudation by the sediment budget: the Miocene core complexes of the Alps. Tectonophysics 330, pp. 1–23.
https://doi.org/10.1016/S0040-1951(00)00209-2

Kuhlemann, J., and Kempf, O. (2002). Post-Eocene evolution of the North Alpine Foreland Basin and its response to Alpine tectonics. Sediment. Geol. 152, pp. 45–78.
https://doi.org/10.1016/S0037-0738(01)00285-8

Kühni, A., and Pfiffner, O. A. (2001). Drainage patterns and tectonic forcing: A model study for the Swiss Alps. Basin Res. 13, pp. 169–197.
https://doi.org/10.1046/j.1365-2117.2001.00146.x

Litty, C., Duller, R., and Schlunegger, F. (2016). Paleohydraulic reconstruction of a 40 ka-old terrace sequence implies that water discharge was larger than today. Earth Surf. Process. Landforms 41, pp. 884–898.
https://doi.org/10.1002/esp.3872

Matter, A. (1964). Sedimentologische Untersuchungen im östlichen Napfgebiet (Entlebuch - Tal der Grossen Fontanne, Kt. Luzern). Eclogae Geol. Helv. 57, pp. 315–429. (in German)

Matter, A., Homewood, P., Caron, C., Rigassi, D., van Stuijvenberg, J., Weidmann, M., et al. (1980). "Flysch and Molasse of western and central Switzerland," in Geology of Switzerland: A Guide Book. Part B Geological Excursions, Eds. P. Homewood and R. Trümpy (Basel: Wepf & Co), pp. 261–293.

Matter, A., and Weidmann, M. (1992). Tertiary sedimentation in the Swiss Molasse: An overview. Eclogae Geol. Helv. 85, pp. 776–777.
https://doi.org/10.5169/seals-167041

Methner, K., Campani, M., Fiebig, J., Löffler, N., Kempf, O., and Mulch, A. (2020). Middle Miocene long-term continental temperature change in and out of pace with marine climate records. Sci. Rep. 10.
https://doi.org/10.1038/s41598-020-64743-5

Meyer-Peter, E., and Müller, R. (1948). Formulas for Bed-Load Transport. Proc. 2nd Meet. Int. Assoc. Hydraul. Res., pp. 39–64.
https://doi.org/1948-06-07

Miller, K. L., Szabó, T., Jerolmack, D. J., and Domokos, G. (2014). Quantifying the significance of abrasion and selective transport for downstream fluvial grain size evolution. J. Geophys. Res. F Earth Surf. 119, pp. 2412–2429.
https://doi.org/10.1002/2014JF003156

Mosbrugger, V., Utescher, T., and Dilcher, D. L. (2005). Cenozoic continental climatic evolution of Central Europe. Proc. Natl. Acad. Sci. U. S. A. 102, pp. 14964–14969.
https://doi.org/10.1073/pnas.0505267102

Paola, C. (2016). A Mind of Their Own: Recent Advances in Autogenic Dynamics in Rivers and Deltas. Autogenic Dyn. Self-Organization Sediment. Syst. 106, 0.
https://doi.org/10.2110/sepmsp.106.04

Paola, C., Heller, P. L., and Angevinet, C. L. (1992). The Large Scale Dynamics Of Grain Size Variation In Alluvial Basins, 1: Theory. Basin Res. 4, pp. 73–90.
https://doi.org/10.1111/j.1365-2117.1992.tb00145.x

Paola, C., and Mohrig, D. (1996). Palaeohydraulics revisited: Palaeoslope estimation in coarse-grained braided rivers. Basin Res. 8, pp. 243–254.
https://doi.org/10.1046/j.1365-2117.1996.00253.x

Paola, C., and Voller, V. R. (2005). A generalized Exner equation for sediment mass balance. J. Geoph. Res. E.Surf. 110, pp. 1–8.
https://doi.org/10.1029/2004JF000274

Parker, G. (1991). Selective sorting and abrasion of river gravel. I: Theory. J. Hydraul. Eng. 117, pp. 131–147.
https://doi.org/10.1061/(ASCE)0733-9429(1991)117:2(131)

Parker, G., Wilcock, P. R., Paola, C., Dietrich, W. E., and Pitlick, J. (2007). Physical basis for quasi-universal relations describing bankfull hydraulic geometry of single-thread gravel bed rivers. J. Geophys. Res. Earth Surf. 112, pp. 1–21.
https://doi.org/10.1029/2006JF000549

Pfiffner, O. A. (1986). Evolution of the north Alpine foreland basin in the Central Alps (Switzerland). Spec. Publs int. Ass. Sediment. 8, pp. 219–228.
https://doi.org/10.1002/9781444303810.ch11

Pfiffner, O. A., Schlunegger, F., and Buiter, S. J. H. (2002). The Swiss Alps and their peripheral foreland basin: Stratigraphic response to deep crustal processes. Tectonics 21, pp. 1-16.
https://doi.org/10.1029/2000TC900039

Rasband, W. S. (1997). ImageJ.
Available at: https://imagej.nih.gov/ij/

Romans, B. W., Castelltort, S., Covault, J. A., Fildani, A., and Walsh, J. P. (2016). Environmental signal propagation in sedimentary systems across timescales. Earth-Science Rev. 153, pp. 7–29.
https://doi.org/10.1016/j.earscirev.2015.07.012

Schlunegger, F. (1999). Controls of surface erosion on the evolution of the Alps: Constraints from the stratigraphies of the adjacent foreland basins. Int. J. Earth Sci. 88, pp. 285–304.
https://doi.org/10.1007/s005310050265

Schlunegger, F., Matter, A., and Mange, M. A. (1993). Alluvial fan sedimentation and structure of the southern Molasse Basin margin, Lake Thun area, Switzerland. Eclogae Geol. Helv. 86, pp. 717–750.
https://doi.org/10.5169/seals-167260

Schlunegger, F., Burbank, D. W., Matter, A., Engesser, B., and Mödden, C. (1996). Magnetostratigraphic calibration of the Oligocence to Middle Miocene (30-15 Ma) mammal biozones and depositional sequences of the Swiss Molasse Basin. Eclogae Geol. Helv. 89, pp. 753–788.
https://doi.org/10.5169/seals-168650

Schlunegger, F., Jordan, T. E., and Klaper, E. M. (1997a). Controls of erosional denudation in the orogen on foreland basin evolution: The Oligocene central Swiss Molasse Basin as an example. Tectonics 16, pp. 823–840.
https://doi.org/10.1029/97TC01657

Schlunegger, F., Leu, W., and Matter, A. (1997b). Sedimentary sequences, seismic facies, subsidence analysis, and evolution of the Burdigalian Upper Marine Molasse Group, central Switzerland. AAPG Bull. 81, pp. 1185–1207.
https://doi.org/10.1306/522B4A19-1727-11D7-8645000102C1865D

Schlunegger, F., Matter, A., Burbank, D. W., and Klaper, E. M. (1997c). Magnetostratigraphic constraints on relationships between evolution of the central Swiss Molasse basin and Alpine orogenic events. GSA Bull. 109, pp. 225–241.
https://doi.org/10.1130/0016-7606(1997)109<0225:MCORBE>2.3.CO;2

Schlunegger, F., Slingerland, R. L., and Matter, A. (1998). Crustal thickening and crustal extension as controls on the evolution of the drainage network of the central Swiss Alps between 30 Ma and the present: Constraints from the stratigraphy of the North Alpine Foreland Basin and the structural evolution of the Alps. Basin Res. 10, pp. 197–212.
https://doi.org/10.1046/j.1365-2117.1998.00063.x

Schlunegger, F., and Willett, S. D. (1999). Spatial and temporal variations in exhumation of the central Swiss Alps and implications for exhumation mechanisms. Geol. Soc. Spec. Publ. 154, pp. 157–179.
https://doi.org/10.1144/GSL.SP.1999.154.01.07

Schlunegger, F., Melzer, J., and Tucker, G. E. (2001). Climate, exposed source-rock lithologies, crustal uplift and surface erosion: A theoretical analysis calibrated with data from the Alps/North Alpine foreland basin system. Int. J. Earth Sci. 90, pp. 484–499.
https://doi.org/10.1007/s005310100174

Schlunegger, F., and Mosar, J. (2011). The last erosional stage of the Molasse Basin and the Alps. Int. J. Earth Sci. 100, pp. 1147–1162.
https://doi.org/10.1007/s00531-010-0607-1

Schlunegger, F., and Norton, K. P. (2013). Headward retreat of streams in the Late Oligocene to Early Miocene Swiss Alps. Sedimentology 60, pp. 85–101.
https://doi.org/10.1111/sed.12010

Schlunegger, F., and Norton, K. P. (2015). Climate vs. tectonics: The competing roles of late Oligocene warming and Alpine orogenesis in constructing alluvial megafan sequences in the North Alpine foreland basin. Basin Res. 27, pp. 230–245.
https://doi.org/10.1111/bre.12070

Schlunegger, F., and Kissling, E. (2015). Slab rollback orogeny in the Alps and evolution of the Swiss Molasse basin. Nat. Commun. 6, pp. 1–10.
https://doi.org/10.1038/ncomms9605

Schlunegger, F., and Castelltort, S. (2016). Immediate and delayed signal of slab breakoff in Oligo/Miocene Molasse deposits from the European Alps. Sci. Rep. 6, 31010.
https://doi.org/10.1038/srep31010

Schlunegger, F., and Garefalakis, P. (2018). Clast imbrication in coarse-grained mountain streams and stratigraphic archives as indicator of deposition in upper flow regime conditions. Earth Surf. Dyn. 6.
https://doi.org/10.5194/esurf-6-743-2018

Schlunegger, F., and Kissling, E. (2022). Slab Load Controls Beneath the Alps on the Source-to-Sink Sedimentary Pathways in the Molasse Basin. Geosci. 12.
https://doi.org/10.3390/geosciences12060226

Shapiro, S. S., Wilk, M. B., and Chen, H. J. (1968). A Comparative Study of Various Tests for Normality. J. Am. Stat. Assoc. 63, pp. 1343–1372.
https://doi.org/10.1080/01621459.1968.10480932

Shapiro, S., and Wilk, M. B. (1965). An Analysis of Variance Test for Normality (Complete Samples). Biom. 52, pp. 591–611.

Sinclair, H. D., Coakley, B. J., Allen, P. A., and Watts, A. B. (1991). Simulation of Foreland Basin Stratigraphy using a diffusion model of mountain belt uplift and erosion - an example from the central Alps, Switzerland. 10, pp. 599–620.
https://doi.org/10.1029/90TC02507

Sissingh, W. (1997). Tectonostratigraphy of the North Alpine Foreland Basin: Correlation of Tertiary depositional cycles and orogenic phases. Tectonophysics 282, pp. 223–256.
https://doi.org/10.1016/S0040-1951(97)00221-7

Spiegel, C., Kuhlemann, J., Dunkl, I., and Frisch, W. (2001). Paleogeography and catchment evolution in a mobile orogenic belt: the Central Alps in Oligo-Miocene times. Tectonophysics 341, pp. 33–47.
https://doi.org/10.1016/S0040-1951(01)00187-1

Sternberg, H. (1875). Untersuchungen über Längen- und Querprofil geschiebeführender Flüsse. Zeitschrift für Bauwes. 25, pp. 483–506. (in German)
Available at: https://digital.zlb.de/viewer/image/15239363_1875/262/

Stock, J. D., Schmidt, K. M., and Miller, D. M. (2008). Controls on alluvial fan long-profiles. Bull. Geol. Soc. Am. 120, pp. 619–640.
https://doi.org/10.1130/B26208.1

Strasky, S., Schlunegger, F., Hänni, R., Häuselmann, P., Mojon, A., and Schwizer, B. (2022). Blatt 1208 Beatenberg. - Geol. Atlas Schweiz 1:25 000, Erläut. 170-171. (in German)
Available at: www.swisstopo.ch

Straub, K. M., Duller, R. A., Foreman, B. Z., and Hajek, E. A. (2020). Buffered, incomplete, and shredded: The challenges of reading an imperfect stratigraphic record. J. Geophys. Res., 93.
https://doi.org/10.1029/2019JF005079

Stürm, B. (1973). Die Rigi Schüttung - Sedimentpetrographie, Sedimentologie, Palaeogeographie, Tektonik. Unpubl. PhD Thesis, Univ. Bern, 96 pp. (in German)

Stutenbecker, L., Tollan, P. M. E., Madella, A., and Lanari, P. (2019). Miocene basement exhumation in the Central Alps recorded by detrital garnet geochemistry in foreland basin deposits. Solid Earth Discuss., pp. 1–26.
https://doi.org/10.5194/se-2019-98

Tucker, G. E., and Slingerland, R. L. (1997). Drainage basin responses to climate change. Water Resour. R. 33, pp. 2031–2047.
https://doi.org/10.1029/97WR00409

van der Boon, A., Beniest, A., Ciurej, A., Gaździcka, E., Grothe, A., et al. (2018). The Eocene-Oligocene transition in the North Alpine Foreland Basin and subsequent closure of a Paratethys gateway. Glob. Planet. Change 162, pp. 101–119.
https://doi.org/10.1016/j.gloplacha.2017.12.009

Vandenberghe, N., Hilgen, F. J., Speijer, R. P., Ogg, J. G., Gradstein, F. M., Hammer, Ø., et al. (2012). The Paleogene Period. Elsevier.
https://doi.org/10.1016/B978-0-444-59425-9.00028-7

Vaz, M. F., and Fortes, M. A. (1988). Grain Size Distribution: The lognormal and the gamma distribution functions. Scr. Metall. 22, pp. 35–40.
https://doi.org/10.1016/S0036-9748(88)80302-8

Ventra, D., and Clarke, L. E. (2018). Geology and geomorphology of alluvial and fluvial fans: Current progress and research perspectives. Geol. Soc. Spec. Publ. 440, pp. 1–21.
https://doi.org/10.1144/SP440.16

Ventra, D., and Nichols, G. J. (2014). Autogenic dynamics of alluvial fans in endorheic basins: Outcrop examples and stratigraphic significance. Sedimentology 61, pp. 767–791.
https://doi.org/10.1111/sed.12077

Wainwright, J., Parsons, A. J., Cooper, J. R., Gao, P., Gillies, J. A., Mao, L., et al. (2015). The concept of transport capacity in geomorphology. Rev. Geophys. 53, pp. 1155–1202.
https://doi.org/10.1002/2014RG000474

Wang, Y., Straub, K. M., and Hajek, E. A. (2011). Scale-dependent compensational stacking: An estimate of autogenic time scales in channelized sedimentary deposits. Geology 39, pp. 811–814.
https://doi.org/10.1130/G32068.1

Whipple, K. X., Parker, G., Paola, C., and Mohrig, D. (1998). Channel Dynamics, Sediment Transport, and the Slope of Alluvial Fans: Experimental Study. Source J. Geol. 10642222, pp. 677–694.
https://doi.org/10.1086/516053

Whittaker, A. C. (2012). How do landscapes record tectonics and climate? Lithosphere 4, pp. 160–164.
https://doi.org/10.1130/RF.L003.1

Whittaker, A. C., Attal, M., and Allen, P. A. (2010). Characterising the origin, nature and fate of sediment exported from catchments perturbed by active tectonics. Basin Res. 22, pp. 809–828.
https://doi.org/10.1111/j.1365-2117.2009.00447.x

Whittaker, A. C., Duller, R. A., Springett, J., Smithells, R. A., Whitchurch, A. L., and Allen, P. A. (2011). Decoding downstream trends in stratigraphic grain size as a function of tectonic subsidence and sediment supply. pp. 1363–1382.
https://doi.org/10.1130/B30351.1

Wickert, A. D., and Schildgen, T. F. (2019). Long-profile evolution of transport-limited gravel-bed rivers. Earth Surf. Dyn. 7, pp. 17–43.
https://doi.org/10.5194/esurf-7-17-2019

Wilcock, P., Pitlick, J., and Cui, Y. (2009). Estimating Bed-Material Transport in Gravel-bed Rivers. Geogr. RMRS-GTR-2, 1–5.

Wolman, M. G. (1954). A method of sampling coarse river-bed material. Am. Geophys. Union 35, pp. 951–956.
https://doi.org/10.1017/CBO9781107415324.004

Wong, M., and Parker, G. (2006). Reanalysis and Correction of Bed-Load Relation of Meyer-Peter and Müller Using Their Own Database. J. Hydraul. Eng. 132, pp. 1159–1168.
https://doi.org/10.1061/(asce)0733-9429(2006)132:11(1159)

Zachos, J. C., Pagani, H., Sloan, L., Thomas, E., and Billups, K. (2001). Trends, rhythms, and aberrations in global climate 65 Ma to present. Science (80). 292, pp. 686–693.
https://doi.org/10.1126/science.1059412

4.11 Appendix A

Appendix A contains the lithostratigraphic profiles of the stratigraphic sections and the correlation of the Magneto Polarity Stratigraphies (MPS) to the Global Time Scale (GTS). In addition, listed in tables, we provided for each stratigraphic section the locations of the individual sites, the thickness of the section at these sites, the approximate ages of the section at these sites, the altitude of the sites and the coordinates. The coordinates are based on the Swiss coordinate reference system CH1903+ (LV95). Please find the indicated references in the bibliography of this appendix A. The lithostratigraphic profiles of the Lake Thun, Rigi, Rossberg, Töss and Hörnli sections and the related data can be found in appendix A of chapter 3.

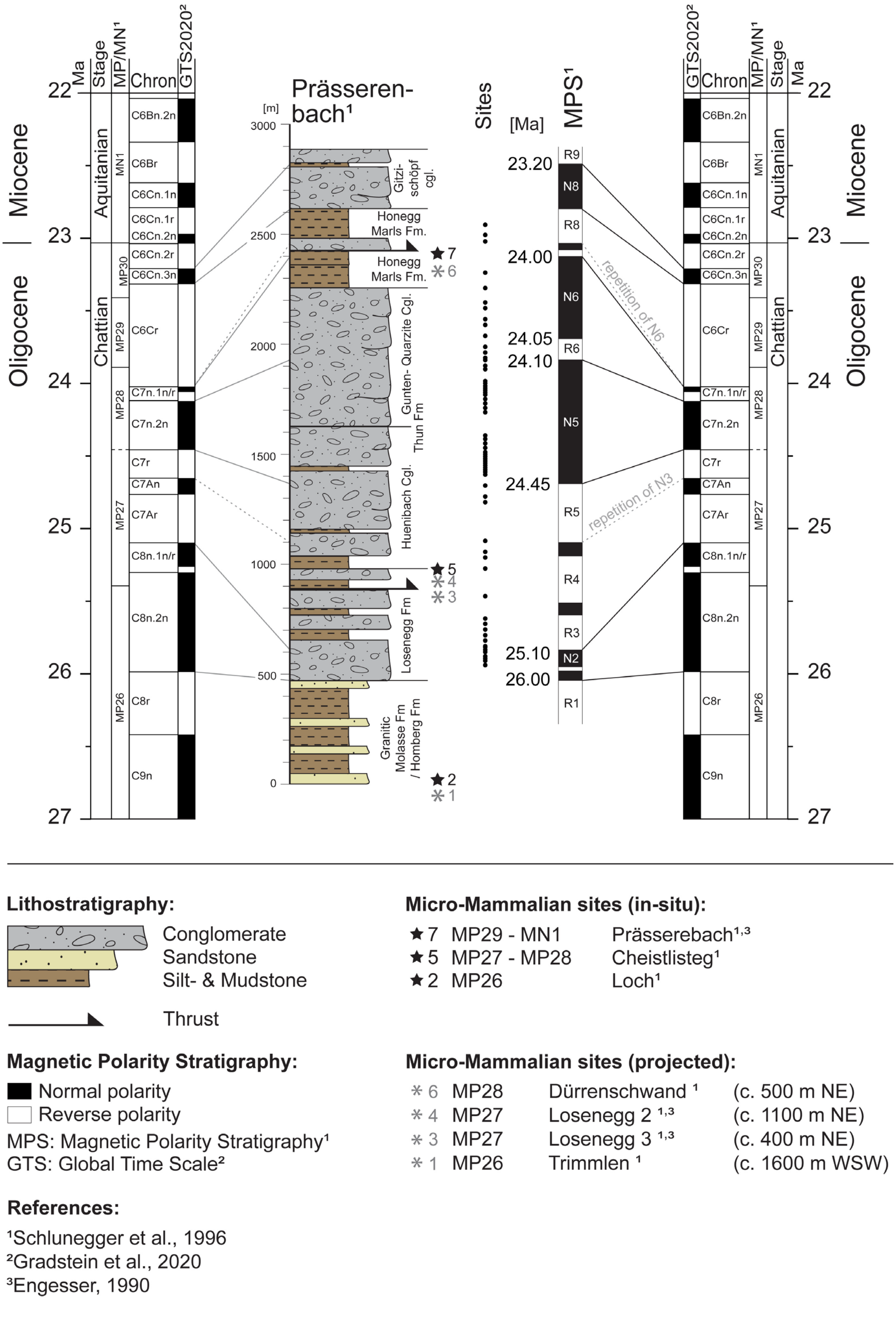

Figure SA4.1: Stratigraphic section and chronological framework of the Prässerenbach section situated in the western Swiss Molasse Basin. Please see also Fig. S3.1b in chapter 3.

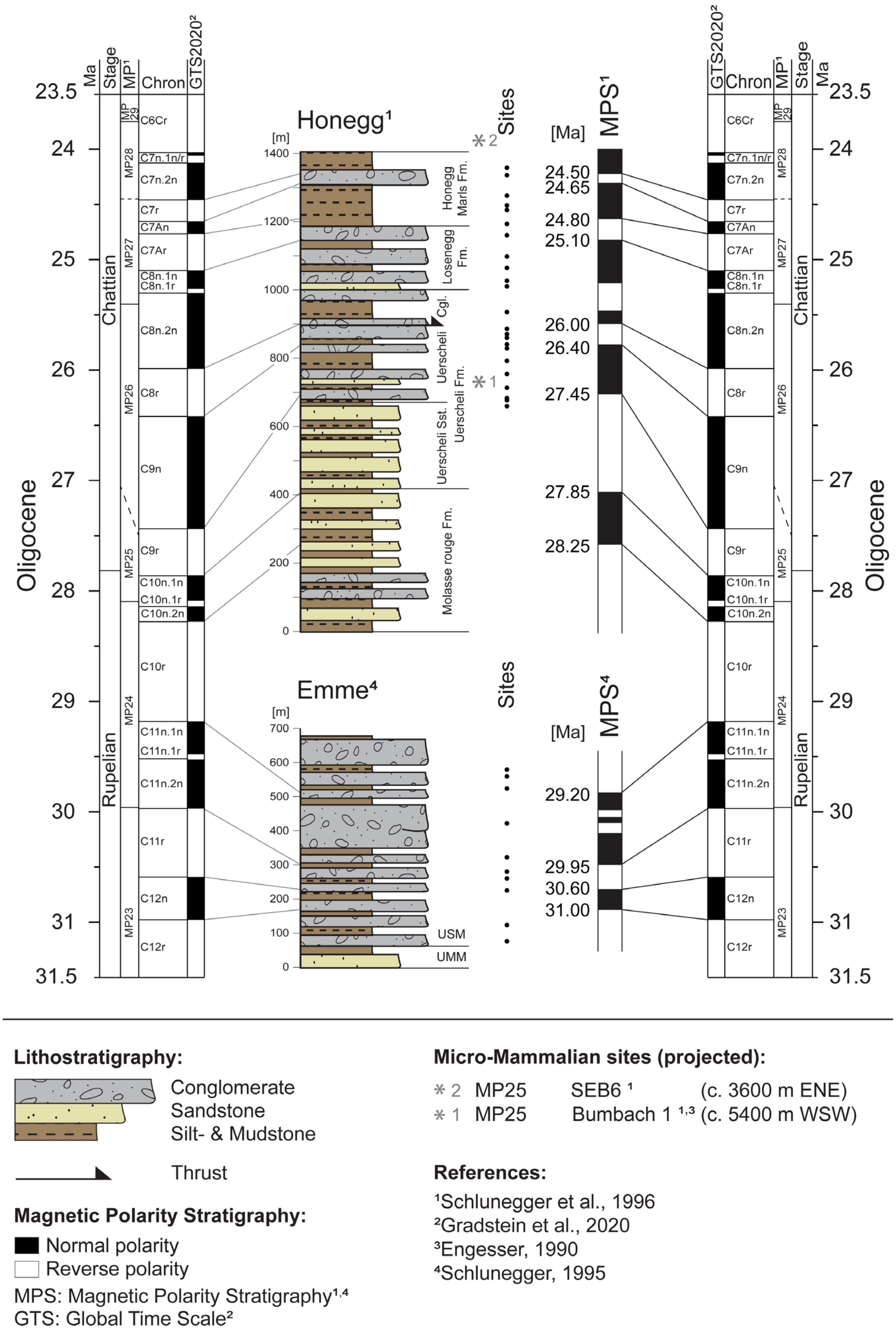

Figure SA4.2: Stratigraphic section and chronological framework of the Emme and Honegg sections situated in the western Swiss Molasse Basin. UMM = Untere Meeres Molasse (Lower Marine Molasse); USM = Untere Süsswasser Molasse (Lower Freshwater Molasse).

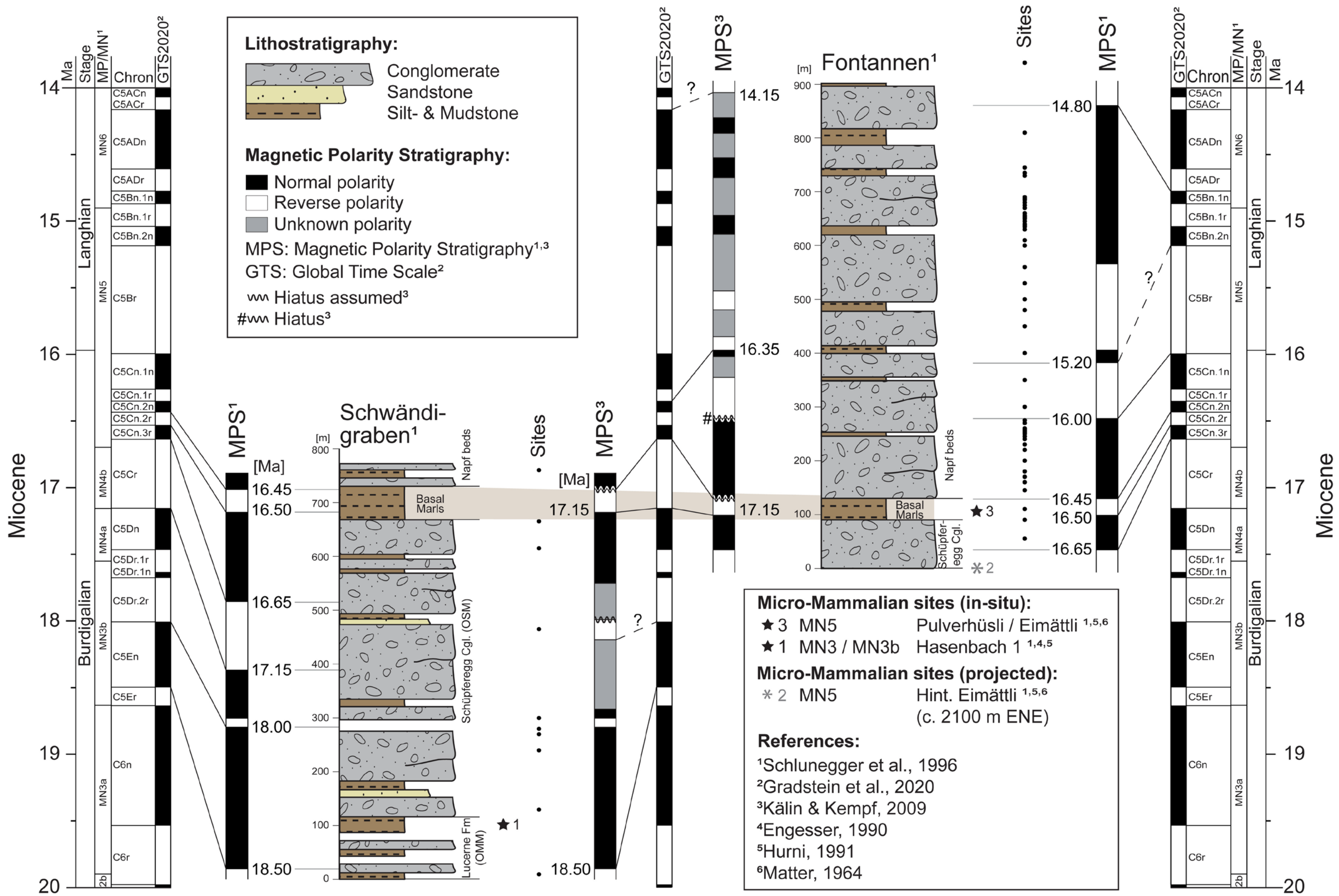

Figure SA4.3: Stratigraphic section and chronological framework of the Schwändigraben and Fontannen sections situated in the western Swiss Molasse Basin. OMM = Obere Meeres Molasse (Upper Marine Molasse); OSM = Obere Süsswasser Molasse (Upper Freshwater Molasse).

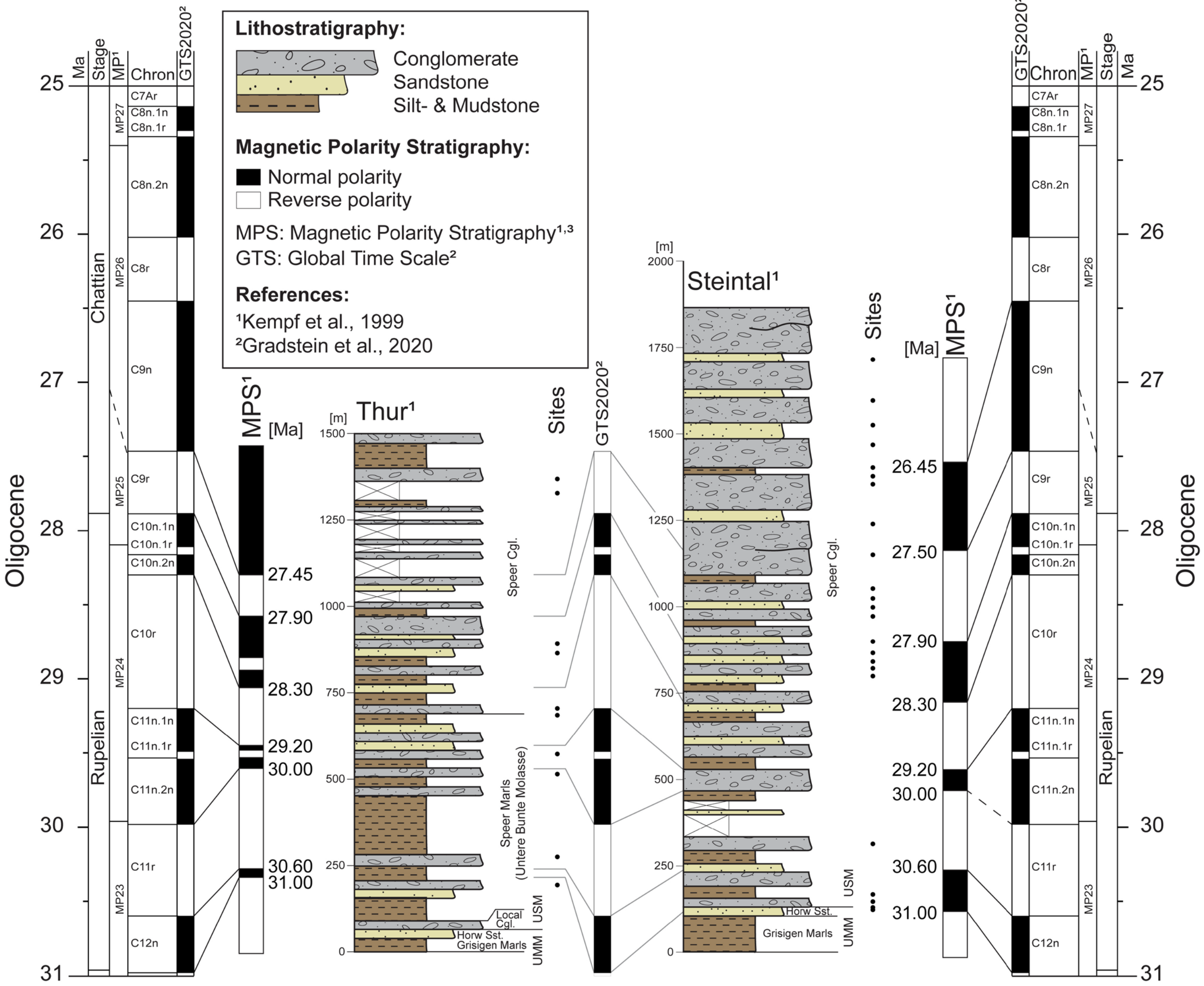

Figure SA4.4: Stratigraphic section and chronological framework of the Thur and Steintal sections situated in the eastern Swiss Molasse Basin. UMM = Untere Meeres Molasse (Lower Marine Molasse); USM = Untere Süsswasser Molasse (Lower Freshwater Molasse).

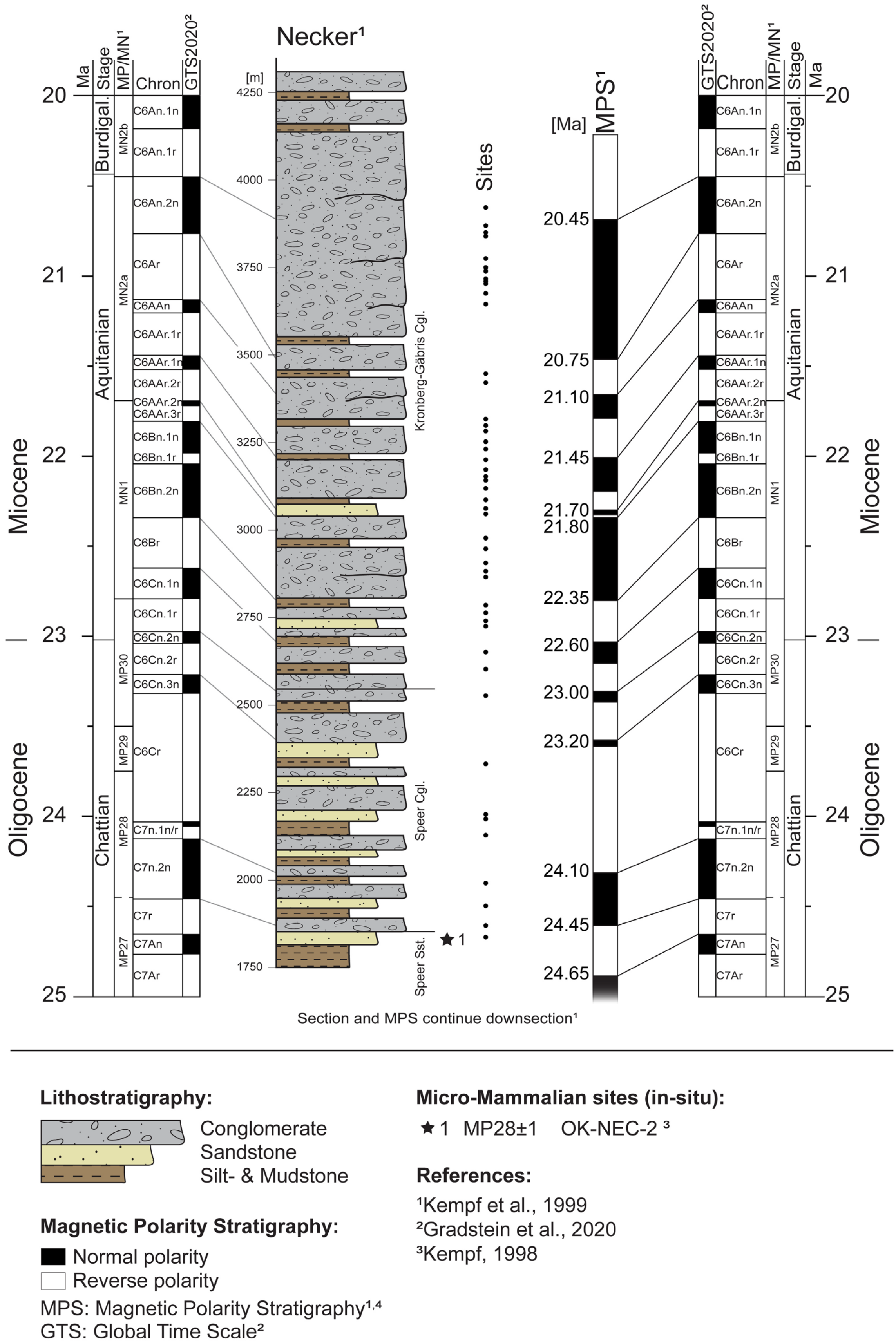

Figure SA4.5: Stratigraphic section and chronological framework of the Necker section situated in the eastern Swiss Molasse Basin.

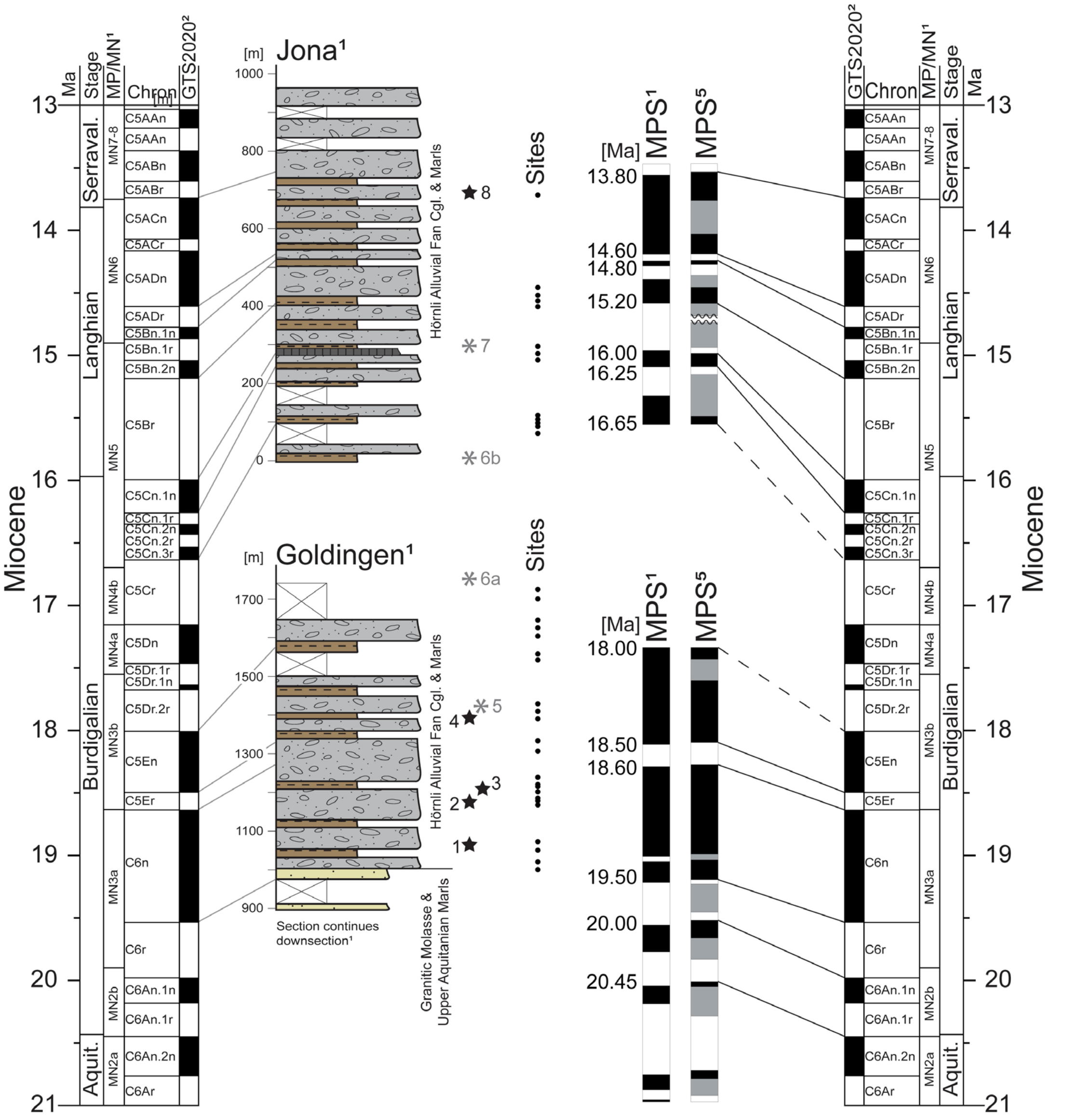

Lithostratigraphy:

- Conglomerate
- Sandstone
- Silt- & Mudstone
- Hüllistein Bed[1]

Magnetic Polarity Stratigraphy:

- Normal polarity
- Reverse polarity

MPS: Magnetic Polarity Stratigraphy[1]
GTS: Global Time Scale[2]

References:

[1]Kempf et al., 1997
[2]Gradstein et al., 2020
[3]Löpfe et al., 2012
[4]Bolliger, 1992
[5]Kälin & Kempf, 2009

Micro-Mammalian sites (in-situ):

★8	up. MN6	Bachtel-Ornberg [1,4]
★4	lo. MN3b	Goldinger-Tobel 8 [1,4]
★3	MN3	Goldinger-Tobel 3 [1,4]
★2	MN3	Goldinger-Tobel 2 [1,4]
★1	lo. MN3a	Goldinger-Tobel 1 [1,4]

Micro-Mammalian sites (projected):

∗7	mid. MN5	Guentisberg [1,4]	(c. 1500 m ENE)
∗6b	MN4b	Hubertingen [3]	(c. 200 m ESE)
∗6a	MN4b	Hubertingen [3]	(c. 2100 m ENE)
∗5	MN3	Goldinger-Tobel 5/6 [1,4]	(c. 250 m ENE)

Figure SA4.6: Stratigraphic section and chronological framework of the Goldingen and Jona sections situated in the eastern Swiss Molasse Basin.

Site	Thickness [m]	Age [Ma]	Altitude [m]	X-Coord. (CH1903+)	Y-Coord. (CH1903+)
73	2990	23.2	569	2621531.5	1173143.8
74	3115	23.1	576	2621541.2	1173193.8
72	2570	23.4	722	2620537.7	1174070.3
71	2560	23.4	664	2620401.8	1174039.9
64	2555	23.4	586	2620210.7	1173841.2
70	2545	23.4	641	2620333.5	1174023.3
69	2540	23.4	629	2620253.0	1173943.9
68	2540	23.4	601	2620227.0	1173951.2
67	2535	23.4	602	2620249.0	1174013.0
65	2520	23.4	602	2620125.8	1173898.7
66	2520	23.4	599	2620186.0	1174004.5
63	2175	23.6	698	2619393.6	1174654.1
62	2160	23.6	717	2619397.2	1174769.6
61	2115	23.6	775	2619401.2	1174889.1
60	2050	23.7	624	2618866.2	1174700.7
59	1990	23.7	646	2618785.3	1174886.7
53	1955	23.7	821	2619000.6	1175134.0
58	1935	23.7	660	2618718.0	1175036.2
52	1890	23.7	840	2618956.3	1175345.7
57	1905	23.7	670	2618678.8	1175113.8
51	1870	23.7	843	2618906.8	1175397.6
56	1885	23.7	677	2618656.6	1175170.9
55	1860	23.8	684	2618628.2	1175247.6
54	1841	23.8	693	2618620.4	1175308.3
50	1815	23.8	836	2618763.4	1175460.6
49	1800	23.8	837	2618749.4	1175502.1
48	1720	23.8	813	2618625.8	1175728.4
47	1710	23.8	814	2618606.6	1175748.6
46	1675	23.8	747	2618348.4	1175686.0
39	1620	23.9	637	2618127.0	1175747.1
43	1600	23.9	713	2618443.8	1176096.5

Table SA4.1: Data of the Lake Thun section in the western Swiss Molasse Basin.

Site	Thickness [m]	Age [Ma]	Altitude [m]	X-Coord. (CH1903+)	Y-Coord. (CH1903+)
42	1595	23.9	737	2618420.2	1176081.6
45	1585	23.9	744	2618262.0	1175950.3
41	1590	23.9	735	2618396.2	1176079.1
40	1580	23.9	756	2618347.0	1176035.3
44	1585	23.9	717	2618450.6	1176148.7
38	1565	23.9	649	2618106.7	1175940.7
37	1555	23.9	655	2618134.4	1176007.6
35	1535	23.9	693	2618172.8	1176094.7
34	1520	23.9	745	2618281.4	1176208.1
36	1530	23.9	684	2618127.4	1176075.1
33	1510	23.9	752	2618281.4	1176245.1
32	1470	23.9	748	2618059.9	1176177.2
31	1390	24.0	741	2617740.5	1176207.3
28	1255	24.1	699	2617389.5	1176420.8
29	1245	24.1	657	2617351.3	1176462.3
27	1240	24.1	690	2617426.2	1176527.2
30	1235	24.1	660	2617343.5	1176485.8
26	1210	24.1	693	2617327.2	1176536.2
25	1200	24.1	694	2617297.0	1176544.9
24	970	24.2	758	2616982.6	1177055.2
23	970	24.2	772	2617025.6	1177090.7
22	930	24.2	777	2616995.4	1177164.8
21	900	24.2	789	2616941.0	1177217.2
20	865	24.2	795	2616855.0	1177274.2
19	815	24.3	810	2616786.2	1177380.6
15	610	24.4	623	2616398.5	1177854.3
14	600	24.4	630	2616328.9	1177836.5
17	565	24.4	686	2616611.0	1178106.5
16	555	24.4	684	2616493.1	1178059.7
18	495	24.4	781	2616683.4	1178319.2
7	230	24.6	753	2615645.0	1178465.6
12	195	24.6	693	2615462.9	1178479.2
11	170	24.6	686	2615452.4	1178551.7
6	160	24.6	741	2615534.0	1178621.3
5	140	24.6	736	2615524.0	1178679.3
10	110	24.6	674	2615392.4	1178710.4
4	100	24.6	731	2615449.9	1178767.8
3	70	24.6	734	2615438.9	1178820.8
9	55	24.7	659	2615298.6	1178824.3
2	30	24.7	729	2615389.0	1178926.8
8	40	24.7	653	2615267.6	1178864.3
1	0	24.7	719	2615411.3	1179048.8

Table SA4.1 (continued): Data of the Lake Thun section in the western Swiss Molasse Basin.

Site	Thickness [m]	Age [Ma]	Altitude [m]	X-Coord. (CH1903+)	Y-Coord. (CH1903+)
1	540	25.7	749	2621551.1	1181489.3
2	560	25.6	737	2621583.4	1181481.4
3	570	25.5	746	2621617.5	1181458.4
4	580	25.5	744	2621643.4	1181443.4
5	600	25.4	745	2621663.7	1181466.0
6	610	25.4	747	2621695.2	1181451.5
7	620	25.3	747	2621711.9	1181429.2
8	625	25.3	752	2621746.7	1181412.9
9	650	25.2	756	2621800.1	1181433.4
10	675	25.1	750	2621875.1	1181462.9
11	700	25.0	754	2621911.8	1181428.7
12	725	24.9	753	2621991.0	1181358.3
13	750	24.8	759	2622005.4	1181285.4
14	850	24.7	770	2622278.5	1181102.9
15	975	24.7	775	2622417.1	1181117.9
16	1025	24.7	776	2622460.9	1181095.4
17	1050	24.6	821	2622289.0	1180708.4
18	1100	24.6	834	2622347.5	1180723.9
19	1300	24.5	860	2622456.6	1180466.0
20	1275	24.5	857	2622455.1	1180398.5
21	1300	24.5	839	2622464.5	1180313.3
22	1350	24.5	853	2622517.4	1180331.6
23	1400	24.5	861	2622575.5	1180316.4
24	1410	24.5	866	2622613.0	1180317.0
25	1420	24.5	867	2622640.1	1180299.4
26	1430	24.5	864	2622652.8	1180283.6
27	1440	24.5	867	2622667.1	1180272.4
28	1450	24.4	863	2622678.3	1180255.4
29	1460	24.4	875	2622709.7	1180217.8
30	1470	24.4	870	2622721.1	1180192.9
31	1480	24.4	872	2622747.0	1180157.1
32	1490	24.4	875	2622747.8	1180099.5
33	1500	24.4	874	2622742.1	1180079.3
34	1520	24.4	882	2622790.8	1180026.8
35	1540	24.4	888	2622812.1	1180022.5
36	1560	24.4	882	2622831.0	1179996.9
37	1575	24.4	892	2622862.0	1179900.9
38	1680	24.3	903	2622925.4	1179863.4
39	1700	24.3	897	2622967.5	1179786.0
40	1720	24.3	898	2622981.0	1179769.5
41	1740	24.3	905	2623014.5	1179772.5

Table SA4.2: Data of the Prässerenbach section in the western Swiss Molasse Basin.

Site	Thickness [m]	Age [Ma]	Altitude [m]	X-Coord. (CH1903+)	Y-Coord. (CH1903+)
42	1760	24.3	907	2623076.9	1179751.3
43	1770	24.3	912	2623109.8	1179647.5
44	1780	24.3	913	2623108.5	1179635.8
45	1790	24.3	917	2623106.0	1179624.8
46	1800	24.2	918	2623078.0	1179602.8
47	1810	24.2	919	2623076.5	1179618.6
48	1820	24.2	919	2623087.1	1179580.1
49	1875	24.2	922	2623084.3	1179535.4
50	1890	24.2	925	2623121.8	1179519.4
51	1915	24.2	926	2623133.4	1179496.5
52	1925	24.2	933	2623162.8	1179428.4
53	1950	24.2	938	2623210.4	1179376.0
54	1975	24.1	946	2623256.9	1179345.4
55	2025	24.0	950	2623305.2	1179312.8
56	2075	23.9	952	2623331.9	1179262.3
57	2100	23.8	953	2623360.2	1179196.1
58	2150	23.7	961	2623367.2	1179161.1
59	2175	23.6	981	2623413.7	1179083.1
60	2240	23.4	1016	2623622.6	1178990.8
61	2310	23.3	1031	2623674.1	1178879.6
62	2450	23.1	1069	2623875.4	1178637.8
63	2480	23.0	1084	2623926.9	1178542.5
64	2525	22.9	1104	2623968.8	1178453.5

Table SA4.2 (continued): Data of the Prässerenbach section in the western Swiss Molasse Basin.

Site	Thickness [m]	Age [Ma]	Altitude [m]	X-Coord. (CH1903+)	Y-Coord. (CH1903+)
1	75	31.3	794	2643987.5	1196968.9
2	125	31.1	822	2644068.4	1196913.2
3	225	30.6	772	2643909.4	1196751.2
4	250	30.4	780	2643936.6	1196698.0
5	275	30.0	777	2643950.6	1196645.5
6	325	29.9	782	2643921.8	1196489.2
7	425	29.5	786	2643885.3	1196382.5
8	540	29.1	802	2643919.7	1196108.1
9	560	29.0	812	2643897.1	1195920.2
10	580	28.9	819	2643896.8	1195711.8

Table SA4.3: Data of the Emme section in the western Swiss Molasse Basin.

Site	Thickness [m]	Age [Ma]	Altitude [m]	X-Coord. (CH1903+)	Y-Coord. (CH1903+)
1	55	16.6	770	2642910.9	1203527.1
2	90	16.5	773	2642807.9	1203569.1
3	110	16.5	774	2642702.8	1203657.8
4	145	16.5	776	2642567.8	1203853.2
6	160	16.4	786	2642517.3	1203914.9
7	170	16.3	792	2642459.1	1203958.4
8	180	16.3	782	2642388.7	1203986.8
9	200	16.2	793	2642290.0	1204114.7
10	220	16.2	794	2642218.6	1204165.9
11	230	16.1	800	2642199.1	1204197.9
12	240	16.1	798	2642101.7	1204258.8
13	245	16.1	811	2642032.7	1204248.3
14	250	16.1	839	2641882.6	1204201.8
15	252.5	16.1	822	2641659.5	1204127.9
16	255	16.1	825	2641570.2	1204096.9
17	257.5	16.1	823	2641482.7	1204098.4
18	260	16.1	831	2641407.7	1204143.6
19	270	16.0	838	2641278.9	1204254.3
20	275	16.0	849	2641084.0	1204320.5
21	300	15.8	947	2641299.8	1204345.4
23	350	15.6	962	2641276.4	1204612.2
24	400	15.2	998	2641381.2	1204687.2
25	450	15.1	1003	2641286.1	1204831.1
26	480	15.0	1022	2641249.0	1205055.0
27	500	15.0	1038	2641121.0	1205024.0
28	530	14.9	1057	2641050.0	1204933.0
29	560	14.9	1146	2641024.2	1205234.7
30	600	14.9	1120	2640916.3	1205339.9
31	610	14.9	1167	2640863.5	1205360.0
32	630	14.9	1105	2640313.2	1205408.6
33	635	14.9	1111	2640241.2	1205364.6
34	637.5	14.9	1118	2640177.7	1205374.6
35	640	14.9	1124	2640157.2	1205308.1
36	645	14.9	1126	2639727.0	1205521.9
37	650	14.8	1125	2639662.4	1205568.4
38	652	14.8	1133	2639461.7	1205583.1
39	654	14.8	1136	2639278.7	1205548.6

Table SA4.4: Data of the Fontannen section in the western Swiss Molasse Basin.

Site	Thickness [m]	Age [Ma]	Altitude [m]	X-Coord. (CH1903+)	Y-Coord. (CH1903+)
40	656	14.8	1161	2639236.4	1205278.8
41	660	14.8	1185	2639408.8	1205009.4
42	670	14.8	1207	2639111.4	1205078.1
43	675	14.8	1211	2639067.9	1205037.1
44	680	14.8	1209	2638980.4	1205078.1
45	685	14.8	1223	2638871.0	1204995.6
46	687.5	14.8	1249	2638925.3	1205110.5
47	940	14.6	1302	2639028.6	1206320.4
48	810	14.8	1217	2639192.4	1206910.0
50	730	14.8	1129	2639382.4	1207184.6
51	735	14.8	1140	2639291.8	1206974.6
52	745	14.8	1144	2639367.8	1206797.6
53	690	14.8	1204	2640303.6	1205614.6

Table SA4.4 (continued): Data of the Fontannen section in the western Swiss Molasse Basin.

Site	Thickness [m]	Age [Ma]	Altitude [m]	X-Coord. (CH1903+)	Y-Coord. (CH1903+)
1	10	18.5	894	2639039.5	1198666.5
3	130	18.3	900	2639003.0	1198855.0
4	240	18.1	920	2638783.5	1198904.0
5	270	18.1	932	2638606.5	1198993.0
6	280	18.0	941	2638601.0	1199068.0
7	300	18.0	941	2638552.5	1199152.0
8	465	16.8	960	2638460.5	1199390.0
9	615	16.6	998	2638188.0	1199627.5
10	665	16.5	1025	2638017.0	1199667.0
11	760	16.3	1114	2637692.5	1199835.5

Table SA4.5: Data of the Schwändigraben section in the western Swiss Molasse Basin.

Site	Thickness [m]	Age [Ma]	Altitude [m]	X-Coord. (CH1903+)	Y-Coord. (CH1903+)
1	670	27.6	912	2632506.7	1185023.2
2	700	27.5	921	2632515.4	1184951.2
3	710	27.5	922	2632515.4	1184951.2
4	720	27.4	923	2632523.0	1184928.4
5	760	26.8	931	2632454.0	1184865.8
6	800	26.6	945	2632407.2	1184779.0
7	880	26.2	950	2632391.4	1184736.3
8	885	26.2	957	2632393.2	1184686.5
9	840	26.4	959	2632394.7	1184667.5
10	850	26.4	962	2632391.4	1184647.7
12	870	26.5	969	2632375.4	1184598.2
13	890	26.1	976	2632383.4	1184557.7
14	940	25.8	982	2632383.0	1184514.2
15	1020	25.5	988	2632388.3	1184462.2
16	1030	25.5	995	2632379.6	1184425.5
17	1070	25.3	999	2632357.9	1184402.5
18	1100	25.2	1002	2632366.9	1184377.5
19	1160	24.9	1015	2632384.6	1184348.0
20	1200	24.8	1018	2632394.1	1184317.5
21	1240	24.7	1024	2632392.6	1184289.5
22	1250	24.7	1045	2632431.6	1184238.8
23	1280	24.7	1051	2632461.0	1184226.6
24	1340	24.5	1089	2632518.8	1184166.0
25	1360	24.4	1097	2632541.0	1184164.9

Table SA4.6: Data of the Honegg section in the western Swiss Molasse Basin.

Site	Thickness [m]	Age [Ma]	Altitude [m]	X-Coord. (CH1903+)	Y-Coord. (CH1903+)
1	190	31.0	773	2734140.0	1231158.5
2	270	30.6	756	2734391.5	1229392.5
3	510	30.1	818	2734256.0	1231087.0
4	570	29.2	797	2734654.5	1230775.0
5	690	28.7	857	2734559.5	1230665.0
6	700	28.5	833	2734541.0	1230484.0
7	870	28.1	868	2734615.5	1230469.0
8	890	28.0	856	2734593.0	1230183.0
9	1330	27.3	859	2734640.0	1230131.5
10	1370	26.9	893	2734593.0	1229408.5

Table SA4.7: Data of the Thur section in the eastern Swiss Molasse Basin.

Site	Thickness [m]	Age [Ma]	Altitude [m]	X-Coord. (CH1903+)	Y-Coord. (CH1903+)
1	150	31.0	990	2728486.0	1230986.0
2	130	30.9	930	2728603.5	1230512.5
3	125	30.9	925	2728574.0	1230527.5
4	160	30.8	940	2728389.5	1230560.0
5	310	30.4	960	2728258.5	1230286.5
7	800	28.3	1180	2727858.5	1229509.0
8	820	28.1	1190	2727872.0	1229463.0
9	840	28.1	1170	2727932.0	1229471.5
10	870	28.0	1190	2727966.5	1229438.5
11	900	27.9	1195	2727964.0	1229395.0
12	1030	27.7	1230	2728031.0	1229290.5
13	980	27.8	1220	2728088.0	1229291.5
14	1000	27.7	1220	2728159.5	1229310.5
15	1050	27.7	1240	2728188.0	1229250.5
16	1150	27.6	1290	2728251.0	1229142.0
17	1240	27.4	1320	2728326.0	1229071.5
19	1400	26.6	1360	2728305.0	1228922.0
20	1470	26.4	1400	2728269.0	1228785.0
21	1600	26.4	1410	2728231.5	1228689.5
22	1380	26.3	1300	2728010.0	1228801.5
23	1360	26.3	1280	2727965.5	1228822.0
24	1530	26.2	1320	2727971.5	1228618.5
25	1720	26.2	1450	2728173.0	1228514.0

Table SA4.8: Data of the Steintal section in the eastern Swiss Molasse Basin.

Site	Thickness [m]	Age [Ma]	Altitude [m]	X-Coord. (CH1903+)	Y-Coord. (CH1903+)
2	270	15.9	575	2709376.0	1234703.0
3	290	15.9	639	2710188.0	1234761.0
4	280	16.0	650	2710373.0	1234793.0
5	105	16.7	569	2711207.0	1234764.0
6	100	16.7	525	2711502.0	1234607.0
7	95	16.7	526	2711781.5	1234744.5
8	90	16.8	528	2711841.0	1234748.0
9	85	16.8	537	2712074.5	1234803.0
10	410	15.3	488	2707910.0	1236224.0
11	415	15.2	535	2708207.0	1236341.0
12	420	15.2	522	2708538.0	1236348.0
13	440	15.1	558	2708841.5	1238075.0
14	690	13.9	790	2708894.0	1236331.5

Table SA4.9: Data of the Jona section in the eastern Swiss Molasse Basin.

Site	Thickness [m]	Age [Ma]	Altitude [m]	X-Coord. (CH1903+)	Y-Coord. (CH1903+)
1	1010	19.5	503	2714641.5	1233780.0
2	1020	19.4	501	2714630.5	1233847.5
3	1040	19.3	506	2714573.5	1233886.0
4	1065	19.3	509	2714517.0	1233909.5
12	1180	19.2	562	2715679.5	1234430.0
13	1185	19.2	562	2715705.5	1234473.0
14	1190	19.1	557	2715705.5	1234443.5
5	1205	19.0	526	2714643.5	1234285.0
7	1215	19.0	530	2714752.5	1234334.0
8	1220	18.8	533	2714801.5	1234315.0
9	1230	18.8	559	2715196.0	1234290.5
16	1310	18.6	592	2716156.5	1235035.5
17	1335	18.5	596	2716149.5	1235136.5
18	1400	18.3	604	2716110.0	1235271.0
19	1410	18.3	609	2716121.5	1235291.2
20	1420	18.3	603	2716091.5	1235338.5
21	1555	18.1	628	2715985.0	1235995.0
22	1560	18.1	642	2716066.0	1236239.0
24	1600	18.0	651	2716182.5	1236498.5
25	1620	18.0	657	2716178.5	1236556.0
26	1640	18.0	663	2716264.0	1236689.0
28	1710	17.8	688	2716601.0	1237186.5
29	1720	17.8	696	2716650.5	1237270.5

Table SA4.10: Data of the Goldingen section in the eastern Swiss Molasse Basin.

Site	Thickness [m]	Age [Ma]	Altitude [m]	X-Coord. (CH1903+)	Y-Coord. (CH1903+)
1	0	14.8	708	2712190.5	1247131.7
2	22	14.7	729	2712179.0	1247310.7
14	288	13.4	995	2713349.0	1247816.8
3	36	14.6	743	2712280.0	1247485.2
11	229	13.7	937	2713305.0	1247953.8
5	98	14.3	805	2712932.5	1247815.3
6	161	14.0	869	2713200.5	1247941.3
7	85	14.4	793	2712820.0	1247831.3
9	198	13.8	906	2713071.0	1248038.3
4	71	14.4	778	2712644.0	1247878.3
10	200	13.8	907	2713200.5	1248116.8
12	275	13.5	982	2713086.5	1248253.3
8	211	13.8	919	2712740.0	1248165.8
15	231	13.7	939	2713699.0	1248641.0

Table SA4.11: Data of the Hörnli section in the eastern Swiss Molasse Basin.

Site	Thickness [m]	Age [Ma]	Altitude [m]	X-Coord. (CH1903+)	Y-Coord. (CH1903+)
54	292	13.40	1025	2714667.9	1239456.0
55	356	13.10	1089	2715099.5	1239592.3
53	270	13.50	1003	2714581.0	1239516.8
50	249	13.59	983	2714683.6	1239571.8
46	239	13.64	973	2714811.6	1239627.8
51	239	13.64	972	2714806.6	1239688.8
44	225	13.71	959	2714295.8	1239791.4
48	232	13.67	966	2714931.6	1240027.4
45	219	13.73	953	2714249.6	1239924.0
49	277	13.46	1010	2715086.6	1240217.4
32	133	14.13	867	2716905.8	1240697.2
33	218	13.74	951	2714215.6	1240008.4
42	245	13.61	979	2715312.8	1240322.0
34	214	13.76	947	2714251.2	1240117.4
29	110	14.24	843	2716234.0	1240676.4
35	212	13.76	946	2714233.2	1240289.8
25	107	14.26	840	2716039.0	1240772.4
31	122	14.18	856	2714410.2	1240363.8
27	111	14.24	844	2714485.4	1240619.4
26	110	14.24	844	2714504.4	1240684.4
28	88	14.34	821	2715654.2	1241018.4
24	109	14.25	843	2715552.8	1241000.4
23	93	14.32	826	2714883.8	1240881.4
36	211	13.77	945	2714186.4	1240722.4
38	210	13.78	944	2714416.0	1240811.2
20	81	14.38	814	2715414.8	1241134.8
39	209	13.78	943	2714498.2	1240885.2
18	78	14.39	812	2715007.8	1241046.8
40	209	13.78	943	2714769.8	1240998.2
19	80	14.38	814	2715371.2	1241170.8
17	72	14.42	806	2715063.8	1241199.8
15	73	14.41	807	2715185.8	1241252.8
41	211	13.77	944	2714858.8	1241201.2
16	64	14.46	797	2715004.0	1241325.2
13	60	14.47	794	2714958.8	1241582.4
14	54	14.50	787	2714843.0	1241834.4
12	51	14.52	784	2714689.0	1241931.4
11	43	14.55	777	2714597.2	1241984.2
10	42	14.55	776	2714477.2	1242125.2
9	20	14.66	753	2714154.0	1242538.2
8	20	14.66	754	2714137.0	1242629.2
7	12	14.69	746	2713901.0	1242992.4
2	12	14.70	746	2713900.0	1243019.4
6	9	14.71	743	2713892.0	1243185.4
5	0	14.75	734	2713863.2	1243216.0
3	21	14.65	755	2713797.0	1243751.2

Table SA4.12 (previous page): Data of the Töss section in the eastern Swiss Molasse Basin.

Site	Thickness [m]	Age [Ma]	Altitude [m]	X-Coord. (CH1903+)	Y-Coord. (CH1903+)
1	1835	24.6	870	2733929.0	1237562.0
3	1870	24.5	871	2733989.0	1237523.5
4	1920	24.3	877	2734076.5	1237461.0
6	1985	24.2	882	2734166.0	1237419.0
8	2125	24.1	898	2734410.0	1237217.0
9	2175	24.0	896	2734447.0	1237227.0
10	2180	23.9	918	2734716.0	1237028.0
11	2330	23.7	917	2734759.0	1237008.0
12	2525	23.1	919	2734873.0	1236925.0
14	2600	23.0	936	2735054.0	1236851.0
15	2650	22.8	939	2735101.0	1236812.0
17	2730	22.4	943	2735202.0	1236763.0
17b	2735	22.4	943	2735216.1	1236756.4
20	2760	22.4	947	2735340.0	1236702.0
21	2780	22.3	958	2735496.0	1236666.0
22	2770	22.3	959	2735569.0	1236660.0
23	2875	22.2	960	2735645.0	1236576.0
24	2900	22.1	961	2735821.0	1236493.0
25	2950	22.0	962	2735881.0	1236495.0
26	2975	22.0	961	2736030.0	1236462.0
28	3050	21.9	979	2736236.0	1236418.0
29	3075	21.9	980	2736324.0	1236429.0
30	3085	21.8	995	2736480.0	1236441.0
32	3125	21.7	1001	2736641.0	1236491.0
33	3150	21.6	1010	2736740.5	1236534.5
34	3160	21.5	1020	2736848.0	1236581.0
36	3175	21.4	1021	2736965.0	1236546.0
39	3250	21.3	1036	2737232.0	1236466.5
40	3290	21.2	1041	2737396.0	1236461.0
41	3425	20.9	1063	2737706.0	1236354.0
42	3450	20.8	1058	2737601.5	1236210.0
44	3230	21.3	1103	2737584.5	1236001.0
46	3650	20.7	1064	2737820.5	1235837.5
47	3680	20.7	1087	2737852.0	1235672.5
49	3710	20.6	1084	2738029.0	1235683.0
50	3720	20.6	1092	2738136.0	1235686.5
51	3730	20.6	1107	2738087.5	1235745.5
52	3750	20.6	1127	2738062.0	1235784.0
53	3725	20.6	1103	2738209.0	1235719.0
54	3735	20.6	1103	2738215.8	1235754.5
55	3740	20.6	1107	2738299.5	1235701.0
56	3850	20.5	1136	2738526.0	1235747.0

Table SA4.13: Data of the Necker section in the eastern Swiss Molasse Basin.

Site	Thickness [m]	Age [Ma]	Altitude [m]	X-Coord. (CH1903+)	Y-Coord. (CH1903+)
57	3870	20.5	1148	2738564.5	1235732.5
58	3300	21.2	1057	2737239.5	1236398.5
59	3310	21.2	1062	2737162.5	1236418.5
60	3320	21.2	1073	2736975.5	1236490.0
62	3210	21.5	1031	2736378.0	1236321.0
63	2880	22.2	1088	2735809.0	1236850.0
64	3235	21.4	1048	2737005.5	1236587.0
74	3875	20.4	1177	2738583.5	1235681.5
75	3775	20.5	1187	2738647.0	1235760.0
77	3925	20.4	1254	2739007.0	1235914.0

Table SA4.13 (continued): Data of the Necker section in the eastern Swiss Molasse Basin.

Site	Thickness [m]	Age [Ma]	Altitude [m]	X-Coord. (CH1903+)	Y-Coord. (CH1903+)
117	2960	24.9	1475	2680880.0	1208486.5
110	2940	24.9	1433	2680597.0	1208479.5
111	2820	25.1	1456	2680374.0	1208711.5
118	2940	24.9	1544	2681096.0	1208782.5
119	3060	24.7	1534	2680915.0	1208843.5
105	2800	25.1	1463	2680221.0	1209506.5
115	2880	25.0	1512	2680915.0	1209416.5
96	2605	25.4	1345	2679439.0	1209858.0
114	2880	25.0	1507	2680950.0	1209555.5
102	2605	25.4	1446	2679469.0	1209984.5
116	2900	25.0	1500	2680828.0	1209664.5
101	2640	25.4	1460	2679433.0	1210042.5
87	2460	25.6	1353	2679172.0	1210116.5
90	2480	25.6	1425	2679044.0	1210344.0
95	2320	25.9	1457	2678738.0	1210675.5
99	2320	25.9	1483	2678785.0	1210679.5
82	2360	25.8	1450	2678509.0	1210843.5
98	2320	25.9	1493	2678707.0	1210769.5
67	1980	26.4	1591	2678324.0	1211191.5
76	2380	25.8	1407	2679200.0	1210867.5
73	2320	25.9	1367	2679192.0	1211042.5
53	1790	26.6	1581	2679414.0	1211703.5
52	1790	26.6	1679	2679183.5	1212011.5
51	1780	26.7	1502	2679306.0	1212472.5
49	1750	26.7	1545	2679537.0	1212535.5
17	1200	27.3	953	2679494.0	1213519.0
18	1200	27.3	968	2679556.0	1213601.0
25	1250	27.2	1046	2679112.0	1213395.5

Table SA4.14: Data of the Rigi section in the central Swiss Molasse Basin.

Site	Thickness [m]	Age [Ma]	Altitude [m]	X-Coord. (CH1903+)	Y-Coord. (CH1903+)
7	1800	26.6	1512	2685180.5	1214980.0
8	1800	26.6	1523	2685238.0	1215022.0
1	2600	25.4	1138	2685422.0	1214216.0
4	2350	25.8	1254	2685402.0	1214495.0
15	2525	25.5	990	2685543.0	1213649.5
2	2600	25.4	1171	2685438.0	1214310.0
5	1850	26.6	1296	2685394.0	1214588.5
14	2500	25.6	1012	2685542.0	1213701.0
6	1850	26.6	1316	2685387.0	1214632.5
3	2350	25.8	1215	2685431.0	1214411.0
16	2500	25.6	1030	2685543.5	1213775.0
9	2600	25.4	1156	2685474.0	1214234.0
12	1800	26.6	1370	2685416.0	1214743.0
13	2000	26.3	1459	2685387.0	1214940.5
10	2600	25.4	1206	2685498.0	1214344.0
11	1850	26.6	1334	2685463.5	1214636.0
27	2425	25.7	1198	2685637.0	1214164.0
22	1850	26.6	1377	2685788.0	1214743.0
20	2350	25.8	1361	2685820.0	1214686.0
21	1850	26.6	1402	2685805.0	1214795.0
19	2350	25.8	1375	2685840.0	1214723.0
18	2350	25.8	1397	2685869.0	1214776.0
23	2400	25.7	1302	2686107.0	1214592.0
26	2475	25.6	1216	2686205.0	1214267.0
24	2425	25.7	1275	2686178.0	1214474.0
25	2475	25.6	1238	2686400.0	1214382.0
007	2475	25.6	1303	2687178.6	1214876.1
006	2425	25.7	1329	2687372.9	1215048.2
28	2550	25.5	1132	2687602.0	1214487.0
29	2600	25.4	1082	2687871.0	1214394.0
001	2475	25.6	1320	2687691.8	1215184.9
002	2425	25.7	1363	2687677.9	1215313.1
003	2425	25.7	1353	2687691.0	1215352.5
004	2400	25.7	1425	2688050.8	1215651.3
005	2400	25.7	1429	2688076.3	1215677.5
30	2650	25.4	869	2689755.5	1215387.5
31	2650	25.4	859	2689809.0	1215449.5
32	2600	25.4	865	2689853.5	1215596.5
33	2600	25.4	874	2689854.0	1215666.5
34	2650	25.4	793	2690468.5	1215740.0
35	2650	25.4	787	2690524.5	1215899.0
36	2600	25.4	777	2690648.5	1216003.0
39	2825	25.1	804	2690888.5	1215271.5

Table SA4.15: Data of the Rossberg section in the central Swiss Molasse Basin.

Site	Thickness [m]	Age [Ma]	Altitude [m]	X-Coord. (CH1903+)	Y-Coord. (CH1903+)
37	2600	25.4	771	2690701.0	1216103.0
38	2800	25.1	816	2690999.5	1215441.5
40	2650	25.4	802	2690853.5	1216084.0
45	2650	25.4	791	2690896.0	1216327.0
41	2600	25.4	821	2690965.0	1216188.0
42	2600	25.4	830	2690998.0	1216236.5
44	2650	25.4	870	2691223.0	1216488.0
43	2600	25.4	860	2691325.5	1216497.5
46	2550	25.5	838	2691643.0	1216994.5
47	2460	25.6	893	2691701.0	1217120.0
010	2650	25.4	968	2694041.4	1218105.2
008	2600	25.4	1006	2694252.9	1218139.2
009	2600	25.4	1094	2694547.9	1218332.3
011	2900	25.0	1212	2696588.8	1218297.5
48	2940	24.9	919	2698276.0	1218342.0
49	2960	24.9	893	2701361.0	1219875.5

Table SA4.15 (continued): Data of the Rossberg section in the central Swiss Molasse Basin.

Section	MPS original (references)	MPS revised (references)	MPS used in this study	Comment
Emme	Schlunegger, 1995	-	original	
Honegg	Schlunegger et al., 1996	-	original	
Prässerenbach	Schlunegger et al., 1996	-	original	
Lake Thun	-	-	-	Calibrated to Prässerenbach; see Garefalakis et al., 2023 (Chapter 3)
Schwändigraben	Schlunegger et al., 1996	Kälin and Kempf, 2009	original	Inferred hiatus; slightly older ages at top according to Kälin & Kempf, 2009
Fontannen	Schlunegger et al., 1996	Kälin and Kempf, 2009	original	Inferred hiatus; slightly older ages at base and top according to Kälin & Kempf, 2009
Rigi	Schlunegger et al., 1997a, 1997b	-	original	
Rossberg	Schlunegger et al., 1997a, 1997b	-	original	
Thur	Kempf et al., 1999	-	original	
Steintal	Kempf et al., 1999	-	original	
Necker	Kempf et al., 1999	-	original	
Jona	Kempf et al., 1997	Kälin and Kempf, 2009	revised	No numerical differences between original and revised MPS
Goldingen	Kempf et al., 1997	Kälin and Kempf, 2009	revised	No numerical differences between original and revised MPS
Töss	-	-	-	Calibrated to Hörnli; see Garefalakis et al., 2023 (Chapter 3)
Hörnli	Kempf et al., 1997	Kälin and Kempf, 2009	revised	No numerical differences between original and revised MPS

Table SA4.16: Source publications of original and revised Magneto Polarity Stratigraphies (MPS) and indication on which framework was used to construct the age models.

Section	Fossil site	Assemblage zone	MP/MN* zone	Reference	X-/Y-Coordinates (CH1903+)
Honegg	Bumbach 1	Bumbach 1	MP25	Engesser, 1990; Schlunegger et al., 1996	2636063.18 / 1185505.63
Honegg	SEB6	Fornant 6	MP25	Schlunegger et al., 1996	2628050.32 / 1181250.81
Prässerenbach	Loch	Oensingen	MP26	Schlunegger et al., 1996	2620740.73 / 1182120.04
Prässerenbach	Trimmlen	Oensingen	MP26	Schlunegger et al., 1996	2619250.00 / 1181525.05
Prässerenbach	Losenegg 2	Boningen	MP27	Engesser, 1990; Schlunegger et al., 1996	2623245.36 / 1181659.80
Prässerenbach	Losenegg 3	Wynau 1	MP27	Engesser, 1990; Schlunegger et al., 1996	2622373.22 / 1181497.85
Prässerenbach	Cheistlisteg	Wynau 1 - Fornant 6	MP27-MP28	Schlunegger et al., 1996	2622425.12 / 1181125.50
Prässerenbach	Dürrenschwand	Fornant 6	MP28	Schlunegger et al., 1996	2624100.35 / 1179200.60
Prässerenbach	Prässerenbach	Rickenbach - Bourdry 2	MP29-MN1	Engesser, 1990; Schlunegger et al., 1996	2623750.27 / 1178709.19
Schwändigraben	Hasenbach 1	Hintersteinbruch	MN3/MN3b	Engesser, 1990; Hurni, 1991; Schlunegger et al., 1996	2639000.49 / 1198824.98
Fontannen	Hint. Eimättli	Vermes 1	MN5	Matter, 1964; Hurni, 1991; Schlunegger et al., 1996	2644750.50 / 1204555.00
Fontannen	Pulverhüsli / Eimättili	Vermes 1	MN5	Matter, 1964; Hurni, 1991; Schlunegger et al., 1996	2642638.16 / 1203487.61
Necker	OK-NEC-2	?	MP28 (±1 Zone)	Kempf, 1998	2733993.98 / 1237607.32
Goldingen	Goldinger Tobel 1	Goldinger Tobel 1	lower MN3a	Bolliger, 1992; Kempf et al., 1997	2714500.74 / 1233909.77
Goldingen	Goldinger Tobel 2	?Goldinger Tobel 1	MN3	Bolliger, 1992; Kempf et al., 1997	2714775.74 / 1234374.76
Goldingen	Goldinger Tobel 3	?Goldinger Tobel 1	MN3	Bolliger, 1992; Kempf et al., 1997	2715050.75 / 1234419.75
Goldingen	Goldinger Tobel 8	Goldinger Tobel 8	lower MN3b	Bolliger, 1992; Kempf et al., 1997	2716125.65 / 1234986.50
Goldingen	Goldinger Tobel 5/6	?Goldinger Tobel 8	MN3	Bolliger, 1992; Kempf et al., 1997	2716400.77 / 1235074.74
Goldingen / Jona	Hubertingen	?	MN4b	Löpfe et al., 2012	2713920.73 / 1235359.78
Jona	Guentisberg	?	middle MN5	Bolliger, 1992; Kempf et al., 1997	2711625.71 / 1235724.78
Jona	Bachtel-Ornberg	Bachtel-Ornberg	upper MN6	Bolliger, 1992; Kempf et al., 1997	2708899.74 / 1238106.05

* Mammal Paleogene / Mammal Neogene

Table SA4.17: Overview of Micro-Mammalian Fossil sites presented in the figures where the chronological framework was reconstructed.

4.12 Bibliography to Appendix A

Bolliger, T. (1992). Kleinsäugerstratigraphie in der miozänen Hörnlischüttung (Ostschweiz). Doc. naturae 75, pp. 1–297. (in German)
https://doi.org/10.3929/ethz-a-000666155

Engesser, B. (1990). Die Eomyidae (Rodentia, Mammalia) der Molasse der Schweiz und Savoyens. Systematik und Biostratigraphie. Schweizerische Paläontologische Abhandlungen 112, pp. 1–144. (in German)

Garefalakis, P., do Prado, A. H., Whittaker, A. C., Mair, D., and Schlunegger, F. (2023). Quantification of sediment fluxes and intermittencies from Oligo-Miocene megafan deposits in the Swiss Molasse basin. Submitted to Basin Research (28 June 2023). *See Chapter 3 of this thesis.*

Gradstein, F. M., Ogg, J. G., Schmitz, M. D., and Ogg, G. M. (2020). Geologic Time Scale 2020. 1390 pp., ISBN: 9780128243602.

Hurni, A. (1991). Geologie und Hydrogeologie des Truebtales. Unpubl. MSc thesis, University of Bern, Switzerland. (in German)

Kälin, D., and Kempf, O. (2009). High-resolution stratigraphy from the continental record of the Middle Miocene Northern Alpine Foreland Basin of Switzerland. Neues Jahrbuch für Geol. und Paläontologie - Abhandlungen 254, pp. 177–235.
https://doi.org/10.1127/0077-7749/2009/0010

Kempf, O., Bolliger, T., Kälin, D., Engesser, B., and Matter, A. (1997). “New Magnetostratigraphic Calibration of Early to Middle Miocene Mammal Biozones of the North Alpine Foreland Basin,” in Actes du Congrès BIochrom’97, eds. J. Aguilar, S. Legendre, J. Michaux, and B. Mammalienne, pp. 547–561.

Kempf, O. (1998). Magnetostratigraphy and facies evolution of the Lower Freshwater Molasse (USM) of eastern Switzerland. Unpubl. PhD thesis, University of Bern, Switzerland. pp. 283.

Kempf, O., Matter, A., Burbank, D. W., and Mange, M. (1999). Depositional and structural evolution of a foreland basin margin in a magnetostratigraphic framework: The eastern Swiss Molasse Basin. Int. J. Earth Sci. 88, pp. 253–275.
https://doi.org/10.1007/s005310050263

Löpfe, R., Zaugg, A., Schlanke, S., and Steinhauser-Zimmermann, R. (2012). Blatt 1113 Ricken - Geol. Atlas Schweiz 1:25 000, Erläut. 142. (in German)
Available at: www.swisstopo.ch

Matter, A. (1964). Sedimentologische Untersuchungen im östlichen Napfgebiet (Entlebuch - Tal der Grossen Fontanne, Kt. Luzern). Eclogae Geol. Helv. 57, pp. 315–429. (in German)

Schlunegger, F. (1995). Magnetostratigraphie und fazielle Entwicklung der Unteren Süsswassermolasse zwischen Aare und Limmat. Unpubl. PhD thesis, University of Bern, Switzerland. pp. 185. (in German)

Schlunegger, F., Burbank, D. W., Matter, A., Engesser, B., and Mödden, C. (1996). Magnetostratigraphic calibration of the Oligocence to Middle Miocene (30-15 Ma) mammal biozones and depositional sequences of the Swiss Molasse Basin. Eclogae Geol. Helv. 89, pp. 753–788.
https://doi.org/10.5169/seals-168650

Schlunegger, F., Matter, A., Burbank, D. W., and Klaper, E. M. (1997a). Magnetostratigraphic constraints on relationships between evolution of the central Swiss Molasse basin and Alpine orogenic events. GSA Bull. 109, pp. 225–241.
https://doi.org/10.1130/0016-7606(1997)109<0225:MCORBE>2.3.CO;2

Schlunegger, F., Jordan, T. E., and Klaper, E. M. (1997b). Controls of erosional denudation in the orogen on foreland basin evolution: The Oligocene central Swiss Molasse Basin as an example. Tectonics 16, pp. 823–840.
https://doi.org/10.1029/97TC01657

4.13 Appendix B

Appendix B contains i) the outcomes of the statistical test, ii) the solutions for the relative mobility function *J*, and iii) the cumulative distribution functions for the GSD, *ln*(GSD), ξ, ξ(*ln*(GSD)) for each individual stratigraphic sections, however, we do not discuss these further. See main text for details of these abbreviations.

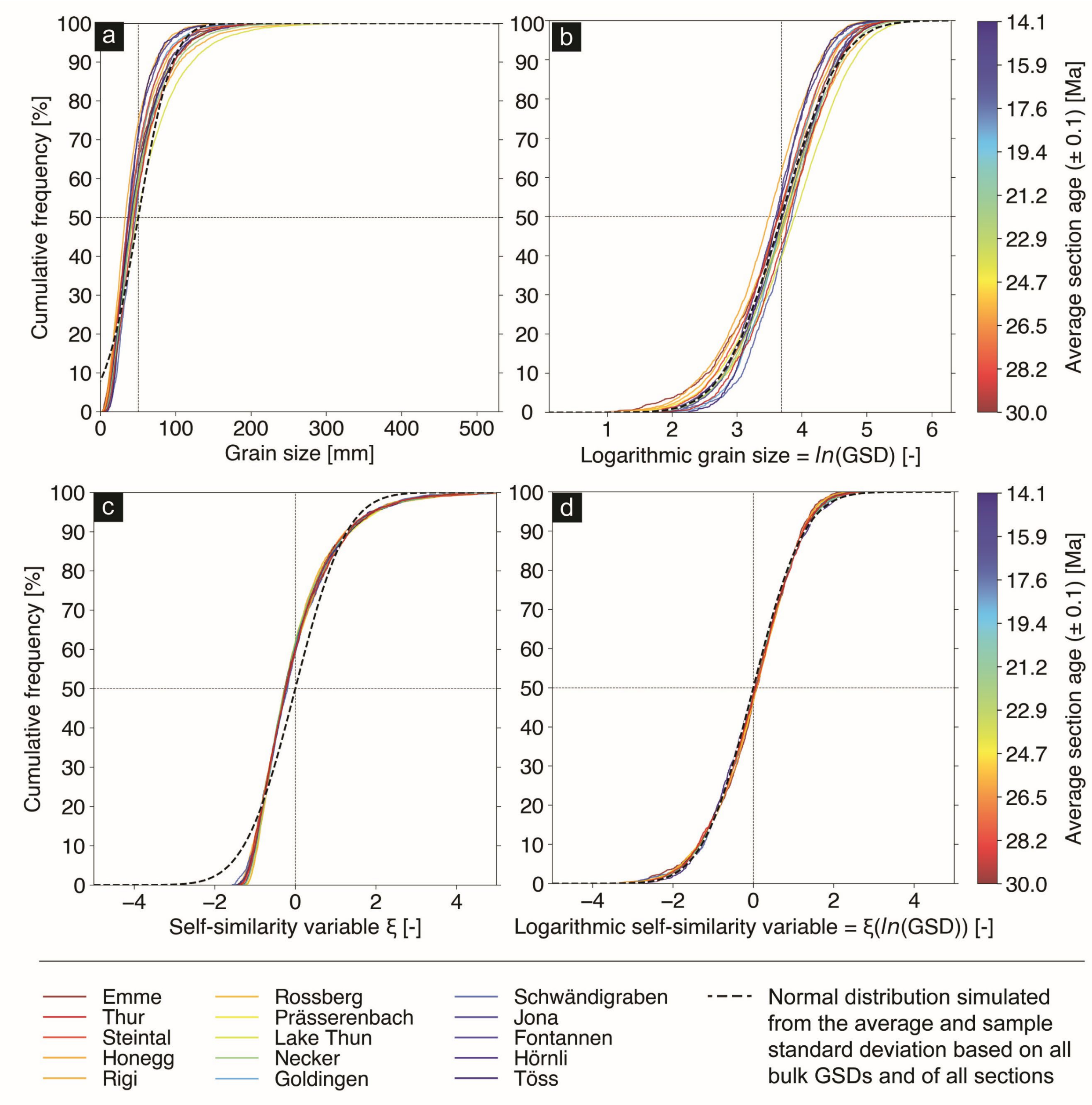

Figure SB4.1: The cumulative distribution functions for each section, now based on the entire dataset, therefore using the **a)** bulk GSD and **b)** bulk log-transformed GSD, and **c)** bulk ξ and **d)** bulk ξ values calculated from the log-transformed GSD. The dotted black line indicates a simulated normal distribution of the data for all sections. The horizontal lines in each figure mark the position of the 50th percentile of this normal distribution, and the vertical line mark the value of the 50th percentile along the x-axis. See Figure 4.5 in main text for comparison.

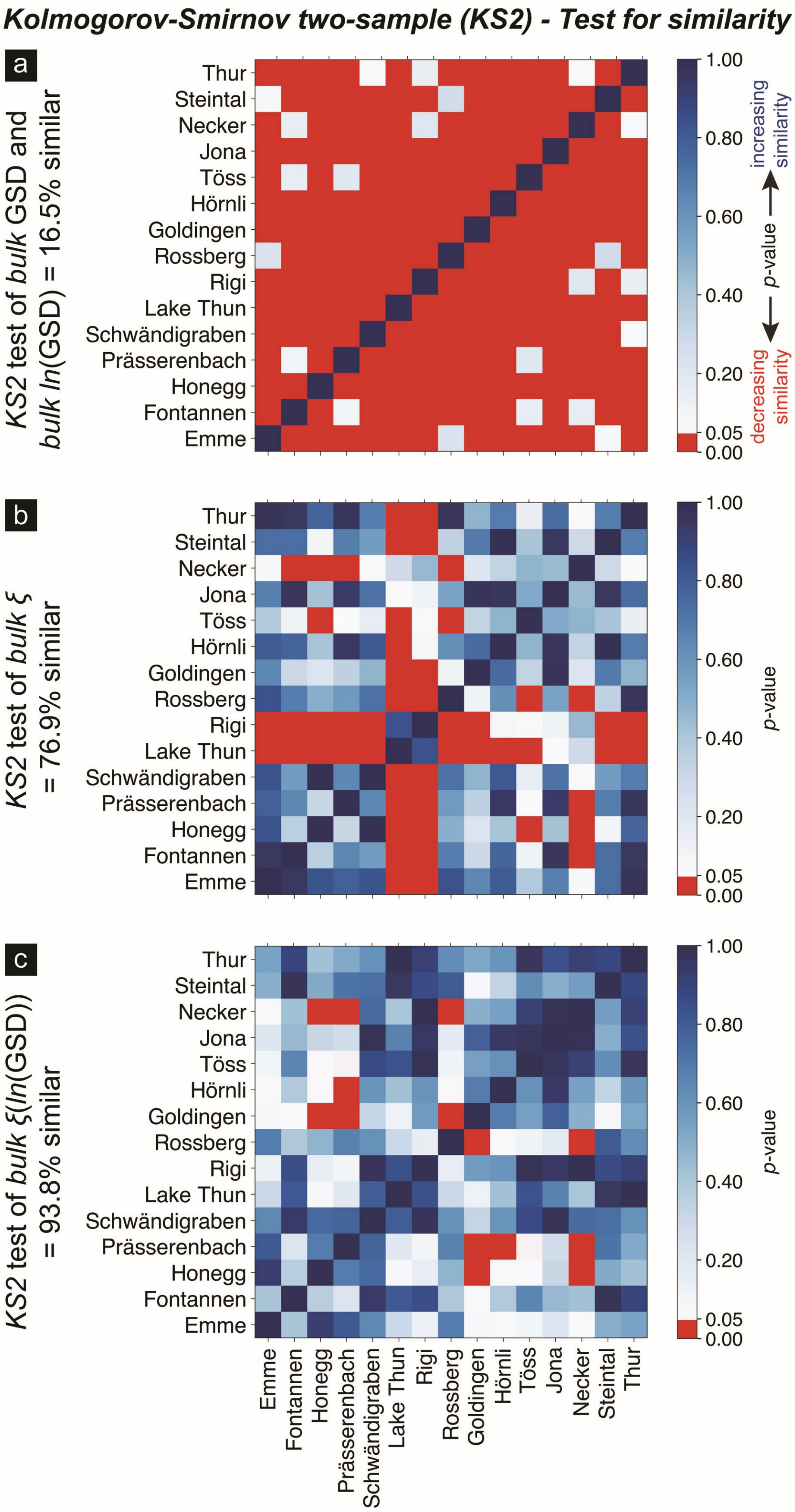

Figure SB4.2: The results of the Kolmogorov-Smirnov two-sample (*KS2*) test for similarity, now based on the entire dataset, therefore using the **a)** the bulk GSD and the log-transformed bulk GSD, **b)** the bulk self-similarity variable ξ and **c)** the ξ values calculated on the bluk log-transformed GSD. The individual datasets of all sections were cross compared against each other. The tests were computed at the 95 % C.I. (i.e., significance level of α = 0.05). See Figure 4.6 in main text for comparison.

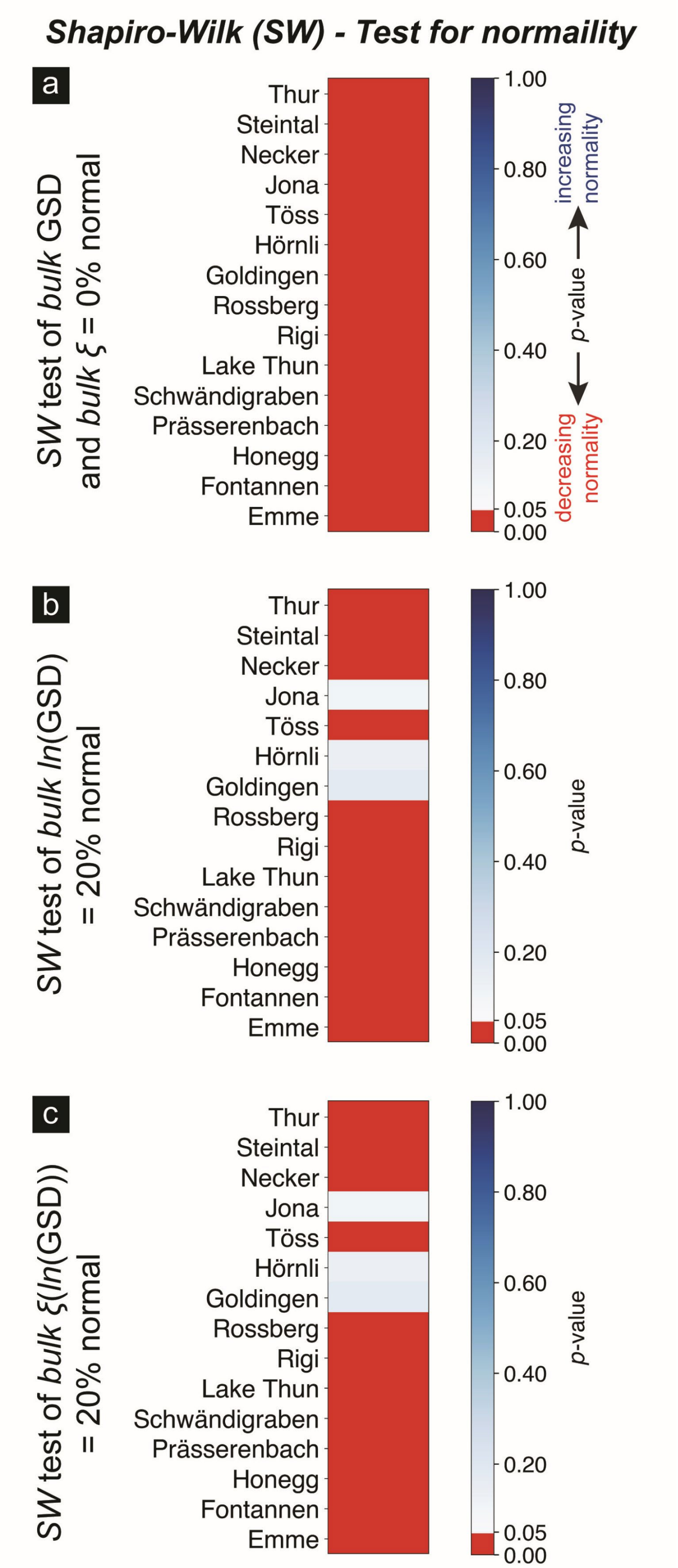

Figure SB4.3: The results of the Shapiro-Wilk (*SW*) test for normality, now based on the entire dataset, therefore using the **a)** the bulk GSD and bulk self-similarity variable ξ-distributions, **b)** the bulk log-transformed GSD, and **c)** the ξ data calculated on the bulk log-transformed GSD. The individual datasets were compared against a normal distribution simulated from the average and sample standard deviation based on the bulk GSDs of all sections. The tests were computed at the 95 % C.I. (i.e., significance level of α = 0.05). See Figure 4.7 in main text for comparison.

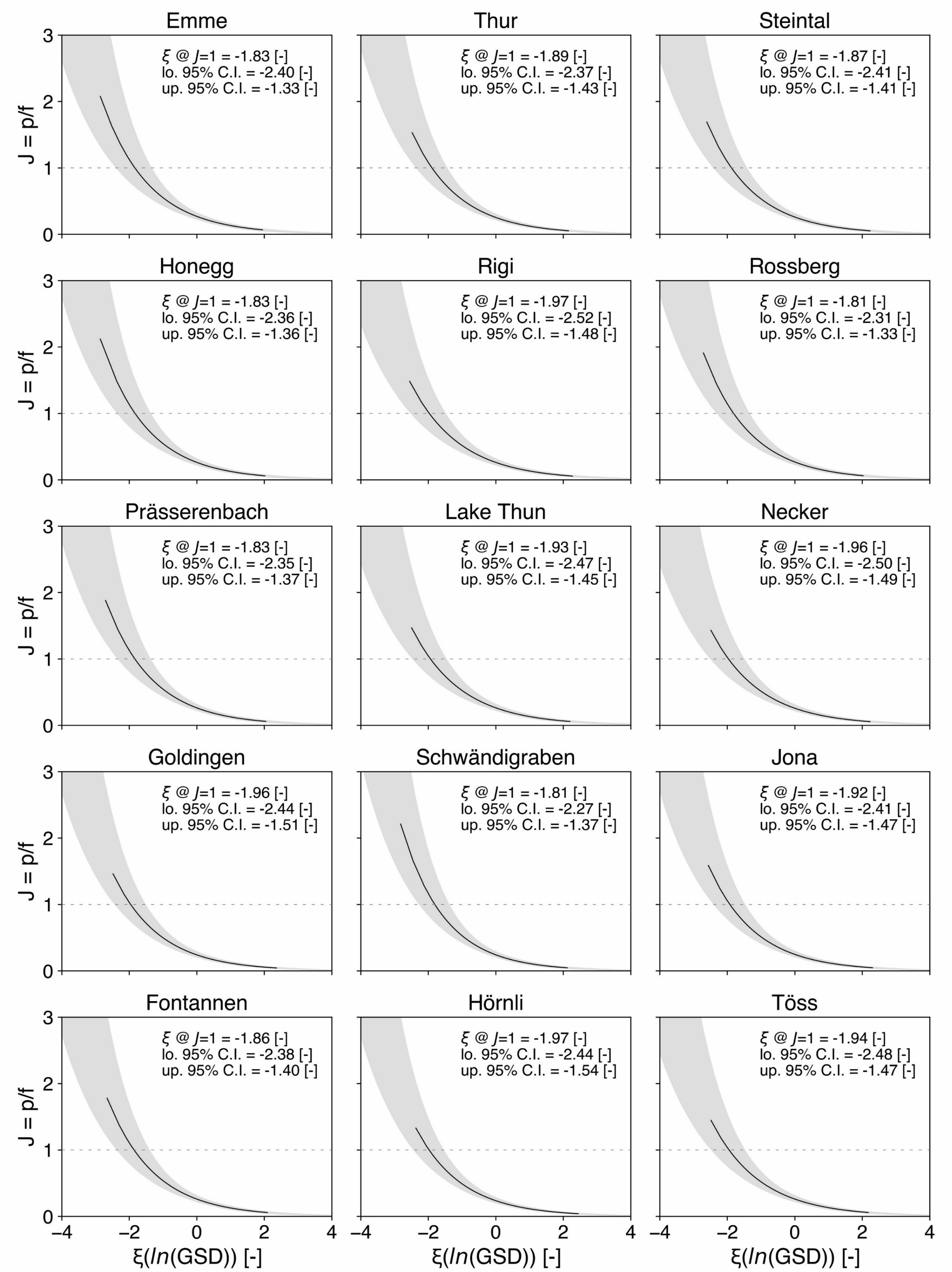

Figure SB4.4: The solutions for the relative mobility function J as a function of *ξ(ln*(GSD)) for all sections individually. The horizontal line at *J* = 1 marks the position of the critical *ξ(ln*(GSD)). The gray-shaded envelopes correspond to the 95 % confidence interval (C.I.; lo. = lower, up. upper confidence interval).

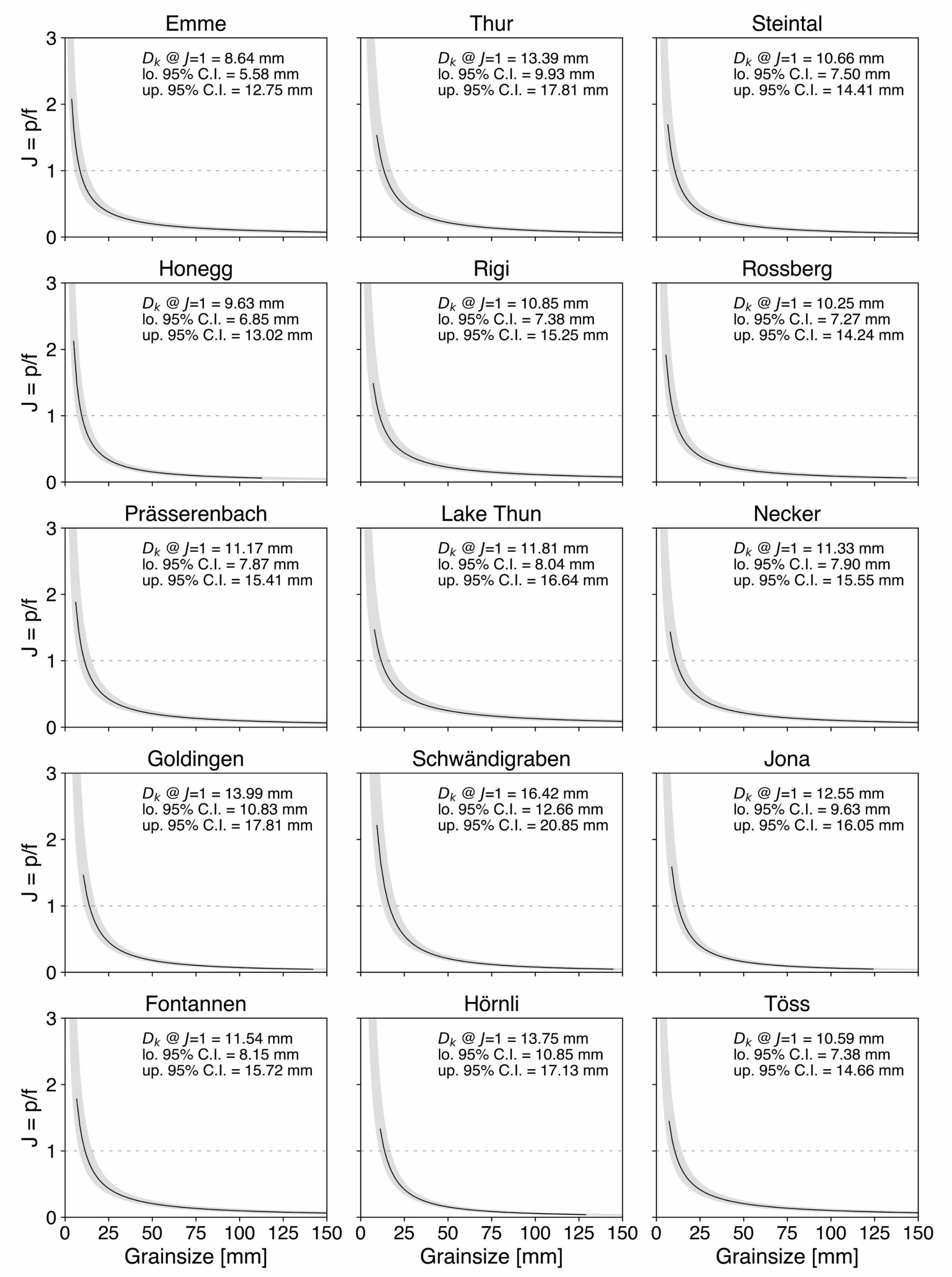

Figure SB4.5: The solutions for the relative mobility function J as a function of the back-calculated grainsize (see Eq. (4.10) in the main text), for all sections individually. The horizontal line at J = 1 marks the position of the critical grain size, which particle has the same probability of being entrained or stored in the substrate. See also main text. The gray-shaded envelopes correspond to the 95 % confidence interval (C.I.; lo. = lower, up. upper confidence interval).

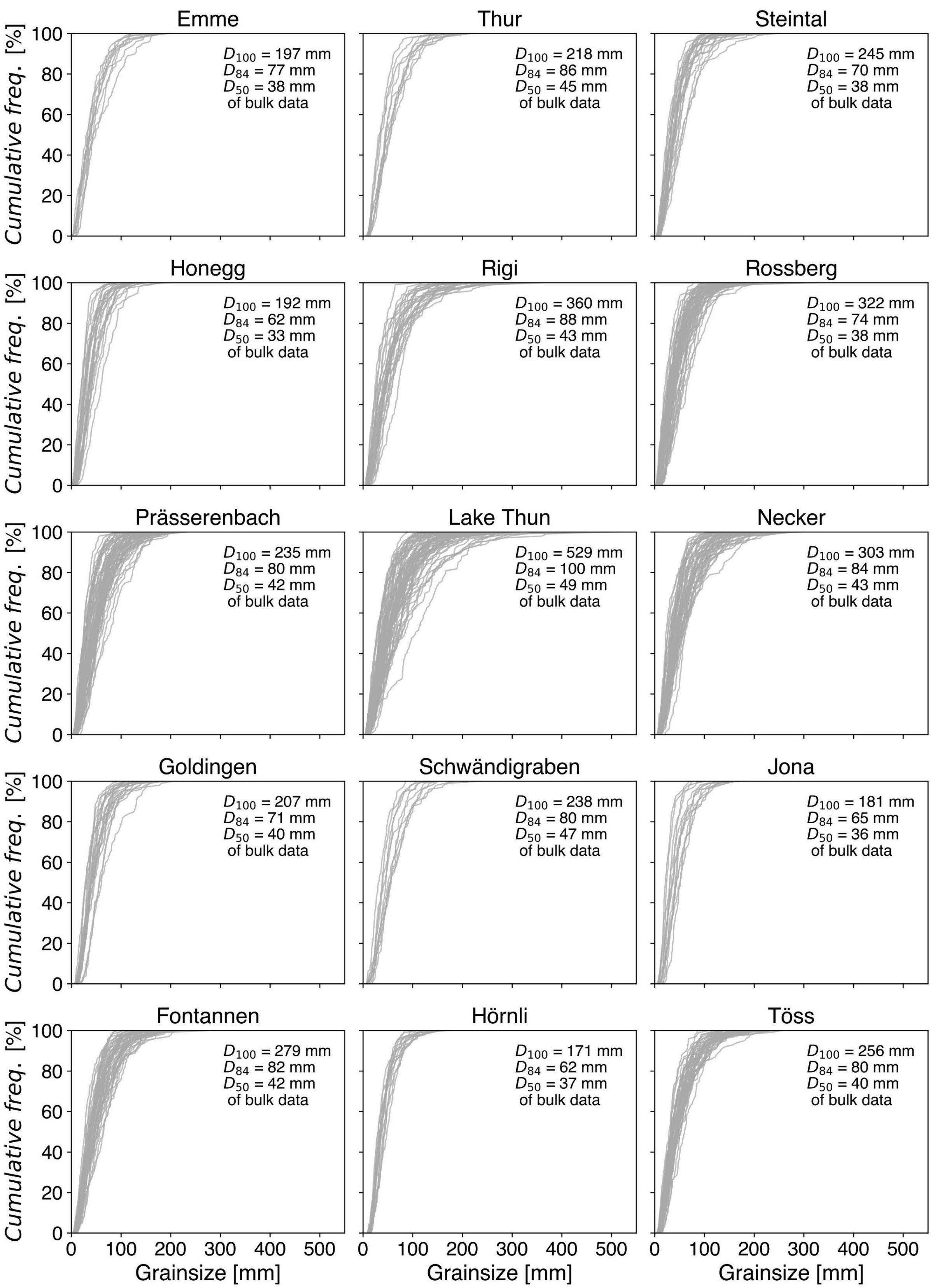

Figure SB4.6: The cumulative distribution functions for the grain size data for all sections individually. The values in the upper right correspond to the maximum (*D_{100}*) grain size and the *D_{84}* and *D_{50}* grain size percentiles of the bulk data (rounded numbers).

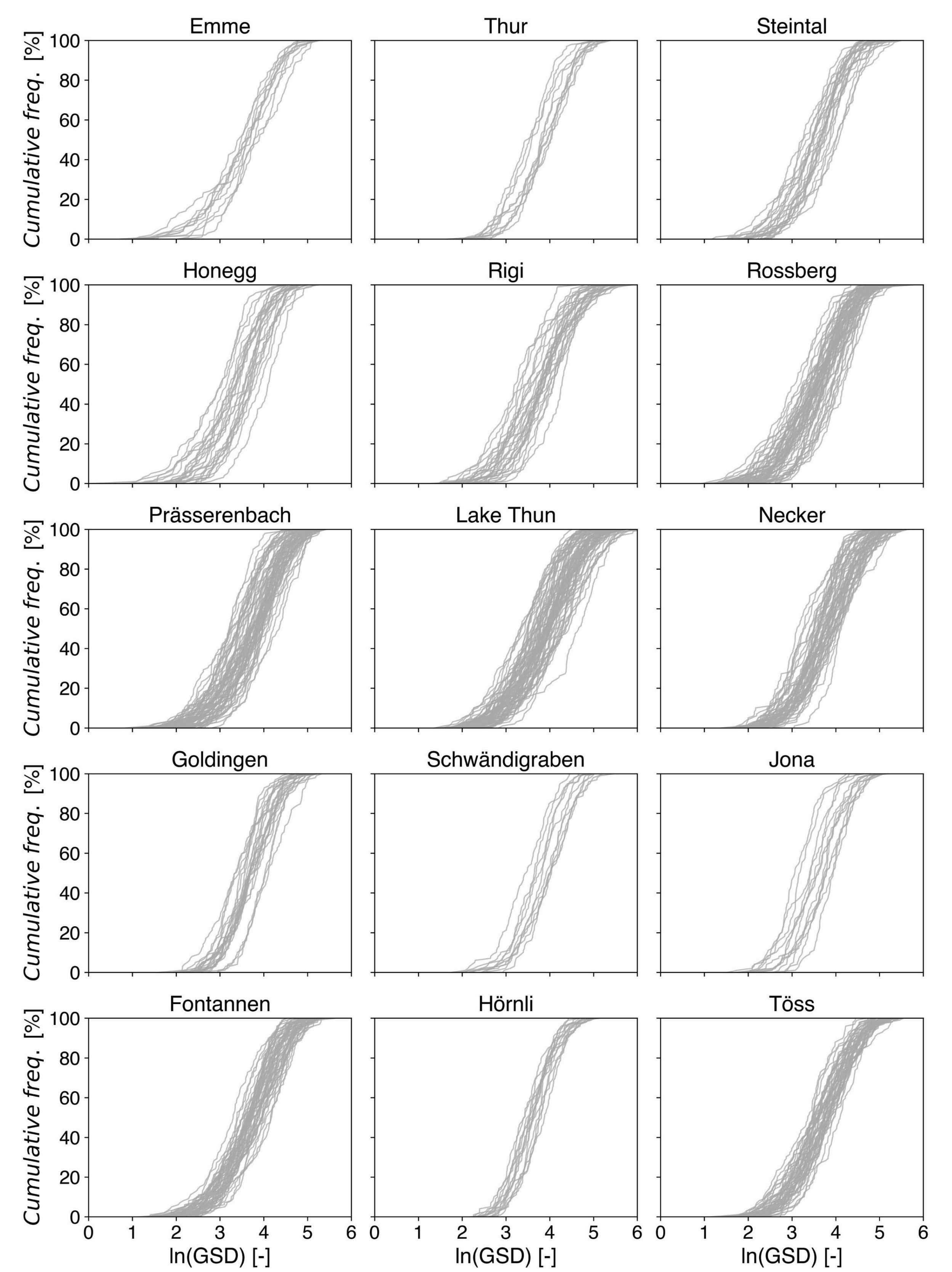

Figure SB4.7: The cumulative distribution functions for the logarithmic grain size data (ln(GSD)) for all sections individually.

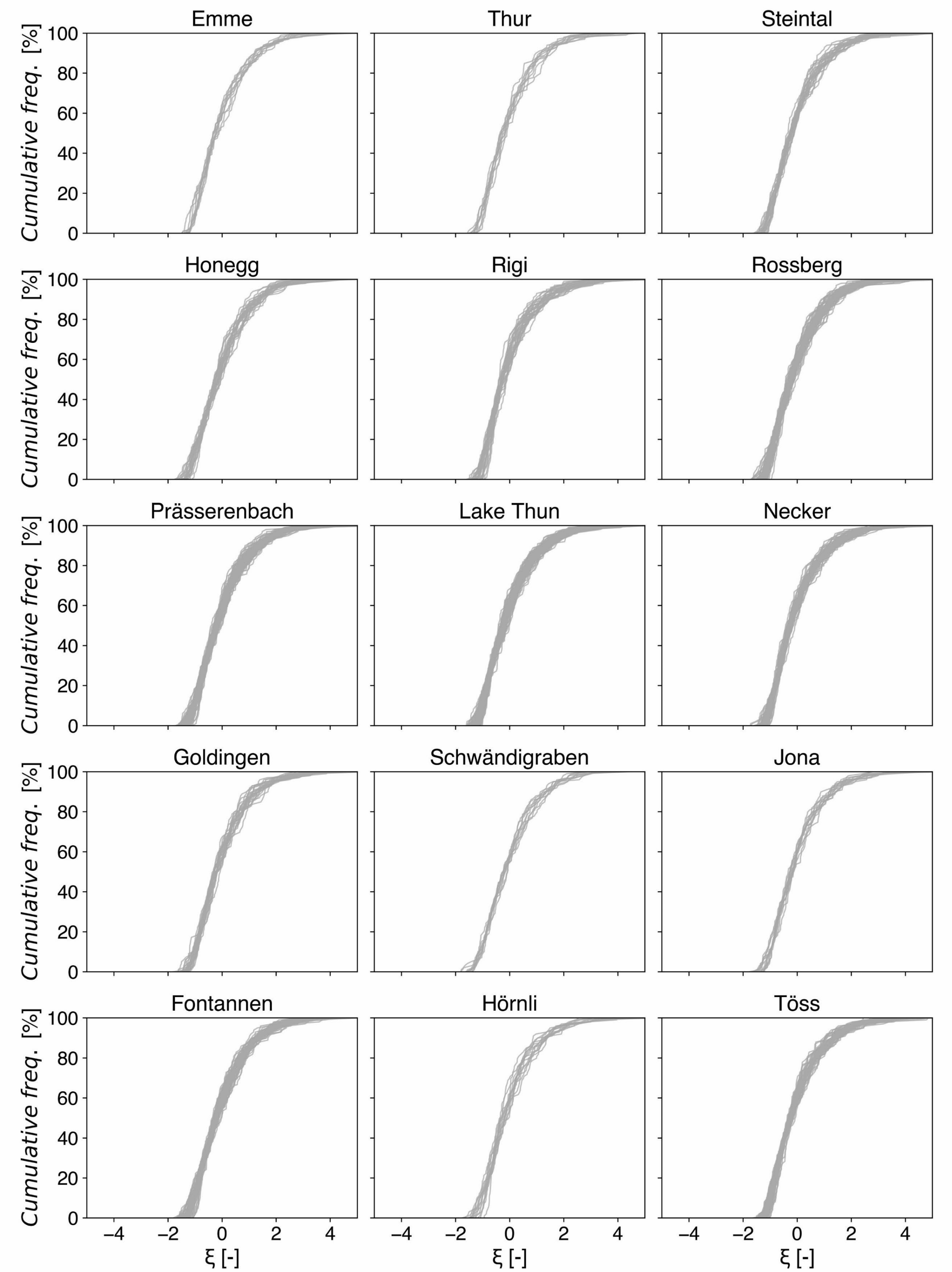

Figure SB4.8: The cumulative distribution functions for the self-similarity variable ξ for all sections individually. See main text for calculations thereof (e.g., Equation 4.2). The curves of the cumulative frequency distribution for all sites (outcrops where grain sizes were measured) per section collapse approximately on one curve, thereby revealing that the different sites are self-similar to each other. See main text for further details.

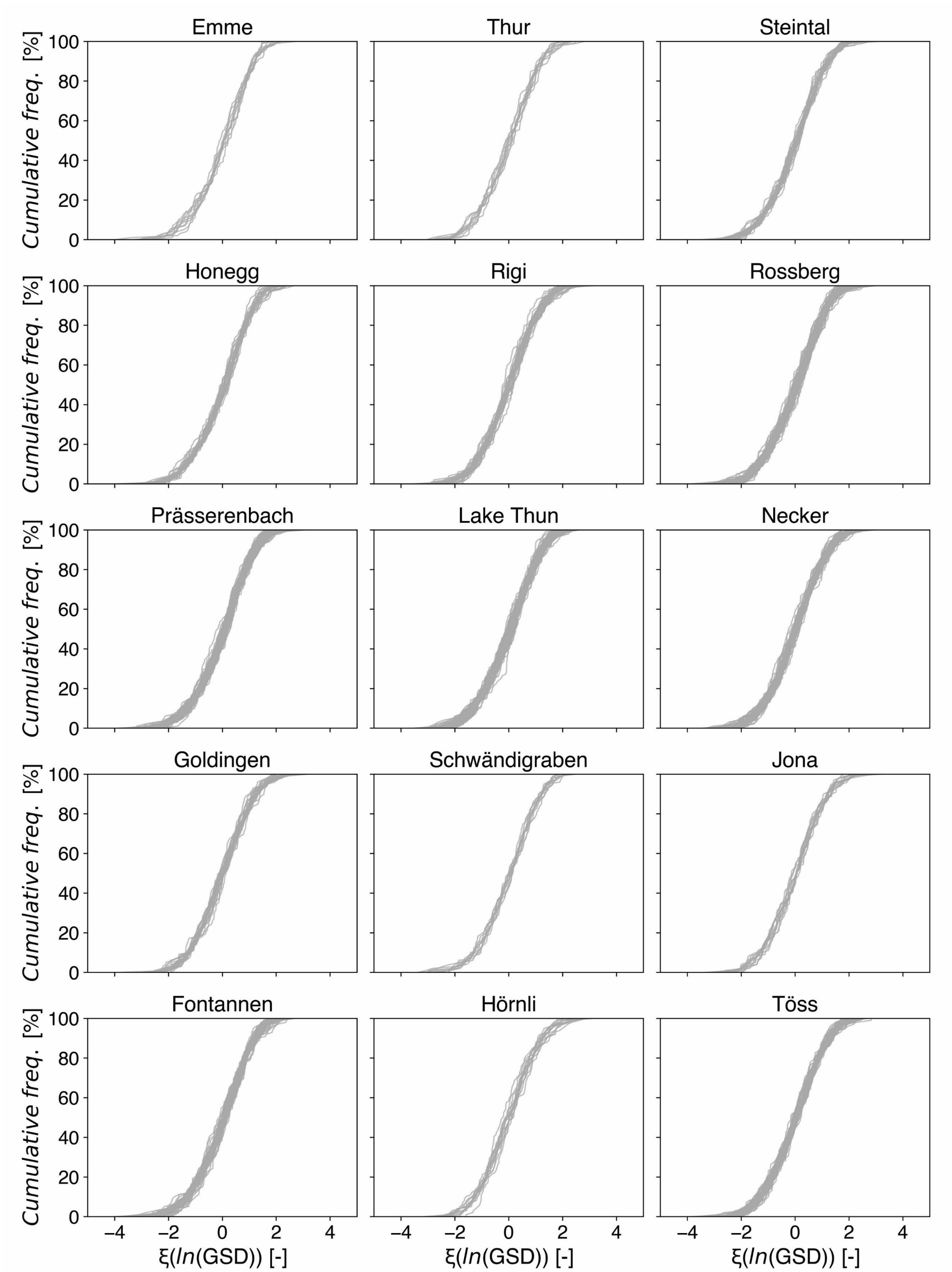

Figure SB4.9: The cumulative distribution functions for the logarithmic self-similarity variable $\xi(ln(\text{GSD}))$ for all sections individually. See main text for calculations thereof (e.g., Equation 4.2). Compared to Fig. SB4.8, the log-transformation does an even better job in collapsing all curves of the cumulative frequency distribution for all sites (outcrops where grain sizes were measured) on one curve per section. See main text for further details.

5.

Thesis conclusion

5.1 Key takeaways of the thesis

In this thesis, I provided insights on how i) grain sizes can be measured from stratigraphic deposits, ii) concepts of sediment transport models can be used to determine sediment fluxes, and related to this, how the intermittency can be calculated at the scale of individual megafan systems, and iii) the concept of relative mobility can be used to determine the critical grain size of sedimentary particles that have the same probability to be in transport or stored in the substrate. All three chapters of this thesis have in common that the related conclusions are based on grain sizes. This is because, concepts and particularly equations that characterise the transport of sedimentary clasts in a river are calibrated to the intermediate *b*-axis of a grain along which clasts are entrained, amongst the three grain axes (Meyer-Peter and Müller, 1948; Wong and Parker, 2006; Ancey, 2020). Therefore, I first summarise the outcomes of *Chapter 2*, where we aimed at providing an answer to the research question 'h*ow precisely can grain sizes be measured from conglomerate beds?'* thereby comparing three grain size measuring techniques, applied to coarse-grained deposits.

5.1.1 Grain sizes measured from stratigraphic deposits

The study outlined in *Chapter 2* was carried out in a Quaternary gravel pit (Finsterhennen, Bern; see e.g., Fig. 1.3 for location), where coarse-grained deposits are exposed as steep headwalls. The orientation of these outcrops, where we have collected the data, is oblique, and it has an orientation that is parallel and perpendicular to the dominant NE-oriented transport direction that was measured from these deposits (Pfander et al., 2022; see also Fig. 2.2). We have measured the size of grains thereby following three different measuring protocols. In particular, we i) measured grain sizes on digital photographs, ii) determined the size of the particle axes by hand and with the help of callipers, and iii) sieved the material to determine the weight of a specific grain size class, and finally transformed these values into grain sizes. In addition, for the measurements carried out on photographs, we followed two different approaches to select the grains to be measured: First, a digital grid was superimposed on the photographs, and second, randomly placed dots were generated on the photographs. We then measured the sizes of the visible axes (both, the longest visible axis, *LVA*; and the shortest visible axis, *SVA*) of the particles that were either marked by a grid-intersection point or by a randomly placed dot. In addition, we were interested in how photo-specific factors could influence the outcomes of our grain size measurements. Therefore, we conducted two approaches where we measured the grains (placed beneath a grid intersection or a dto, see above) both on the original photographs, which come along with distortion effects brought on by the camera lens, and on the ortho-corrected photographs. We applied a statistical test (Kolmogorov-Smirnov test; see section 2.3.4.2 for description) to determine whether the different photo-formats (distorted and ortho-corrected) and measuring techniques (grid and dots) yield the same results. Finally, we compared the outcomes of all measuring approaches, here represented by three grain size percentiles D_{16}, D_{50} and D_{84}, using a statistical test to quantify the deviation of the grain size percentiles from the 1:1 line in a X:Y-diagram (the line where X=Y; e.g., Fig. 2.5). This was done upon calculating the *Concordance Correlation Coefficient* (*CCC*; see section 2.3.6 for description).

We concluded in *Chapter 2* that grain size measurements from outcrops is best achieved by photo-analysis of the deposits. Our study revealed that the grain sizes measured on both photo-types (distorted and ortho-corrected) generally yielded the same results for all cross-comparisons. We also found that the results were not dependent on whether the grains to be measured were selected underneath intersections of lines (grid) or beneath randomly placed dots. Furthermore, the obtained grain size datasets seem to be independent of the outcrop orientation in relation to the paleo-discharge direction measured from these (Pfander et al., 2022). Upon comparing the different grain size percentiles from the various measuring techniques with each other, the measurements of the *LVA* on photos yielded datasets that have a good correlation to the grain size data which we established through sieving of the same material. When compared to the sizes of the *b*-axis measured by hand and calliper, both, the photo- and sieving-approaches tend to underestimate the *b*-axis by c. 17 % and 15 %, respectively. Likewise, the shortest visible axis (*SVA*) from the photo datasets underestimates the *c*-axes measured by hand and calliper by c. 24 %. If the underlying grain size distribution is consequently corrected for such a ratio, then both distributions (i.e., from the dataset measured by hand and calliper and from that measured on the images) yield almost identical values within related uncertainties. This is particularly the case for the grain size percentiles D_{16} and D_{50}. A good agreement between both datasets also remained for the D_{84} after such a correction was applied (Fig. 2.7a).

In summary, *Chapter 2* highlights how grains from stratigraphic deposits can be measured and statistically analysed, thereby providing estimates on their uncertainties. It additionally shows that the lengths of the intermediate *b*-axis of particles are likely underestimated by 17 % if measured from matrix- or grain-supported deposits.

5.1.2 Sediment fluxes and intermittencies calculated from the stratigraphic record

Chapter 3 provides insights on how we determined sediment fluxes and intermittencies for coarse-grained stratigraphic deposits recording the construction of alluvial fan sedimentation in the Swiss Molasse. The related calculations arise from the self-similar grain size fining model (Fedele and Paola, 2007), that allows to estimate the long-term sediment flux, and from equations of sediment transport that allow to determine the short-term instantaneous sediment flux or bedload flux (Meyer-Peter and Müller, 1948). The ratio of these sediment fluxes is defined as the intermittency factor – a measure for the system's activity – yielding an estimate on how frequently a river accomplishes its transport work on a yearly basis.

The self-similar grain size fining model builds on the basis that, in a fluvial system, grain sizes system decrease in the downstream direction because of selective deposition and entrainment of different-sized clasts (Fedele and Paola, 2007). An important aspect is that this grain size fining occurs at a given ratio between the mean and the standard deviation, which can be expressed as the self-similarity variable ξ (e.g., Equation 3.5). In a fluvial system, the related values remain approximately constant for any site at a given downstream position. We provided statistical analyses to validate whether this is true for any fan, thereby applying the Kolmogorov-Smirnov test (section 3.3.3.1). Furthermore, the self-similar grain size fining model has the advantage that it provides estimates on a system's sediment flux, upon acquiring data on the grain size and information on the subsidence only. To this end, we measured grain sizes along three sections, where the proximal-distal relationships of alluvial fan sedimentation is still preserved, which we named, for simplicity, the western, central and eastern fans (i.e., Lake Thun, Rigi-Rossberg and Töss-Hörnli sections, respectively, see for locations e.g., Fig. 1.3). The chronological framework of these fans has been established by previous authors (Schlunegger et al., 1996, 1997a; Kempf and Matter, 1999), but has been recalibrated to the recent Geologic Time Scale GTS2020 (Gradstein et al., 2020). Together with information on the thicknesses of the stratigraphic sections, we were able to calculate the sediment accumulation rates, which can be assumed as a proxy of the local subsidence beneath the fans. Given this dataset, we applied the self-similar grain size fining model for the first time to stratigraphic deposits encountered in the Swiss Molasse Basin. In addition, we implemented the governing equations into a combined bootstrapping and Monte Carlo framework, to statistically determine our outcomes at the 95 % confidence level.

The results outlined in *Chapter 3* showed that the grain size values disclosed a fining trend from proximal towards distal locations on the paleo-fans. The western fan has the most prominent decrease in grain sizes from c. 100 mm at the inferred apex, to c. 30 mm 11 km farther downsystem, whereas the central and eastern fans revealed a decrease from c. 50 to 30 mm along c. 32 and 12 km, respectively (e.g., Fig. 3.6). When the grain size data is transformed into the self-similarity variable ξ (see above), the data of any individual site where we measured grain sizes all collapsed on the same curve (Fig. 3.9). Therefore, we could show that the dataset for each of the fan system is self-similar when the transformation into the self-similarity variable ξ is applied. This suggests that the sorting of the material on downstream locations of these fans remained approximately constant. This is additionally supported by the outcomes of the Kolmogorov-Smirnov test, that yielded almost identical results if the data from all sites are cross-compared to each other (Fig. 3.9). This shows that the underlying datasets are statistically similar to each other.

We then applied the grain size fining model to estimate the long-term sediment fluxes that were recorded by the stratigraphic deposits of the three fans. The results yielded largely different values for each fan. The western fan recorded a sediment flux of c. 17 $km^2\ Myr^{-1}$, the central fan of c. 39 $km^2\ Myr^{-1}$ and the eastern fan of c. 7 $km^2\ Myr^{-1}$, with related uncertainties expressed by the 95 % confidence level (see e.g., Table 3.1 for these values and uncertainties thereof). The calculations of the bedload fluxes, which is a measure for how much sediment a paleoriver could transport throughout the year, revealed similar patterns for the three fans. The rivers on the western fan could have transported c. 9000 $km^2\ Myr^{-1}$, the rivers on the central and western fans both c. 6000 $km^2\ Myr^{-1}$ (Table 3.1). The ratio of these sediment flux estimates provides an approximation of the intermittency of these dispersal systems. Consequently, the western fan could have accomplished its mean annual transport work in c. 17 $h\ yr^{-1}$, the central fan in 55 $h\ yr^{-1}$, and the eastern fan in 10 $h\ yr^{-1}$. These outcomes suggest that the paleorivers that were recorded by deposits exposed along the three analysed proximal-distal sections, accomplished their sedimentary work between a few hours and up to a few days per year. Amongst the three fans, the central fan was, however, the most active system, whereas both the western and eastern fans were probably more intermittent.

We interpreted that the tectono-geomorphological evolution of the adjacent Central Alps had a strong influence on the paleorivers and thus the related transport work of these. This was particularly the case of the western and central systems, albeit sharing similar climatic conditions. In that context, the formation of the central fan was most likely controlled by the legacy of the slab break-off of the oceanic lithosphere of the European plate at c. 32 – 30 Ma (Schlunegger and Castelltort, 2016), whereas the western fan was constructed when the related environmental adjustments reached a balance between crustal uplift and surface erosion. For the eastern fan, we discussed that the exhumation of the crystalline external massifs and associated tectonic unroofing in the core of the Alps possibly reduced the sediment supply to the Swiss Molasse Basin. This reduction occurred because of a reorganisation of the drainage network in the Central Alps, with the consequence that the flow-paths became longer and less steep (Kühni and Pfiffner, 2001). We considered that the low supply rates of sediment explains the low activity of the dispersal systems on the eastern fan.

In summary, *Chapter 3* highlights that reconstructions of the sediment flux budgets and the intermittencies of the paleorivers on alluvial megafans offer an ideal tool to unravel the dynamics of these routing systems. And the study revealed how the evolution of the Central Alps influenced the construction of stratigraphic sections that recorded alluvial fan sedimentation in the Swiss Molasse.

5.1.3 Estimates on the relative mobility for the stratigraphic record

In *Chapter 4*, we applied the concept of relative mobility to estimate the competence of the paleostreams to transfer the supplied material (Fedele and Paola, 2007). In this context, the relative mobility function *J* can be used to compute such relative mobility, and the corresponding results can be deviated from grain size datasets alone (Equation 4.3). For the case where $J = 1$, sediment particles with a given size have the same probability of being entrained or deposited in the substrate (see sections 4.3 and 4.4.4 for details). We considered this specific grain size as the critical grain size. We thus established a set of grain size data, measured from 15 stratigraphic sections that are situated in the Swiss Molasse. The analysed stratigraphic sections were placed in a chronological framework by previous authors (Schlunegger et al., 1996; Kempf et al., 1997; Schlunegger et al., 1997a; Kempf and Matter, 1999), which we recalibrated to the Geologic Time Scale GTS2020 (Gradstein et al., 2020). The sections record sedimentation on alluvial fans and cover the time span between c. 31 and 13 Ma.

Because the application of the concept of the relative mobility implicitly requires the underlying grain size data to follow a normal distribution, we applied a logarithmic transformation on the dataset. Furthermore, the grain size data needs to be transformed into the self-similarity variable ξ (see above and e.g., Equation 4.2), which is a procedure where at a given site each grain size value is normalised by the mean and standard deviation. The grain size dataset, which we collected from the stratigraphic sections, was statistically analysed, and we applied tests to validate if two datasets are similar to each other (Kolmogorov-Smirnov test, section 4.4.3) and if the datasets follow a normal distribution (Shapiro-Wilk test, section 4.4.3). Following the statistical analyses of the grain size data, their transformation and the calculation of the relative mobility expressed by a critical grain size (see above), we finally aimed at estimating how grain sizes and the relative mobility changed through time and space in the Swiss Molasse basin.

The results of *Chapter 4* showed that the values of the D_{84} and D_{50} grain size percentiles are on average c. 40 and 80 mm, respectively. The statistical test for normality revealed that the underlying grain size distributions (GSD) do follow a log-normal distribution. Accordingly, a transformation into logarithmic space is necessary (*ln*(GSD)). Likewise, upon transforming the grain size distributions into the self-similarity variable ξ, related distributions are similar to each other when the data of all stratigraphic sections are cross-compared (e.g., Fig. 4.5). Moreover, the same test for similarity applied to the ξ-distributions, but calculated on the log-transformed GSDs, revealed a higher statistical similarity between the various distributions determined for the different sections. Therefore, for the following calculations of the relative mobility, we considered the ξ(*ln*(GSD)) dataset only. The results showed that the dispersal systems could in average entrain particles that had grain sizes smaller than c. 12 mm (e.g., Fig. 4.12).

Finally, we compared these outcomes to changes in the tectonic processes in the source area, the sediment supply, and the climate conditions, particularly during the time when the conglomerates were accumulating in the Molasse basin. Because these conditions largely control the grain sizes on the alluvial fans, we would have expected large differences through time. However, a comparison of the D_{84} and D_{50} grain size percentiles, to the aforementioned driving forces revealed no obvious correlations at the scale of the basin. We therefore suggested that the formation rate of accommodation space and the rate at which sediment was supplied to the fans, occurred in pace. This yielded in grain size values that were approximately constant through time and at the scale of the basin (Fig. 4.13). We acknowledge, that if grain sizes did change through time, the differences were too small to be statistically significant. Furthermore, at c. 20 Ma, the Molasse basin experienced a transgression of the Burdigalian seaway (Allen et al., 1985) and a backstepping of the depocenters of the alluvial megafans (Schlunegger and Norton, 2015). The combination of these was considered to have occurred because of a reduction of sediment supply to the basin. The development of the sedimentary facies thus recorded such shifts in the controlling conditions at the basin scale, however, the granulometric properties of grains are possibly not as sensitive to such driving forces as sedimentary environments. Likewise, shifts in grain sizes alone might not be fully conclusive for inferring changes of the tectonic and erosional processes in the Alpine hinterland.

In summary, *Chapter 4* provided insights into the tectono-geomorphologic evolution of the Swiss Molasse Basin and the Central Alps, which influenced the construction of alluvial megafans, that were preserved as stratigraphic sections. The concept of relative mobility was applied for the first time to these Oligo-Miocene deposits, thereby revealing that the dispersal systems on the related fans were only capable to transport grains that had sizes smaller than c. 12 mm.

5.2 Critical reflexion and outlook

One of our professors at the Institute of Geological Sciences in Bern always reminded us that "*a good thesis is never completely finished*". There is always room for improvement and (re-)validation of the data and their interpretation. In this section, I thus aim to critically reflect on some of the main findings or related concepts.

As a major scientific output of *Chapter 2*, we suggested that a correction applied to grain size data, related to the values of the longest visible axis (*LVA*) measured on photographs, improves the correlation between the sizes of the *LVA* and the *b*-axis of a grain, of which the latter was measured by hand and with a calliper and exposes the full length of this intermediate grain axis. The experiment of the study was carried out on loosely-packed Quaternary gravels, which disclose some differences to densely-packed and cemented Oligo-/Miocene conglomerate beds discussed in *Chapters 2* and *3*. These conglomerate beds, for instance, experienced post-depositional compaction due to their burial (Kuhlemann et al., 2002). However, both types of deposits also share a high similarity in their architecture, such as the arrangement of clasts or the sedimentary structures of the entire conglomerate bed. This is likely a consequence of the underlying transport processes, which were similar for both type of sediments. In this regard, although the Finsterhennen gravel pit records sequences of glacio-fluvial deposits, the layer we examined was predominantly of fluvial origin (Pfander et al., 2022). This is important because the shape of particles is also related to the size of the intermediate axis (Zingg, 1935; Blott and Pye, 2007). Because the predominantly glacially transported clasts have a more angular geometry (Pfander et al., 2022), the related axes' are probably different. Consequently, despite the minor differences, these two types of deposits (gravels and conglomerates) share similarities regarding their architecture and the underlying processes leading to these sediments. Therefore, the reader might wonder why I did not apply a correction on the grain size values for the studies outlined in *Chapters 3* and *4*. There are several explanations for this, but I would like to emphasise some points which I consider to be more relevant:

- First off, our proposed ratios to correct a potential underestimation of the intermediate *b*-axis from stratigraphic deposits might be different for various types of sediments, although the presented outcomes are in good agreement with the results of similar experiments that were, notably, also carried out on fluvial gravels (Adams, 1979; Storz-Peretz and Laronne, 2013; Stähly et al., 2017). Therefore, the application of our proposed correction factor is likely limited to similar and fluvial deposits only.

- Second, grain size measurements are always related to uncertainties (e.g., measuring errors, biases due to undersampling or statistical uncertainties upon calculating specific grain size percentile values). As outlined in *Chapter 2*, the average statistical uncertainties (at the 95 % confidence level) of the grain size percentiles D_{16}, D_{50} and D_{84} calculated from the values from the photo measurements (both *LVA* and *SVA*) were c. ±16, ±13, and ±14 %, respectively (e.g., section 2.6). The proposed correction factor is on average c. +17%. Therefore, a correction of the grain size data is likely already included by the spread of the uncertainties.

- Third, and probably most important, such a correction applied to the obtained grain size data, yields in most of the cases a linear shift of the desired results. Therefore, the pattern or trends might not change at all. However, there exist several cases where a correction is likely more appropriate. For instance, when the grain size data measured from sediments will be used to solely determine the paleohydraulics of a system; or when the goal is to compare the related outcomes to those of recent deposits. In such cases, a correction is suitable, not only because related concepts are mainly based on estimates of grain sizes, but also because the variables in the underlying equations include exponentiation operations, which might change the related outcomes drastically.

- Finally – grain size acquisition techniques underwent major advances over the last few years. For instance, more recently, automatic identification of grains in digital images have strongly improved (e.g., Purinton and Bookhagen, 2019; Mair et al., 2023). Future applications with a focus on measuring grain sizes in images will likely apply such methods, which likely yield more precise measurements, measured in shorter time and larger quantities of measured grains. However, despite these improvements, these more recent methods still face the problem of grain occlusion, particularly when measuring particles from stratigraphic deposits. Therefore, a corresponding correction of the acquired grain size data is still appropriate.

Therefore, and based on these reasons, as our grain size dataset of *Chapter 3* was used to determine the intermittency of alluvial fans, which we cross-compared amongst similar systems that were constructed in the geological past, we did not aim at comparing the outcomes to recent analogues or providing estimates of the various sediment budgets only. Likewise, *Chapter 4* also considered grain size data as the basis, however, a correction thereof would likely result in a linear shift of our outcomes, but the presented pattern would not change. Therefore, we did not apply any correction on the data that we used in *Chapters 3* and *4*, respectively, which I consider as acceptable regarding the related purposes.

The outcomes of *Chapters 3* and *4* include an application of several models, which were the grain size fining model and the related relative mobility (Fedele and Paola, 2007). These concepts have been applied to Cenozoic stratigraphic deposits (Duller et al., 2010; Whittaker et al., 2011; Parsons et al., 2012; Allen et al., 2013) as well as to more recent Quaternary deposits, for both, active and inactive systems (D'Arcy et al., 2017; Brooke et al., 2018; Harries et al., 2018). The underlying concepts and equations have been thoroughly reviewed by related researchers and implemented in different programming languages (e.g., in Matlab; Brooke et al., 2018). The advantage of using such computational implementations clearly lies in the relatively well-established approaches to calculate and propagate uncertainties for various parameters and variables. Likewise, such implementations also do offer a basis to critically review related equations. Unfortunately, although given the precious and very advancing research that has been done on these concepts, we still lack a quantitative revision of the underlying models. Although e.g., Duller et al. (2010) or also Armitage et al. (2011) provided us with a prosperous analysis thereof, both of these authors come to the conclusion that the limitations of the model arises from the calculations that were done in ACRONYM4 (Parker, 1991). Consequently, a thorough revision of the underlying concepts, specifically implemented in the ACRONYM4 model, could highly improve the quality of the grain size fining model, and further strengthen its application. As suggestion, the implementation of the Fedele & Paola (2007) model into the landscape evolution model *fastscape* (Braun and Willett, 2013) could yield a critical review on the governing equations.

5.3 Bibliography

Adams, J., 1979. Gravel Size Analysis from Photographs. Journal of the Hydraulics Division 10, pp. 1247–1255. https://doi.org/10.1061/JYCEAJ.0005283

Allen, P. A., Armitage, J. J., Carter, A., Duller, R. A., Michael, N. A., Sinclair, H. D., et al. (2013). The *Qs* Problem: Sediment volumetric balance of proximal foreland basin systems. Sedimentology 60, pp. 102–130. https://doi.org/10.1111/sed.12015

Allen, P. A., Mange-Rajetky, M. A., Matter, A., and Homewood, P. (1985). Dynamic paleogeography of the open Burdigalian seaway, Swiss Molasse Basin. Eclogae Geol. Helv. 78, pp. 351–381. https://doi.org/10.5169/seals-165661

Ancey, C. (2020). Bedload transport: a walk between randomness and determinism. Part 1. The state of the art. J. Hydraul. Res. 58, pp. 1–17. https://doi.org/10.1080/00221686.2019.1702594

Armitage, J. J., Duller, R. A., Whittaker, A. C., and Allen, P. A. (2011). Transformation of tectonic and climatic signals from source to sedimentary archive. Nat. Geosci. 4, pp. 231–235. https://doi.org/10.1038/ngeo1087

Blott, S. J., and Pye, K. (2007). Particle shape: A review and new methods of characterization and classification. Sedimentology 55, pp. 31–63. https://doi.org/10.1111/j.1365-3091.2007.00892.x

Braun, J., and Willett, S. D. (2013). A very efficient O(n), implicit and parallel method to solve the stream power equation governing fluvial incision and landscape evolution. Geomorphology 180–181, pp. 170–179. https://doi.org/10.1016/j.geomorph.2012.10.008

Brooke, S. A. S., Whittaker, A. C., Armitage, J. J., D'Arcy, M., and Watkins, S. E. (2018). Quantifying Sediment Transport Dynamics on Alluvial Fans From Spatial and Temporal Changes in Grain Size, Death Valley, California. J. Geophys. Res. Earth Surf. 123, pp. 2039–2067. https://doi.org/10.1029/2018JF004622

D'Arcy, M., Whittaker, A. C., and Roda-Boluda, D. C. (2017). Measuring alluvial fan sensitivity to past climate changes using a self-similarity approach to grain-size fining, Death Valley, California. Sedimentology 64, pp. 388–424. https://doi.org/10.1111/sed.12308

Duller, R. A., Whittaker, A. C., Fedele, J. J., Whitchurch, A. L., Springett, J., Smithells, R., et al. (2010). From grain size to tectonics. J. Geophys. Res. Earth Surf. 115, pp. 1–19. https://doi.org/10.1029/2009JF001495

Fedele, J. J., and Paola, C. (2007). Similarity solutions for fluvial sediment fining by selective deposition. J. Geophys. Res. Earth Surf. 112, pp. 1–13. https://doi.org/10.1029/2005JF000409

Gradstein, F. M., Ogg, J. G., Schmitz, M. D., and Ogg, G. M. (2020). Geologic Time Scale 2020. 1390 pp., ISBN: 9780128243602.

Harries, R. M., Kirstein, L. A., Whittaker, A. C., Attal, M., Peralta, S., and Brooke, S. (2018). Evidence for Self-Similar Bedload Transport on Andean Alluvial Fans, Iglesia Basin, South Central Argentina. J. Geophys. Res. Earth Surf. 123, pp. 2292–2315. https://doi.org/10.1029/2017JF004501

Kempf, O., Bolliger, T., Kälin, D., Engesser, B., and Matter, A. (1997). "New Magnetostratigraphic Calibration of Early to Middle Miocene Mammal Biozones of the North Alpine Foreland Basin," in Actes du Congrès BIochrom'97, Eds. J. Aguilar, S. Legendre, J. Michaux, and B. Mammalienne, pp. 547–561.

Kempf, O., and Matter, A. (1999). Magnetostratigraphy and depositional history of the Upper Freshwater Molasse (OSM) of eastern Switzerland. Eclogae Geol. Helv. 92, pp. 97–103. https://doi.org/10.5169/seals-168650

Kempf, O., Matter, A., Burbank, D. W., and Mange, M. (1999). Depositional and structural evolution of a foreland basin margin in a magnetostratigraphic framework: The eastern Swiss Molasse Basin. Int. J. Earth Sci. 88, pp. 253–275. https://doi.org/10.1007/s005310050263

Kuhlemann, J., Frisch, W., Sz, B., and Dunkl, I. (2002). Post-collisional sediment budget history of the Alps: tectonic versus climatic control. pp. 818–837. https://doi.org/10.1007/s00531-002-0266-y

Kühni, A., and Pfiffner, O. A. (2001). Drainage patterns and tectonic forcing: A model study for the Swiss Alps. Basin Res. 13, pp. 169–197. https://doi.org/10.1046/j.1365-2117.2001.00146.x

Mair, D., Witz, G., Do Prado, Ariel H., Garefalakis, P., and Schlunegger, F. (2023). Automated detecting, segmenting and measuring of grains in images of fluvial sediments: The potential for large and precise data from specialist deep learning models and transfer learning. Earth Surf. Proc. And Landforms, pp. 1-18. https://doi.org/10.1002/esp.5755

Meyer-Peter, E., and Müller, R. (1948). Formulas for Bed-Load Transport. Proc. 2nd Meet. Int. Assoc. Hydraul. Res., pp. 39–64. http://resolver.tudelft.nl/uuid:4fda9b61-be28-4703-ab06-43cdc2a21bd7

Parker, G. (1991). Selective sorting and abrasion of river gravel. I: Theory. J. Hydraul. Eng. 117, pp. 131–147. https://doi.org/10.1061/(ASCE)0733-9429(1991)117:2(131)

Parsons, A. J., Michael, N. A., Whittaker, A. C., Duller, R. A., and Allen, P. A. (2012). Grain-size trends reveal the late orogenic tectonic and erosional history of the south-central Pyrenees, Spain. J. Geol. Soc. London. 169, pp. 111–114. https://doi.org/10.1144/0016-76492011-08

Pfander, J., Schlunegger, F., Serra, E., Gribenski, N., Garefalakis, P., and Akçar, N. (2022). Glaciofluvial sequences recording the Birrfeld Glaciation (MIS 5d–2) in the Bern area, Swiss Plateau. Swiss J. Geosci. 115. https://doi.org/10.1186/s00015-022-00414-z

Purinton, B., and Bookhagen, B. (2019). Introducing PebbleCounts: A grain-sizing tool for photo surveys of dynamic gravel-bed rivers. Earth Surf. Dyn., pp. 1–33. https://doi.org/10.5194/esurf-7-859-2019

Schlunegger, F., Burbank, D. W., Matter, A., Engesser, B., and Mödden, C. (1996). Magnetostratigraphic calibration of the Oligocence to Middle Miocene (30-15 Ma) mammal biozones and depositional sequences of the Swiss Molasse Basin. Eclogae Geol. Helv. 89, pp. 753–788. https://doi.org/10.5169/seals-168650

Schlunegger, F., and Castelltort, S. (2016). Immediate and delayed signal of slab breakoff in Oligo / Miocene Molasse deposits from the European Alps. Nat. Sci. Rep. 6, pp. 1–11. https://doi.org/10.1038/srep31010

Schlunegger, F., Matter, A., Burbank, D. W., and Klaper, E. M. (1997a). Magnetostratigraphic constraints on relationships between evolution of the central Swiss Molasse basin and Alpine orogenic events. GSA Bull. 109, pp. 225–241. https://doi.org/10.1130/0016-7606(1997)109<0225:MCORBE>2.3.CO;2

Schlunegger, F., Matter, A., Burbank, D. W., Leu, W., Mange, M., and Màtyàs, J. (1997b). Sedimentary sequences, seismofacies and evolution of depositional systems of the Oligo/Miocene Lower Freshwater Molasse Group, Switzerland. Basin Res. 9, pp. 1–26. https://doi.org/10.1046/j.1365-2117.1997.00029.x

Schlunegger, F., and Norton, K. P. (2015). Climate vs. tectonics: The competing roles of late oligocene warming and alpine orogenesis in constructing alluvial megafan sequences in the north alpine foreland basin. Basin Res. 27, pp. 230–245. https://doi.org/10.1111/bre.12070

Stähly, S., Friedrich, H., and Detert, M. (2017). Size ratio of fluvial grains' intermediate axes assessed by image processing and square-hole sieving. J. Hydraul. Eng. 143, pp. 1–6. https://doi.org/10.1061/(ASCE)HY.1943-7900.0001286

Storz-Peretz, Y., and Laronne, J. B. (2013). Automatic grain sizing of vertical exposures of gravelly deposits. Sediment. Geol. 294, pp. 13–26. https://doi.org/10.1016/j.sedgeo.2013.05.004

Whittaker, A. C., Duller, R. A., Springett, J., Smithells, R. A., Whitchurch, A. L., and Allen, P. A. (2011). Decoding downstream trends in stratigraphic grain size as a function of tectonic subsidence and sediment supply. pp. 1363–1382. https://doi.org/10.1130/B30351.1

Wong, M., and Parker, G. (2006). Reanalysis and Correction of Bed-Load Relation of Meyer-Peter and Müller Using Their Own Database. J. Hydraul. Eng. 132, pp. 1159–1168. https://doi.org/10.1061/(ASCE)0733-9429(2006)132:11(1159)

Zingg, T. (1935). Beitrag zur Schotteranalyse. Schweiz. Miner. Petrogr. Mitt. 15, pp. 39–140. (in German) https://doi.org/10.3929/ethz-a-000103455

List of Figures

Chapter 1

Chapter 2

Chapter 3

Chapter 4

List of Tables

Chapter 2

Chapter 3

Please note, the figures and tables presented in the appendices are not listed here.

Declaration of Consent

on the basis of Article 18 of the PromR Phil.-nat. 19

Name/First Name:	Garefalakis, Philippos
Registration Number:	14-109-144
Study program:	Doctorate, Phil. Nat., University of Bern
	Bachelor ☐ Master ☐ Dissertation ☑
Title of the thesis:	Quantifying Sediment Dynamics and Grain Size Characteristics in the Swiss Molasse and Quaternary Deposits
Supervisors:	Prof. Dr. Fritz Schlunegger, University of Bern
	Prof. Dr. Alexander C. Whittaker, Imperial College London

I declare herewith that this thesis is my own work and that I have not used any sources other than those stated. I have indicated the adoption of quotations as well as thoughts taken from other authors as such in the thesis. I am aware that the Senate pursuant to Article 36 paragraph 1 litera r of the University Act of September 5th, 1996 and Article 69 of the University Statute of June 7th, 2011 is authorized to revoke the doctoral degree awarded on the basis of this thesis.

For the purposes of evaluation and verification of compliance with the declaration of originality and the regulations governing plagiarism, I hereby grant the University of Bern the right to process my personal data and to perform the acts of use this requires, in particular, to reproduce the written thesis and to store it permanently in a database, and to use said database, or to make said database available, to enable comparison with theses submitted by others.

Place, Date Bern, 8th December 2023

Philippos Garefalakis